Spring 2018

Instabilities in nematic liquid crystal films and droplets

Michael-Angelo Y.-H. Lam
New Jersey Institute of Technology

ABSTRACT

INSTABILITIES IN NEMATIC LIQUID CRYSTAL FILMS AND DROPLETS

by
Michael-Angelo Y.-H. Lam

The dynamics of thin films of nematic liquid crystal (NLC) are studied. Nematic liquid crystals are a type of non-Newtonian fluid with anisotropic viscous effects (due to the shape of the molecules) and elasticity effects (due to interacting electrical dipole moments). Exploiting the small aspect ratio in the geometry of interest, a fourth-order non-linear partial differential equation is used to model the free surface of the thin films. Particular attention is paid to the interplay between the bulk elasticity and the preferred orientation (boundary condition) of NLC molecules at the two interfaces: the substrate and the free surface. This work is a collection of three previously published papers and some recent unpublished work. Two main topics are covered: 1) the flow of thin films of NLC down an inclined substrate under gravity, and 2) the stability of thin NLC films on a horizontal substrate under the influence of surface tension, internal elastic effects, and fluid/solid interactions. Using a combination of analytical and computational techniques allows for a novel understanding of relevant instability mechanisms, and of their influence on transient and fully developed fluid film morphologies. While the analytical results in this thesis focus on NLC films, these results may be extended to a variety of other thin film models. Finally, a numerical code that utilizes a graphics processor unit (GPU) is presented, and the significant performance gains are discussed.

INSTABILITIES IN NEMATIC LIQUID CRYSTAL FILMS AND DROPLETS

by
Michael-Angelo Y.-H. Lam

A Dissertation
Submitted to the Faculty of
New Jersey Institute of Technology
and Rutgers, The State University of New Jersey–Newark
in Partial Fulfillment of the Requirements for the Degree of
Doctor of Philosophy in Mathematical Sciences

Department of Mathematical Sciences, NJIT
Department of Mathematics and Computer Science, Rutgers–Newark

May 2018

APPROVAL PAGE

INSTABILITIES IN NEMATIC LIQUID CRYSTAL FILMS AND DROPLETS

Michael-Angelo Y.-H. Lam

Dr. Linda J. Cummings, Dissertation Co-Advisor Date
Professor of Mathematical Sciences and Associate Dean, New Jersey Institute of Technology, Newark, NJ

Dr. Lou Kondic, Dissertation Co-Advisor Date
Professor of Mathematical Sciences and Director of CAMS, New Jersey Institute of Technology, Newark, NJ

Dr. Shahriar Afkhami, Committee Member Date
Associate Professor of Mathematical Sciences, New Jersey Institute of Technology, Newark, NJ

Dr. Catalin C. Turc, Committee Member Date
Associate Professor of Mathematical Sciences, New Jersey Institute of Technology, Newark, NJ

Dr. Thomas P. Witelski, Committee Member Date
Professor of Mathematics, Duke University

BIOGRAPHICAL SKETCH

Author: Michael-Angelo Y.-H. Lam

Degree: Doctor of Philosophy

Date: May 2018

Undergraduate and Graduate Education:

- Doctor of Philosophy in Mathematical Sciences,
  New Jersey Institute of Technology, Newark, NJ, 2018
- Master of Science in Mathematical Sciences,
  New Jersey Institute of Technology, Newark, NJ, 2010
- Bachelor of Science in Applied Mathematics and Applied Physics,
  New Jersey Institute of Technology, Newark, NJ, 2009

Major: Mathematical Sciences

Publications:

M.-A. Y.-H. Lam, M. Malej, F. Shi, and K. Ghosh, Profiling and optimization of FUNWAVE-TVD on high performance computing (HPC) machines. *Technical Report CHETN-X-X.* USACE Engineer Research and Development Center (in print) (2018).

M.-A. Y.-H. Lam, L. J. Cummings, and L. Kondic, Stability of thin fluid films characterised by a complex form of effective disjoining pressure. *J. Fluid Mech.* 841, 925-961 (2018).

M. A. Lam, L. J. Cummings, T.-S. Lin, L. Kondic, Three-dimensional coating flow of nematic liquid crystal on an inclined substrate. *Europ. J. Appl. Maths.* 26 647-669, (2015).

M. A. Lam, L. J. Cummings, T.-S. Lin, L. Kondic, Modeling flow of nematic liquid crystal down an incline. *J Eng. Math.* 6 97-113, (2014).

Presentations:

Instability in nematic liquid crystal films and GPU computing. *NJIT CAMS Research Day*, Newark, NJ, 2018.

Growth and interaction of colloid nuclei. *American Physical Society 70th Annual Division of Fluid Dynamics Meeting*, Denver, CO, 2017.

Optimization in FUNWAVE-TVD with parallel I/O. *FUNWAVE-TVD Workshop*, University of Delaware, Newark, DE, 2017.

Weak free surface anchoring model for partially wetting nanoscale nematic liquid crystal films. *Society for Industrial and Applied Mathematics Conference on Computational Science and Engineering*, Atlanta, GA, 2017.

Nucleation type instabilities in partially wetting nanoscale nematic liquid films. *American Physical Society 69th Annual Division of Fluid Dynamics Meeting*, Portland, OR, 2016.

Instabilities in nematic liquid crystals films and drops. *American Physical Society 68th Annual Division of Fluid Dynamics Meeting*, Boston, MA, 2015.

Modeling flow of nematic liquid crystal down and incline. *American Physical Society 66th Annual Division of Fluid Dynamics Meeting*, Pittsburgh, PA, 2013.

Posters:

The growth of colloid nuclei under Microgravity. *Dana Knox Student Research Showcase*, New Jersey Institute of Technology, Newark, NJ, 2018.

Weak free surface anchoring model for partially wetting nanoscale nematic liquid crystal films. *Dana Knox Student Research Showcase*, New Jersey Institute of Technology, Newark, NJ, 2017.

Instabilities in thin nematic liquid crystal films. *13th Annual Conference on Frontiers in Applied and Computational Mathematics*, New Jersey Institute of Technology, Newark, NJ, 2016

Diffusion limited aggregation and Saffman-Taylor instability in non-Newtonian Hele-Shaw flow. *13th Annual Conference on Frontiers in Applied and Computational Mathematics*, New Jersey Institute of Technology, Newark, NJ, 2016

Mathematical model for thin nematic liquid crystal films. *Dana Knox Student Research Showcase*, New Jersey Institute of Technology, Newark, NJ, 2015.

Instabilities in 3D flow of nematic liquid crystal films down an incline. *11th Annual Conference on Frontiers in Applied and Computational Mathematics*, New Jersey Institute of Technology, Newark, NJ, 2014

Glycerol & nematic liquid crystal in a Hele-Shaw cell: electric field effects. *10th Annual Conference on Frontiers in Applied and Computational Mathematics*, New Jersey Institute of Technology, Newark, NJ, 2013

To my parents, Linda and Michael.

ACKNOWLEDGMENT

I would first like to give thanks to my dissertation advisors, Linda Cummings and Lou Kondic, for, without their support, guidance, and great patience, I would not have reached my potential. They have taught me the intricacies of performing research, and more importantly, and to their own frustration, the importance of communicating results to a wider audience. I would also like to thank my advisors for giving me the freedom to pursue my interest in scientific computing. Next, I want to give thanks to my committee members Shahriar Afkhami, Catalin Turc, and Thomas Witelski, for their advice has helped me think more critically about research.

I would also like to thank David Horntrop for his mentorship during my early career that led me from an undergraduate student to a doctoral candidate. Next, I would like to thank Michael Booty, for giving me the benefit of the doubt, allowing me the opportunity to improve myself. I would also like to give thanks to the Department of Mathematical Sciences, which has guided me from a freshman to the completion of my doctoral degree and has dealt with me for the past thirteen years. I also acknowledge the support by NSF Grants DMS-0908158, DMS-1211713, and CBET 1604351.

I would also like give thanks to my high school teachers, Julie Arthur, John Jackson, and Tim Pascoe, for their support and latitude (sometimes to their own annoyance) who inspired my love for mathematics and physics; and nurtured my dream to reach this point.

Lastly, I would like to give thanks my family. First, my parents, Linda and Michael (Kwok-Leung), for all their love and support gave me a happy life. Their hard work has given me opportunities they never had, making this all possible. I would also like to thank my older siblings, Elliott and Kimberly, for always looking out for me, despite being the annoying little brother. Lastly, I would like to give thanks to

my family, my extended family, and my friends back in the Bahamas, for my fondest memories are of the times we spent together, and leaving the Bahamas to pursue my career was the hardest decision I made in my life.

TABLE OF CONTENTS

TABLE OF CONTENTS
(Continued)

Chapter **Page**

TABLE OF CONTENTS
(Continued)

Chapter **Page**

LIST OF TABLES

LIST OF FIGURES

Figure **Page**

LIST OF FIGURES
(Continued)

Figure **Page**

LIST OF FIGURES
(Continued)

Figure **Page**

LIST OF FIGURES
(Continued)

Figure **Page**

LIST OF FIGURES
(Continued)

Figure **Page**

LIST OF FIGURES
(Continued)

Figure **Page**

LIST OF FIGURES
(Continued)

Figure **Page**

LIST OF FIGURES
(Continued)

Figure **Page**

LIST OF FIGURES
(Continued)

Figure **Page**

LIST OF FIGURES
(Continued)

Figure **Page**

CHAPTER 1

INTRODUCTION

In many industrial applications involving fluid films, the geometry is such that the film thickness is small relative to typical lateral dimensions of the film. Exploiting this difference in scales, a long wave (lubrication) approximation to the governing equations for fluid flow may be derived and the spatial dimension of the problem reduced by one. Within this framework, the flow of thin layers (films) of fluids has been studied under a variety of physical configurations, e.g. [5–19].

Thin films of liquid crystals (LCs), and particularly of nematic liquid crystals (NLCs), find wide industrial application in display devices, due to their optical properties (birefringence) and electric field response. The reader is referred to the books by Castellano [20] and Johnstone [21] for a history of liquid crystal display (LCD) development. The dielectric tensor for NLC is anisotropic which may lead to very large refractive indices, a property used in the design of superlenses, capable of overcoming the resolution limits of conventional imaging techniques (diffraction limit) [22]. The dielectric property may also be used to accurately control electromagnetic waves, a desired feature in the design of devices for the purposes of optical imaging, space communication and object detection by lasers [23]. The reader is referred to the review paper by Palffy-Muhoray [23] for more information on these and many other applications.

Nematic liquid crystals (NLC) are fluid-like substances typically composed of rod like molecules with a dipole moment associated with the anisotropic axis (the axis parallel with the length of the rod-like molecule). The interactions of the dipole moments cause molecules to align locally, giving rise to an elastic response; however, in general, fluid flow and external forces may distort the local alignment. Therefore, liquid crystals behave as a state of matter intermediate between a fluid,

where molecules are allowed to flow, and a solid, having some short-range order to orientation of molecular. In addition, due to the anisotropic rheology (rod-like molecules), viscosity depends on fluid flow relative to the local orientation of molecules.

At a surface or interface, nematic liquid crystal molecules have a preferred orientation, a phenomenon known as anchoring. The local molecular orientation is characterized by a *director field*: a unit vector representing the average direction of the long axis of the molecules. Liquid crystal in the hybrid aligned nematic (HAN) state has a specific molecular orientation: the polar angle (with respect to the normal to the substrate), θ, of the liquid crystal molecules varies linearly over the film thickness, that is, $\theta = c_1 z + c_2$, where c_1 and c_2 are constants determined by the anchoring conditions and z is aligned with the polar axis $\theta = 0$.

This thesis is divided into four parts and is a collection of three previously published papers [24–26] and some current work yet to be published. The first two chapters discuss the flow of the thin NLC film down an inclined substrate. In the first chapter, the governing equation is simplified to two-dimensional flow, and we focus on traveling-wave solutions, which may translate stably or exhibit instabilities in the flat film behind the traveling front. These instabilities which are parallel to the flow, are distinct from the usual transverse instability of downslope flow and may be analyzed and explained by linear stability analysis of a flat translating film. In the second chapter, these results are extended to three-dimensional flow, and we investigate the interactions between the parallel instabilities and transverse instabilities.

There last two chapters of this thesis focus on instabilities (dewetting) of flat films of NLC on a horizontal substrate. The third chapter focuses on two-dimensional flow where a combination of analytical and computational techniques allows us to reach novel understanding of relevant instability mechanisms, and of their influence on transient and fully developed fluid film morphologies. In particular, we discuss in detail the patterns of drops that form as a result of instability, and how the

properties of these patterns are related to the instability mechanisms. The fourth chapter extends these results to three-dimensional flow and discusses numerical code developed by the author that utilizes GPUs allowing simulations of large domain sizes to be performed that are not feasible with serial CPU computations. The capability to simulate on large domains is essential to extend our results from two-dimensional to three-dimensional flow.

We also note that while this thesis focuses on thin films of NLC, the analytical techniques presented may be applied to other thin film models, and the GPU code may be easily modified to simulate other thin film models.

CHAPTER 2

MODELING FLOW OF NEMATIC LIQUID CRYSTAL DOWN AN INCLINE

One approach to modeling the spreading of nematic liquid crystal droplets is within the framework of the long wave approximation. Within this context, different anchoring conditions have been considered, including various combinations of weak anchoring and strong anchoring (a Dirichlet condition on the director field) at the free surface and underlying substrate [5, 12, 14, 16, 27, 28]. In an alternative approach, energetic arguments were used to derive an equation governing free surface evolution [29]. This approach leads to predictions that differ from those of earlier work [5, 27, 28]. The differences between the approaches were recently reconciled [12, 13], leading to consistent predictions.

In experiments [30–32], spreading droplets of nematic liquid crystals exhibit a diverse range of instabilities. Moreover, these instabilities exists in regimes where a Newtonian droplet would be stable. In this chapter we consider a paradigm problem that highlights some key features of NLC coating flows and the differences with Newtonian cases [10, 15]: the flow of a thin film of NLC down an inclined substrate. This chapter builds upon an earlier model [16] and modifies the free surface conditions to be thermodynamically consistent [17]. The resulting long wave model is a modified version of that model presented in [12], containing an additional term related to the component of gravity in the downslope direction.

2.1 Model Derivation

As was noted by Rey and Denn [33], the Leslie-Ericksen equations [34] are applicable for NLC composed of rigid rod-like molecules with no spatiotemporal variations in the scalar order parameter (a measure of how well a unit vector represents the local

average orientation of LC molecules). Moreover, it was noted that the Leslie-Ericksen equations have been very successful in modeling NLCs with low molar mass. For other materials, such as NLC polymers (flexible rods), there may exist spatiotemporal dependencies in the order parameter, and other theories may be more appropriate to describe such flows: for example, the Landau-de Gennes tensor model (a generalization of the Leslie-Ericksen theory) or the Doi theory (a probabilistic description). In this thesis, variations in the scalar order parameter are not considered, and we work with the Leslie-Ericksen theory throughout. The reader is referred to the review paper by Rey and Denn [33] for further information on the strengths and weaknesses of the various models.

The main dependent variables within the Leslie-Ericksen formulation are the velocity field, $\mathbf{v} = (v_1, v_2, v_3)$; and the director field,

$$\mathbf{n} = (n_1, n_2, n_3) = (\sin\theta\cos\phi, \sin\theta\sin\phi, \cos\theta) \ .$$

The Leslie-Ericksen equations describe conservation of energy, momentum, and mass for a nematic liquid crystal in terms of $\mathbf{v}$ and $\mathbf{n}$. The governing equations are

$$\frac{\partial W}{\partial n_i} + \left(\frac{\partial W}{\partial n_{i,j}}\right)_{,j} - G_i = 0 \ , \tag{2.1}$$

$$\frac{\partial \Pi}{\partial x_i} + G_k \frac{\partial n_k}{\partial x_i} + \frac{\partial \tau_{ij}}{\partial x_j} = 0 \ , \tag{2.2}$$

$$\frac{\partial v_i}{\partial x_i} = 0 \ , \tag{2.3}$$

where we use subscript notation such that

$$F_{,j} = \frac{\partial F}{\partial x_j} \quad \text{and} \quad n_{i,j} = \frac{\partial n_i}{\partial x_j} \ ,$$

where F is some quantity. Here the important quantities are: total potential energy, Π; bulk elastic distortion (Frank) energy, W; kinetic rotational energy associated with viscous forces in each direction, G_i; and the viscous non-Newtonian stress tensor, τ_{ij}.

The bulk elastic energy W for NLC is given by

$$2W = K_1 \left(\nabla \cdot \mathbf{n}\right)^2 + K_2 \left(\mathbf{n} \cdot \nabla \times \mathbf{n}\right)^2 + K_3 \left|\mathbf{n} \times \nabla \times \mathbf{n}\right|^2$$

where K_i, $i = 1, 2, 3$, are elastic constants related to pure splay, pure twist and pure bend distortions. Note that W is zero if and only if the director field, $\mathbf{n}$, is constant.

The elastic constants are of the same order of magnitude, and it is common to make the so-called one constant approximation [5, 12, 16, 31, 35–37], $K = K_1 = K_2 = K_3$, reducing W to

$$2W = K \left(\left(\nabla \cdot \mathbf{n}\right)^2 + \left|\nabla \times \mathbf{n}\right|^2\right). \tag{2.4}$$

The remaining quantities are given by

$$G_i = \gamma_1 N_i + \gamma_2 e_{ik} n_k \ , \quad \Pi = p + W + \psi_g \ ,$$

$$N_i = -\dot{n}_i - \omega_{ik} n_k \ , \quad e_{ij} = \tfrac{1}{2}\left(\tfrac{\partial v_i}{\partial x_j} + \tfrac{\partial v_j}{\partial x_i}\right) \ , \quad \omega_{ij} = \tfrac{1}{2}\left(\tfrac{\partial v_i}{\partial x_j} - \tfrac{\partial v_j}{\partial x_i}\right) \ ,$$

$$\tau_{ij} = \alpha_1 n_k n_p e_{kp} n_i n_j + \alpha_2 N_i n_j + \alpha_3 N_j n_i + \alpha_4 e_{ij}$$

$$+\alpha_5 e_{ik} n_k n_j + \alpha_6 e_{jk} n_k n_i \ ,$$

where p is the pressure and ψ_g is the gravitational potential. The constants γ_i and α_i are viscosities, satisfying $\gamma_1 = \alpha_3 - \alpha_2$ and $\gamma_2 = \alpha_6 - \alpha_5$. Furthermore the α_i satisfy the Onsager relation, $\alpha_2 + \alpha_3 = \alpha_6 - \alpha_5$.

We consider flow of a thin film of NLC down an inclined substrate, as indicated in Figure 2.1. We define our coordinates (x, y, z) such that the in-plane coordinates (x, y) point down and across the incline, respectively, and z is perpendicular to the plane of the substrate; χ is the inclination angle. In our formulation, we follow [12] but include a new gravitational potential, $\psi_g = -g\rho z \cos\chi + g\rho x \sin\chi$, where g is the gravitational acceleration and ρ is the density of the NLC.

As noted in the Introduction, NLC molecules have a preferred orientation with respect to a surface, a phenomenon known as anchoring [33, 38]. At a free surface, the

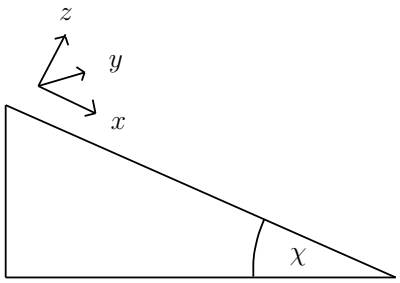

Figure 2.1 A diagram showing the coordinate system used relative to the substrate.

director often prefers to align normal to the surface (so-called homeotropic anchoring). At a solid substrate, the anchoring is determined by the chemical interactions between the NLC and the substrate. It is common in applications that substrates are treated chemically to impose planar anchoring with respect to the surface. In our analysis we assume strong planar anchoring at the substrate $z = 0$ (the director field is always at the preferred orientation, which here is parallel to the substrate), and weak homeotropic anchoring at the free surface $z = h$ [35], discussed in § 2.1.1 below. Variations on these anchoring conditions are easily addressed within the current framework.

2.1.1 Long Wave Approximation

Let h_0 be a representative film height, L be the lengthscale of variations in the x direction, U be the characteristic flow velocity down the plane and μ be a representative viscosity scale. Defining the aspect ratio, $\delta = h_0/L \ll 1$, we scale variables as follows

$$(x, y, z) = (L\hat{x}, L\hat{y}, L\delta\hat{z}) \ , \quad (u, v, w) = (U\hat{x}, U\hat{y}, U\delta\hat{z}) \ , \quad t = \frac{L}{U}\hat{t}, \tag{2.5}$$

where hatted variables are dimensionless. Inspection of the energy (2.4) and momentum balance (2.2) then suggests the following scalings:

$$W = \frac{K}{L^2\delta^2}\hat{W} \quad \text{and} \quad p = \frac{\mu U}{\delta^2 L}\hat{p}. \tag{2.6}$$

Using (2.5) and (2.6), two dimensionless parameters may be defined:

$$\mathcal{B} = \delta^3 \rho g L^2/(\mu U) \text{ and } \tilde{\mathcal{N}} = K/(\mu U L), \tag{2.7}$$

the Bond and inverse Ericksen numbers, respectively.

Energetics of the Director Field In this section, we follow the novel approach to the energetics of the director field presented in [12]. In terms of the dimensionless variables, and dropping the hats, to leading order the bulk energy (2.4) is

$$2W = \theta_z^2 + \phi_z^2 \sin\theta \tag{2.8}$$

and energy conservation (2.1) becomes

$$\frac{\partial W}{\partial n_i} + \left(\frac{\partial W}{\partial n_{i,j}}\right)_j + \delta\tilde{\mathcal{N}}\bar{G}_i = 0\ , \quad \bar{\mathbf{G}} = \left(u_z n_3, v_z n_3, u_z n_1 + v_z n_2\right)^T \tag{2.9}$$

where the terms in $\bar{\mathbf{G}} = (\bar{G}_1, \bar{G}_2, \bar{G}_3)^T$ are the leading order terms of $\mathbf{G} = (G_1, G_2, G_3)^T$ in (2.1). If $\tilde{\mathcal{N}} = O(1)$, then the coupling term, $\bar{\mathbf{G}}$, in (2.9) is of lower order. This implies that the time scale on which elastic reorientation occurs is faster than the time scale of fluid flow. In this limit (2.9) reduces to the Euler-Lagrange equations. The energy of the system, J, consists only of the bulk energy, W, and the surface energy $\mathcal{G}$ associated with the weak (conical) homeotropic anchoring at the free surface. Therefore

$$J = \int_0^h \int_\Omega \tilde{\mathcal{N}} W \, dS dz + \int_\Omega \mathcal{G} \, dS \tag{2.10}$$

where Ω is the fluid domain in the (x, y)-plane.

To find the energy minimum, we use a variational approach and consider small variations in the director angles, ϕ and θ. Using integration by parts for the volume

integral in (2.10), the vanishing of the bulk terms in the first variation of J leads to

$$\theta_{zz} = \frac{\phi_z}{2}\sin 2\theta \qquad \text{in} \qquad \Omega \cup \{0 < z < h\}\ , \tag{2.11}$$

$$\left[\phi_z \sin^2\theta\right]_z = 0 \qquad \text{in} \qquad \Omega \cup \{0 < z < h\}. \tag{2.12}$$

The surface contribution, $\mathcal{G}$, is assumed to be independent of the angle ϕ (conical anchoring), therefore the vanishing of the surface contributions leads to

$$\phi_z \sin^2\theta = 0 \qquad \text{in} \qquad \Omega \cap \{z = h\}\ , \tag{2.13}$$

$$\mathcal{G}_{\bar{\theta}} + \tilde{\mathcal{N}}\theta_z = 0 \qquad \text{in} \qquad \Omega \cap \{z = h\}\ , \tag{2.14}$$

where $\bar{\theta}$ is the director angle on the free surface i.e. $\bar{\theta}(x, y, t) = \theta(x, y, z = h, t)$. Equations (2.12) and (2.13) show that the angle ϕ must be independent of z, which reduces (2.11) to $\theta_{zz} = 0$. Satisfying the strong anchoring condition on the substrate, $\mathcal{S}$ ($z = 0$ here), gives

$$\phi(x, y, t) = \phi_{\mathcal{S}}(x, y)\ , \quad \theta\ = a(x, y, t)z + \frac{\pi}{2}\ , \tag{2.15}$$

where $\phi_{\mathcal{S}}$ is assumed specified. If strong anchoring is imposed on both surfaces, then in a very thin film, adjusting between two antagonistic angles leads to unrealistically large energy penalties in the bulk. To resolve this issue we impose weak homeotropic anchoring, with energy $\mathcal{G}(\bar{\theta})$, at the free surface. This means that the director angle θ is approximately zero at the free surface only for thick films ($h \gg 1$), but it can depart from zero significantly for very thin films ($h \ll 1$). More precisely, we write (consistent with (2.15))

$$\theta = \frac{\pi}{2}\left(1 - \frac{m(h)}{h}z\right) \tag{2.16}$$

where $m(h)$ is a monotonically increasing function such that $m(0) = 0$ and $m(\infty) = 1$. This function $m(h)$ is directly related to the surface anchoring energy $\mathcal{G}$ via equation

(2.14). Using the chain rule, we find

$$\frac{d\mathcal{G}}{dh} = \mathcal{G}_{\bar{\theta}}\frac{d\bar{\theta}}{dh} = -\tilde{\mathcal{N}}a\frac{d\bar{\theta}}{dh} = -\mathcal{N}\frac{m(h)m'(h)}{h}$$

where $\mathcal{N} = \pi^2\tilde{\mathcal{N}}/4$ is the scaled inverse Ericksen number. We choose the same form for $m(h)$ as was used in [12],

$$m(h) = f(h;b)\frac{h^\alpha}{h^\alpha + \beta^\alpha}\ , \quad f(h;b) = \frac{1}{2}\left[\tanh\left(\frac{h-2b}{w}\right) + 1\right]. \tag{2.17}$$

Here, $b \ll 1$ is the thickness of a preexisting precursor film that is assumed to be present in all our numerical simulations; and $\alpha,\ \beta > 0$ are constants that tune the relaxation of the anchoring at the free surface. The functional form of $m(h)$ corresponds to choosing a specific form of the free surface anchoring energy $\mathcal{G}(\bar{\theta})$ (it is easily checked that the corresponding $\mathcal{G}(\bar{\theta})$ has a unique minimum at $\bar{\theta} = 0$). The function $f(h;b)$ provides a continuous 'cutoff' behavior, i.e., it imposes planar anchoring at the free surface to match with that at the substrate when the film height goes below the precursor thickness, b. The constant w provides control over the range of h for which such planar anchoring is imposed.

Flow Equations Under the long wave scalings coupled with the assumed form of the director field given by (2.15) and (2.16), to leading order momentum conservation (2.2) becomes

$$\nabla\left(p + \mathcal{N}m^2\right) + \mathcal{U}\hat{\mathbf{i}} = \frac{\partial}{\partial z}\left[\begin{pmatrix} B_1 & B_3 \\ B_3 & B_2 \end{pmatrix}\begin{pmatrix} u_z \\ v_z \end{pmatrix}\right], \tag{2.18}$$

$$\frac{\partial p}{\partial z} = -\mathcal{D}\ , \tag{2.19}$$

where $\nabla = (\partial_x, \partial_y)^T$, $\hat{\mathbf{i}} = (1,0)^T$,

$$\mathcal{U} = \mathcal{B}\sin\chi \quad , \quad \mathcal{D} = \mathcal{B}\cos\chi \tag{2.20}$$

and B_i are given by

$$B_1 = A_1 + A_2 \cos 2\phi \ , \quad B_2 = A_1 - A_2 \cos 2\phi \ , \quad B_3 = A_2 \sin 2\phi \ ,$$

$$\begin{aligned} A_1 &= 1 + (\alpha_5 - \alpha_2)\cos^2\theta + \alpha_1 \sin^2\theta \cos^2\theta + \frac{\alpha_3 + \alpha_6}{2}\sin^2\theta \ , \\ A_2 &= \alpha_1 \sin^2\theta \cos^2\theta + \frac{\alpha_3 + \alpha_6}{2}\sin^2\theta. \end{aligned}$$

To proceed, we first integrate (2.19). To fix the constant of integration we assume that in the direction normal to the surface, fluid stresses (elastic and viscous) are balanced by surface tension,

$$p + \mathcal{N} m^2 = -\mathcal{C}\nabla^2 h \quad \text{on } z = h(x, y, t) \ , \tag{2.21}$$

where

$$\mathcal{C} = \delta^3 \gamma / (\mu U) \tag{2.22}$$

is the inverse capillary number and γ is surface tension. The left hand side of (2.18) is now known explicitly and furthermore is independent of z, therefore (2.18) may be integrated. To find the constant of integration, note that in the directions tangential to the surface, fluid stresses are balanced by surface energy gradients,

$$-\tilde{\mathcal{N}}\left[\theta_z \nabla\theta + \theta_z^2 \nabla h\right] + \begin{pmatrix} B_1 & B_3 \\ B_3 & B_2 \end{pmatrix} \begin{pmatrix} u_z \\ v_z \end{pmatrix} = \tilde{\mathcal{N}} \nabla \mathcal{G} = -\mathcal{N} \frac{m m'}{h} \nabla h$$

on $z = h(x, y, t)$. Substituting for θ given by (2.16) in the above equation,

$$\begin{pmatrix} B_1 & B_3 \\ B_3 & B_2 \end{pmatrix} \begin{pmatrix} u_z \\ v_z \end{pmatrix} = 0 \quad \text{on } z = h(x, y, t). \tag{2.23}$$

Integrating (2.18) over the film height and imposing (2.23) at the free surface, we find a matrix equation for u_z and v_z,

$$\left[\mathbf{F}(h) + \mathcal{U}\hat{\mathbf{i}}\right](h-z) = \begin{pmatrix} B_1 & B_3 \\ B_3 & B_2 \end{pmatrix} \begin{pmatrix} u_z \\ v_z \end{pmatrix} \tag{2.24}$$

where

$$\mathbf{F}(h) \;=\; \nabla\left(p + \tilde{\mathcal{N}}W\right) = \mathcal{D}\nabla h - \mathcal{C}\nabla\nabla^2 h + \mathcal{N}\frac{m^2 - hmm'}{h^3}\nabla h.$$

We assume there is no penetration and no slip at the substrate: $w = u = v = 0$ on $z = 0$; and we enforce the kinematic condition (to leading order) at the free surface, $h_t(x, y, t) = w(x, y, z = h, t)$. The conservation of mass (2.3) may then be integrated over the film height to obtain

$$h_t + \int_0^h \nabla \cdot (u, v)^T \, dz = 0. \tag{2.25}$$

The determinant of the B_i matrix on the right hand side of (2.24) is $D = A_1^2 - A_2^2$. Assuming $|A_1| \neq |A_2|$ this matrix is non-singular and may be inverted to obtain u_z and v_z. We also have the following identities

$$\int_0^h u_z(h-z)\, dz = \int_0^h u \, dz, \quad \int_0^h v_z(h-z)\, dz = \int_0^h v \, dz$$

which we use to combine expressions (2.24) and (2.25) to yield

$$h_t + \int_0^h \nabla \cdot \left(E(h)\left[\mathbf{G}(h) - \mathcal{U}\hat{\mathbf{i}}\right]\right) \, dz = 0 \tag{2.26}$$

where the matrix $E(h)$ is defined by

$$E(h) = \int_0^h \frac{1}{D} \begin{pmatrix} B_2 & -B_3 \\ -B_3 & B_1 \end{pmatrix} (h - z')^2 \, dz'. \tag{2.27}$$

The integral in (2.27) is difficult to evaluate directly, therefore we follow [12] in using a two point trapezoidal rule for its estimate. This reduces (2.26) to the following

fourth order nonlinear parabolic partial differential equation for the film thickness, h,

$$h_t + \nabla \cdot \left(\mathcal{C} h^3 \tilde{\nabla} \nabla^2 h - \mathcal{D} h^3 \tilde{\nabla} h - \mathcal{N} M(h) \tilde{\nabla} h \right) + \mathcal{U} \hat{\nabla} h^3 = 0 \tag{2.28}$$

where

$$M(h) = m^2 - hmm' , \tag{2.29}$$

$$\begin{aligned} \tilde{\nabla} &= \left[\lambda I + \nu \begin{pmatrix} \cos 2\phi & \sin 2\phi, \\ \sin 2\phi & -\cos 2\phi \end{pmatrix} \right] \begin{pmatrix} \partial_x \\ \partial_y \end{pmatrix} , \\ \hat{\nabla} &= \left[\lambda + \nu \cos 2\phi \right] \partial_x + \nu \sin 2\phi \partial_y + 2\nu \left[\phi_y \cos 2\phi - \phi_x \sin 2\phi \right] , \end{aligned}$$

$$\lambda = \frac{2 + \alpha_3 + \alpha_6}{4\left(1 + \alpha_3 + \alpha_6\right)} , \quad \nu = -\frac{\alpha_3 + \alpha_6}{4\left(1 + \alpha_3 + \alpha_6\right)}$$

and $m(h)$ is defined by equation (2.17). Note that for the majority of nematic liquid crystals, $-1 < \alpha_3 + \alpha_6 < 0$, therefore $\lambda > \nu > 0$ and $\tilde{\nabla}$ has positive coefficients.

2.2 Analysis: Two-Dimensional Flow

To simplify the analysis and gain preliminary insight into the phenomena captured by the model, only two dimensional flow will be considered for the remainder of this chapter, with a full investigation of the characteristics of the 3D model deferred to the following chapter. Under this restriction, $\phi = 0$, π are the only consistent values for the substrate anchoring. In either case, this leads to a factor of $\lambda + \nu$ in front of all spatial derivatives, which may be removed by rescaling time. Under this rescaling, equation (2.28), in two space dimensions with a free surface $z = h(x,t)$, becomes

$$h_t + \left[\mathcal{C} h^3 h_{xxx} - \mathcal{D} h^3 h_x - \mathcal{N} M(h) h_x + \mathcal{U} h^3 \right]_x = 0, \tag{2.30}$$

with $M(h)$ defined in (2.29) and dimensionless parameters as defined in (2.7), (2.20) and (2.22). It should be noted that if $\mathcal{N} = 0$, (2.30) describes the flow of a Newtonian

thin film down an inclined plane [39]. In 2D and in the absence of a contact line, a Newtonian film described within the long wave approximation with inertial effects ignored flows stably down an inclined surface with only a hump (capillary ridge) forming near the front of the fluid. Therefore any qualitatively different behavior exhibited by (2.30), in particular instabilities, may only result from the term in $\mathcal{N}$.

2.2.1 Traveling Front Solution

Motivated by known results for Newtonian films [10, 18], we first seek traveling-wave solutions, $h(x,t) = H(x - Vt) = H(s)$, where V is the wave speed. Inserting this ansatz into (2.30) and integrating once with respect to the new variable $s = x - Vt$, gives

$$-VH + \mathcal{C}H^3H''' - \mathcal{D}H^3H' - \mathcal{N}M(H)H' + \mathcal{U}H^3 = c \tag{2.31}$$

where c is a constant of integration. Applying the far field boundary conditions, $H(s \to \infty) = b$ and $H(s \to -\infty) = h_0$, where h_0 is the free surface height behind the front and b is the precursor thickness, the front velocity satisfies

$$V = \mathcal{U}\left(h_0^2 + h_0 b + b^2\right). \tag{2.32}$$

The above expression is the usual traveling front speed for a Newtonian film; however, recall that a factor of $\lambda + \nu$ has been scaled out of the 2D governing equation (2.30).

2.2.2 Linear Stability of a Flat Film

We start by carrying out linear stability analysis (LSA) of a uniform film, which describes the situation far behind the traveling front. Consider a flat film with a small perturbation, $h(x,t) = h_0 + \epsilon h_1(x,t)$, where $\epsilon \ll 1$. Substituting this form of the solution into (2.30), the $\mathrm{O}(\epsilon)$ equation is

$$\frac{\partial h_1}{\partial t} + \mathcal{C}h_0^3\frac{\partial^4 h_1}{\partial x^4} - \mathcal{D}h_0^3\frac{\partial^2 h_1}{\partial x^2} - \mathcal{N}M\left(h_0\right)\frac{\partial^2 h_1}{\partial x^2} + 3\mathcal{U}h_0^2\frac{\partial h_1}{\partial x} = 0. \tag{2.33}$$

Assuming plane wave form $h_1 = e^{\omega t + ikx}$ leads to the dispersion relation

$$\omega = -\left(\mathcal{C}h_0^3 k^2 + \left[\mathcal{D}h_0^3 + \mathcal{N}M\left(h_0\right)\right]\right)k^2 - 3\mathcal{U}h_0^2 ki. \tag{2.34}$$

The wavenumber k is real, and for instability we require $\mathrm{Re}(\omega) > 0$ for some range of k. Hence the sign of the term $h_0^3\mathcal{D} + \mathcal{N}M(h_0)$ determines the stability of the film: if it is negative then there is a range of unstable wavenumbers. By assumption, $\mathcal{D}$, $\mathcal{N} > 0$, thus $M(h)$, given by equation (2.29), must be negative for some range of film heights for instability. Figure 2.2 shows $M(h)/h^3$ and Figure 2.3 the dispersion relation in the unstable regime. In this case the modes $|k| \in (0, k_c)$ are unstable, where

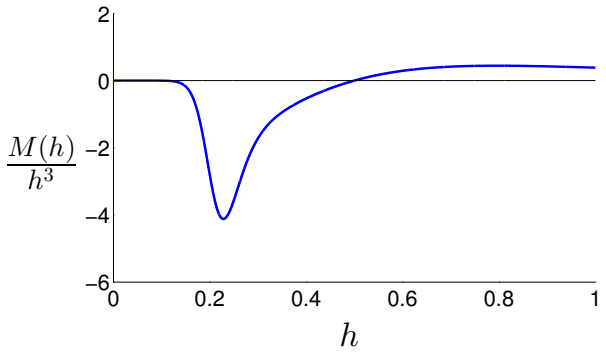

Figure 2.2 A plot of $M(h)/h^3$ where $M(h)$ is given by (2.29) and $m(h)$ is defined in (2.17) with $\alpha = 2$, $\beta = 0.5$ and $w = 0.05$. For a thin film of height h such that $M(h)/h^3 < 0$, elastic effects are destabilizing.

$$k_c = \sqrt{-\frac{1}{\mathcal{C}}\left[\mathcal{D} + \frac{\mathcal{N}M(h_0)}{h_0^3}\right]}. \tag{2.35}$$

Furthermore, the fastest growing mode is given by

$$k_m = \sqrt{-\frac{1}{2\mathcal{C}}\left[\mathcal{D} + \frac{\mathcal{N}M(h_0)}{h_0^3}\right]} \tag{2.36}$$

and its growth rate is

$$\omega_m = \frac{1}{4\mathcal{C}}\left[\mathcal{D} + \frac{\mathcal{N}M(h_0)}{h_0^3}\right]^2. \tag{2.37}$$

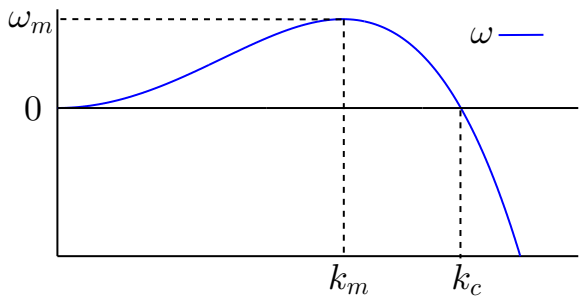

Figure 2.3 An example of the dispersion relationship (2.34) in the unstable regime ($\mathcal{D}h_0^3 + \mathcal{N}M(h_0) < 0$). Plane wave disturbances with wavenumber $k \in [0, k_c]$ are unstable.

We will assume throughout that the precursor film ahead of the traveling front lies in the stable regime of film thicknesses.

2.2.3 Absolute and Convective Instability

It is known from earlier work [39], that if $\mathcal{N} = 0$ and $\mathcal{D} > 0$, there exist stable traveling fronts, solutions to equation (2.31). Furthermore, based on other results [10], for $\mathcal{N} = 0$ and $\mathcal{D} < 0$ (a Newtonian film "hanging" on an inverted substrate), it is known that a traveling front may exhibit several types of instabilities. It is of interest to analyze the analogous instabilities that arise within the context of the present model, specified by equation (2.30).

Within the unstable regime, it is instructive to discuss the evolution of surface perturbations. We may exploit existing results by noting that (2.33) may be transformed to the linearized symmetric Kuramoto-Sivashinsky (KS) equation. Following [10], we consider a moving reference frame, rescaling variables as

$$\eta = \sqrt{\frac{-\left[\mathcal{D}h_0^3 + \mathcal{N}M(h_0)\right]}{\mathcal{C}h_0^3}}\left(x - 3\mathcal{U}h_0^2 t\right) \ , \quad \tau = \frac{\left[\mathcal{D}h_0^3 + \mathcal{N}M(h_0)\right]^2}{\mathcal{C}h_0^3} t \ . \tag{2.38}$$

Under this transformation (2.33) reduces to

$$h_\tau + h_{\eta\eta\eta\eta} + h_{\eta\eta} = 0.$$

We now consider the velocity of the left- and right-hand boundaries (denoted $-$ and $+$ respectively) of an expanding "wave packet" of perturbations to a flat film of height h_0. Following the techniques in [40], the velocities of the expanding wave packet boundaries are found numerically as $(\eta/\tau)_\pm = \pm 1.622$. Reverting to x and t variables yields, for the boundaries of the wave packet,

$$\left(\frac{x}{t}\right)_\pm = 3\mathcal{U}h_0^2 \pm 1.622\sqrt{-\frac{\left[\mathcal{D}h_0^3 + \mathcal{N}M(h_0)\right]^3}{\mathcal{C}h_0^3}}. \tag{2.39}$$

The expression under the square root is real since we are (by assumption) in the unstable regime. Comparing the wave packet velocity (2.39) to the traveling front velocity (2.32), we see that the right going wave packet boundary ("+" sign) is always faster than the traveling front for $b < h_0$. This boundary may therefore always be ignored, since it will move to the (stable) precursor side of the traveling front. There are three different cases to be considered for the left wave packet boundary ("$-$" sign), which we now discuss.

Type 1 (Stable) The left wave packet boundary also travels faster than the front,

$$V < (x/t)_- .$$

For this case, perturbations propagate ahead of the traveling front (into the physical region occupied by the stable precursor) and are thus never observed.

Type 2 (Convectively Unstable) The left wave packet boundary velocity is slower than the front velocity but still positive,

$$0 < (x/t)_- < V.$$

In this case, perturbations grow, and propagate more slowly than the front itself. Since the wave-packet velocity is positive it travels to the right, thus does not propagate beyond the initial front position. The film remains flat behind the initial front.

Type 3 (Absolutely Unstable) The left wave packet boundary velocity is negative,

$$(x/t)_- < 0 \,,$$

hence travels to the left. Similarly to the Type 2, perturbations grow; but since the wave packet travels to the left, the disturbance is not confined, and the entire film is ultimately destabilized.

2.3 Computational Results and Discussion

In this section the results obtained from numerical simulations of equation (2.30) are compared to the analytical and LSA predictions derived in §2.2. To simplify the parameter study, unless stated otherwise, we vary $\mathcal{N}$, and for the other parameters we use the values specified in Table 2.1. The numerical simulations are based on a Crank-Nicolson (implicit) discretization scheme coupled with a Newton-Raphson iterative method to evaluate the nonlinear terms and an adaptive time stepping scheme. The reader is referred to [12] for more information on the numerical method. To study the dynamics of a traveling front, the domain and boundary conditions are given by

$$h(x_0,t) = h_0, \quad h(x_L,t) = b, \quad h_x(x_0,t) = h_x(x_L,t) = 0, \tag{2.40}$$

where we set $x_0 = 0$ and $x_L = 400$. We use the following initial condition (IC),

$$h(x,0) \;=\; \frac{(h_0 - b)}{2} \tanh\left[-5\,(x - x_f)\right] + \frac{h_0 + b}{2} \tag{2.41}$$

which transitions monotonically from height h_0 behind the front at $x = x_f$ to the precursor thickness, b, ahead of the front. We set the initial front position x_f to be far from the boundaries: more precisely for $x \in [x_0, x_L]$, $x_f = 2\,(x_L + x_0)\,/3$. For

Table 2.1 Values of the Parameters Chosen for the Simulations

Parameter	Value	Parameter	Value	Parameter	Value
$\mathcal{C}$	1	β	0.5	$\mathcal{B}$	$\sqrt{2}$
$\mathcal{D}$	1	α	2	χ	$\pi/4$
$\mathcal{U}$	1	w	0.05		
h_0	0.25	n	5000		
b	0.1				

Values of the parameters chosen for the simulations (except where specified otherwise). Here, n is the number of discretization points.

simulations of a perturbed flat film, the initial condition

$$h(x,0) \;=\; h_0\left\{1+0.1\exp\left[-\frac{k}{10}\left(x-x_c\right)^2\right]\cos\left[k\left(x-x_c\right)\right]\right\} \tag{2.42}$$

is used, where x_c is the center of the interval, and k is given by (2.36). In the unstable regime ($\mathcal{D}+\mathcal{N}M(h)/h^3<0$), the maximum of the growth rate (2.37) with respect to h corresponds to the minimum of $M(h)/h^3$,

$$h_0=\max_h \omega_m=\min_h \frac{M(h)}{h^3},$$

therefore for any $\mathcal{N}$, $\mathcal{C}$, $\mathcal{U}$ and $\mathcal{D}$ considered, the same h_0 maximizes (2.37). Hence, with fixed α, β, and w, we may fix h_0 and analyze instability in the ($\mathcal{C}$, $\mathcal{D}$, $\mathcal{N}$, $\mathcal{U}$) or ($\mathcal{B}$, χ, $\mathcal{C}$, $\mathcal{N}$) parameter spaces.

2.3.1 Traveling Wave

To analyze the validity of our predictions for traveling wave speed (2.32), we have carried out simulations using (2.41) as initial condition. Table 2.2 shows that for Type 1 (stable) cases, the relative difference between the front speed V predicted by (2.32) and the average speed of the front calculated from numerical simulations is less than 1% (the average speed was computed by averaging over a period of time sufficiently

Table 2.2 Comparison of LSA Predictions given by (2.32) with the Average Front Speed Calculated from Numerical Simulations

Parameters	Type	Numerical V	Analytical V	Relative Difference (%)
Default	2	0.1004	0.0975	2.9
$\mathcal{U} = 2$	1	0.1948	0.1950	0.1
$h_0 = 0.35$	1	0.1670	0.1675	0.3
$\mathcal{N} = 2$	3	0.1202	0.0975	18.9
$b = 0.05$	1	0.0769	0.0775	0.8
$\mathcal{C} = 2$	2	0.0973	0.0975	0.2
$\mathcal{D} = 2$	2	0.0974	0.0975	0.1
$\beta = 0.8$	1	0.0976	0.0975	0.1

Unless specified otherwise in the 'Parameters' column, $\mathcal{N} = 1.25$ with other parameters as given in Table 2.1.

long that the results do not depend on the length of the averaging period). For the unstable Types 2 and 3, instabilities may interact with the front, causing oscillations in the height of the capillary ridge (the hump that forms behind the traveling front, seen in the Type 1 simulations in Figure 2.4) as well in the front speed.

Figure 2.4 compares the height profiles for various $\mathcal{N}$ at $t \sim 400$. Larger $\mathcal{N}$ leads to stronger instability, as expected based on (2.37). In this expression, $M(h) < 0$ thus increasing $\mathcal{N}$ results in larger growth rates, ω_m. To compare with the LSA results, Figure 2.5 gives the LSA predictions based on (2.36). We note that although the agreement between the LSA and numerical results is not perfect, the LSA captures the monotonic increasing dependence of k_m on $\mathcal{N}$ when $M(h) < 0$.

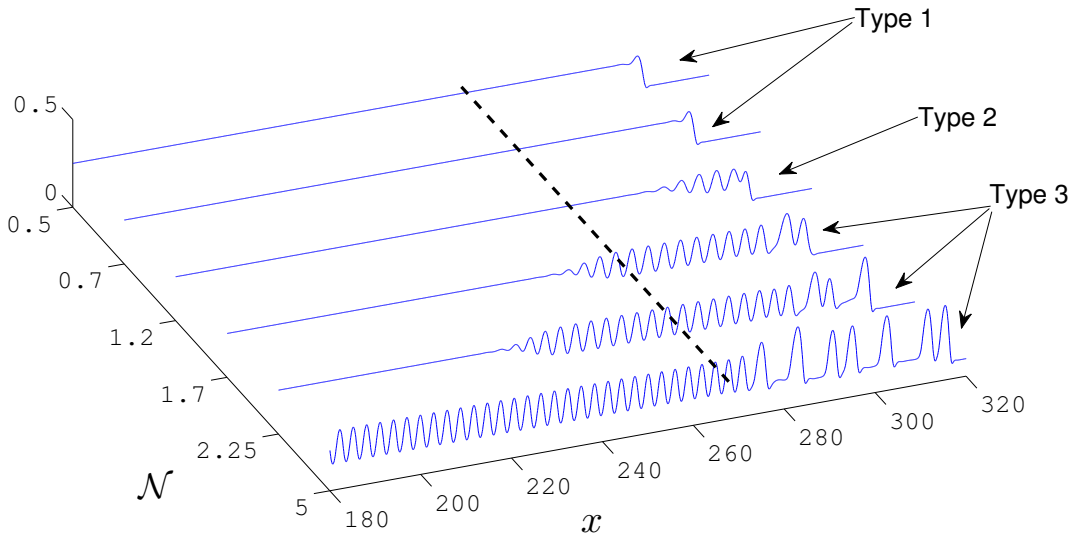

Figure 2.4 Comparison of height profiles at $t \sim 400$ for various values of $\mathcal{N}$. The vertical dashed line denotes the initial front position.

2.3.2 Stable, Convectively Unstable and Absolutely Unstable Traveling Waves

As mentioned in §2.2.3, there are three cases to consider for the left wave packet boundary. The threshold between the Type 1 and Type 2 regimes is found by equating the front speed (2.32) to the wave packet speed given by (2.39). The transition from Type 2 to Type 3 is given by the parameter set such that the speed of the left-hand boundary of the wave packet is zero. We also consider the stability threshold of a perturbed flat film, specified by the requirement that the $O(k^2)$ coefficient in the dispersion relation (2.34) vanishes. In terms of $\mathcal{N}$, with parameters as specified in the caption of Table 2.1, these regimes are:

$$\begin{aligned}
&\text{Stable Perturbed Flat Film:} && 0 < \mathcal{N} < 0.2810 \\
&\text{Type 1 (Stable Traveling Front):} && 0.2810 < \mathcal{N} < 0.9351 \\
&\text{Type 2 (Convectively Unstable):} && 0.9351 < \mathcal{N} < 1.3480 \\
&\text{Type 3 (Absolutely Unstable):} && 1.3480 < \mathcal{N}
\end{aligned}$$

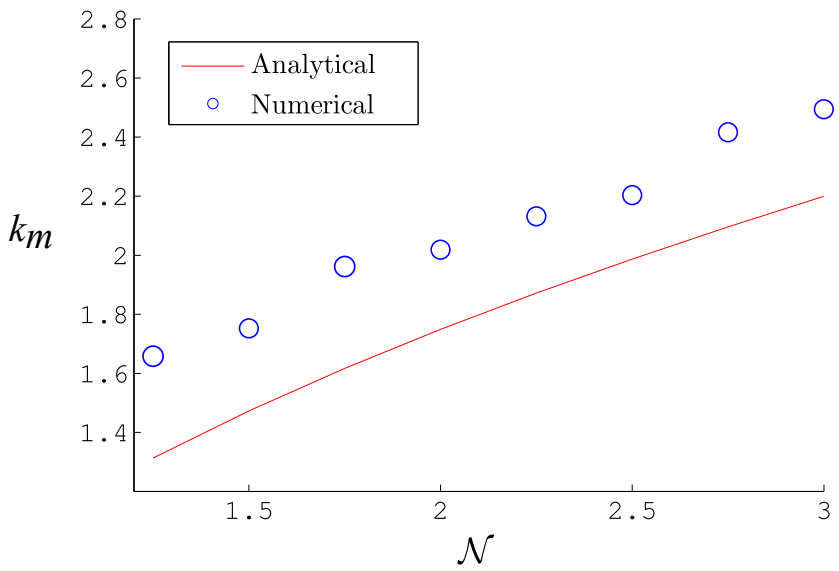

Figure 2.5 Comparison of the LSA prediction given by (2.36) with average wave number k calculated from direct numerical simulations of (2.30). Plots are a function of $\mathcal{N}$ with other parameters as specified in Table 2.1.

In what follows we concentrate on the unstable regimes, and consider the evolution of a traveling front, as well as of a perturbed flat film for $\mathcal{N} = 0.7, 1.2, 1.7$ (Type 1, 2, and 3 respectively).

Figure 2.6 shows a perturbed flat film in the Type 1 regime, $\mathcal{N} = 0.7$. We see that the perturbation does not decay, but instead slowly spreads over the film, while being convected to the right (the positive x-direction). On the other hand, Figure 2.7 shows that the analogous traveling front is stable once the capillary ridge has formed at the front. This is as expected since here the left wave packet boundary is predicted to move faster than the front itself; this can be also seen by direct comparison of the speed of perturbation in Figure 2.6 and of the front in Figure 2.7.

Figure 2.8 shows a perturbed flat film in the Type 2 regime, $\mathcal{N} = 1.2$. We observe stronger instability (initial perturbation grows noticeably in amplitude) compared to the Type 1 case and also the initial formation of solitary-like waves, similar to those observed for hanging films [10]. The waves do not propagate beyond the center, x_c,

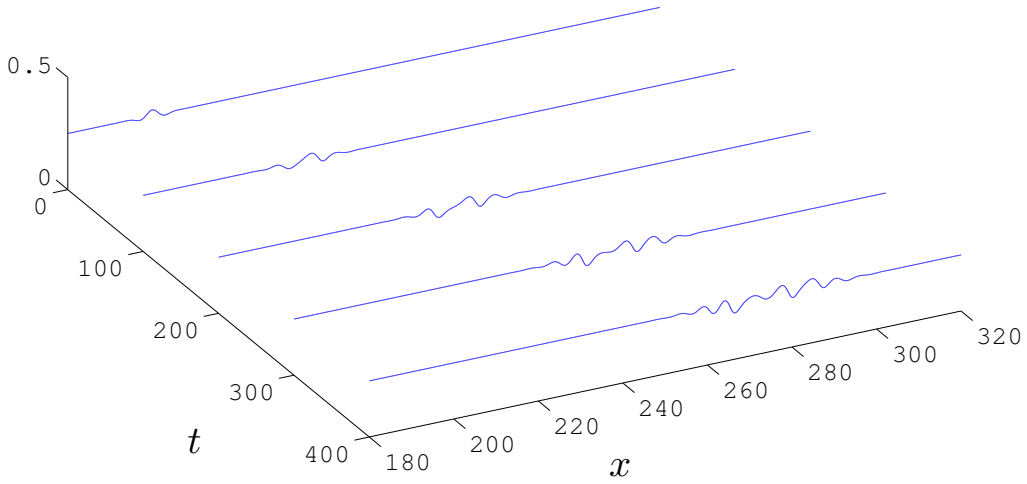

Figure 2.6 Height profiles for a perturbed flat film (2.42) in the Type 1 regime for $\mathcal{N} = 0.7$. From top to bottom, $t = 0,\ 100,\ 200,\ 300,\ 400$.

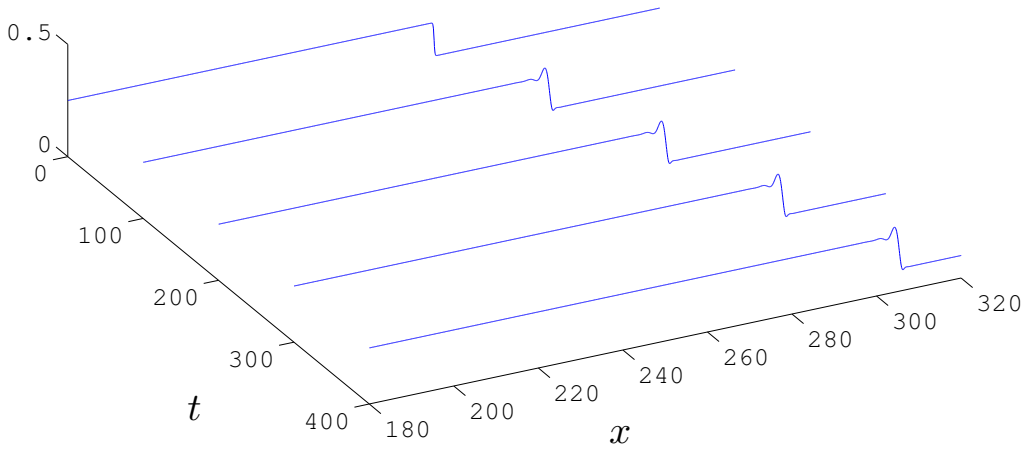

Figure 2.7 Height profiles for traveling front (2.41) in the Type 1 regime for $\mathcal{N} = 0.7$. From top to bottom, $t = 0,\ 100,\ 200,\ 300,\ 400$.

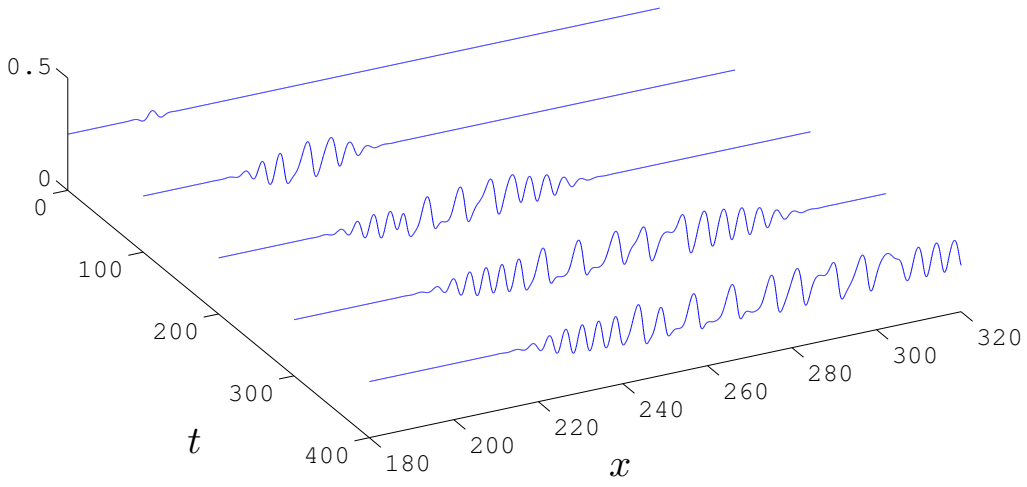

Figure 2.8 Height profiles for a perturbed flat film (2.42) in the Type 2 regime for $\mathcal{N} = 1.2$. From top to bottom, $t = 0,\ 100,\ 200,\ 300,\ 400$.

of the initial perturbation (2.42), suggesting convective instability. Figure 2.9 shows the corresponding results for a traveling front. We confirm that the left boundary of the perturbation is traveling to the right (velocity is positive) and the front remains flat behind the initial front position, showing consistently the convective nature of the instability.

In the Type 3 regime ($\mathcal{N} = 1.7$), absolute instability is observed for both a perturbed flat film, and for a traveling front, as shown in Figures 2.10 and 2.11, respectively. The left wave packet boundary propagates to the left and therefore would eventually destabilize the entire film behind the front.

2.3.3 Parametric Dependence

To study the effect of the inclination angle, first recall the relationship between $\mathcal{D}$, $\mathcal{U}$, $\mathcal{B}$, and χ, which is given in (2.20). To be consistent with previous simulations (model parameters are given in Table 2.1), we fix $\mathcal{B} = \sqrt{2}$ and study the effect of χ on the stability regimes. Figure 2.12 shows the stability zones in the $(\chi, \mathcal{N})$-plane with other

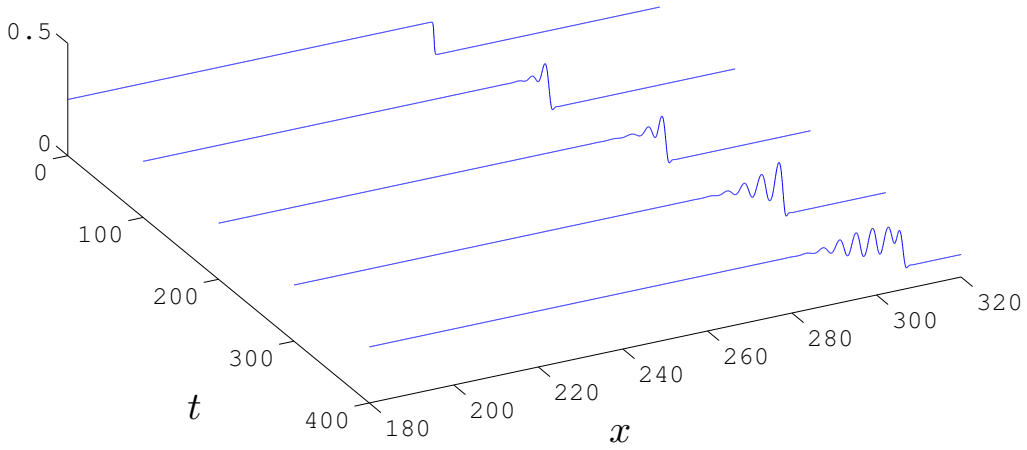

Figure 2.9 Height profiles for traveling front (2.41) in the Type 2 regime for $\mathcal{N} = 1.2$. From top to bottom, $t = 0,\ 100,\ 200,\ 300,\ 400$.

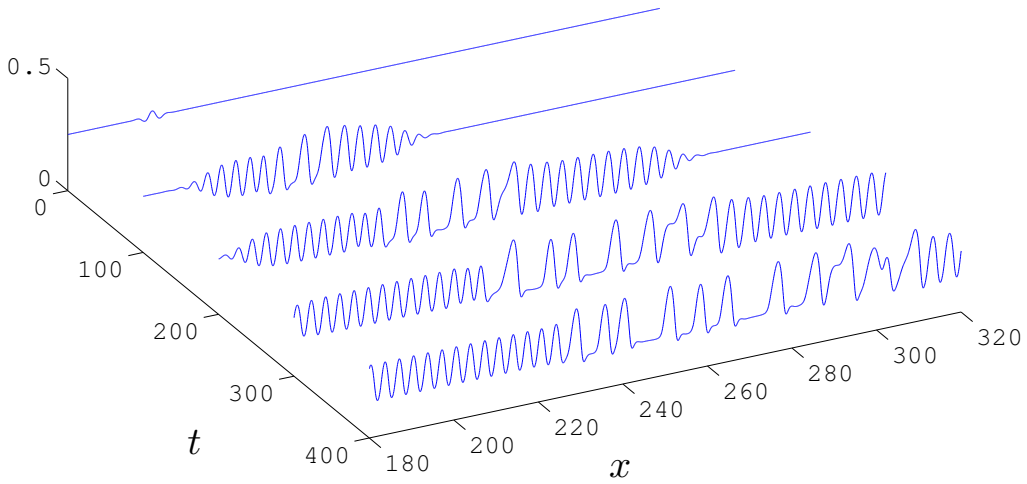

Figure 2.10 Height profiles for a perturbed flat film (2.42) in the Type 3 regime for $\mathcal{N} = 1.7$. From top to bottom, $t = 0,\ 100,\ 200,\ 300,\ 400$.

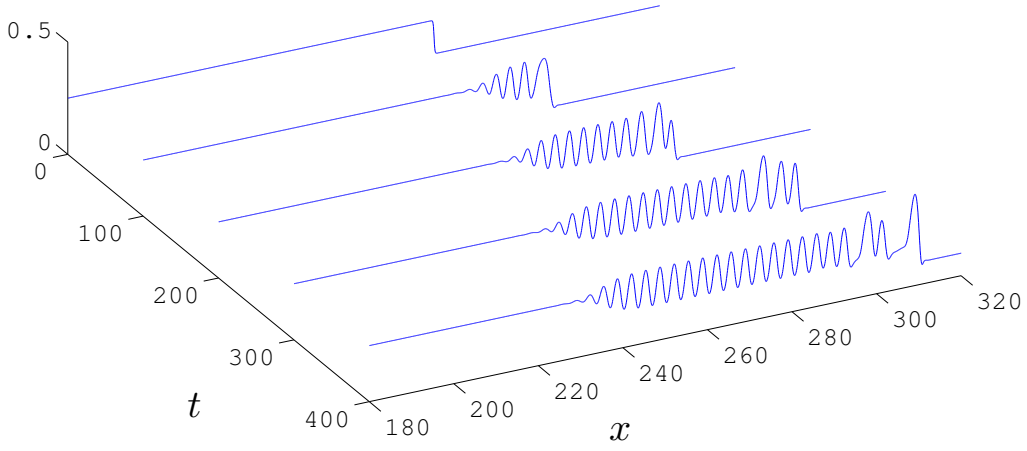

Figure 2.11 Height profiles for traveling front (2.41) in the Type 3 regime for $\mathcal{N} = 1.7$. From top to bottom, $t = 0,\ 100,\ 200,\ 300,\ 400$.

parameters defined in Table 2.1. It can be seen that, when $\mathcal{N}$ is large enough, for any small angle of inclination, χ, the film is absolutely unstable. The dependence on χ may be surprising: this figure shows that increasing χ may lead to a transition from absolutely unstable (Type 3) to convectively unstable (Type 2), and even to Type 1, where a traveling front is stable. An example where all three (in)stability regimes are possible by varying only the inclination angle is shown by the dash-dotted line $\mathcal{N} = 0.6$ in Figure 2.12. We note that the effect of $\mathcal{C}$ and $\mathcal{B}$ on the results is as expected, with larger values of both $\mathcal{C}$ and $\mathcal{B}$ stabilizing the flow.

It is of interest to discuss the stability zones in terms of the intrinsic parameters: h_0 and χ. In Figures 2.13 to 2.15 we plot the stability zones for three values of $\mathcal{N}$ with fixed values for all other parameters, given in Table 2.1. We observe rich structure involving transitions between stability and instability within the considered parameter space, with the general trend that the surface becomes increasingly unstable for larger values of $\mathcal{N}$, as expected.

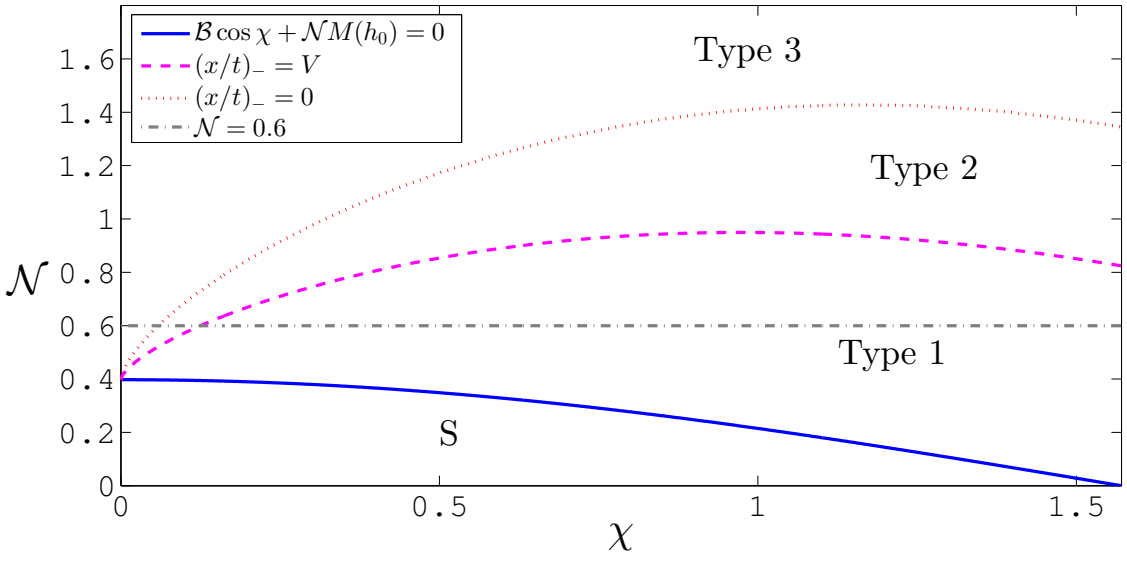

Figure 2.12 A plot of the stability zones for a traveling front in the $(\chi, \mathcal{N})$-plane. The dashed-dotted line gives an example where, by varying the inclination angle χ, all three stability regimes are possible. Note the entire region below the dashed curve is a stable regime for a traveling front. In this and the following figures, S denotes the region (below the solid curve), in which a perturbed flat film is stable. Note that V is defined by equation (2.32) and the transformation between the $(\mathcal{D}, \mathcal{U})$-plane and $(\mathcal{B}, \chi)$-plane is defined by equation (2.20).

2.4 Conclusions

To summarize, we find that in contrast to Newtonian films, 2D flows of nematic liquid films down an incline may be unstable with respect to surface perturbations. Furthermore, the analysis and simulations suggest that, depending on the physical parameters of the system, a traveling front can be stable, convectively unstable, or absolutely unstable. Consideration of perturbed flat films leads to consistent results. Relating the parameters in our dispersion relation back to the angle of inclination χ, we find an interesting interplay between the destabilizing effects of gravity and the liquid crystalline nature of the film, such that for a given $\mathcal{N}$ (inverse Ericksen number) an increase of χ may bring the film from the absolute to the convective instability regime, and even stabilize a traveling front.

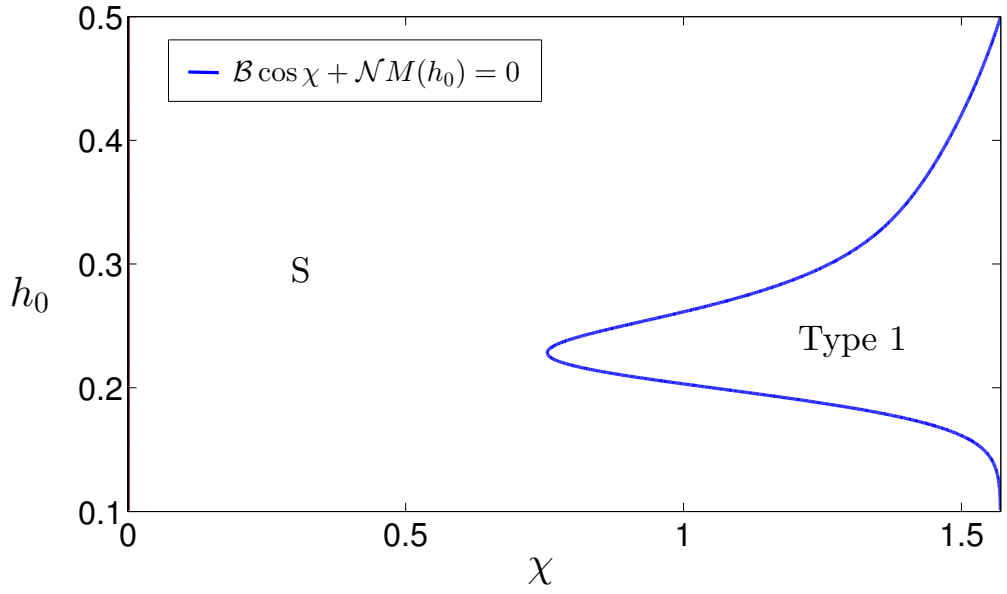

Figure 2.13 A plot of the stability zones for a traveling front in the (χ, h_0)-plane for $\mathcal{N} = 0.25$. S denotes the stable region.

There are striking parallels between the results obtained in this chapter and those obtained by for the flow of a Newtonian fluid on an inverted substrate [10] or for the flow of a Newtonian fluid on the outer surface of a vertical cylinder [15]. For Newtonian films, surface instability is caused by destabilizing gravity; for NLC films it is due to the interplay between elastic properties and the anchoring conditions.

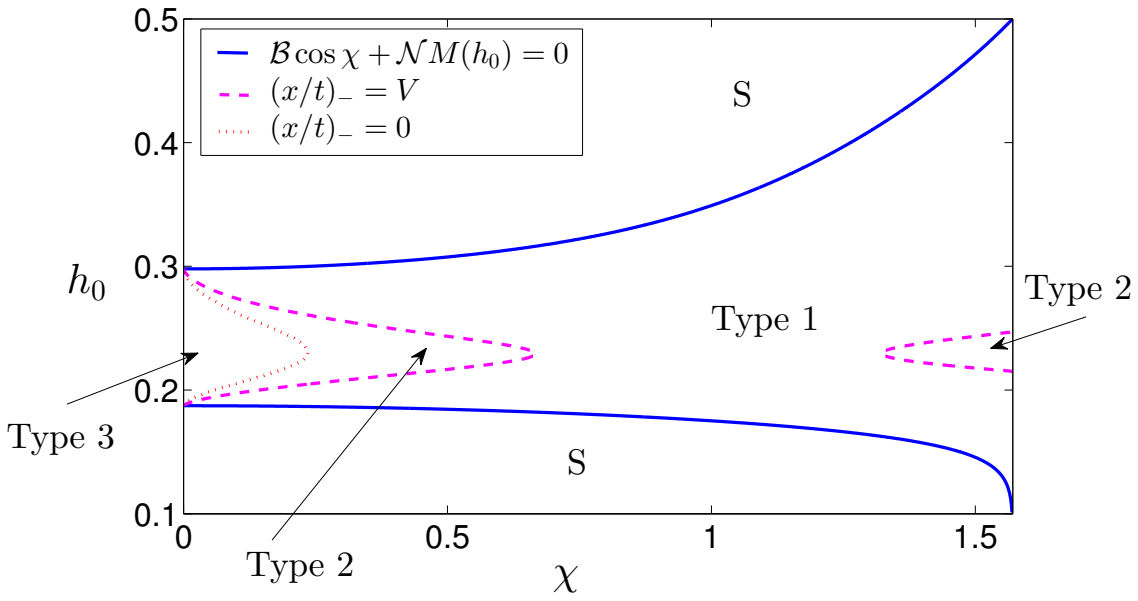

Figure 2.14 A plot of the stability zones for a traveling front in the (χ, h_0)-plane for $\mathcal{N} = 0.8$. S denotes stable regions.

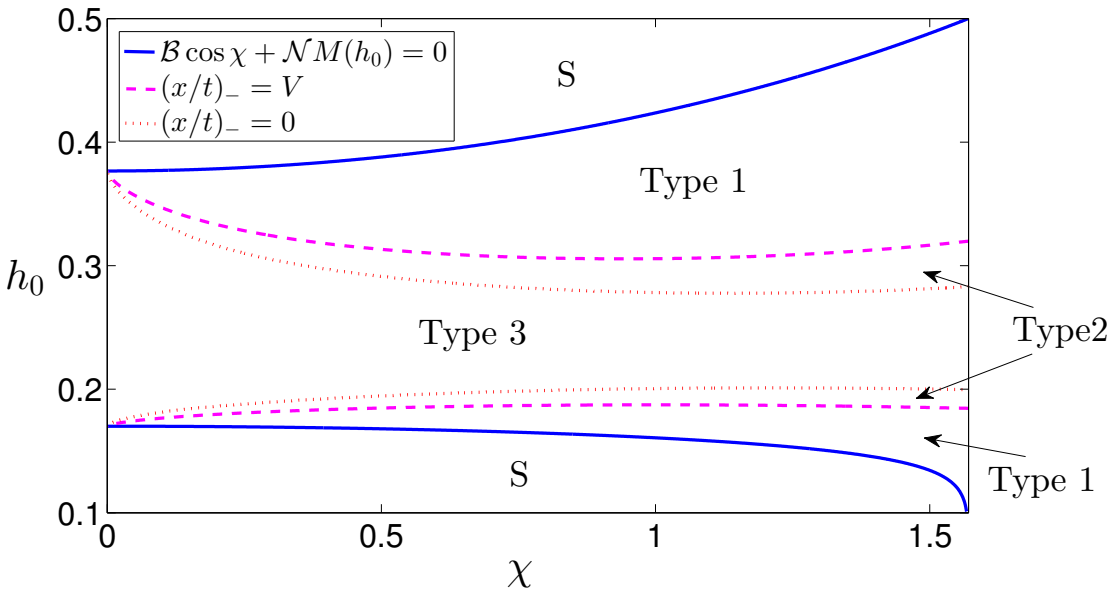

Figure 2.15 A plot of the stability zones for a traveling front in the (χ, h_0)-plane for $\mathcal{N} = 2.0$. S denotes stable regions.

CHAPTER 3

THREE-DIMENSIONAL COATING FLOW OF NEMATIC LIQUID CRYSTAL ON AN INCLINED SUBSTRATE

3.1 Governing Equations

In this chapter we analyze a long-wave model for the three-dimensional flow of NLC down an inclined plane. The model is an asymptotic approximation to the Leslie-Erickson equations [34], a set of partial differential equations modeling conservation of mass, momentum and energy for the NLC. The dependent variables are the velocity field, $\hat{\mathbf{v}} = (\hat{u}, \hat{v}, \hat{w})$; and the director field, $\mathbf{n} = (\sin\theta\cos\phi, \sin\theta\sin\phi, \cos\theta)$. Hatted symbols denote dimensional quantities and unaccented symbols are dimensionless. The reader is referred to the previous chapter for a complete derivation of the long wave model; a brief overview is given in what follows.

The momentum equations in the Leslie-Erickson model may be thought of as an extension to the Navier-Stokes equations, where the total stress tensor is composed of an isotropic component due to pressure, $\hat{p}$; and two anisotropic components: viscous effects, characterized by six coefficients, $\hat{\alpha}_i$ $(i = 1, 6)$; and elastic response, characterized by three constants, $\hat{K}_i$ $(i = 1, 2, 3)$. The elastic constants are of the same order of magnitude, and we follow many other authors in making the so-called one constant approximation [5, 12, 16, 31, 35–37], $\hat{K} = \hat{K}_1 = \hat{K}_2 = \hat{K}_3$.

The coordinates $(\hat{x}, \hat{y}, \hat{z})$ are defined such that $(\hat{x}, \hat{y})$ are in the plane of the inclined substrate, with $\hat{x}$ pointing down the line of greatest descent, and $\hat{z}$ is normal to the substrate. The angle of inclination of the substrate to the horizontal is denoted by χ. In addition, five scaling parameters are defined: $\hat{H}$, a representative film height; $\hat{L}$, a typical lengthscale in the $\hat{x}$ direction; $\hat{U}$, a characteristic velocity in the $\hat{x}$ direction; $\hat{\mu}$, a representative viscosity scale; and $\Delta\theta$, the difference in the preferred anchoring angles at the substrate and at the free surface. Defining the fluid film aspect ratio,

$\delta = \hat{H}/\hat{L} \ll 1$, we scale variables as follows:

$$(\hat{x}, \hat{y}, \hat{z}) = L(x, y, \delta z) \ , \quad (\hat{u}, \hat{v}, \hat{w}) = U(u, v, \delta w) \ , \quad \hat{t} = \frac{\hat{L}}{\hat{U}} t \ , \quad \text{and} \quad \hat{\alpha}_i = \mu \alpha_i, \tag{3.1}$$

where $\hat{\mu} = \hat{\alpha}_4/2$ is the viscosity of an analogous simple fluid i.e. with $\alpha_4 = 1$ and $\alpha_i = 0$ for $i \neq 4$, the viscous stress tensor is isotropic and models a simple fluid with viscosity $\hat{\mu}$.

We neglect inertia (which will be insignificant for the type of coating flows we consider), but retain the effects of surface tension and gravity, both of which will be important in our model. Under the scalings given by (3.1), five nondimensional parameters are defined: $\mathcal{B}$, the Bond number; $\mathcal{C}$, the inverse capillary number; $\mathcal{N}$, the scaled inverse Ericksen number; η, a scaled effective anisotropic viscosity; and $b \ll 1$, the dimensionless precursor layer thickness. In terms of the physical parameters, these nondimensional quantities are given by

$$\mathcal{B} = \frac{\delta^3 \hat{\rho} \hat{g} \hat{L}^2}{\hat{\mu} \hat{U}} \ , \quad \mathcal{C} = \frac{\delta^3 \hat{\gamma}}{\hat{\mu} \hat{U}} \ , \quad \mathcal{N} = \Delta\theta^2 \frac{\hat{K}}{\hat{\mu} \hat{U} \hat{L}} \ , \quad \eta = \frac{\hat{\alpha}_3 + \hat{\alpha}_6}{\hat{\mu}} \ , \quad \text{and} \quad b = \frac{\hat{b}}{\hat{H}} \tag{3.2}$$

where $\hat{b}$ is the dimensional precursor layer thickness, $\hat{g}$ is the gravitational acceleration, $\hat{\gamma}$ is surface tension, and $\hat{\rho}$ is the density. In this chapter, we consider the precursor film thickness, b, as a given parameter, fixing its value at 0.1 throughout. Detailed discussion regarding the influence of the value of b on simulation behavior for Newtonian flows may be found in [41].

In (3.2), we assume elasticity is of moderate strength, $\mathcal{N} = O(\delta^0)$. One could of course consider different limits; for example strong elasticity, $\mathcal{N} = O(\delta^{-1})$; and weak elasticity, $\mathcal{N} = O(\delta)$. The case of strong elasticity is not within the scope of this thesis and with the exception of neglecting lower order terms, it is unclear whether an analytically tractable model could be obtained. A weak elasticity model was considered by Carou *et al.* [42] in the framework of blade coating of a NLC.

3.1.1 Energetics: Weak Anchoring Model

In the case of moderate elasticity, the time scale on which elastic reorientation occurs across the layer, $\hat{\mu}\hat{H}^2/\hat{K}$, is much faster than the time scale of fluid flow, $\hat{L}/\hat{U}$. Under this assumption, a variational approach may be used to minimize the energy, giving

$$\phi = c_3(x, y, t) \ , \quad \theta \ = c_1(x, y, t)z + c_2(x, y, t) \ . \tag{3.3}$$

As mentioned in the Introduction, liquid crystal molecules have a preferred orientation with respect to an interface (anchoring); therefore, the functions $c_i(x, y, t)$ $(i = 1, 2, 3)$ must satisfy appropriate anchoring (boundary) conditions. Two observations may be made: First, ϕ is independent of z, thus may only be determined by the anchoring imposed by the substrate or free surface. Second, in general, the anchoring condition on the polar angle θ differs between the substrate $\mathcal{S}$ and the free surface $\mathcal{F}$; therefore, for very thin films, there may be a large energy penalty in the bulk. To simplify the modeling, and in line with available experimental data, we assume that anchoring at the substrate is *planar*, and much stronger than the *homeotropic* (perpendicular) anchoring at the free surface [14, 30, 32]. Furthermore, to avoid an elastic stress singularity as the film height $h \to 0$ we allow the free surface anchoring, $\theta_{\mathcal{F}}$, to relax to the substrate anchoring, $\theta_{\mathcal{S}}$, for very thin films. Under these rather general assumptions, (3.3) takes the form

$$\phi = \phi_{\mathcal{S}}(x, y) \quad \text{and} \quad \theta = \theta_{\mathcal{S}} + (\theta_{\mathcal{F}} - \theta_{\mathcal{S}}) \, \frac{m(h)}{h} z \ , \tag{3.4}$$

where $m(h)$ is a monotonically increasing function such that $m(0) = 0$ and $m(\infty) = 1$. The function $m(h)$ is related to the free surface energy $\mathcal{G}(h)$ [1] by [5, 12, 24],

$$\frac{\partial \mathcal{G}(h)}{\partial h} = -\mathcal{N} \frac{m(h)m'(h)}{h} \ . \tag{3.5}$$

[1] The more usual expression for surface energy as a function of anchoring angle at the free surface, $\mathcal{G}(\theta)$, may be obtained by use of (3.4).

We use the following functional form for $m(h)$ (see previous chapter for motivation)

$$m(h) = f(h)\frac{h^\alpha}{h^\alpha + \beta^\alpha} \ , \quad f(h) = \frac{1}{2}\left[1 + \tanh\left(\frac{h-2b}{w}\right)\right] \ , \tag{3.6}$$

where $\alpha, \beta, w > 0$ are parameters to be chosen. The parameter β is a characteristic film thickness, above which free surface anchoring effects are dominant and below which free surface anchoring is relaxed; whereas α influences the rate of change of anchoring relaxation with respect to film height. The value of w corresponds to a characteristic range of film heights around the precursor thickness, below which free surface anchoring corresponds to that on the substrate, and above which the weak anchoring controlled by α and β applies. Note that with our chosen form of $m(h)$, the free surface energy $\mathcal{G}$ may be shown to be close to that proposed (phenomenologically) by Rapini and Papoular [30, 43].

3.1.2 Long Wave Equation

Asymptotic reduction of the momentum equations of the Leslie-Ericksen model [34] using the small aspect ratio of the film and neglecting inertial effects (see Chapter 2 for more details) leads to the following fourth order non-linear partial differential equation for the free surface height, $h(x, y, t)$,

$$h_t + \nabla \cdot \left(\mathcal{C}h^3\tilde{\nabla}\nabla^2 h - \left[\mathcal{D}h^3 + \mathcal{N}M\left(h\right)\right]\tilde{\nabla}h\right) + \mathcal{U}\mathcal{L}h^3 = 0 \ , \tag{3.7}$$

where

$$M(h) = m^2 - hmm' \ , \tag{3.8}$$

$$\mathcal{U} = \mathcal{B}\sin\chi \ , \quad \mathcal{D} = \mathcal{B}\cos\chi \ , \tag{3.9}$$

$$\tilde{\nabla} = \left[\lambda I + \nu\begin{pmatrix} \cos 2\phi & \sin 2\phi, \\ \sin 2\phi & -\cos 2\phi \end{pmatrix}\right]\begin{pmatrix} \partial_x \\ \partial_y \end{pmatrix} \ , \tag{3.10}$$

$$\mathcal{L} = \left[\lambda + \nu\cos 2\phi\right]\partial_x + \nu\sin 2\phi\partial_y + 2\nu\left[\phi_y\cos 2\phi - \phi_x\sin 2\phi\right] \ , \tag{3.11}$$

$$\lambda = \frac{2+\eta}{4\,(1+\eta)}\ , \quad \nu = -\frac{\eta}{4\,(1+\eta)}\ , \tag{3.12}$$

and $m(h)$ is defined by equation (3.6). Several properties of the above model should be noted: first, λ and ν are both singular at $\eta = -1$. Furthermore, if $\eta < -1$, $\tilde{\nabla}$ has negative coefficients, which would result in surface tension having a destabilizing effect. However, for those NLCs for which data are available, $-1 < \eta < 0$; therefore only values within this range are considered in this thesis. There are two parameters in the above model that differentiate it from the analogous Newtonian model: $\mathcal{N}$, a measure of the elastic response due to the antagonistic anchoring conditions (the difference in anchoring angles between the free surface and substrate); and η, a measure of non-Newtonian viscous effects due to the azimuthal anchoring on the substrate, ϕ. If $\eta = \mathcal{N} = 0$, we recover a model for a Newtonian fluid; therefore, within the framework of the present model, the response due to antagonistic polar anchoring conditions and azimuthal substrate anchoring may be analyzed independently.

For direct numerical simulations, the governing equation (3.7) is solved on a rectangular domain $\Omega = [x_0, x_L]\times[y_0, y_L]$. To reduce the influence of the boundaries on fluid flow, in the streamwise (x) direction the free surface height is assumed constant at the ends of the domain (modeling conditions in the far field, recalling the assumed downslope flow); and in the transverse (y) direction, we prescribe periodic boundary conditions. Specifically,

$$h(x_0, y, t) = H_0\ , \quad h(x_L, y, t) = b\ , \quad h_x(x_0, y, t) = h_x(x_L, y, t) = 0\ , \tag{3.13}$$

$$\text{and} \quad h_y(x, y_0, t) = h_y(x, y_L, t) = h_{yyy}(x, y_0, t) = h_{yyy}(x, y_L, t) = 0\ , \tag{3.14}$$

where H_0 is the film thickness behind the front and b is the precursor film thickness ahead of the front. For linear stability analysis, the governing equation is solved on

the unbounded domain and (3.13) is modified as follows:

$$h(-\infty, y, t) = H_0 \ , \quad h(\infty, y, t) = b \ , \text{ and } \quad h_x(-\infty, y, t) = h_x(\infty, y, t) = 0 \ . \quad (3.15)$$

The linear stability analysis assumes the solution is periodic in y.

We consider only two cases of azimuthal surface anchoring in this chapter: substrate anchoring parallel to flow, $\phi = 0 \pmod{\pi}$; and perpendicular to flow, $\phi = \pi/2 \pmod{\pi}$. Note that either choice of azimuthal substrate anchoring permits two-dimensional traveling wave solutions (discussed in the following section). Under this restriction, (3.10) and (3.11) simplify to

$$\tilde{\nabla} = \begin{pmatrix} \kappa_1 & 0 \\ 0 & \kappa_2 \end{pmatrix} \nabla \ , \quad \mathcal{L} = \kappa_1 \partial_x \ , \quad (3.16)$$

where

$$\kappa_1 = \begin{cases} \frac{1}{2(1+\eta)} & \phi = 0 \bmod \pi \\ \frac{1}{2} & \phi = \frac{\pi}{2} \bmod \pi \end{cases} \ , \quad \kappa_2 = \begin{cases} \frac{1}{2} & \phi = 0 \bmod \pi \\ \frac{1}{2(1+\eta)} & \phi = \frac{\pi}{2} \bmod \pi \end{cases} \ . \quad (3.17)$$

3.2 Two-Dimensional Flow Revisited

For two-dimensional flow, (3.7) simplifies to,

$$h_t + \kappa_1 \left(\mathcal{C} h^3 h_{xxx} - \left[\mathcal{D} h^3 + \mathcal{N} M(h) \right] h_x + \mathcal{U} h^3 \right)_x = 0 \ . \quad (3.18)$$

In the previous chapter, which we now briefly review, it was shown that there exists a traveling wave solution, $h(x,t) = h_0(x - Vt) = h_0(s)$, where V is the traveling speed. The traveling solution $h_0(s)$ satisfies,

$$-V h_0 + \kappa_1 \left[\mathcal{C} h_0^3 h_0''' - \mathcal{D} h_0^3 h_0' - \mathcal{N} M(h_0) h_0' + \mathcal{U} h_0^3 \right] = c \ , \quad (3.19)$$

where c is a constant of integration. Imposing the far field conditions (3.15), c and V are found to satisfy

$$c = -\kappa_1 \mathcal{U} H_0 b \left(H_0 + b\right) \ , \qquad V = \kappa_1 \mathcal{U} \left(H_0^2 + H_0 b + b^2\right) \ . \tag{3.20}$$

To understand the dynamics behind the traveling front, the stability of a perturbed, traveling flat film was analyzed: the flat film was found to be unstable if

$$H_0^3 \mathcal{D} + \mathcal{N} M(H_0) < 0 \ , \tag{3.21}$$

where, recall, $M(h)$ is defined by (3.8). Since $\mathcal{N} > 0$ the elastic response is stabilizing for $M(H_0) > 0$ and destabilizing for $M(H_0) < 0$. In the unstable regime, the growth rate of the most unstable mode is given by

$$\omega_m = \kappa_1 \frac{H_0^3}{4\mathcal{C}} \left[\mathcal{D} + \frac{\mathcal{N} M(H_0)}{H_0^3}\right]^2 \ . \tag{3.22}$$

In addition, within the unstable regime, an expression for the velocity of the boundaries of an imposed disturbance, or wave packet, was derived,

$$\left(\frac{x}{t}\right)_{\pm} = 3\kappa_1 \mathcal{U} H_0^2 \pm 1.622 \kappa_1 \sqrt{-\frac{\left[\mathcal{D} H_0^3 + \mathcal{N} M(H_0)\right]^3}{\mathcal{C} H_0^3}}, \tag{3.23}$$

where '+' and '−' denote the velocity of the right and left wave packet boundaries respectively. Comparing V in (3.20) to (3.23), the three classes of solutions defined in [11, 24] are obtained: Type 1 (stable; $V < (x/t)_-$), Type 2 (convectively unstable; $0 < (x/t)_- < V$), and Type 3 (absolutely unstable; $(x/t)_- < 0$). Note that both V and $(x/t)_-$ share a common factor of κ_1, thus the transitions between stability regimes are independent of κ_1.

To simplify the parameter study when we extend our results to three-dimensional flow, we vary η, $\mathcal{N}$, and $\mathcal{D}$ and fix the remaining parameters as in Table 3.1(a). Furthermore, we restrict $\mathcal{D}$ (which, together with $\mathcal{U}$, fixes χ and $\mathcal{B}$, see (3.9)) to just two values, corresponding to flow down an inclined substrate or flow down a vertical

Table 3.1 Values of the Parameters Chosen for the Simulations (Except where Specified Otherwise)

(a)

Parameter	Value	Parameter	Value	Parameter	Value
$\mathcal{C}$	2	β	0.5	Δx	0.1
$\mathcal{U}$	2	α	2	Δy	0.1
H_0	0.4	w	0.05		
b	0.1				

(b)

Parameter	Value
$\mathcal{D}$	1
$\mathcal{B}$	$\sqrt{5}$
χ	$\tan^{-1}(2)$

(c)

Parameter	Value
$\mathcal{D}$	0
$\mathcal{B}$	2
χ	$\pi/2$

Here, Δx and Δy are the partition spacings in the x and y domains respectively. (a) Parameters used for all simulations. (b) Additional parameters for flow down an inclined substrate. (c) Additional parameters for flow down a vertical substrate.

substrate, as given in Tables 3.1(b) and 3.1(c), respectively. The streamwise stability regimes in the $\mathcal{N}$ domain (with other parameters as fixed in Tables 3.1) are given in Tables 3.2(a) and 3.2(b) for flow down an inclined and vertical substrate, respectively. Note that, with the chosen values of α, β, b, w, the choice of H_0 corresponds to an unstable elastic response, $M(H_0) < 0$.

3.3 Transverse Stability of a Traveling Front

In this section, we expand our analysis of the two-dimensional problem [24] to three-dimensional flow; in particular, we study the transverse stability of a traveling fluid front. A traveling Newtonian front flowing down an inclined plane ($\mathcal{N} = \eta = 0, \mathcal{D} > 0$) is known to be unstable with respect to transverse perturbations [18]. With $\mathcal{U}$ fixed,

Table 3.2 Streamwise Stability Regimes in $\mathcal{N}$ Domain with all Other Parameters Fixed.

(a)

Stability Regime	Value of $\mathcal{N}$
Type 1	$\mathcal{N} < 7.1$
Type 2	$7.1 < \mathcal{N} < 11.4$
Type 3	$11.4 < \mathcal{N}$

(b)

Stability Regime	Value of $\mathcal{N}$
Type 1	$\mathcal{N} < 8.9$
Type 2	$8.9 < \mathcal{N} < 12.2$
Type 3	$12.2 < \mathcal{N}$

(a) Flow down an inclined substrate where parameters are given in Tables 3.1(a) and 3.1(b). (b) Flow down a vertical substrate where parameters are given in Tables 3.1(a) and 3.1(c).

increasing $\mathcal{D}$ has a stabilizing effect. Negative values of $\mathcal{D}$ (corresponding to flow on an inverted plane) have also been studied for Newtonian flow: in the two-dimensional case [10] such flow can exhibit the Types 1, 2 and 3 streamwise instability described in §3.2, while in the three-dimensional case [11], increasing $|\mathcal{D}|$ has a destabilizing effect on transverse perturbations. We proceed to analyze transverse perturbations within the context of the present model.

Following standard techniques applied to thin films [8], we begin the analysis by assuming a solution of the form

$$h(x, y, t) = h_0(s) + \epsilon h_1(s, y, t) \ , \tag{3.24}$$

where $|\epsilon| \ll 1$, $s = x - Vt$, V is given by (3.20), $h_0(s)$ is a stable (Type 1) traveling front solution and $h_1(s, y, t)$ is a perturbation. Substituting (3.24) into the governing equation (3.7) and integrating with respect to s, the traveling wave equation (3.19) is obtained at the leading order. At order ϵ, we derive the following (linear) equation for h_1,

$$\frac{\partial h_1}{\partial t} + \nabla \cdot (\mathcal{C}\mathcal{L}_{\mathcal{C}}[h_1] - \mathcal{D}\mathcal{L}_{\mathcal{D}}[h_1] - \mathcal{N}\mathcal{L}_{\mathcal{N}}[h_1]) + \mathcal{U}\mathcal{L}_{\mathcal{U}}[h_1] \tag{3.25}$$

where

$$\mathcal{L}_{\mathcal{C}} = h_0^3\tilde{\nabla}\nabla^2 + 3h_0^2\tilde{\nabla}\nabla^2 h_0 \ , \qquad \mathcal{L}_{\mathcal{D}} = h_0^3\tilde{\nabla} + 3h_0^2\tilde{\nabla}h_0$$
$$\mathcal{L}_{\mathcal{N}} = M(h_0)\tilde{\nabla} + M'(h_0)\tilde{\nabla}h_0 \ , \qquad \text{and} \quad \mathcal{L}_{\mathcal{U}} = 3h_0^2\partial_s + 6h_0\partial_s h_0 \ .$$

The operators $\mathcal{L}_i$ $(i = \mathcal{C}, \mathcal{D}, \mathcal{N}, \mathcal{U})$ are linear with respect to h_1; therefore, assuming that h_1 is a composition of Fourier modes, each mode may be considered separately, i.e. $h_1 = g(s,t)e^{iqy}$. To derive the dispersion relationship, we let $g(s,t) = \zeta(s)e^{\sigma t}$, where σ is the growth rate. Substituting this form into (3.25), we obtain

$$\sigma\zeta = c_4(h_0)\partial_{ssss}\zeta + c_3(h_0)\partial_{sss}\zeta + c_2(h_0;q)\partial_{ss}\zeta + c_1(h_0;q)\partial_s\zeta + c_0(h_0;q)\zeta \qquad (3.26)$$

where

$$\begin{aligned}
c_4(h_0) &= -\mathcal{C}\kappa_1 h_0^3, \\
c_3(h_0) &= -3\mathcal{C}\kappa_1 h_0^2\partial_s h_0, \\
c_2(h_0;q) &= 2\mathcal{C}\lambda q^2 h_0^3 + \kappa_1\left[\mathcal{D}h_0^3 + \mathcal{N}M(h_0)\right], \\
c_1(h_0;q) &= 3\kappa_1\left[\mathcal{C}h_0^2\left(\partial_s h_0 q^2 - \partial_{sss}h_0\right) + 6\mathcal{D}h_0^2\partial_s h_0 + 2\mathcal{N}\partial_s h_0' M'(h_0) - 3\mathcal{U}h_0^2\right] + V, \\
c_0(h_0;q) &= c_{00}(h_0;q) + c_{01}(h_0;q) + c_{03}(h_0;q) + c_{04}(h_0) \ , \\
c_{00}(h_0;q) &= -\mathcal{C}h_0\left[\kappa_2 h_0^2 q^4 + \kappa_1\left[6\partial_s h_0\partial_{sss}h_0 + 3h_0\partial_{ssss}h_0\right]\right], \\
c_{01}(h_0;q) &= \mathcal{D}h_0\left[-\kappa_2 h_0^2 q^2 + \kappa_1\left[6\left(\partial_s h_0\right)^2 + 3h_0\partial_{ss}h_0\right]\right], \\
c_{02}(h_0;q) &= \mathcal{N}\left[-\kappa_2 M(h_0)q^2 + \kappa_1\left[M'(h_0)\partial_{ss}h_0 + \left(\partial_s h_0\right)^2 M''(h_0)\right]\right], \\
c_{03}(h_0) &= -6\mathcal{U}\kappa_1 h_0\partial_s h_0,
\end{aligned}$$

with λ given by (3.12), and κ_i $(i = 1, 2)$ by (3.17). To extract the growth rate, σ, for a fixed q, (3.26) is discretized, implementing a finite difference method to estimate the derivatives of ζ. For some partition $\{s_n\}$ of s, (3.26) is approximated by

$$\left(A(h_0;q) - \sigma\right)\zeta_n = 0 \ , \qquad (3.27)$$

where $\zeta_n = \zeta(s_n)$ and $A(h_0, q)$ is the finite difference matrix. Since only the largest eigenvalue is required, a power iterative method is sufficient to calculate the growth rate for each value of q, as was done by Lin & Kondic [11].

3.3.1 Small Wavelength Approximation

To validate the results obtained by solving the eigenvalue problem (3.27), in this section we present an asymptotic approximation to the dispersion relation in the limit of small wave numbers, $|q| \ll 1$. Note that (3.26) contains only even powers of q; therefore, we asymptotically expand ζ and σ in q^2,

$$\sigma = \sigma_0 + q^2\sigma_1 + O(q^4) \qquad \text{and} \qquad \zeta = \zeta_0 + q^2\zeta_1 + O(q^4)\ . \tag{3.28}$$

For a fixed q, the front position is modified from $s = 0$ (unperturbed) to $s = s_b(y,t) = \epsilon e^{iqy+\sigma t}$. At the front position, the film height is given by, $h(s_b, y, t) = b$. Linearizing about the unperturbed front position, $s = 0$,

$$\epsilon e^{iqy+\sigma t}\left[\zeta_0(0) - \partial_s h_0(0)\right] + O\left(\epsilon^2\right) + O\left(q^2\right) = 0\ . \tag{3.29}$$

Setting $\zeta_0(0) = \partial_s h_0(0)$, the boundary condition at the fluid front is satisfied to the second order in ϵ and q. It is then reasonable to assume that $\zeta_0(s)$ takes the form

$$\zeta_0(s) = \partial_s h_0(s)\ . \tag{3.30}$$

Substituting (3.28) and (3.30) into (3.25), order ϵq^0 terms of the dispersion relationship may be expressed as

$$\sigma_0 \partial_s h_0 = \left[-V h_0 + \kappa_1\left[\mathcal{C} h_0^3 h_0''' - \mathcal{D} h_0^3 h_0' - \mathcal{N} M(h_0) h_0' + \mathcal{U} h_0^3\right]\right]_{ss}\ , \tag{3.31}$$

and recalling the two-dimensional traveling wave equation, (3.19), $\sigma_0 = 0$.

To simplify the order ϵq^2 terms, it is assumed that perturbations only occur near the front position (the fluid flow is undisturbed in the far-field); therefore, subject to

the boundary conditions (3.15), h_0 and ζ_1 must satisfy

$$h_0(s \to -\infty) = H_0 \ , \quad h_0(s \to \infty) = b \ , \text{ and } \quad \zeta_1(s \to \pm\infty) = 0 \ . \tag{3.32}$$

To proceed, we integrate the order ϵq^2 terms of (3.25) with respect to s over the infinite line. The majority of the terms may be integrated exactly and, applying the far field conditions (3.32), evaluate to zero. The remaining non-zero terms may be expressed as

$$\sigma_1 = \frac{\kappa_2}{H_0 - b} \int_{-\infty}^{\infty} \left[\mathcal{C} h_0^3 \partial_{sss} h_0 - \mathcal{D} h_0^3 \partial_s h_0 - \mathcal{N} M(h_0) \partial_s h_0 \right] ds \ . \tag{3.33}$$

Substituting (3.19) in the integrand of the above expression, the small q approximation to the dispersion relation is

$$\sigma = q^2 \frac{\kappa_2 \mathcal{U}}{H_0 - b} \int_{-\infty}^{\infty} \left[(h_0 - H_0)\,(h_0 - b)\,(h_0 + H_0 + b) \right] \, ds + O(q^4) \ . \tag{3.34}$$

In two dimensions, κ_1 and κ_2 (which depend on η; see (3.17)) influence only the traveling wave speed, V, given by (3.20). The functional form of $H(s)$ is independent of η; hence the integral (3.34) does not depend on η. Note, for parallel substrate anchoring, κ_2 is a constant, thus the small q analysis in this case is independent of η. Recalling $\eta \in (-1, 0)$, we see from (3.17) that for perpendicular anchoring, increasing $|\eta|$ strengthens transverse instabilities.

To analyze the effect of other parameters, note that while the solution $h_0(s)$ depends on $\mathcal{C}$, $\mathcal{D}$, $\mathcal{N}$ and $\mathcal{U}$, the integrand in (3.34) is not directly dependent on these parameters. This suggests that the effect of these parameters on transverse stability may be predicted by knowing their influence on the shape of the traveling wave solutions, $h_0(s)$. The integrand in (3.34) is zero for $h_0(s) = h_0$ and $h_0(s) = b$; thus, the main contribution to the integrand comes from the region near the front. For a Newtonian fluid, increasing $\mathcal{D}$ (while keeping other parameters fixed) decreases the size of the capillary ridge in two-dimensional numerical simulations [8]. Furthermore,

analysis of transverse perturbations for Newtonian fluids predicts that increasing $\mathcal{D}$ has a stabilizing effect. In the model presented, for a destabilizing elastic response in a flat film ($M(h_0) < 0$), increasing $\mathcal{N}$ increases the size of the capillary ridge in two-dimensional simulations [24]; therefore, increasing $\mathcal{N}$ is expected to have a destabilizing effect on transverse perturbations. For a stabilizing elastic response, $M(h_0) > 0$, the opposite is expected.

3.3.2 Influence of Elastic Response and Substrate Anchoring

To compute the growth rates predicted by the linear stability analysis, a (Type 1) traveling wave solution, $h_0(s)$, is required. Since (3.19) is highly non-linear, an analytical solution is not feasible. Therefore, subject to the boundary conditions given by (3.13), the two-dimensional governing equation, (3.18), is evolved numerically until the initial condition has converged to a stable traveling wave. The initial condition is given by

$$h(x,0) = \frac{(H_0 - b)}{2} \tanh\left[-5\,(x - x_f)\right] + \frac{H_0 + b}{2}\,, \quad x_f = \frac{2(x_0 + x_L)}{3}\,, \tag{3.35}$$

a film profile that at x_f transitions from a film of thickness h_0, to a film of thickness b, the precursor layer.

The numerical method employed to evaluate the two-dimensional governing equation, (3.18), is based on a Crank-Nicholson type discretization scheme coupled with an adaptive time stepping method. To account for the non-linear terms, a Newton-Raphson iterative solver is implemented. The reader is referred to the paper by Lin *et al.* [12] for further information about the numerical method employed.

In addition to the small-q analysis described above, we also solve the eigenvalue problem (3.27) numerically for a range of q-values. To do this we adapt the method of Lin & Kondic [11] which computes only the largest eigenvalue σ for each value of q. As mentioned in §3.1.2, the effects of the elastic response, $\mathcal{N}$, and azimuthal

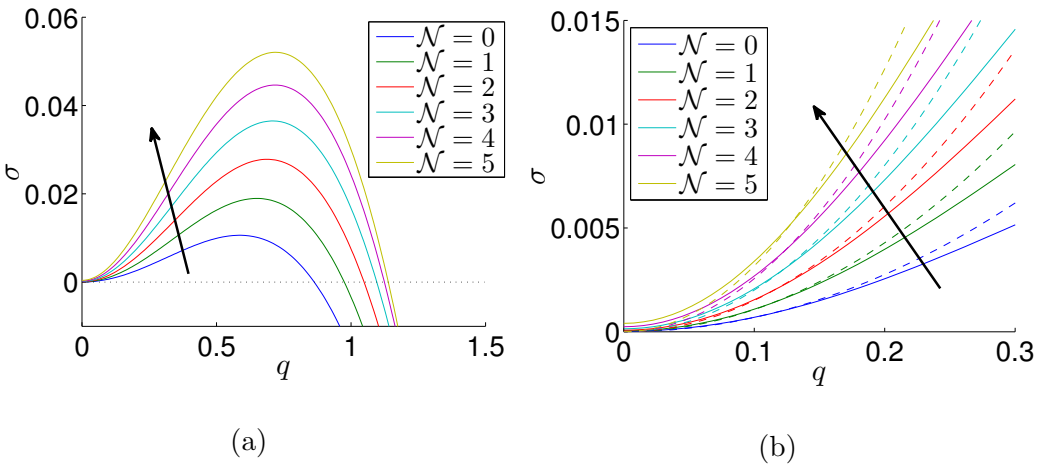

(a) (b)

Figure 3.1 (a) Influence of $\mathcal{N}$ on the dispersion relationship as given by the numerical solution of the full eigenvalue problem, (3.27). (b) Comparison between numerical results of the eigenvalue problem (solid lines) and small-q approximation (dashed lines), (3.34). Arrows denote increasing $\mathcal{N}$. Dispersion curves ignore azimuthal substrate anchoring ($\eta = 0$) and describe flow down a vertical substrate. Parameters are given in Tables 3.1(a) and 3.1(c).

substrate anchoring, η, may be studied independently; therefore, to begin the analysis, we consider flow down a vertical substrate with $\eta = 0$. Figure 3.1a plots the dispersion relationship for various values of $\mathcal{N}$ computed using numerical solutions to the eigenvalue problem, (3.27). The results are compared to the small-q approximations, (3.34), in Figure 3.1b. It may be seen that there is a good agreement between the two methods for small q and both methods capture the expected influence of $\mathcal{N}$.

To analyze the influence of azimuthal substrate anchoring, we continue to consider flow down a vertical substrate but now fix $\mathcal{N} = 2$ and vary η. In the case of parallel anchoring, η has no influence on the small q approximation, (3.34); therefore, only the dispersion relation calculated using the eigenvalue problem, (3.27), is shown. In Figure 3.2, which shows the results for the case of substrate anchoring parallel to the flow direction, we observe that increasing $|\eta|$ has negligible influence for small q (as we would anticipate, since the small q analysis results were independent of η in this case); however, for larger q, increasing $|\eta|$ has a destabilizing effect. In the case of perpendicular substrate anchoring, the effect of η on the dispersion relation

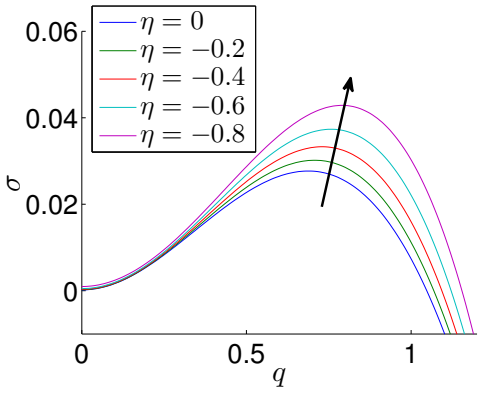

Figure 3.2 Influence of η, in the case of planar substrate anchoring parallel to the flow direction, on the dispersion relationship as given by the eigenvalue problem, (3.27). Arrow denotes the direction of increasing $|\eta|$. Here $\mathcal{N} = 2$ with other parameters given in Tables 3.1(a) and 3.1(c).

computed from the eigenvalue problem is shown in Figure 3.3a and compared to the small-q approximation in Figure 3.3b. We observe three trends as $|\eta|$ increases: the maximum growth rate increases; the wave number, q, corresponding to the maximum growth rate decreases; and the range of unstable modes decreases.

3.4 Numerical Simulations: Three-Dimensional Flow

In this section we present direct numerical simulations of Eq. (3.7), which describes the evolution of the free surface for nematic liquid crystal flowing down an incline. We implement an Alternating Direction Implicit (ADI) type method with adaptive time stepping; see [11] for the details of implementation, and [44] for a more general discussion of the use of ADI in the context of nonlinear high-order parabolic equations. To reduce the size of the computational domain, the grid is expanded dynamically in the streamwise (x) direction such that the free surface height is always sufficiently flat at the boundaries of the computational domain. The grid is shifted so that the lengths of the flat regions at the boundaries are equal. This corresponds to undisturbed flow at the boundaries (3.13). The initial length of the x domain, $L_x = x_L - x_0$, is fixed at $L_x = 40$ for all simulations. In the y direction, symmetry boundary conditions are

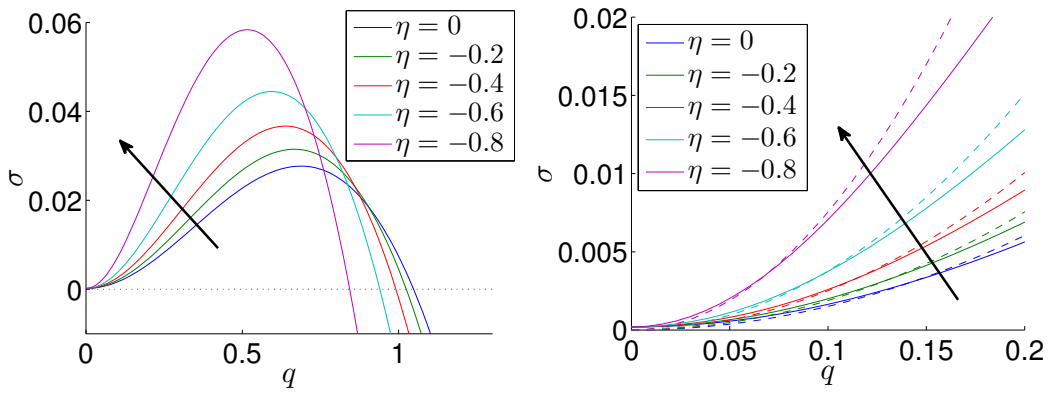

(a) (b)

Figure 3.3 (a) Influence of η, in the case of planar substrate anchoring perpendicular to the flow direction, on the dispersion relation as given by the numerical solution of the full eigenvalue problem, (3.27). (b) Comparison between numerical results of eigenvalue problem (solid line) and small-q approximation (dashed line), (3.34). Arrows denote the direction of increasing $|\eta|$. Here $\mathcal{N} = 2$ with other parameters given in Tables 3.1(a) and 3.1(c).

imposed. The length of the y domain is fixed according to the initial condition of interest.

To generate an initial condition, for a fixed y, the numerical traveling wave solution is shifted and then interpolated to an equispaced (x, y) grid. Specifically, if $\{\hat{x}_i\}$ is the partition of the traveling wave solution, the shifted partition is defined as $\tilde{x}_i(y) = \hat{x}_i + \Delta x_f(y)$, where $\Delta x_f(y)$ is the perturbation to the front position. Using cubic splines, the solution at nodes $\{\tilde{x}_i(y)\}$ is interpolated to an equispaced partition, $\{x_j\}$. This is equivalent to

$$h(x, y, t = 0) = h_0(x - \Delta x_f(y)) \; . \tag{3.36}$$

In addition, the initial condition is shifted such that the initial unperturbed front position, x_{f0}, is the same for all simulations i.e. $x_f(y) = x_{f0} + \Delta x_f(y)$ where $x_{f0} = 24$.

To analyze transverse instabilities, we fix the length of the y domain to be one wavelength of a plane wave, i.e.,

$$x_f(y) = -A\cos\left(q\left[y - y_0\right]\right) \ , \quad q = \frac{2\pi}{y_L - y_0} \ , \tag{3.37}$$

where $A = 0.1$ is the magnitude of the perturbation and for simplicity $y_0 = 0$. Furthermore, with the exception of extracting growth rates to validate the dispersion relation for different q, y_L is set to correspond approximately to the most unstable mode for the Newtonian case ($\mathcal{N} = 0$ and $\eta = 0$). Specifically, for flow down an inclined substrate, $y_L = 13$, and for flow on a vertical substrate, $y_L = 11$.

To simulate coating flows that appear in practice, we also consider the flow of a nematic liquid crystal on a wider y domain. In this case, the front position is perturbed by a superposition of cosine waves with random coefficients. Specifically, the perturbed front position and y domain are defined as

$$x_f(y) = \sum_{n=1}^{N=20} a_n \cos\left(q_n\left[y - y_0\right]\right) \ , \quad q_n = \frac{n\pi}{y_L - y_0} \ , \quad y_L = 100 \ , \tag{3.38}$$

where a_n are randomly chosen in the interval $[-0.1, 0.1]$.

Note that with double precision arithmetic (round-off error on the scale of 10^{-16}), numerical noise is expected to grow on the time scale

$$T_M = \frac{14\ln 10}{\tau} \ , \tag{3.39}$$

where τ is the growthrate of an instability (streamwise or transverse). It is assumed that numerical noise becomes significant when the magnitude of numerical noise instability grows to that of the numerical accuracy of the ADI method, $\Delta x^2 = \Delta y^2 = 0.01$. Our simulations focus on the time scales that are short compared to T_M and therefore numerical noise is not expected to influence the results.

3.4.1 Streamwise Stable Flow (Type 1)

In this section we present numerical simulations of a Newtonian flow and a NLC flow in the Type 1 regime (stable to streamwise perturbations), on an inclined and vertical substrate. The influence of the azimuthal anchoring is ignored, $\eta = 0$. The height profiles of a Newtonian flow on a vertical substrate ($\mathcal{D} = 0$) are shown in Figure 3.4. It is observed that the initial perturbation present in Figure 3.4a grows into a finger, which eventually evolves to a stable size and and then translates steadily down the substrate. The existence of the steady traveling solution may be similar as discussed in [9], where it is predicted that stable non-trivial traveling waves may exist for certain parameter values. Analysis of this phenomenon is not within the scope of this thesis and we refer the reader to [9] for further discussion. Figure 3.5 shows the corresponding results for a film of NLC, with $\mathcal{N} = 2$. Initially a single central finger forms and at later times, secondary fingers evolve along the y boundaries. Recalling Figure 3.1a, for $\mathcal{N} = 2$, the critical wavelength is approximately 6. This suggests that the y domain, $0 \leq y \leq 11$, is large enough to allow other modes (secondary fingers) to develop.

Figure 3.6 shows the results for Newtonian and Type 1 NLC flow down an inclined substrate ($\mathcal{D} = 1$). The dynamics are qualitatively similar to those for the vertical substrate, hence we show film height profiles only at the final time, corresponding to the solution snapshots of Figures 3.4c and 3.5b. Increasing $\mathcal{D}$ is observed to have stabilizing effect, as evidenced by the smaller finger lengths observed in Figure 3.6.

Growth Rate of Transverse Perturbations To extract the growth rate from simulation results, we track the position (along the x-axis) of the central finger's tip and root, $x_t(t)$ and $x_r(t)$, respectively. The location of the centre of the finger is defined as $x_c(t) = [x_t(t) + x_r(t)]/2$, and the length of the finger as $L(t) = x_t(t) - x_r(t)$. Following the investigation of §3.3.2, we first consider flow down a vertical substrate

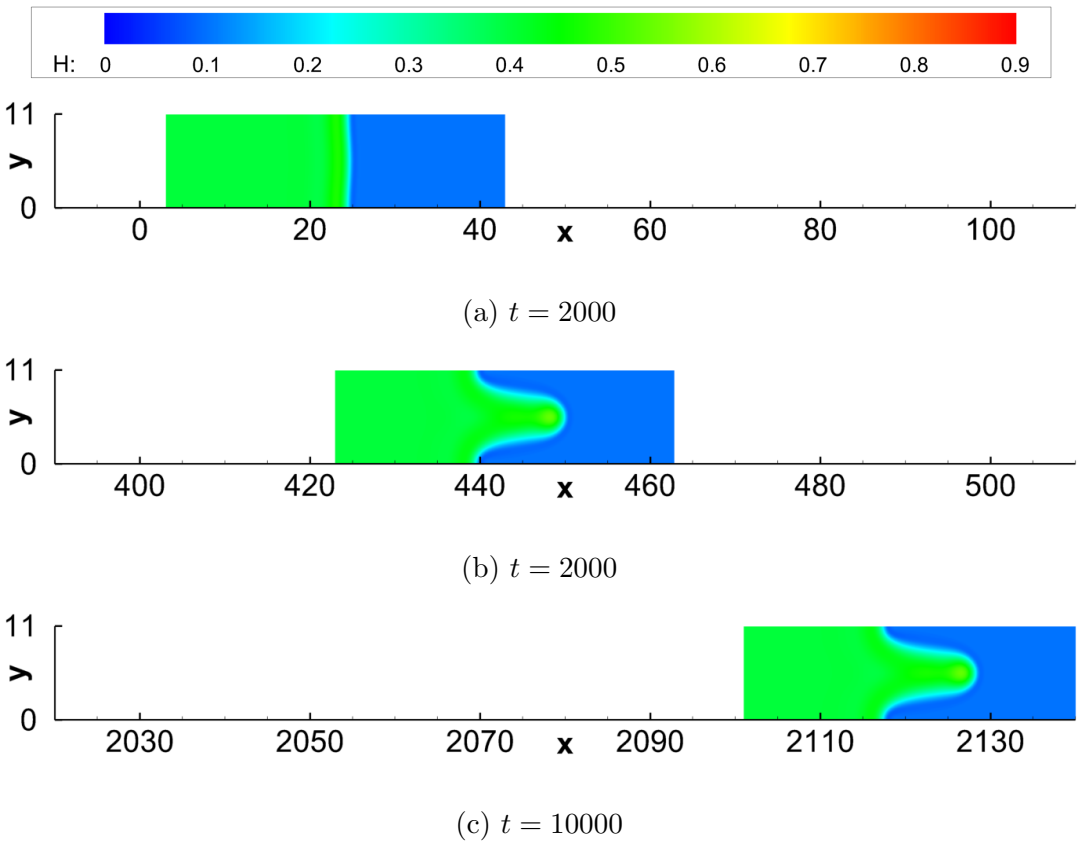

(a) $t = 2000$

(b) $t = 2000$

(c) $t = 10000$

Figure 3.4 Height profile of a Newtonian ($\mathcal{N} = 0$ and $\eta = 0$) flow down a vertical substrate ($\mathcal{D} = 0$) at various times. $T_M = 3000$ and other parameters are given in Tables 3.1(a) and 3.1(c).

where the azimuthal substrate anchoring is ignored ($\eta = 0$) and vary the elastic response parameter, $\mathcal{N}$.

Changing the reference frame to one moving with the speed of the two-dimensional traveling wave, V given in (3.20), the position of the finger tip and root are shown in Figures 3.7a and 3.7b. It may be seen that there exist at least two spreading regimes; initially, the finger tip and root travel at velocities close to the two-dimensional traveling wave speed, V. As the finger evolves, the velocities deviate from V, but appear to be nearly constant in time. The center of the finger, $x_c(t)$, in the reference frame of the traveling wave, is shown in Figure 3.7c. At first, the center of the finger travels at the two-dimensional traveling wave speed, suggesting that the velocities of the finger tip and root are equal but opposite. For later times, the finger

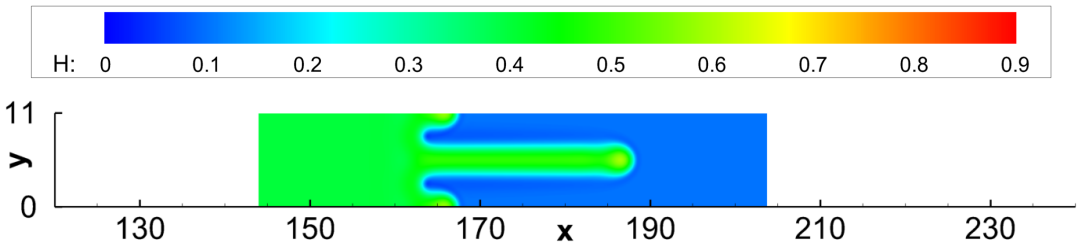

(a) $t = 700$

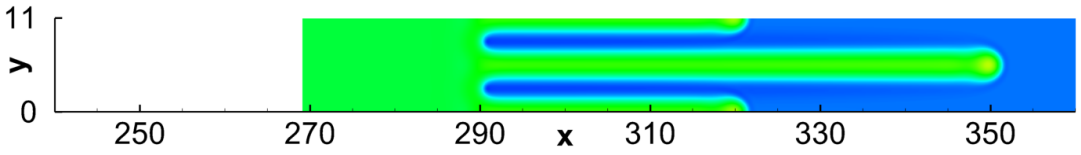

(b) $t = 1400$

Figure 3.5 Height profile of a Type 1 ($\mathcal{N} = 2$) flow down a vertical substrate ($\mathcal{D} = 0$) at various times. Here the azimuthal substrate anchoring is ignored ($\eta = 0$), and other parameters are given in Tables 3.1(a) and 3.1(c). The initial front position, $x_f \approx 24$, and the initial condition is similar to Figure 3.4a.

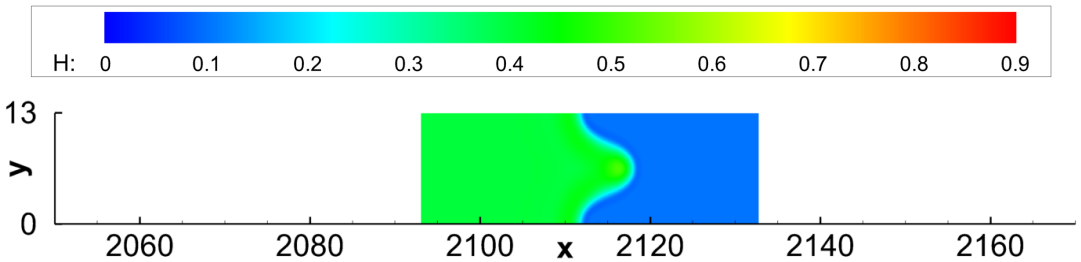

(a) $t = 10000$

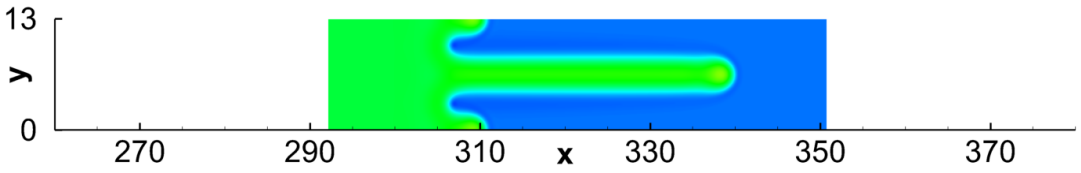

(b) $t = 1400$

Figure 3.6 Height profiles of (a) Newtonian ($\mathcal{N} = 0$ and $\eta = 0$) flow; and (b) Type 1 ($\mathcal{N} = 2$) flow down an inclined substrate ($\mathcal{D} = 1$) where the azimuthal substrate anchoring is ignored ($\eta = 0$). For earlier times, the evolution of the height profile are qualitatively similar to Figures 3.4 and 3.5. Other parameters are given in Tables 3.1(a) and 3.1(b).

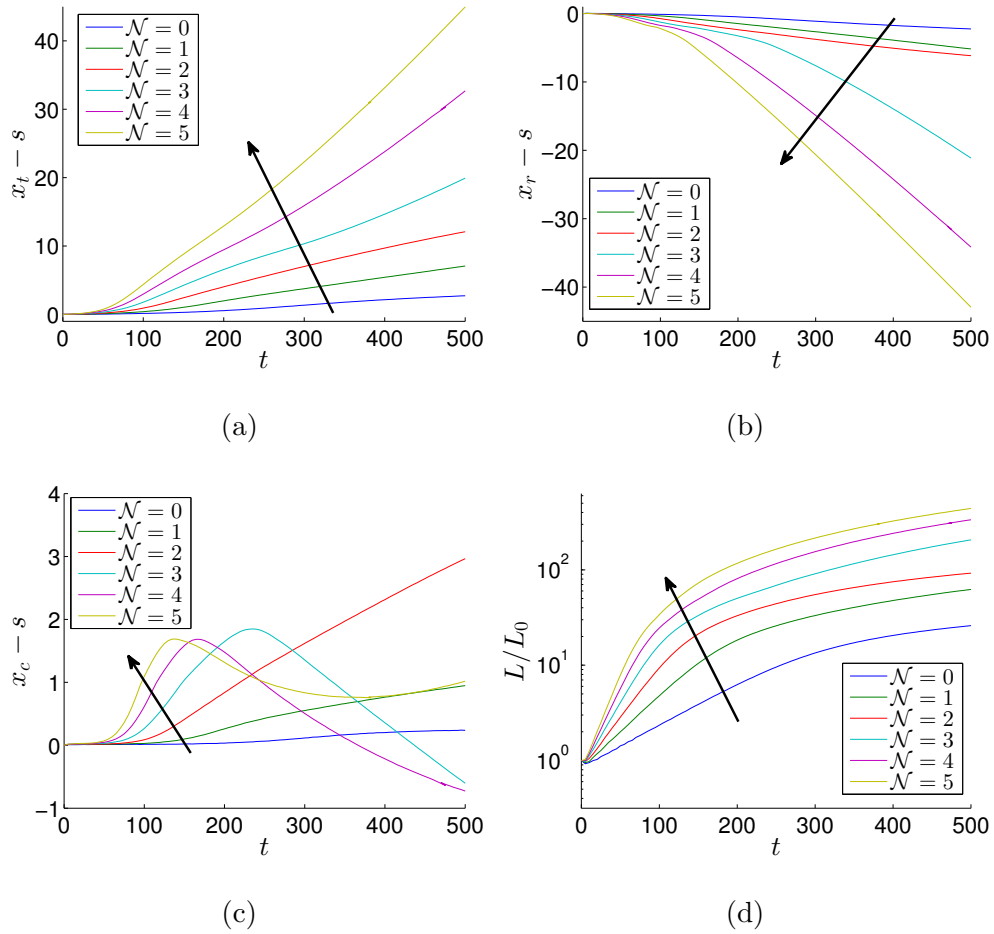

Figure 3.7 Effect of $\mathcal{N}$ on (a) position of perturbation tip, (b) position of perturbation root, (c) centre of perturbation and (d) length of perturbation. The arrows denote increase of $\mathcal{N}$. Note the positions in (a), (b) and (c) are plotted in the reference frame $x - s = x - Vt$ where $V = 0.21$, given by (3.20). Here $\eta = 0$ and other parameters are given by Tables 3.1(a) and 3.1(c).

center velocity may vary depending on the value of $\mathcal{N}$; however, the center of the finger always remains near the two-dimensional traveling wave front position. This suggests that while the tip of the finger travels further down the substrate than the two-dimensional traveling wave solution, the area of the substrate coated by a film of uniform thickness is less than it would be if the film were stable with respect to transverse perturbations.

Figure 3.7d plots the finger length normalized by the initial length, $L_0 = 2A = 0.2$, on a semi-log scale. It may be seen that initially fingers grow exponentially in

time, as anticipated, but at later times, growth rates decrease. Extracting the growth rate, σ, from the linear regions observed in Figure 3.7d, the dispersion relation found numerically by solving (3.27) may be validated. To proceed, we consider a Type 1 flow ($\mathcal{N} = 2$) with three types of azimuthal substrate anchoring: substrate anchoring where the azimuthal angle is ignored ($\eta = 0$), planar substrate anchoring that is parallel to flow with $\eta = -0.8$, and planar substrate anchoring that is perpendicular to flow with $\eta = -0.8$. Figure 3.8 shows that there is excellent agreement between growth rates extracted from direct simulations of (3.27), and the growth-rate given by numerically solving the discretized eigenvalue problem for all three cases considered. These results validate the influence of η and $\mathcal{N}$ on transverse stability predicted by the eigenvalue problem in the both cases of the azimuthal substrate anchoring.

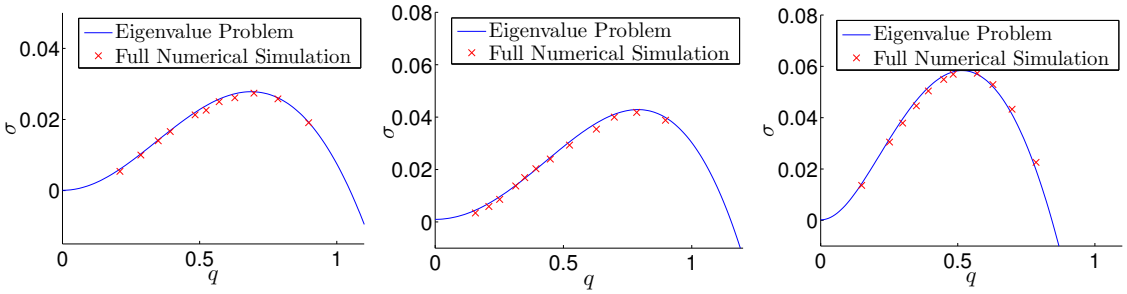

(a) (b) (c)

Figure 3.8 Comparison of dispersion relation computed using the eigenvalue problem (3.27) and growth rate extracted from direct numerical simulations, described in §3.4.1. Dispersion curves are calculated for a Type 1 ($\mathcal{N} = 2$) down a vertical substrate where (a) azimuthal substrate anchoring has been ignored ($\eta = 0$), (b) parallel azimuthal substrate anchoring with $\eta = -0.8$, and (c) perpendicular azimuthal substrate anchoring with $\eta = -0.8$. Other parameters are given in Tables 3.1(b) and 3.1(c).

3.4.2 Streamwise and Transverse Instability (Type 2 and Type 3)

In this subsection we discuss several numerical simulations where transverse and streamwise instabilities are present simultaneously. We ignore the azimuthal substrate anchoring initially and consider flow down a vertical substrate ($\mathcal{D} = 0$) and inclined

substrate ($\mathcal{D} = 1$). The values of $\mathcal{N}$ are chosen such that either Type 2 or Type 3 solutions are expected [24] (see Table 3.2). Other parameters are given in Table 3.1. In the case of a vertical substrate (Table 3.1(c)), Figures 3.9 and 3.10 show the evolution of the free surface height for a Type 2 flow ($\mathcal{N} = 9$) and Type 3 flow ($\mathcal{N} = 12$), respectively. For flow down an inclined substrate (Table 3.1(b)), the evolution of the height profiles for Type 2 flow ($\mathcal{N} = 10$) and Type 3 flow ($\mathcal{N} = 16$) is shown in Figures 3.11 and 3.12, respectively. Comparing the numerical results, first note the initial perturbed front position, $x_f \approx 24$, relative to the unstable region. For Type 2 flows, it is expected that the streamwise instability behind the front does not propagate (in the x direction) beyond the initial front position; Figures 3.9 and 3.11 confirm this expectation. By contrast, Figures 3.10 and 3.12 show that for a Type 3 flow, the streamwise instabilities propagate beyond the initial front position, a result expected from the two-dimensional analysis (presented in detail in [24] and summarized in §3.2). These results suggest that the classifications of solutions in two dimensions (Type 1, 2 & 3) carry over to the three dimensional case.

In the simulations presented, we observe two types of qualitative dynamics: tear formation (e.g. $x \approx 80$ in Figure 3.9a) and semi-stable traveling ridges (e.g. $x \approx 40$ in Figure 3.12a). Examining Figures 3.9, 3.10 and 3.11, it may be seen that streamwise instabilities occur behind the front, resulting in dewetting in the center. The dewetted region grows in the x and y directions, resulting in the initial finger breaking from the front, forming a tear like shape. Behind the dewetting region, analogous instabilities occur near the y boundaries and form secondary tears. This process alternates between the two types of tear formation. Newly formed tears appear to briefly accelerate after breakup; however, tears will eventually elongate and connect with other tears in the streamwise direction. Considering a larger domain in the y-direction, Figure 3.13 shows the height profiles for a Type 3 flow down a vertical substrate where the front position has been perturbed by the superposition

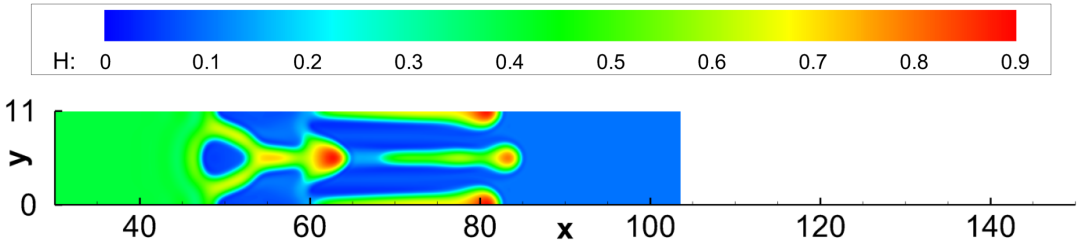

(a) $t = 150$

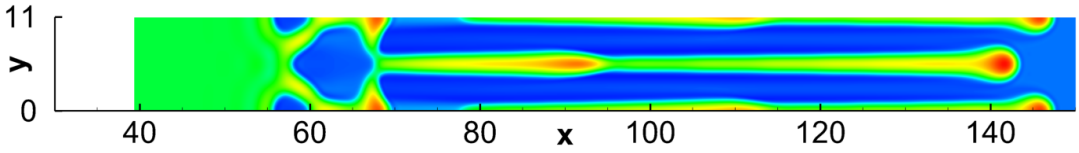

(b) $t = 300$

Figure 3.9 Height profile of a Type 2 ($\mathcal{N} = 9$) flow down a vertical substrate at various times. Here the azimuthal substrate anchoring is ignored ($\eta = 0$), and other parameters are given in Tables 3.1(a) and 3.1(c). The initial front position, $x_f \approx 24$, and the initial condition is similar to Figure 3.4a.

of cosine waves with random coefficients (see (3.38)). It may be seen that similar tear formation occurs.

For a Type 3 flow down an inclined substrate, Figure 3.12, we observe the formation of traveling ridges behind the front. The ridges appear to be analogous to solitary-like waves observed in two-dimensional simulations [10, 24]. Similarly to the tear formation flows, streamwise instabilities occur behind the front; however, the dewetting regions grow rapidly in the transverse direction, splitting the film in the streamwise direction. This may be seen in Figure 3.12a, where the dewetted region behind the newly forming ridge is elongated. This suggests that the instability in the streamwise direction is stronger than the instability in the transverse direction. Newly formed ridges, however, do not persist and eventually destabilize in the transverse direction. For later times, Figure 3.12b, it appears that the formation of new ridges terminates. Simulating this type of flow on a larger y domain with a randomly-

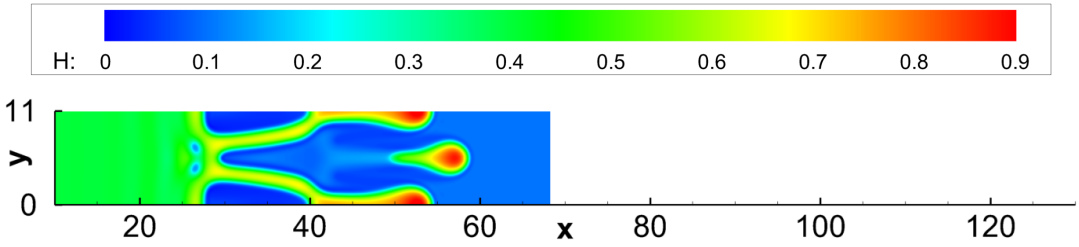

(a) $t = 120$

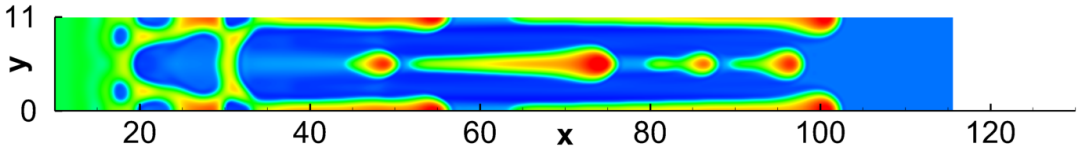

(b) $t = 220$

Figure 3.10 Height profile of a Type 3 ($\mathcal{N} = 12$) flow down a vertical substrate at various times. Here the azimuthal substrate anchoring is ignored ($\eta = 0$), and other parameters are given in Tables 3.1(a) and 3.1(c). The initial front position, $x_f \approx 24$, and the initial condition is similar to Figure 3.4a.

perturbed front position, Figure 3.14 shows that ridge formation still occurs for a Type 3 flow down an inclined surface.

The existence of the semi-stable traveling ridges may be due to the initial competition between transverse instability and streamwise instability. When tear formation is observed, Figure 3.12, the transverse perturbation of the front grows by a non-negligible amount before the streamwise instability occurs. In the case of ridge formation, the streamwise instability occurs well before the transverse perturbation has time to grow sufficiently. This suggests that instability is stronger in the streamwise direction, which is supported by the rapid breakup observed in the x direction. Therefore, initially, the shape of the patterns that form behind the front seems to be governed by the streamwise instability. This results in a film profile that is similar to two-dimensional solutions, but has been extended and perturbed in the y direction. For later times, the ridges destabilize at a rate similar to that of the originally perturbed front.

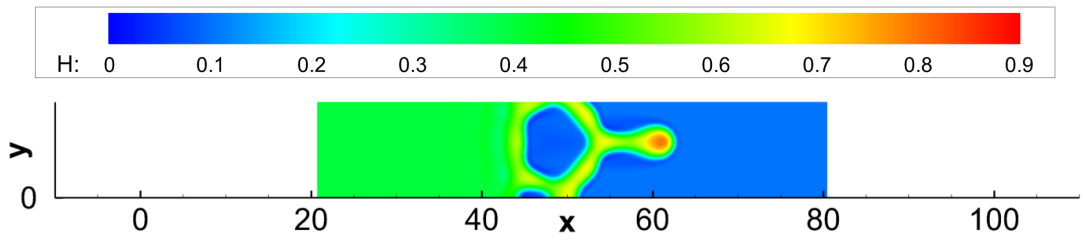

(a) $t = 90$

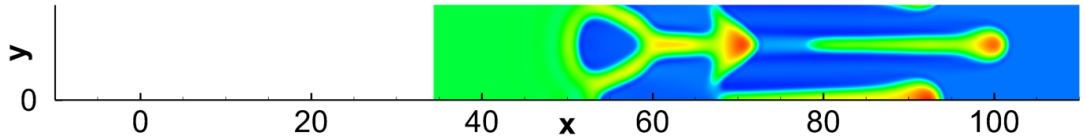

(b) $t = 180$

Figure 3.11 Height profile of a Type 2 ($\mathcal{N} = 10$) flow down an inclined substrate at various times. Here the azimuthal substrate anchoring is ignored ($\eta = 0$), and other parameters are given in Tables 3.1(a) and 3.1(b). The initial front position, $x_f \approx 24$, and the initial condition is similar to Figure 3.4a.

Influence of Azimuthal Substrate Anchoring For a spreading nematic liquid crystal drop on a horizontal substrate, it is known that, for radially-asymmetric azimuthal substrate anchoring $\phi(x, y)$, the anchoring pattern imposed on the substrate is reflected in the shape and structure of the spreading droplet [12]: broadly speaking, for planar substrate anchoring patterns the flow is fastest in the direction parallel to the anchoring direction, and slowest in the direction perpendicular to the anchoring. Figures 3.15 and 3.16 show the influence of parallel and perpendicular substrate anchoring, respectively, on a Type 2 flow down a vertical substrate ($\mathcal{N} = 9$) for various values of η. For the parameters considered, the height profiles at $t = 80$ are shown in Figures 3.15 and 3.16. In the case of parallel substrate anchoring, Figure 3.15 shows that increasing $|\eta|$ elongates the finger in the direction of anchoring. For perpendicular substrate anchoring, it may be seen that structure behind the finger, observed in Figure 3.16a, is destroyed in Figures 3.16b and 3.16c. Given that tear

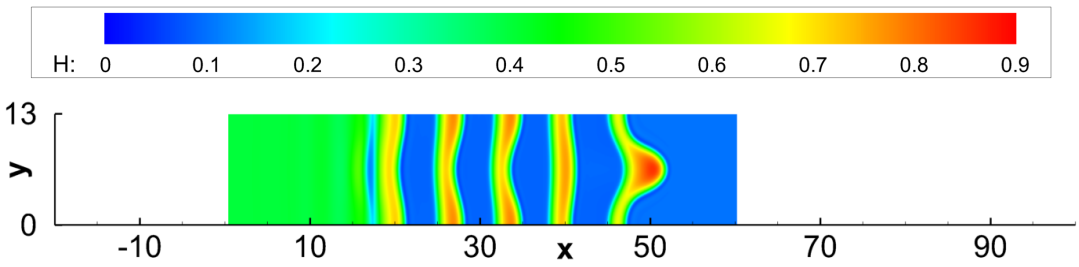

(a) $t = 65$

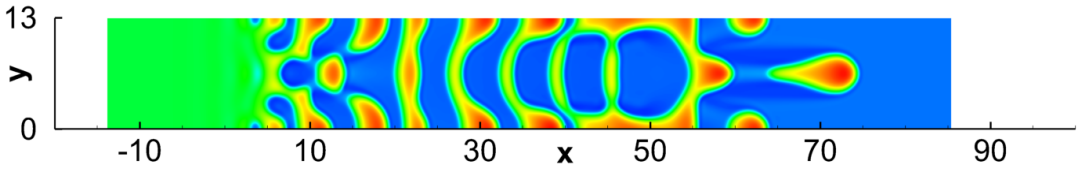

(b) $t = 110$

Figure 3.12 Height profile of a Type 3 ($\mathcal{N} = 16$) flow down an inclined substrate at various times. Here the azimuthal substrate anchoring is ignored ($\eta = 0$), and other parameters are given in Tables 3.1(a) and 3.1(b). The initial front position, $x_f \approx 24$, and the initial condition is similar to Figure 3.4a.

formation eventually occurs, the earlier onset of the breakup suggests that increasing $|\eta|$ strengthens the instability in the transverse direction.

3.5 Conclusions

To summarize, we have analyzed the flow of a nematic liquid crystal film down an inclined substrate, with weak homeotropic anchoring at the free surface, and strong planar anchoring at the substrate. Two specific cases of substrate anchoring were considered: parallel or perpendicular to the streamwise direction. The model we derive admits two-dimensional traveling waves for these simple anchoring scenarios. These traveling waves may be unstable to both transverse and streamwise perturbations. For flows that are streamwise stable, we have derived an asymptotic approximation to the dispersion relationship for transverse perturbations and validated the analysis by extracting the growth rates of transverse perturbations from direct numerical

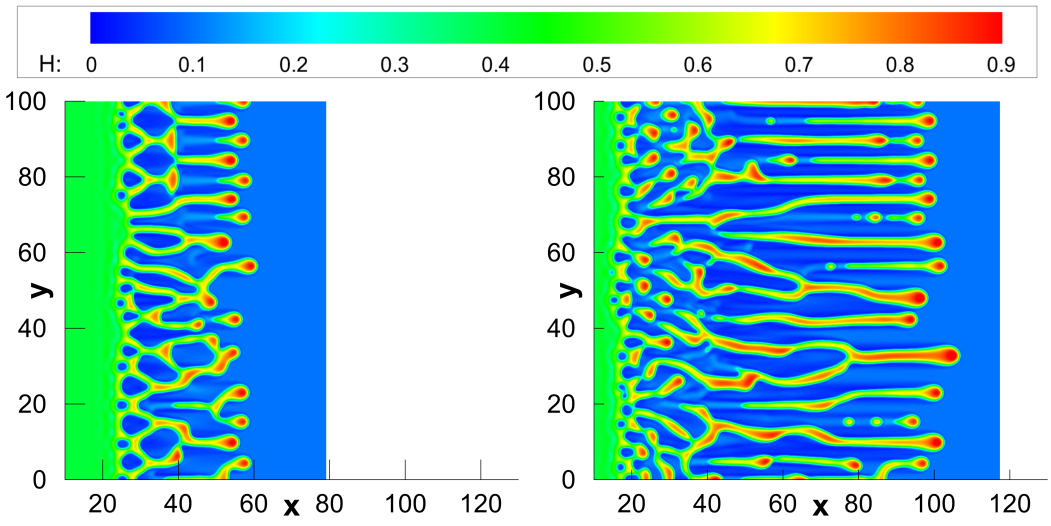

(a) $t = 90$ (b) $t = 180$

Figure 3.13 Height profile of a Type 3 ($\mathcal{N} = 12$) flow down a vertical substrate ($\mathcal{D} = 0$) at various times. Here the azimuthal substrate anchoring is ignored ($\eta = 0$) and other parameters are given in Tables 3.1(a) and 3.1(c). The initial front position, $x_{f0} = 24$.

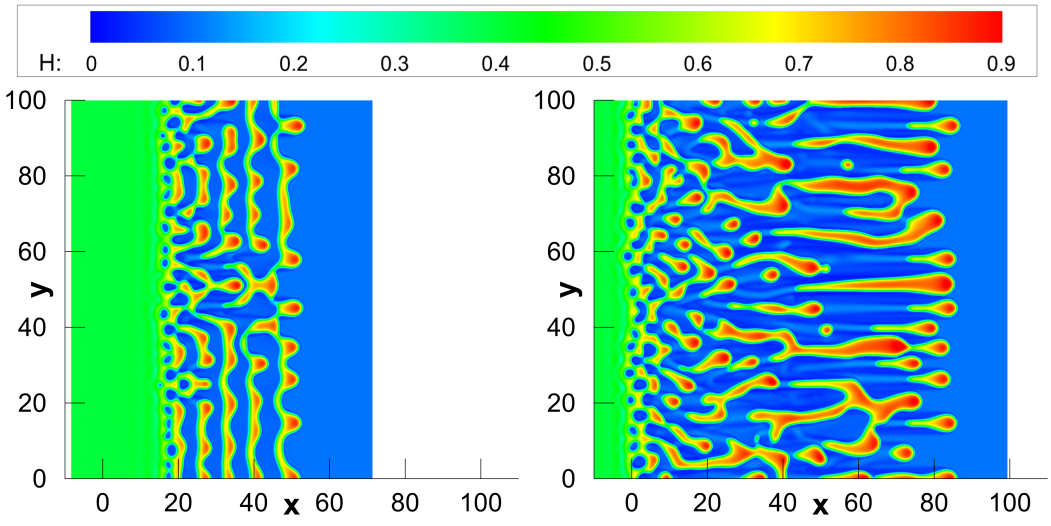

(a) $t = 65$ (b) $t = 100$

Figure 3.14 Height profile of a Type 3 ($\mathcal{N} = 16$) flow down a inclined substrate ($\mathcal{D} = 1$) at various times. Here the azimuthal substrate anchoring is ignored ($\eta = 0$) and other parameters are given in Tables 3.1(a) and 3.1(b). The initial front position, $x_{f0} = 24$.

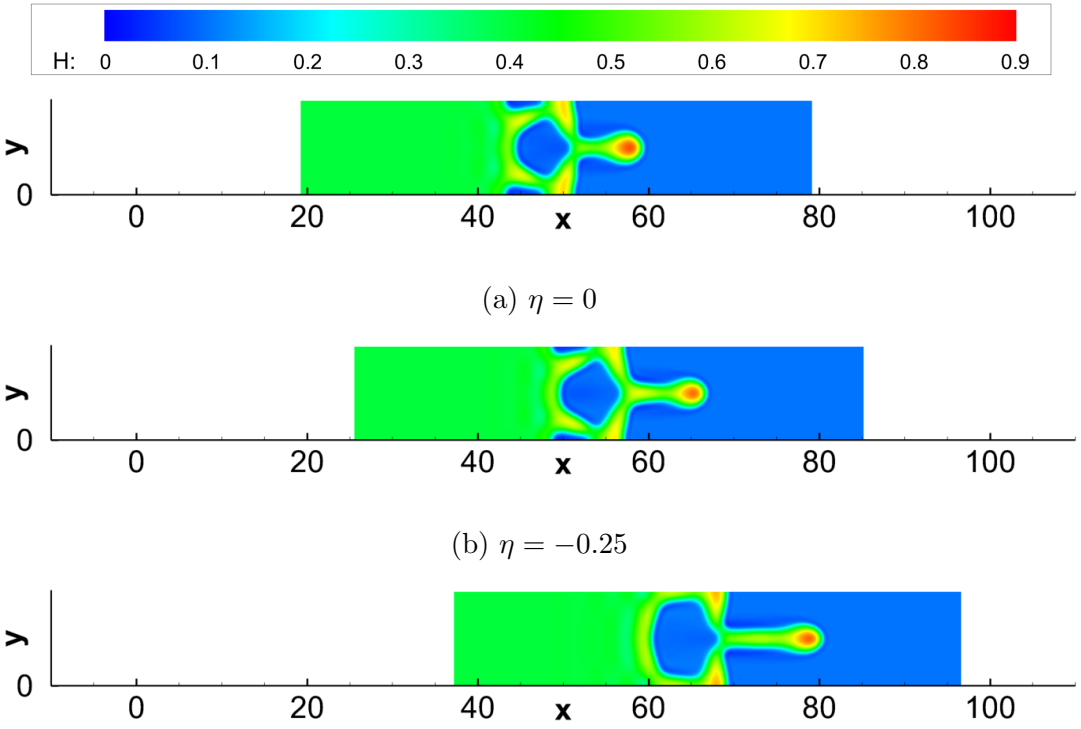

(a) $\eta = 0$

(b) $\eta = -0.25$

(c) $\eta = -0.5$

Figure 3.15 Influence of η and parallel azimuthal substrate anchoring on the evolution of the height profile of a Type 2 flow ($\mathcal{N} = 9$) down a vertical substrate. Height profiles are at a fixed later time, $t = 80$. Other parameters are given in Tables 3.1(a) and 3.1(c).

simulation of the governing equation. In the presence of streamwise and transverse instabilities, we observe rich dynamics when considering the evolution of the free surface height. In addition, simulations suggest that the influence of azimuthal substrate anchoring is similar to that observed for spreading nematic liquid crystal drops on a horizontal substrate [12]. We hope that our computational results will inspire future experimental investigations that may provide additional insight regarding the model used.

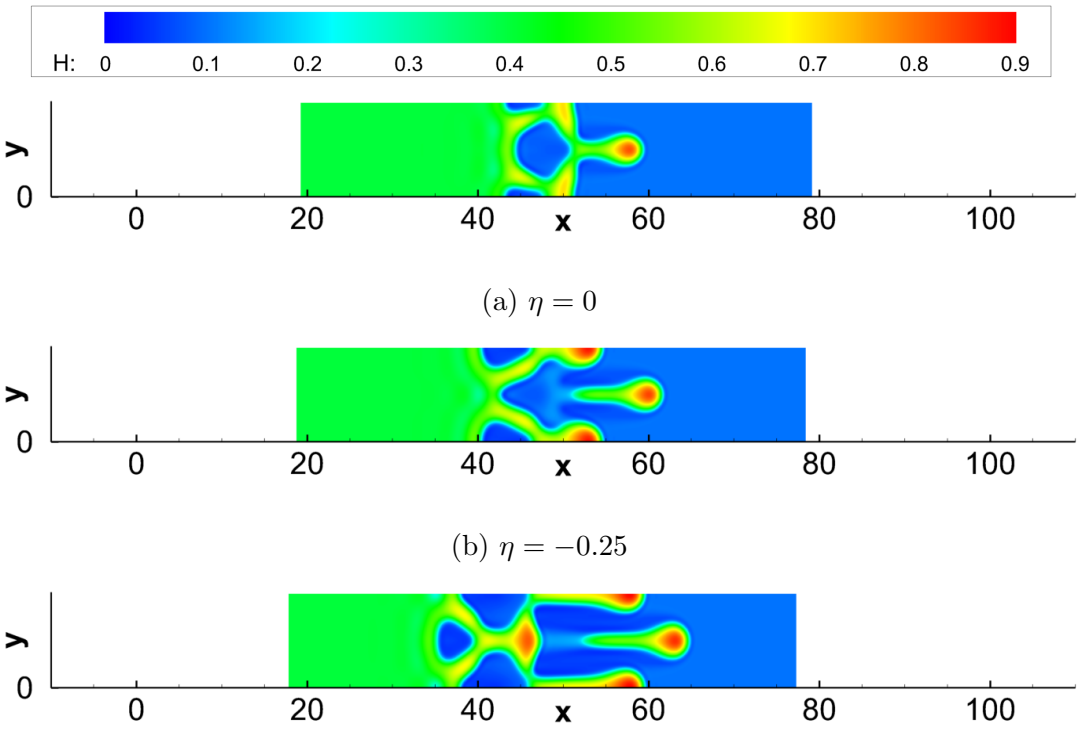

(a) $\eta = 0$

(b) $\eta = -0.25$

(c) $\eta = -0.5$

Figure 3.16 Influence of η and perpendicular azimuthal substrate anchoring on the evolution of the height profile of a Type 2 flow ($\mathcal{N} = 9$) down a vertical substrate. Height profiles are at a fixed later time, $t = 80$. Other parameters are given in Tables 3.1(a) and 3.1(c).

CHAPTER 4

STABILITY OF THIN FLUID FILMS CHARACTERIZED BY A COMPLEX FORM OF EFFECTIVE DISJOINING PRESSURE

Thin films, characterized by a small ratio of film thickness to typical lateral lengthscale, arise in many applications on scales that range from nano to macro. Recently, there has been much interest in instabilities of thin films on the nanoscale, in particular for polymeric films [4, 45, 46]; nematic liquid crystal (NLC) films [1, 3, 30, 31, 47]; and metal films [48, 49], to name just a few examples. In many of the considered cases, the instabilities that develop are complicated by interplay of a number of different effects. On the nanoscale, these necessarily include fluid/solid interaction, often modeled by including in the governing equations a disjoining pressure term that plays an important role in determining the film stability. The relevant forms of the disjoining pressure may be rather complicated, reflecting, for example, complex Si/SiO_2 substrates in the case of polymer films [4], or complex physics of the fluid/solid interaction in the case of metal films [50, 51] and the references therein. Often, it is convenient to include additional physical effects to form a so-called "effective disjoining pressure"; these may include additional forces of electromagnetic origin, such as for ferrofluids in electric or magnetic fields [52]. For NLC films, such effective disjoining pressure is often called a structural disjoining pressure, since it includes the elastic forces that are due to the local structure of the director field (molecular orientation). Most work on this type of problem is carried out within the framework of long wave theory, which allows for simplifications of otherwise extremely complex free surface problems; we adopt this approach also.

In the context of NLC films, there are several experimental studies of dewetting on the nanoscale [1, 30, 31, 47]. For thin NLC films deposited on SiO_2 wafers, the films were found to be unstable (dewetted) for a certain range of thicknesses, referred to

as the "forbidden range" by Cazabat *et al.* [30]. Several different physical instability mechanisms have been proposed, and the discussion regarding the relevance of each is far from complete. Possibly relevant physical effects discussed in the literature include thermal effects [1, 31] and the pseudo-Casimir effect [47], as well as the interplay of elastic and disjoining pressure already discussed above [2].

The functional form of the (effective) disjoining pressure turns out to be similar for many of the setups discussed above; for example, for NLC films, the elastic effects lead to a disjoining pressure qualitatively similar to that found for polymer films on Si/SiO_2 substrates, or even for Newtonian films under inverted gravity conditions (hanging films) [10, 12]. This chapter is motivated by NLC films, however as discussed above, the results are generally applicable for many other thin films with a similar form of effective disjoining pressure (see Figure 4.1 later in the text).

Various instability mechanisms relevant to thin films have been discussed in the literature. For example, in addition to the standard linear stability analysis, which focuses on instabilities due to the presence of random infinitesimal perturbations (often called spinodal dewetting), there are instabilities due to the presence of nucleation centers [46, 53–55]. Seemann *et al.* [53] further separate nucleation instabilities into two types: heterogeneous nucleation, characterized by nucleation holes with random (Poisson) distribution that emerge within a sharp time window; and homogeneous nucleation, possibly of thermal origin in experiments, where breakup is continuous and more and more nucleation holes form. In a similar direction, Thiele *et al.* [54], and Diez and Kondic [55], considered the metastable and absolutely stable regimes (stability of films with respect to perturbations of finite size). In this chapter, we explore these various stability regimes in the context of our NLC model and demonstrate parallels between stability properties of our model and the works of others [46, 53–55], as well as similarities and differences between the referenced works. More precisely, we analyze in detail how the change of film thickness leads to different stability

regimes, and the role of the disjoining pressure properties. We furthermore carry out numerical simulations of dewetting, and discuss the connection between instability mechanisms and the properties of the drop patterns that form during the final stages of instability development. We discuss the dynamics that result, both as a consequence of non-local infinitesimal perturbations (covering the whole fluid domain), and of finite size localized perturbations. Considering both types of perturbations allows us to put together a detailed instability diagram covering the full range of film thicknesses.

The remainder of this chapter is organized as follows. In § 4.1 we outline the derivation of the governing equation in the context of NLC films, highlighting differences between our model and others in the literature, especially with regard to the form of the effective disjoining pressure. In addition, appropriate scalings and physical parameters are discussed, and linear stability analysis (LSA) of a flat film is presented. The issues of particular relevance to NLC films are mostly considered in this section. We then proceed with a general discussion of film instability. In § 4.2 we discuss so-called spinodal instabilities, due to the presence of global (random) perturbations, intended to model the noise that is always present in physical experiments. Among other topics, we here discuss the formation of secondary (satellite) drops that are found only for a specific range of film thicknesses, and the distance between the emerging drops, whose dependence on the film thickness shows unexpected and rich structure. In § 4.3 we consider the influence of localized perturbations (nucleation centers) on the film stability. In this section we also apply the Marginal Stability Criterion to help us develop additional analytical insight regarding instability development; this approach (to the best of our knowledge) has not yet been discussed in the present context. We discuss both linearly stable and metastable regimes of instability. § 4.4 summarizes our findings: of particular interest to the reader may be Figure 4.20, which provides a summary of the various instability mechanisms found and discussed throughout this chapter.

4.1 Problem Formulation

We first outline our model for NLC films of thickness on the nano/micro scale, but emphasize that our results are of relevance to other types of thin films (such as polymeric films), which may be described by long-wave equations similar to ours (equation (4.10) later) and which involve an effective disjoining pressure qualitatively similar to that sketched in Figure 4.1b. Note that the additional local maximum shown in Figure 4.1b, that is not present in Figure 4.1a, is important in determining the film stability [56, 57]. In this thesis, such a maximum results from the nematic contribution; for polymer films on a Si/SiO_2 substrate it may be due to the interaction of the polymer film with both SiO_2 and Si layers [4].

For the thin films that we consider, the effects of gravity are negligible; however, liquid/solid interactions, neglected in the previous chapters become important. Our model derives from the Leslie-Ericksen equations [34], which comprise a fluid momentum equation plus incompressibility, analogous to Navier-Stokes; and an additional equation modeling conservation of energy (linear translational energy of the NLC molecules, and angular energy about each NLC molecule's center of mass). The fluid momentum equation differs from Navier-Stokes in two key ways: 1) by introducing a new anisotropic stress tensor (linear momentum), and 2) by an additional term modeling angular momentum. For brevity, the full derivation of the long wave model from the Leslie-Ericksen equations is skipped in this chapter; we present just a brief overview, highlighting where the modeling differs from the previous chapters.

There are three crucial quantities in our long wave model: h, the free surface height; and the angles θ, ϕ that characterize the director field, $\mathbf{n}$, a unit vector representing the local average orientation of the long axis of the rod-like NLC molecules. It is convenient to express the director field in spherical coordinates, $\mathbf{n} = (\sin\theta\cos\phi, \sin\theta\sin\phi, \cos\theta)$, and consider the dependent variables θ, the azimuthal angle; and ϕ, the polar angle, which vary with the film height h; see Figure 4.2

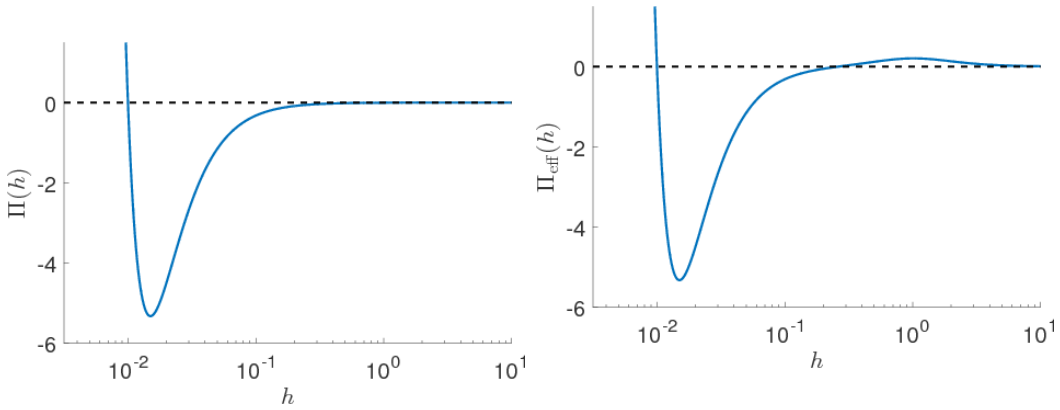

(a) Disjoining pressure $\Pi(h)$ (4.9)

(b) Effective disjoining pressure $\Pi_{\text{eff}}(h)$ (4.8)

Figure 4.1 Disjoining and effective disjoining pressures as functions of h, the film thickness.

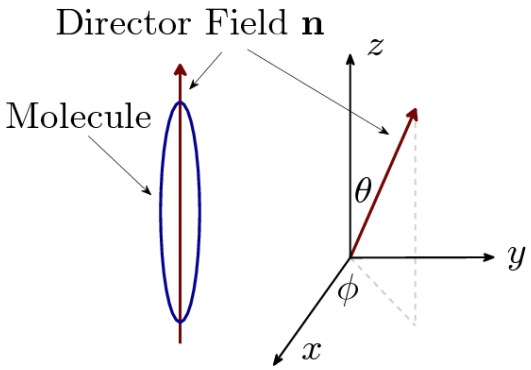

Figure 4.2 Schematic of the director field of the liquid crystal molecules relative to the Cartesian coordinates.

for a schematic. Note that throughout this chapter we use hats to distinguish between dimensional and dimensionless variables or parameters, hatted quantities being dimensional.

Analogous to Newtonian fluid models we include surface tension with constant surface energy density $\hat{\gamma}$, and liquid/solid interaction with volume energy density $\hat{A}$ (proportional to the Hamaker constant). Unique to NLCs (with respect to simple fluids) are the isotropic viscosity stress tensor, characterized by 6 coefficients, $\hat{\alpha}_i$ $(i = 1, 6)$; and the elastic response, characterized by three constants $\hat{K}_i$ $(i = 1, 2, 3)$. Similar to other authors [31, 35–37], we use the one-constant approximation, $\hat{K} =$

$\hat{K}_1 = \hat{K}_2 = \hat{K}_3$. Furthermore, under the long wave approximation, only three of the six viscosities ($\hat{\alpha}_3$, $\hat{\alpha}_4$, and $\hat{\alpha}_6$) are relevant.

To nondimensonalise the Leslie-Ericksen equations five scaling factors are defined: $\hat{H}$, the film thickness; $\hat{L}$, the lengthscale of variations in the plane in the film, $(\hat{x}, \hat{y})$; $\delta = \hat{H}/\hat{L}$, the small aspect ratio; $\hat{U}$, a characteristic flow velocity; $\hat{T}_F = \hat{L}/\hat{U}$, the timescale of fluid flow; and $\hat{\mu} = \hat{\alpha}_4/2$, a representative viscosity scale analogous to the Newtonian viscosity (with $\hat{\alpha}_i = 0$ for $i \neq 4$, the isotropic viscosity stress tensor reduces to a simple Newtonian stress tensor). The choice of the scales is based on experimental data, and is further discussed in § 4.1.3.

4.1.1 Weak Free Surface Anchoring

In addition to the fluid flow timescale, $\hat{T}_F$, we may consider the timescale of elastic reorientation across the layer, $\hat{T}_R = \hat{\mu}\hat{H}^2/\hat{K}$. Assuming the timescale of reorientation is much faster than that of fluid flow, a quasistatic approximation (instantaneous elastic equilibrium) can be justified, and the energy equation may be solved to give the director field, $\mathbf{n}$, as a function of the instantaneous film height, h. We have already shown in previous chapters that the spherical director angles θ and ϕ are then given as

$$\theta = a(x, y, t)z + \theta_S(x, y, t) \quad \text{and} \quad \phi = \phi_S(x, y, t)\ , \tag{4.1}$$

where $a(x, y, t)$ depends on the free surface height, $h(x, y, t)$, as discussed below. The functions θ_S and ϕ_S depend on the preferred orientation of the NLC molecules at the interfaces, a phenomenon known as anchoring. We assume that the anchoring on the substrate is stronger than that at the free surface, and therefore that $\theta_S(x, y)$ and $\phi_S(x, y)$ are imposed by the substrate. In line with observations for physical systems, we assume θ_S is constant, while $\phi_S(x, y)$ may vary only spatially. This solution for the director field feeds into the anisotropic stress tensor. The particular state here in which θ is linear in z is often called the hybrid aligned nematic (HAN) state of NLCs.

In general, the preferred polar anchoring angles at the free surface, θ_F, and at the substrate, θ_S (both assumed constant), are different (antagonistic anchoring). For very thin films, adjusting between these anchoring conditions incurs a large energy penalty in the bulk of the film. To reduce the energy penalty for very thin films, we allow the (weakly anchored) free surface director angle $\theta_{\mathcal{F}}$ to relax to the same value as the (strongly anchored) substrate director angle $\theta_{\mathcal{S}}$ for very thin films. Specifically, we take

$$\theta = \theta_{\mathcal{S}} + (\theta_{\mathcal{F}} - \theta_{\mathcal{S}})\frac{m(h)}{h}z \ , \tag{4.2}$$

$$m(h) = g(h)\frac{h^2}{h^2+\beta^2} \ , \quad g(h) = \frac{1}{2}\left[1+\tanh\left(\frac{h-2b}{w}\right)\right] \ , \tag{4.3}$$

where $m(h)$ is a relaxation function (directly related to the anchoring energy at the free surface) in which β is the thickness scale at which the bulk elastic energy is comparable to the free surface anchoring energy, and $g(h)$ is a 'cut-off' function (controlled by w) that enforces the substrate anchoring on the free surface when the film thickness is close to the equilibrium film thickness, b (discussed in more detail later in the text).

Note that with this form of the director field, thicker NLC films are in the HAN state, while films close to the equilibrium thickness have a director field nearly homogeneous across the film thickness. This transition between the states is in agreement with several other models [30, 35, 47]. Furthermore, dimensional analysis shows that our lengthscale β may be related to the extrapolation length discussed in the literature [35, 37, 58].

4.1.2 Long Wave Model

To derive a long wave model for nanoscale thin films, we modify the model used in previous chapters, by neglecting gravity and including fluid-solid interaction via disjoining pressure. With this modification, there are five nondimensional parameters: $\mathcal{C}$, the inverse Capillary number, representing the ratio of surface tension and viscous

forces; $\mathcal{K}$, the ratio of the forces due to disjoining pressure and those due to viscous effects; $\mathcal{N}$, a scaled inverse Ericksen number, representing the ratio of elastic and viscous forces; λ and ν, scaled effective viscosities. In terms of physical parameters,

$$\mathcal{C} = \frac{\delta^3 \hat{\gamma}}{\hat{\mu}\hat{U}} \,, \quad \mathcal{K} = \frac{\delta^2 \hat{A}\hat{L}}{\hat{\mu}\hat{U}} \,, \quad \mathcal{N} = (\Delta\theta)^2 \frac{\hat{K}}{\hat{\mu}\hat{U}\hat{L}} \,, \quad \Delta\theta = \theta_{\mathcal{F}} - \theta_{\mathcal{S}} \,, \tag{4.4}$$

$$\lambda = \frac{2+\eta}{4\,(1+\eta)} \,, \quad \nu = -\frac{\eta}{4\,(1+\eta)} \,, \quad \eta = \frac{\hat{\alpha}_3 + \hat{\alpha}_6}{\hat{\mu}} \,, \tag{4.5}$$

where, recall, $\hat{\mu} = \hat{\alpha}_4/2$. For the remainder of the chapter, only two-dimensional geometry will be considered; we leave the three-dimensional case for the next chapter. With this restriction ϕ can be at most piecewise constant, with value(s) $\phi = 0$ (substrate anchoring parallel to the x-axis) or $\phi = \pi/2$ (anchoring perpendicular to the x-axis). The governing equation for the free surface height, $h(x,t)$, may then be expressed as

$$h_t + \left[\Phi\left(\mathcal{C}h^3 h_{xxx} + h^3 \Pi_{\text{eff}}{}'(h) h_x\right)\right]_x = 0 \,, \tag{4.6}$$

$$\Phi = \begin{cases} \Phi_{\parallel} & = \lambda - \nu \quad (\phi = 0) \\ \Phi_{\perp} & = \lambda + \nu \quad \left(\phi = \frac{\pi}{2}\right) \end{cases} \,. \tag{4.7}$$

Here $\Phi_{\parallel}$ denotes substrate azimuthal anchoring parallel to the x-axis ($\phi = 0$) and $\Phi_{\perp}$ denotes anchoring perpendicular to the x-axis ($\phi = \pi/2$); note that the value of Φ influences only the timescale of fluid flow. Furthermore, if $\eta = 0$ in (4.5), the governing equation (4.6) is independent of ϕ and our model corresponds to a fluid of isotropic viscosity. The effective disjoining pressure is defined as

$$\Pi_{\text{eff}}(h) = \mathcal{K} f(h) + \frac{\mathcal{N}}{2}\left[\frac{m(h)}{h}\right]^2 \,, \tag{4.8}$$

with $m(h)$ as defined in (4.3) above. Here, the second term on the right hand side is the response due to the antagonistic anchoring conditions, while the first term

corresponds to the disjoining pressure, taken here to be of power-law form

$$\Pi(h) = \mathcal{K} f(h) = \mathcal{K} \left[\left(\frac{b}{h} \right)^3 - \left(\frac{b}{h} \right)^2 \right] . \tag{4.9}$$

The form of the effective disjoining pressure, (4.8), is similar to that considered by Vandenbrouck *et al.* [2]; however, there are two important differences: (i), the (first) term in (4.9) considered here contains the repulsive term (Born repulsion) preventing the film thickness from reaching zero; such a term is crucial if one wants to carry out simulations; and (ii), in the model of Vandenbrouck *et al.* [2], the free surface azimuthal anchoring is assumed to be determined by the average initial thickness of the film and does not evolve with h. The power-law form of disjoining pressure (4.9) is used extensively in the literature; for a review see Craster and Matar [59] and for further background regarding solid-fluid interactions, see the book by Israelachvili [60].

In the case (assumed henceforth) that ϕ is constant globally, a simple rescaling of time in (4.6) yields

$$h_t + \left[\mathcal{C} h^3 h_{xxx} + h^3 \Pi_{\text{eff}}{}'(h) h_x \right]_x = 0 , \tag{4.10}$$

with Π_{eff} as defined in (4.8). This equation will be considered in the rest of this chapter. Note that in this model nematic effects enter only through modification of the disjoining pressure, by adding the structural component. Figure 4.1 shows typical forms of the disjoining pressure obtained using the parameter values discussed in the following section. The effective disjoining pressure proposed in (4.8) is similar to that expected for many other thin film problems, in particular the well-studied polymer films on Si/SiO_2 substrates [45]. Therefore the results that we present in the rest of the thesis are of relevance to a wide class of complex fluids.

We note that equation (4.10) may be alternatively derived using the variational or gradient dynamics formulation [61, 62]. In this thermodynamically motivated

approach the governing equation is expressed as

$$h_t + \nabla \cdot \left[Q(h) \nabla \left(\frac{\delta F}{\delta h} \right) \right] = 0 \, , \tag{4.11}$$

where $Q(h)$ is the mobility function, and F is the free energy functional. Lin *et al.* [13] showed that, with consistent boundary conditions, the gradient dynamics formulation is equivalent to the long wave approximation of the Leslie-Ericksen equations. In terms of our model, $Q(h) = h^3$ and

$$F(h) = -\mathcal{C} \left[1 + \frac{(\nabla h)^2}{2} \right] - \frac{\mathcal{K} b^2}{2h} \left[\frac{b}{h} - 2 \right] + \mathcal{N} \left[\frac{m(h)^2}{2h} - \int^h \frac{m(s) m'(s)}{s} \, ds \right] \, . \tag{4.12}$$

4.1.3 Scalings and Physical Parameters

We now discuss the choice of scaling parameters mentioned in the beginning of § 4.1 and the material parameters in (4.4) and (4.5) for our model of thin NLC films (4.8) and (4.10). In experimental studies of dewetting of NLC films, the film thickness is typically of the order 10 to 100 nanometers [2, 3]; therefore we set the representative film height $\hat{H}$ (used to scale z) to 100 nm. For temperatures far from a phase transition, the lower bound of the forbidden range of thickness is a few nanometers (it corresponds, in the experiments of Cazabat *et al.* [30], to a trilayer of molecules). We define this lower bound to correspond to the equilibrium film thickness and set it as $\hat{b} = 1$ nm. Bulk elastic energy is expected to be comparable to surface anchoring energy for film thicknesses in the 100 nanometers range; therefore we set $\hat{\beta} = 100$ nm. Periodic undulations are observed on the free surface of films with a height on the order of $\hat{H}$, and in experiments [3, 30], the wavelength of such undulations is observed to be in the range of 10-100 μm. Choosing the length scale in the (x, y) domain $\hat{L} = 10$ μm, we fix the aspect ratio $\delta = \hat{H}/\hat{L} = 10^{-2}$. We choose the timescale of fluid flow $\hat{T}_F = \hat{L}/\hat{U}$ to match the timescale on which undulations develop in experiments, typically seconds to minutes [3]; thus we set $\hat{T}_F = 1$ s, corresponding to a velocity scale $\hat{U} = 10$ μm s^{-1}.

The remaining parameters to be specified are: $\hat{\gamma}$, the surface tension; $\hat{K}$, the bulk elastic constant; θ_F, free surface azimuthal anchoring angle; θ_S, substrate azimuthal anchoring angle; $\hat{A}$, a force per unit volume, proportional to the Hamaker constant; and $\hat{\mu}$, a representative viscosity. Many experimental studies [2, 30–32, 63, 64] use the cyanobiphenyl (nCB) series of liquid crystals (where n refers to the number of carbons in the aliphatic tail), in particular, 4-Cyano-4'-pentylbiphenyl (5CB). Therefore, we choose these physical parameters to match 5CB data. It is noted by Cazabat *et al.* [30] that, due to impurities in the NLC, published measurements of surface tension are scattered. However, to estimate the order of the non-dimensional parameters in our model, we note that surface tension appears typically to be of order 10^{-2} N m^{-1} [30, 33]. The elastic constant, $\hat{K}$, is of the order 10^{-11}–10^{-10} N [32, 65]. For the nCB series of NLCs, the molecules prefer to align normal to the free surface (homeotropic anchoring) and in practice, substrates are often chosen and treated such that molecules align parallel to the substrate e.g. SiO_2; therefore we set $\theta_F = 0$ and $\theta_S = \pi/2$. Accurate values for the characteristic viscosity of 5CB are scarce in the literature; however, Mechkov *et al.* [29] was able to fit solutions of a thin film equation to experimental results (this chapter considers micron-scale drop thicknesses and the model used assumes strong free surface anchoring and neglects fluid/solid interactions) with $\hat{\mu}$ of order 10^{-2} Pa s, a value in line with reported data [66]. Taking account of this available data, we choose $\hat{K} = 1 \times 10^{-11}$ N, $\hat{\gamma} = 60 \times 10^{-3}$ N m^{-1}, and $\hat{\mu} = 60 \times 10^{-3}$ Pa s.

In summary, the dimensional scaling factors are then fixed as

$$\hat{L} = 10\ \mu\text{m}\ , \quad \hat{H} = 100\ \text{nm}\ , \quad \hat{T}_F = 1\ \text{s}\ , \quad \hat{U} = 10\ \mu\text{m s}^{-1}\ . \tag{4.13}$$

Note that with the chosen thickness scale, $\hat{T}_R = \hat{\mu}\hat{H}^2/\hat{K} = 60\ \mu$s, thus we satisfy the assumption in § 4.1.1 that the timescale of elastic reorientation across the layer ($\hat{T}_R$) is much slower than that of fluid flow ($\hat{T}_F$). In addition, with the value of the contact

angle to be discussed in § 4.1.3, the contact line velocity of a spreading NLC drop measured by Poulard and Cazabat [32] (at the chosen contact angle) is of a similar order to our derived velocity scale $\hat{U}$.

Based on the scales discussed above, the dimensionless parameters we use (at least, for our initial investigations) are

$$\delta = 0.01 \ , \ \ \mathcal{C} = 0.0857 \ , \ \ \mathcal{N} = 1.67 \ , \ \ \mathcal{K} = \left[0.0017 \ \mathrm{m^3 J^{-1}}\right] \hat{A} \ , b = 0.01 \ , \ \ \beta = 1 \ , \tag{4.14}$$

and $\hat{A}$, the volume energy density associated with fluid/solid interaction forces (here assumed to have units of $\mathrm{Jm^{-3}}$), is discussed next.

Contact Angle To define a value for $\hat{A}$ and thus $\mathcal{K}$ (see (4.4), (4.14)) we relate the spreading parameter (a function of the contact angle) to the stored energy per unit area of the film using the Young-Laplace equation [55]. The spreading parameter $\hat{S}$ is given by

$$\hat{S} = \hat{\gamma}(1 - \cos\vartheta_c) = \hat{E}(\hat{h} = \infty) = -\int_{\hat{b}}^{\infty} \hat{\Pi}_{\mathrm{eff}}(\hat{h}) \, d\hat{h} \ , \tag{4.15}$$

where ϑ_c is the equilibrium contact angle, $\hat{E}(\hat{h})$ is the stored energy per unit area, and $\hat{\Pi}_{\mathrm{eff}}(\hat{h}) = (\hat{\mu}\hat{U}/\delta\hat{L})\Pi_{\mathrm{eff}}(h)$, where Π_{eff} is defined by (4.8): the usual disjoining pressure plus the elastic "structural" component, dependent on the function $m(h)$ and with prefactor $\mathcal{N}$. This elastic term of the integral in (4.15) cannot be evaluated analytically, due to the complicated functional form of $m(h)$ as defined in (4.3). However, direct numerical integration shows (for the chosen values of b, β, and w), that the value of (4.15) is almost the same if the approximation $g(h) = 1$ in the definition of $m(h)$ is made (less than 1% difference). Setting $g(h) = 1$, the integral in (4.15) may be evaluated analytically; but the result is not simple to work with. Therefore, we asymptotically expand in $\varepsilon = b/\beta = 0.01 \ll 1$ and retain the leading order term. The contact angles for NLC on Si (or SiO_2) substrates were measured by

Poulard and Cazabat [32] to be around 10^{-2}–10^{-1} radians; thus assuming the contact angle is small, $\vartheta_c \ll 1$, (4.15) may be expressed as

$$\hat{A} = \frac{\hat{\gamma}\vartheta_c^2}{\hat{b}}\left(1 + \kappa\left[\frac{\pi}{4}\varepsilon + O(\varepsilon^4)\right]\right) , \quad \kappa = \frac{\hat{K}}{\hat{\gamma}\hat{b}\vartheta_c^2} . \tag{4.16}$$

To express (4.16) in terms of the nondimensional parameters (4.14), the order ε^4 term in (4.16) is neglected, and the approximated equation is multiplied by $\delta/\hat{\mu}\hat{U}$ to yield

$$\mathcal{K}b \approx \mathcal{C}\left(\frac{\vartheta_c}{\delta}\right)^2 + \frac{\mathcal{N}}{\beta\pi} , \tag{4.17}$$

where $b = \hat{b}/\hat{H}$ is the dimensionless equilibrium thickness. For the chosen values of $\hat{\gamma}$ and $\hat{K}$, and $\vartheta_c = 0.06$, $\kappa\pi\varepsilon/4 \approx 0.364$ in (4.16), therefore, it is reasonable to neglect the elastic contribution to the spreading parameter. This is in agreement with liquid crystals of low molar mass, where the anchoring energy on the free surface is usually significantly smaller than the isotropic surface tension energy [67]. Neglecting the elastic term in (4.16) then, $\hat{A} = \hat{\gamma}\vartheta_c^2/\hat{b}$, and with $\vartheta_c = 0.06$, we then obtain $\mathcal{K} = 36.0$.

4.1.4 Linear Stability Analysis (LSA)

We now focus on the stability properties of a flat film, and in particular on the influence of the average film thickness, H_0. For this purpose, we first carry out LSA of a flat film solution to our governing equation (4.10). Assuming a solution of the form $h(x,t) = H_0 + \epsilon e^{iqx+\omega t}$ where $0 < \epsilon \ll 1$, substitution in (4.10) yields the dispersion relation

$$\omega = -H_0^3\left[\mathcal{C}q^2 - \Pi_{\text{eff}}{}'(H_0)\right]q^2 , \tag{4.18}$$

where

$$\Pi_{\text{eff}}{}'(h) = \mathcal{K}f'(h) - \mathcal{N}\frac{M(h)}{h^3} ; \quad M(h) = m^2(h) - hm(h)m'(h); \tag{4.19}$$

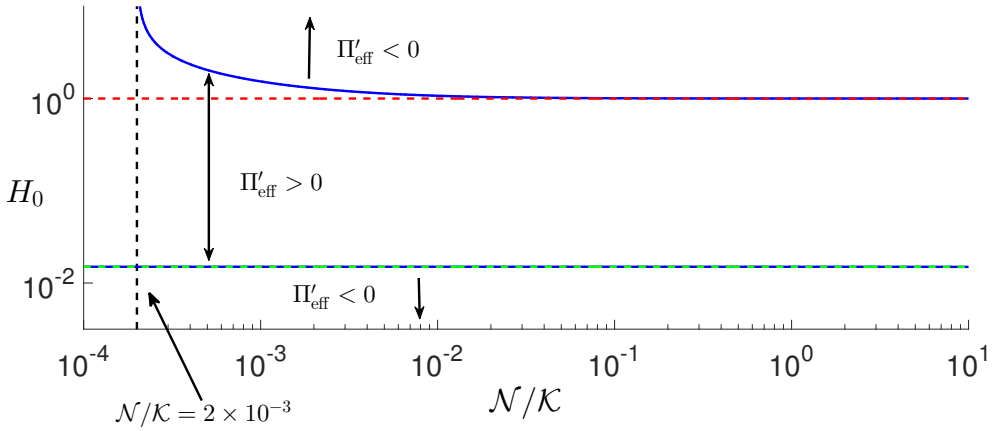

Figure 4.3 The zeros of (4.20) (blue curves), the zero of $M(H_0)$ (dashed red line); and the zero of $f'(H_0)$ (dashed cyan line, lying almost entirely on the lower blue curve). The region enclosed by the blue curves denotes film thicknesses H_0 that are linearly unstable, i.e. $\Pi_{\text{eff}}{}'(H_0) > 0$. The dashed black line corresponds to a critical $\mathcal{N}/\mathcal{K}$ value; below that value, the destabilizing effect of fluid/solid interaction is stronger than the stabilizing elastic response.

with $f(h)$ defined by (4.9), $m(h)$ by (4.3) and parameters $\mathcal{C}$, $\mathcal{K}$, and $\mathcal{N}$ by (4.4); their values are given in § 4.1.3.

Assuming that q is real, a film is always stable if $\Pi_{\text{eff}}{}'(H_0) < 0$, and is unstable otherwise. Therefore, the values of H_0 for which the film is unstable are determined by the roots of

$$\frac{\Pi_{\text{eff}}{}'(H_0)}{\mathcal{K}} = f'(H_0) - \frac{\mathcal{N}}{\mathcal{K}} \frac{M(H_0)}{H_0^3} \,, \tag{4.20}$$

which are calculated numerically and plotted (as two blue curves) in Figure 4.3 in the $(\mathcal{N}/\mathcal{K}, H_0)$-plane. In addition the roots of $f'(H_0) = 0$ and $M(H_0) = 0$ are also plotted. Denoting the two roots of (4.20) as H_- (the smaller root) and H_+ (the larger root), and noting that the region enclosed by blue curves corresponds to $\Pi_{\text{eff}}{}'(H_0) > 0$, Figure 4.3 demonstrates that for $H_0 \in (H_-, H_+)$, a flat film is unstable; therefore, we conjecture that the unstable range of film thicknesses in our model may be related to a range of so-called "forbidden thicknesses" noted experimentally by Cazabat *et*

al. [30] for comparable films. It can be seen that, for the range of $\mathcal{N}/\mathcal{K}$ considered, H_- is closely approximated by the zero of the disjoining pressure $f'(H_-) \approx 0$; thus $H_- \approx 3b/2$ (see (4.9)): the lower thickness threshold between linear stability and instability is primarily determined by fluid/solid interaction forces.

For $\mathcal{N}/\mathcal{K} > 0.01$, the largest root of (4.20), H_+, corresponds approximately to the root of $M(H_0)$, suggesting that for sufficiently strong elasticity, the upper threshold between linear instability and stability is determined by the antagonistic anchoring conditions (elastic response). For $H_0 \gg b = 0.01$, we may simplify $M(H_0)$ (see its definition in (4.19)) by setting $g(H_0) = 1$ in (4.3), and $H_+ \approx \beta$ can be found analytically. This is confirmed numerically using the values from §4.1.3, which give $\mathcal{N}/\mathcal{K} = 0.0514$; the second root of (4.20) is then found to be $H_+ \approx 1.0150 \approx \beta$ (see (4.14)).

In the linearly unstable regime, only perturbations with wavenumber $q \in (0, q_c)$ are unstable; here q_c is the critical wavenumber given by $q_c = \sqrt{\Pi_{\text{eff}}'(H_0)/\mathcal{C}}$ (see (4.18)). The most unstable mode is given by $q_m = q_c\sqrt{2} = 2\pi/\lambda_m$, with the growth-rate

$$\omega_m = \frac{Q(H_0)\left[\Pi_{\text{eff}}'(H_0)\right]^2}{4\mathcal{C}} = \frac{H_0^3\left[\Pi_{\text{eff}}'(H_0)\right]^2}{4\mathcal{C}}\,, \tag{4.21}$$

(see (4.11)). We will use these quantities later in the text. Note that in dimensionless form, q_c and q_m do not depend on the mobility function $Q(h)$ and the range(s) of unstable thicknesses is/are determined by $\Pi_{\text{eff}}(h)$. Furthermore, the mobility function only affects the growth rate of the instability.

4.1.5 Comparison to Other Models

There are several differences between the effective disjoining pressure used in our model (4.8) and others used in the literature. Unique to our model is weak free surface anchoring, which relaxes the free surface azimuthal anchoring as the film height evolves. This leads to a critical thickness value, β, below which the elastic

contribution (ignoring fluid/solid interaction forces) is linearly destabilizing for a flat film, and above which it is linearly stabilizing. Furthermore, and as discussed above, Figure 4.3 shows that for $\mathcal{N} \gg \mathcal{K}$, $H_+ \approx \beta$, i.e. the upper bound between linear instability and stability is controlled by the elastic response. In comparison, the model presented by Vandenbrouck *et al.* [2] sets the free surface azimuthal anchoring condition to be a constant for all film thickness (the value of which is determined by the average initial film thickness). This is equivalent to strong anchoring ($m(h) = 1$ in our model), which leads to the elastic response being always linearly stabilizing; therefore, in the theory of Vandenbrouck *et al.* [2], the upper threshold between linear instability and stability, H_+, is determined by the balancing of the destabilizing disjoining pressure and the stabilizing elastic response, regardless of the values of $\mathcal{N}$ and $\mathcal{K}$.

Furthermore, we note that the effective disjoining pressure term in our model may be expressed as

$$\begin{aligned} \Pi_{\text{eff}}{}'(h)h_x &= \mathcal{K}f'(h)h_x - \frac{\mathcal{N}}{h^3}\left[m^2(h) - hm(h)m'(h)\right]h_x \\ &= \mathcal{K}f'(h)h_x - \frac{\mathcal{N}m^2(h)}{h^3}h_x - \frac{\nabla\mathcal{G}(h)}{h}\ , \end{aligned} \tag{4.22}$$

where $\nabla\mathcal{G}(h)$ is the gradient of the free surface anchoring energy. The derivation of $\mathcal{G}(h)$ is nontrivial and we refer the reader to the the previous chapters for further details. Since the second term on the right hand side of the last equation in (4.22) is always stabilizing, instability arises from the gradients of the free surface anchoring energy (the last term in (4.22)), present only for non-constant $m(h)$ (i.e., only for weak anchoring). Thus our model includes an alternative instability mechanism due to elastic forces not captured by the model in Vandenbrouck *et al.* [2].

Excluding the h^{-3} term, the effective disjoining pressure in our model (4.8) is qualitatively similar to the total disjoining pressure derived by Ziherl *et al.* [47]. This term is, however, essential for the purpose of carrying out numerical simulations. In

the work by Ziherl *et al.* [47], the structural component to the disjoining pressure was derived by first considering the elastic energy due to fluctuations in the director field from some initial state. A critical thickness was defined such that, below this threshold, the initial director field state is uniform, and above, the director field is in the HAN state. Therefore our model has similar underlying physical mechanisms driving instability: 1) transition between a uniform director field for thin films to the HAN state for thick films; 2) interplay between bulk elastic energy and surface anchoring energy as the film thickness changes; and 3) inclusion of fluid/solid interaction forces.

However, there are also the following key differences: 1) the transition between the planar state and the HAN state is continuous in our model, whereas it is discontinuous in Ziherl *et al.* [47]; 2) Ziherl *et al.* [47] assumed that the anchoring at the free surface was stronger than that at the substrate, therefore the uniform director field state for thin films was homeotropic in their model, while it is planar in ours; 3) to obtain similar linearly stable and unstable film thickness values with their model would require setting $\beta \approx 0.2$; and 4) only the total disjoining pressures are similar between the two models, the individual components (elastic contribution and disjoining pressure minus the h^{-3} term), are qualitatively different.

4.1.6 Numerical Scheme

In the following sections we will present a number of numerical simulations of our model in order to study its behaviour in detail. To solve the governing equation (4.10) numerically, we choose a spatial domain $x \in [0, x_L]$, and enforce the following boundary conditions,

$$h_x(0,t) = h_{xxx}(0,t) = 0 \quad \text{and} \quad h_x(x_L,t) = h_{xxx}(x_L,t) = 0 \,, \tag{4.23}$$

where the right boundary x_L is chosen as appropriate for the initial condition considered. The numerical method employed is a fully-implicit Crank-Nicolson type

discretization scheme, with adaptive time stepping. A Newton iterative method is implemented at each time step to deal with nonlinear terms. More details about the implemented numerical scheme, as well as discussion of its convergence properties can be found in Lin *et al.* [11], and Witelski and Bowen [44]. For all numerical simulations $\Delta x = b = 0.01$; such a level of discretization is sufficient to resolve accurately the length scales of interest. Unless stated otherwise, the parameters in governing equation (4.10) are as given in § 4.1.3.

4.2 Films Exposed to Global Perturbations

In this section, we present simulation results for films of thickness H_0 with superimposed perturbations that are nonlocal in character (cover the whole domain) and are intended to model infinitesimal random perturbations that are expected to be present in physical experiments. We focus on investigating film thicknesses in the linearly unstable regime, $H_0 \in (H_-, H_+) \approx (0.015, 1.015)$, and the morphology of dewetted films as a function of H_0. We start by discussing results for films perturbed by a single wavelength, on a domain equal in size to the imposed perturbation wavelength, and then proceed to consider random perturbations and large domains.

4.2.1 Simulations: Single Wavelength Perturbation

To begin, we validate the numerical scheme by comparing the growth rates extracted from numerical simulations to the expression (4.18) derived from LSA. The initial condition is of the form

$$h(x, t = 0; H_0, q) = H_0 \left[1 + 0.01 \cos(qx)\right] \ , \quad x \in [0, x_L] \ , \quad x_L = \frac{2\pi}{q} \ , \tag{4.24}$$

where H_0 and q will be used to parameterize (4.24). From LSA, the evolution of the above initial condition is approximately given by $h(x,t) = H_0[1 + 0.01e^{\omega t}\cos(qx)]$, i.e., at early times, the perturbation to the flat film grows exponentially. To extract the

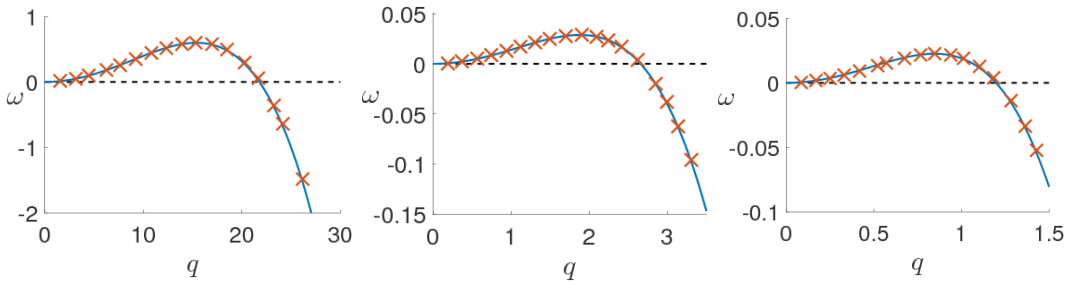

(a) $H_0 = 0.05$ (b) $H_0 = 0.3$ (c) $H_0 = 0.8$

Figure 4.4 Comparison of the dispersion relationship (solid blue curves) (4.18), and the growth rates extracted from numerical simulations (×) for $H_0 = 0.05$, 0.3 and 0.6. Other parameters are given in §4.1.3.

growth rate from a simulation, we first compute the difference between the numerical solution at the center of the domain and the initial film thickness: specifically, we compute $E(t) = h(x_L/2, t) - H_0 \approx 0.01 H_0 e^{\omega t}$. Thus using a linear least squares method to fit $\log(E(t))$, the growth rate, ω, is given by the gradient of the line of best fit. In Figure 4.4, the growth rates extracted from simulations are compared to those given by the dispersion relation. We see that the numerical simulations and LSA agree extremely well over the range of unstable film thicknesses and q-values considered.

To proceed, we investigate in detail the long-time evolution of the free surface height, in particular, how the resulting film morphologies depend on the initial film thickness, H_0. To simplify the parameter space, we fix $q = q_m$ (thus $x_L = \lambda_m$) in (4.24) for the remainder of this section. Figure 4.5 shows the free surface evolution of the NLC film for several different values of the initial average film thickness, H_0. Initially, the perturbation grows, eventually forming large drops at the domain boundaries, as expected from LSA, and an additional secondary drop at the center. Note that to properly visualize smaller drops, we plot the free surface height on a log scale. On timescales much longer than the breakup time, comparable to ω_m^{-1}, different dynamics emerge, however, depending on the film thickness H_0. For thinner films, shown in

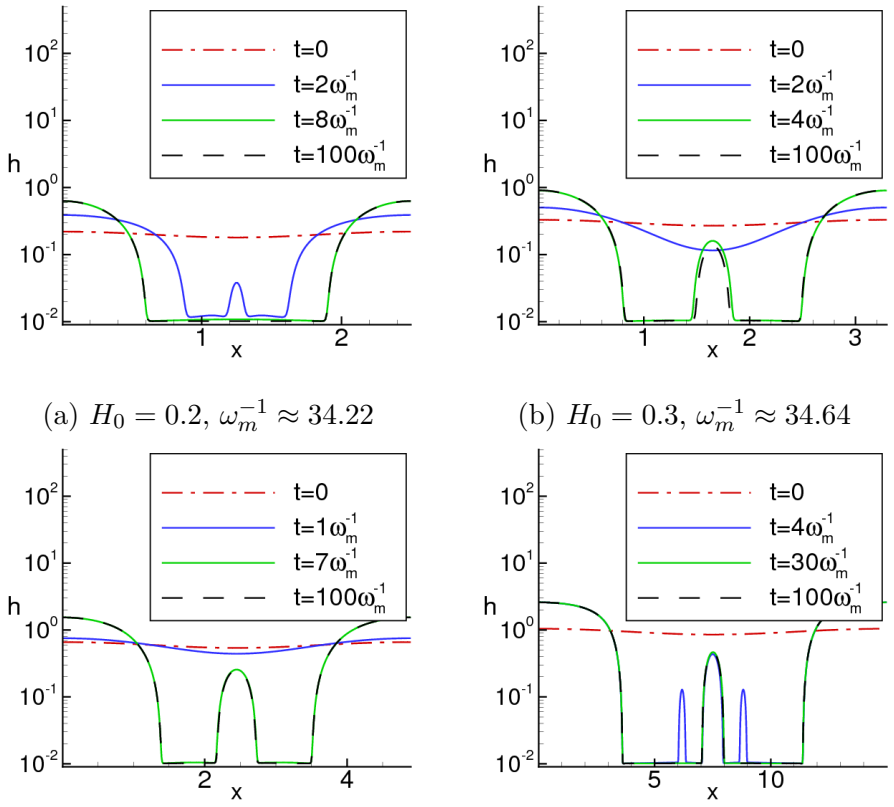

(a) $H_0 = 0.2$, $\omega_m^{-1} \approx 34.22$

(b) $H_0 = 0.3$, $\omega_m^{-1} \approx 34.64$

(c) $H_0 = 0.6$, $\omega_m^{-1} \approx 19.21$

(d) $H_0 = 0.95$, $\omega_m^{-1} \approx 423.4$

Figure 4.5 Free surface evolution for various initial average film thicknesses, H_0. The initial condition is given by (4.24) with $x_L = \lambda_m$. Other parameters are given in §4.1.3.

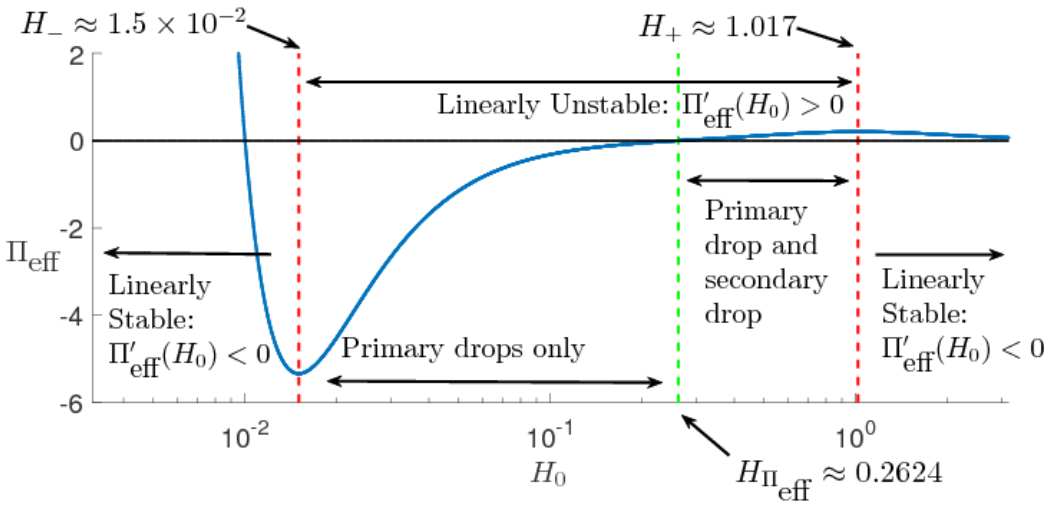

Figure 4.6 A summary of the final states obtained in simulations and their relationship to the effective disjoining pressure. The region enclosed by the dashed red lines is unstable. The dashed green line, at $H = H_{\Pi_{\text{eff}}}$, corresponds to the zero of the effective disjoining pressure. These line patterns will be used consistently for all remaining figures in this chapter.

Figure 4.5a, the secondary drop persists for a short time only; while for thicker films, see Figures 4.5b and 4.5c, the secondary drops exist on a long time scale. For films near the critical thickness of linear instability, see Figure 4.5d, we observe an additional set of tertiary drops forming on either side of the secondary drop. These tertiary drops form at the same time as the primary drops, and exist on a timescale that is longer than that of dewetting, but shorter than that on which the secondary drop persists. We note that the times considered here are not asymptotically long, as considered by Glasner and Witelski [68].

Our simulations reveal that droplets may be classified according to their heights, with distinct droplet sizes emerging at different times over the course of a simulation. Figure 4.6 shows schematically our findings regarding film stability and existence of secondary drops on time scales that are long compared to ω_m^{-1}. The region enclosed by the dashed red lines denotes the linearly unstable regime (determined by the zeros of $\Pi_{\text{eff}}{}'(h)$, see (4.19)), and the dashed green line corresponds to $H_{\Pi_{\text{eff}}} \approx 0.2624$, the zero of the effective disjoining pressure Π_{eff} (4.8). The secondary drops are found

only for film thicknesses with positive disjoining pressure, as we discuss further below in § 4.2.2. To the best of our knowledge, this finding is novel, and is one of the predictions of this chapter. It would be of interest to verify it experimentally, not only for NLC films, but also for other films where positive disjoining pressures may be found, for example, for polymer films where positive disjoining pressure is due to fluid/substrate interaction; or for ferrofluid films in electric or magnetic fields [52].

4.2.2 Simulations: Multiple Random Perturbations

To test the connection between the formation of secondary drops and the sign of the disjoining pressure, we carried out simulations in large domains with imposed perturbations of random amplitudes. The initial condition is defined as

$$h(x, t = 0; H_0, x_L) = H_0 \left[1 + \epsilon\chi(x; x_L)\right], \quad \chi(x; x_L) = \sum_{n=1}^{300} a_n \cos\left(\frac{nx}{x_L}\right), \quad x \in [0, x_L], \tag{4.25}$$

where $a_n \in [-1, 1]$ are uniformly distributed, ϵ is chosen such that $|\epsilon\chi(x; x_L)| \leq 0.01$ (i.e. the total perturbation size is bounded by 0.01) , and H_0 and x_L will be used to parameterize (4.25). Note that for each simulation shown, a new set of random coefficients, a_n, are generated.

Figure 4.7 shows the free surface evolution for initial condition (4.25) with $x_L = 10\lambda_m$, and the same parameters and same range of initial thicknesses, H_0, as in Figure 4.5. The main observation is that a minimum film thickness is still required for formation of long-lived secondary drops.

To discuss this finding in more detail, we also consider the drop sizes, defined by the heights of drop centers, H_l. Figure 4.8 shows a histogram of the log of the drop heights extracted from simulations corresponding to the same H_0 values as used in Figure 4.7, but carried out on a larger domain ($x_L = 50\lambda_m$) to improve statistics. We see that for $H_0 < H_{\Pi_{\text{eff}}}$, Figure 4.8a, the distribution is unimodal; and for $H_0 > H_{\Pi_{\text{eff}}}$, Figures 4.8b-4.8d, the distribution is bimodal (recall that $H_{\Pi_{\text{eff}}}$ is the zero of the

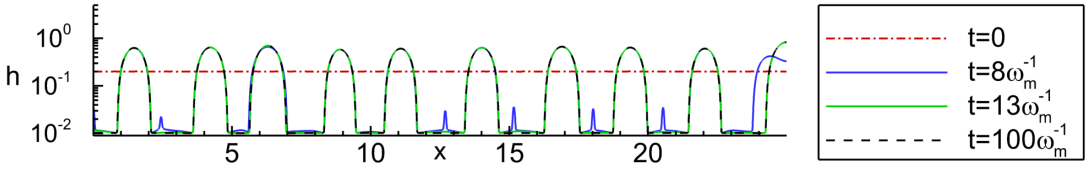

(a) $H_0 = 0.2$, $\omega_m^{-1} \approx 34.22$

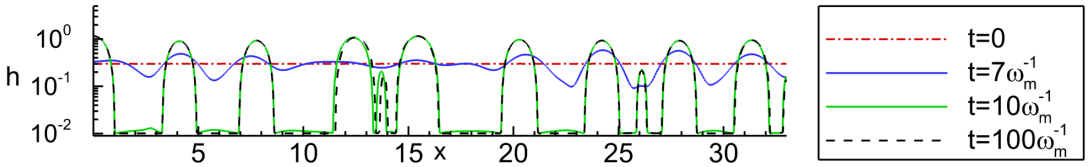

(b) $H_0 = 0.3$, $\omega_m^{-1} \approx 34.64$

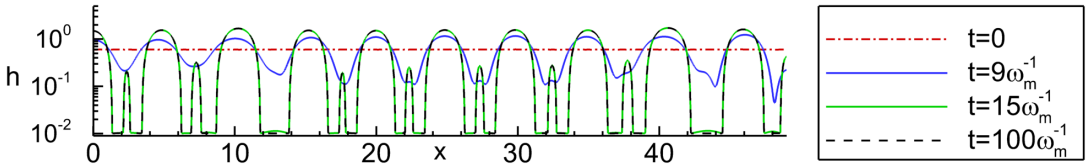

(c) $H_0 = 0.6$, $\omega_m^{-1} \approx 19.21$

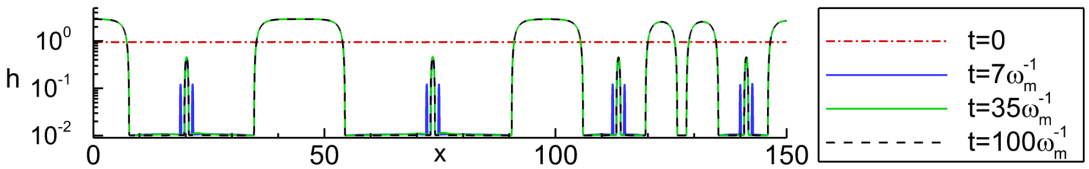

(d) $H_0 = 0.95$, $\omega_m^{-1} \approx 423.4$

Figure 4.7 Free surface evolution for various initial average film thicknesses, H_0. The initial condition is given by (4.25) with $x_L = 10\lambda_m$. Other parameters are given in §4.1.3.

effective disjoining pressure, $\Pi_{\text{eff}}(H_{\Pi_{\text{eff}}}) = 0$). In addition, the dashed black line denotes the initial film thickness H_0, and it may be seen that H_0 provides an adequate threshold value between (larger) primary drops and (smaller) secondary drops (if they exist). The relevance of the dashed gold lines will be discussed shortly in § 4.2.3, but for now, note that as $H_0 \to H_+$ (see Figure 4.8d), the height of primary drops converges to the rightmost gold line.

To further illustrate the generality of our finding that secondary drops occur only if $\Pi_{\text{eff}}(H_0) > 0$, we next consider the mode(s) of the drop heights, $\bar{H}_l$, the value(s) of which is/are given by the peak(s) of the distribution of H_l in the histograms in Figure 4.8, for two values of β (the parameter defining the thickness where the bulk elastic energy is comparable to surface anchoring energy, see (4.8)). Figure 4.9 plots $\bar{H}_l$ as a function of H_0: part (a) corresponds to the parameters used in Figure 4.8 ($\beta = 1$) and part (b) shows data for simulations with $\beta = 2$. We clearly see that, in both cases, the secondary droplets appear only for film heights such that $\Pi_{\text{eff}}(H_0) > 0$, and that H_0 (black dashed line) can be used to differentiate primary and secondary drops.

4.2.3 Relation to Previous Work

Before closing this section we comment on the relation of our results to those previously reported in the literature on instabilities of polymer films. To begin, we extract the distances, D_l, between neighbouring primary drop centres (ignoring secondary drops with $H_l < H_0$), and normalise D_l by λ_m. Figure 4.10 shows the mean distance, $\bar{D}_l$, for both the present model (Figure 4.10a) and for the Newtonian equivalent (Figure 4.10c). For H_0 not near the boundaries ($H_\mp$) of the linearly unstable regime (for Newtonian films, $H_+ \to \infty$ within the present model that ignores gravity), $\bar{D}_l \approx 1.15\lambda_m$, consistent with LSA. Near the boundaries, however, $\bar{D}_l$ increases dramatically and is no longer related to λ_m. For very thin films (near H_-), the increase of $\bar{D}_l$ is

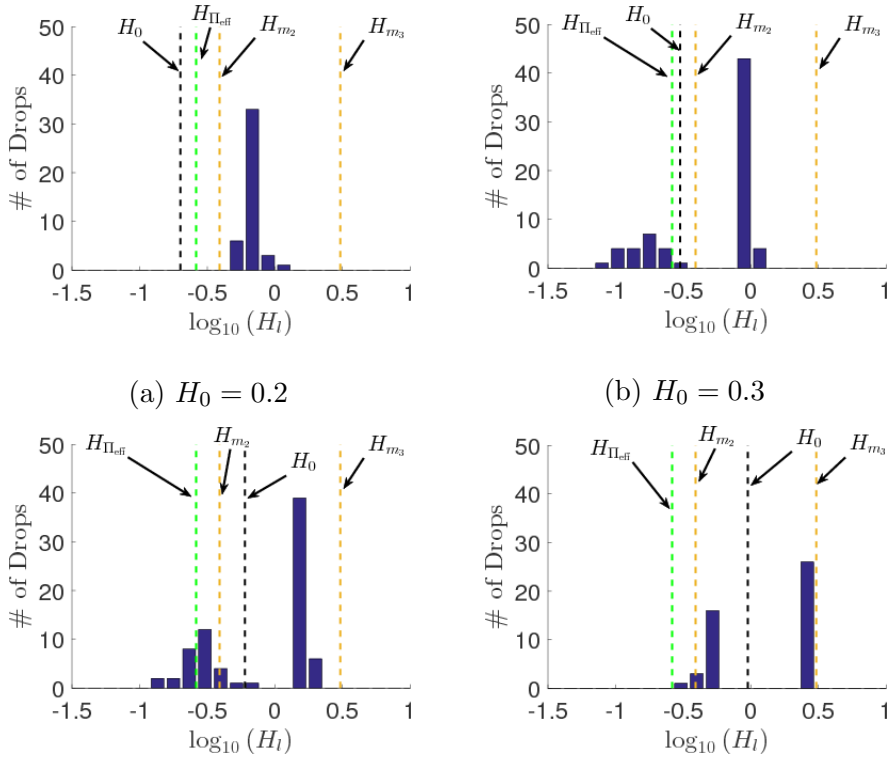

(a) $H_0 = 0.2$ (b) $H_0 = 0.3$

(c) $H_0 = 0.6$ (d) $H_0 = 0.95$

Figure 4.8 Histogram of initial individual drop heights extracted from the corresponding simulations in Figure 4.7. We see that when $\Pi_{\text{eff}}(H_0) > 0$, panels (b), (c), and (d), the distribution is bimodal (primary and secondary drops), whereas for $\Pi_{\text{eff}}(H_0) < 0$, panel (a), the distribution is unimodal (primary drops only). The black dashed line denotes the initial film thickness H_0 and dashed gold lines denote the range of metastable thicknesses, to be discussed in § 4.3.2.

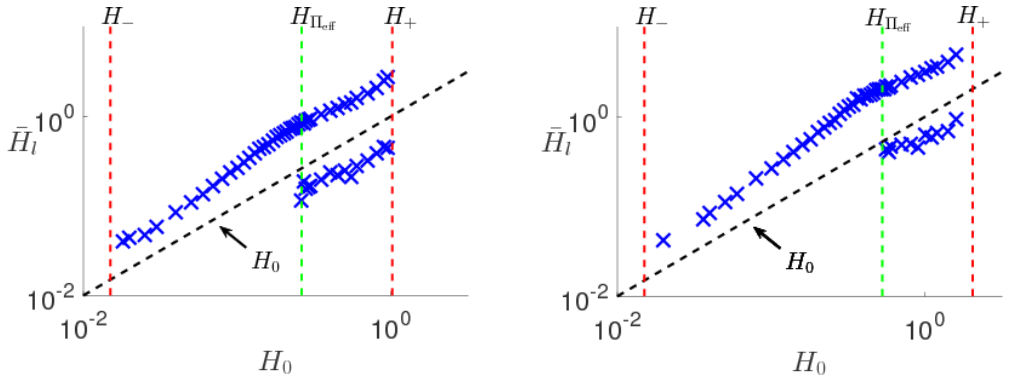

Figure 4.9 Mode(s) of drop heights (peak(s) of histogram data in Figure 4.8) for (a) $\beta = 1$, and (b) $\beta = 2$. When $\Pi_{\rm eff}(H_0)$ changes from negative to positive values (green dashed line), the distribution of the height of drop centres transitions from unimodal (primary drops only) to a bimodal distribution (primary and secondary drops). Furthermore, the initial film thickness, H_0 (black dashed line), proves an adequate threshold between the heights of the primary and secondary drops. Note that for $\beta = 1,\ 2$, $H_{\Pi_{\rm eff}} = 0.2624,\ 0.5275$, respectively.

due to coarsening occurring on a time scale similar to that of dewetting; therefore, drops merge before the entire film completely dewets. For thicker films (near H_+) the increase in the distance between drop centres appears to be due to a different mechanism that appears rather general, since it is operational for both NLC and Newtonian films. Note that for the same range of thicknesses, Seemann *et al.* [53] suggest that thermal (homogeneous) nucleation may be relevant; our results suggest that even without thermal effects (not included in our model), similar behaviour may emerge. The significance of Figure 4.10b is discussed in §4.3 later. More detailed comparison with experimental observations requires three dimensional simulations that will be discussed in the next chapter. For now, we note that the comparison with dewetting experiments by Vandenbrouck *et al.* [2] is favorable: for a 42.8 nm thick NLC film considered in this chapter, ($H_0 = 0.428$), our model predicts $\lambda_m = 39.2$ μm which is near the experimentally measured characteristic length scale of 30 μm. Furthermore, the timescale for dewetting to occur in experiments is about 6-7 minutes, which is close to simulations results, $15\omega_m^{-1} = 5.6$ minutes with $\omega_m^{-1} = 22.47$ at $H_0 = 0.428$.

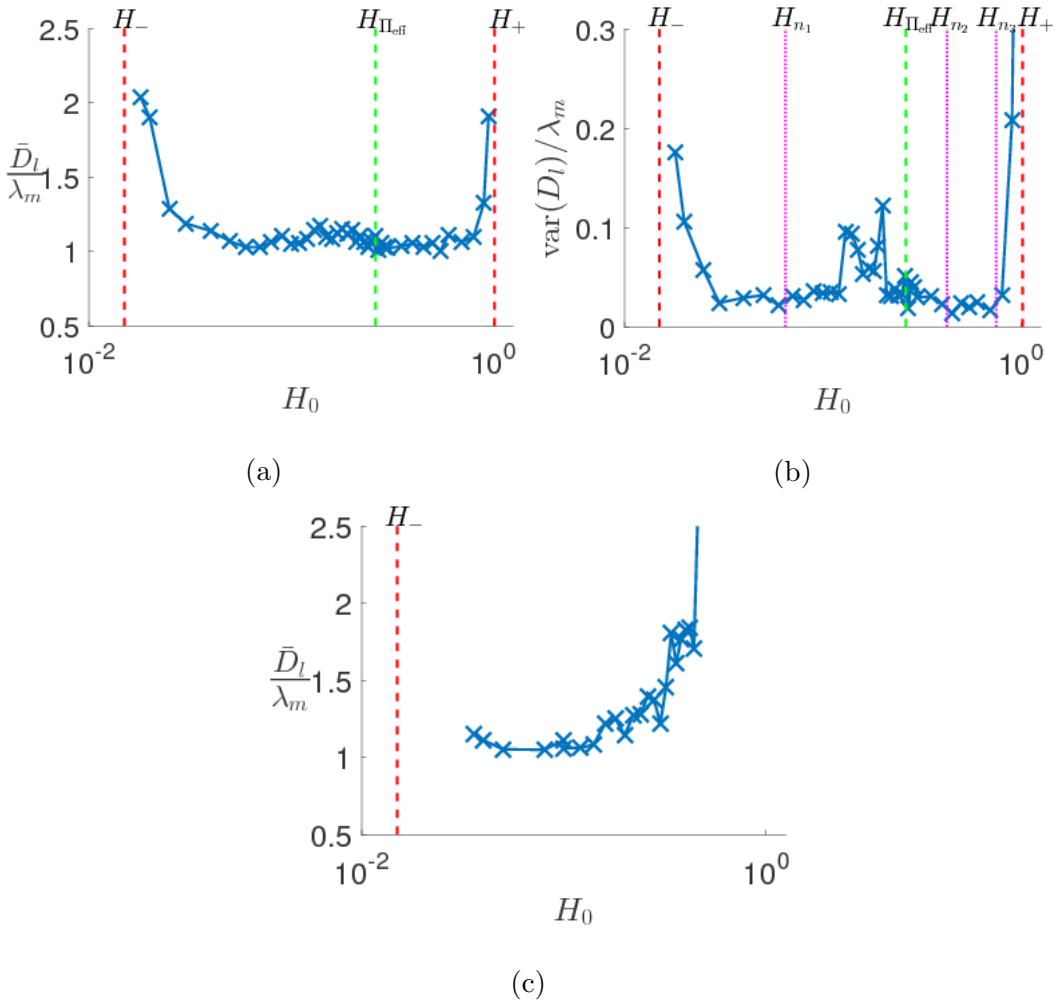

Figure 4.10 (a) Mean spacing between primary drop ($H_l > H_0$) centers, $\bar{D}_l$, normalized by λ_m; and (b) (variance in $D_l)/\lambda_m$, for a randomly perturbed NLC film of thickness H_0. The dotted magenta lines denote thickness threshold values extracted from simulations of a film exposed to localized perturbations. The derivation and meaning of these lines will further discussed in § 4.3 and compared; for now, we note the increase in the variance in the region bounded by H_{n_1} and H_{n_2}, and the region bounded by H_{n_1} and H^+. (c) Distance between drop centers (no secondary drops) for a Newtonian film ($\mathcal{N} = 0$). Note that here there is no upper bound between linear instability and stability (i.e. H^+ is not defined) and all films thicker than H_- (dashed red line) are unstable.

Regarding the formation of secondary drops, we note that previous works [46,54] do not report their existence. A possible reason for this may be the difference in scales. To see this, consider the ratio $\rho = H_+/H_-$. For the problem considered here, $\rho = O(10^2)$, while in Thiele *et al.* [54], and Sharma and Verma [46], $\rho = O(1)$. Therefore, in the present problem it is possible to distinguish clearly features that may be invisible for smaller ρ. While we are unaware of experimental evidence of smaller secondary drops forming during the dewetting of thin films of NLC on a solid substrate, drops of different sizes have been observed on liquid substrates, [30]. Similar smaller drops are observed in experiments with metal films [69, 70].

Next, we discuss the shape of the primary drops. Figure 4.7 shows that for $H_0 \to H_+$, the base of these drops widens. Such behavior is found consistently for simulations with initial film thickness in the linearly unstable regime. In the example shown in Figure 4.7d, the larger (primary) drops are approximately flat for ten or more length units, then transition in height to the equilibrium film; therefore, ignoring the secondary drops, Figure 4.8d may be interpreted as showing coexistence of two flat films, resembling NLC films observed on silicon (or silicon oxide) substrates [30]. Similarly to our results, as $H_0 \to H^+$, Sharma and Verma [46] observe the height profiles transitioning from "hills and valleys" (e.g., Figure 4.7c) to "pancakes" (wide drops), see Figure 4.7d.

Sharma and Verma [46] also show that an analytical result may be obtained for the minimum (equilibrium film thickness) and the maximum (height of drop centers) of steady state solutions. We will discuss an extension of these results to our setup later in § 4.3.2; for the present purposes it is sufficient to mention the prediction that, for sufficiently long times, the thickness value denoted by H_{m_3} in Figure 4.8 should be reached. We observe such behavior only for $H_0 \lessapprox H_{m_3}$ for the times considered. Once again, it is quite possible that the details of the influence of the film thickness

could not be captured in Sharma and Verma [46] due to insufficient separation of scales.

4.3 Films Exposed to a Localized Perturbation

In this section, we focus on instabilities induced by a localized perturbation, with the main motivation of comparing and contrasting results with those of the preceding section where the film was perturbed globally. In physical experiments, localized perturbations (also referred to as nucleation centers) may be due to impurities, substrate defects, or some localized modification of the film structure. To facilitate the comparison between the influence of local and global perturbations on film stability, we still model such localized perturbations by perturbing the initial film thickness, anticipating that this is sufficient to gain basic insight into the influence of more complex perturbation types, listed above, that may occur in physical experiments.

We use the following initial condition

$$h(x, t = 0) = H_0 \left[1 - d \exp\left(- \left[\frac{x}{0.2W} \right]^2 \right) \right] , \tag{4.26}$$

i.e., a film of thickness H_0 with a localized perturbation at the left boundary, $x = 0$, where a line of symmetry is assumed. The parameters W and d control the width and depth of the perturbation, respectively.

The section below is separated into two parts: First, in § 4.3.1, we consider the linearly unstable regime. Here, we describe first the computational results and then consider an analytical approach, based on marginal stability analysis. This approach allows us to gain better insight into instability development, in particular regarding emerging wavelengths. In the second part, § 4.3.2, we discuss the results relevant to linearly stable films.

4.3.1 Linearly Unstable Regime

Here we fix $d = 0.1$ and $W = \lambda_m$ in (4.26). The domain length is initially set to $5\lambda_m$, and the right boundary is dynamically expanded as a simulation progresses. Our simulations should therefore be representative of a localized perturbation imposed on a film of infinite extent.

Computational Results Figure 4.11 shows simulation results obtained with initial condition (4.26) and using the same parameter sets as in Figures 4.5 and 4.7, as well as an additional thickness value, $H_0 = 0.05$. The main observation is that the localized perturbation propagates to the right and successively touches down forming drops; however, comparing these results to those obtained using random infinitesimal perturbations we note two main differences: first, no secondary drops are seen for localized perturbations; and second, the distance between drops is close to λ_m only for some values of H_0; for example, in Figure 4.11 the agreement with LSA is found only for $H_0 = 0.05$ and $H_0 = 0.6$, panels (a) and (d), respectively. Note that while in panel (c) two different drop heights are observed (see $x \approx 2$ and $x \approx 14$), the magnitude of the drop heights is similar; therefore, we do not classify the smaller drops as secondary drops as was done in the previous section. The emergence of different drop heights with similar magnitude was observed by others [71] and will be further discussed in § 4.3.1.

To investigate further the dewetting process we calculate the mean distance between drop centers, $\bar{D}_l$. Figure 4.12a shows the results; to improve statistics, the simulations are carried out in large domains expanded in time to $320\lambda_m$. We observe the existence of four different regimes characterized by the magnitude of $\bar{D}_l/\lambda_m$, separated by three distinct film heights (marked by the dotted magenta lines showing where $\bar{D}_l/\lambda_m \approx 1.1$, to characterize departure from LSA predictions) and denoted H_{n_1}, H_{n_2}, and H_{n_3}. We see that in the regions marked R I and R III, the distance

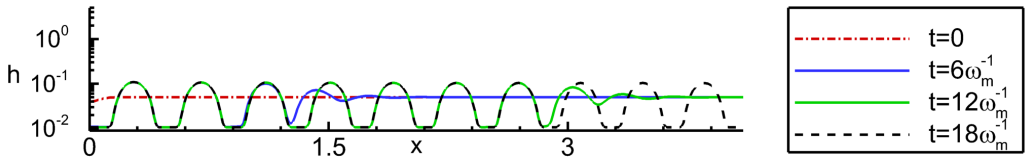

(a) $H_0 = 0.05$, $\omega_m^{-1} \approx 1.681$

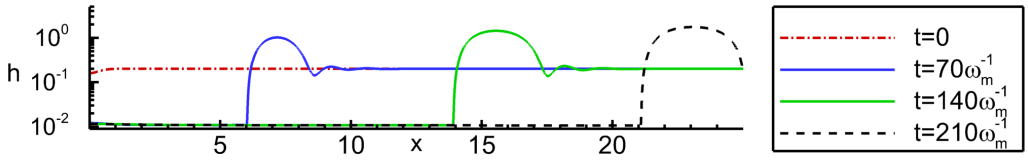

(b) $H_0 = 0.2$, $\omega_m^{-1} \approx 34.22$

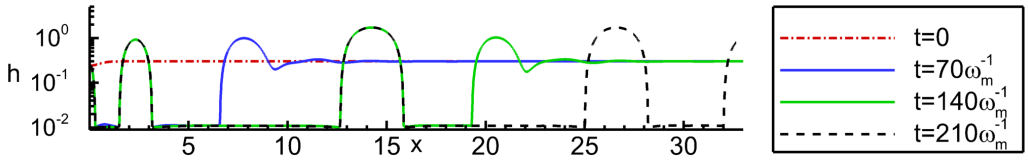

(c) $H_0 = 0.3$, $\omega_m^{-1} \approx 34.64$

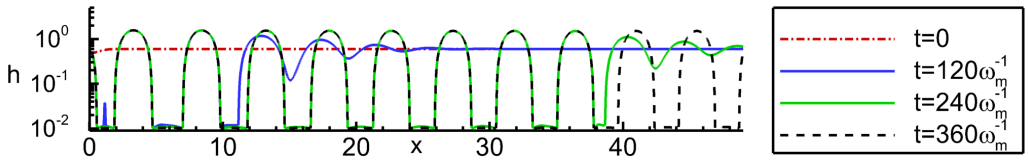

(d) $H_0 = 0.6$, $\omega_m^{-1} \approx 19.21$

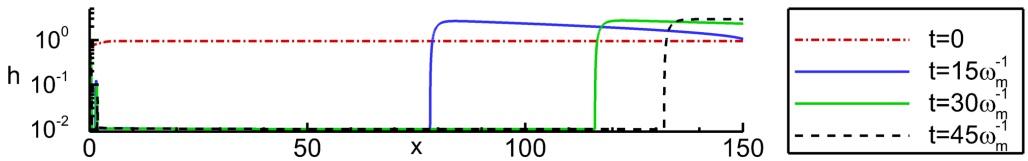

(e) $H_0 = 0.95$, $\omega_m^{-1} \approx 423.4$

Figure 4.11 The free surface evolution for various initial average film thicknesses, H_0. The initial condition is given by (4.26). Note that the film profiles shown in (b) and (e) form drops, but for times longer than shown here. The domain size shown in each panel is $10\lambda_m$; the simulation domains extend beyond the right boundary. The other parameters are given in §4.1.3.

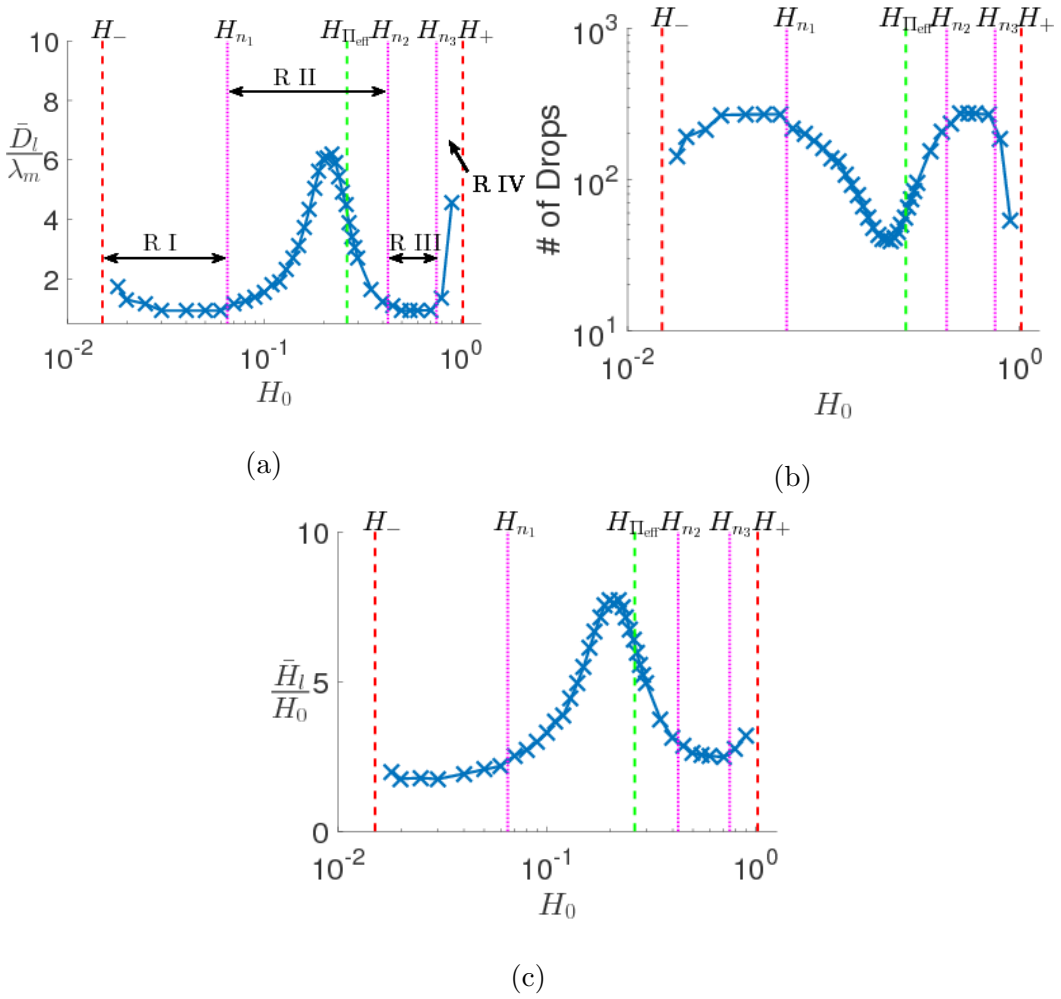

Figure 4.12 (a) The mean distance between drop centers, $\bar{D}_l$, normalized by λ_m, at $t = 350\omega_m^{-1}$; (b) The corresponding number of drops; and (c) The mean height of drop centers, $\bar{H}_l$, normalized by H_0. The magenta dotted lines correspond to the values of H_0 for which $\bar{D}_l/\lambda_m$ crosses the value 1.1. The other parameters are given in §4.1.3.

between drop centers is well approximated by λ_m; however, there exist regions R II and R IV, where there is no correlation between $\bar{D}_l$ and λ_m.

Regimes for which $\bar{D}_l \not\approx \lambda_m$ have been reported before [54, 55] for different thin film models; however, the main findings differ from those presented here. Thiele *et al.* [54], and Diez and Kondic [55] both identify a $\bar{D}_l \not\approx \lambda_m$ regime near the upper threshold H_+ between linear instability and stability (see the R IV regime in Figure 4.12a). The work by Thiele *et al.* [54] furthermore discusses a corresponding regime close to H_-; in the present formulation, this is a subset of the R I region very close to H_- where, similarly to the results for a film exposed to random perturbations (see Figure 4.10a) the difference between $\bar{D}_l$ and λ_m is due to coarsening occurring on the considered time scale. Thiele *et al.* [54] describe this transition to the $\bar{D}_l \not\approx \lambda_m$ regime as a super/subcritical transition (spinodal to nucleation-dominated regime). A new finding of this chapter is the existence of multiple super/subcritical transitions (our R II and R IV regimes).

Before exploring the instability development due to a local perturbation more rigorously, we first note a connection to our previous results for randomly perturbed films. Recalling the results for the mean distance between drop centres, $\bar{D}_l$, for films exposed to random perturbations (see Figure 4.10a), while $\bar{D}_l/\lambda_m \approx 1.15$ mostly everywhere, there appears to be small peak in $\bar{D}_l/\lambda_m$ in the thickness range corresponding to the R II regime. To highlight this connection further, in Figure 4.10b the variance in D_l/λ_m is plotted as a function of the initial film thickness H_0. We see that the variance increases in the R II and R IV regime, suggesting that there is a connection between the results for randomly and locally perturbed films. A possible explanation of this connection is that on large domains, the film does not dewet everywhere at the same time even if exposed to random perturbations; therefore, at the locations where the film dewets initially, the solution may appear as due to a localised perturbation, with retracting fronts modifying the distance between the

drops that form eventually. The influence of these fronts may result in a large variance, explaining the results captured by Figures 4.10a and 4.10b.

We also note a possible connection to the theoretical and experimental results presented by Diez and Kondic [55]; Seemann *et al.* [53]; and Thiele *et al.* [54]. Seemann *et al.* [53] suggest that as $H \to H_+$ (or H_-), where by definition $\Pi_{\text{eff}}{}'(H_+) = 0$ ($\Pi_{\text{eff}}{}'(H)$ corresponds to $\phi''(h)$ in the referenced work), the barrier to nucleation vanishes, thus nucleation by thermal activation is possible. While our model does not include thermal effects, our results are similar to those observed by Seemann *et al.* [53]. Therefore, the R IV regime in our results, and the nucleation reported by Diez and Kondic [55], and Thiele *et al.* [54] (again no thermal effects considered), may be analogous to the thermal nucleation regime.

We note that under appropriate scaling, solutions of the form $h(x,t) = H_0[1 + \epsilon h_1(x,t) + \epsilon^2 h_2(x,t) + O(\epsilon^3)]$, where $0 < \epsilon \ll 1$, are to leading order independent of the model parameters. The scalings are as follows:

$$h = H_0\Psi\ , \quad x = \sqrt{\frac{\mathcal{C}}{\Pi_{\text{eff}}{}'(H_0)}}\zeta\ , \quad \text{and} \quad t = \frac{\mathcal{C}}{Q(H_0)\left[\Pi_{\text{eff}}{}'(H_0)\right]^2}\tau\ , \tag{4.27}$$

where for generality we keep the general mobility function, $Q(h)$. The rescaled leading order equation is

$$h_{1,\tau} + h_{1,\zeta\zeta\zeta\zeta} + h_{1,\zeta\zeta} = 0, \tag{4.28}$$

and the mode of maximum growth and its corresponding growth rate are $\check{q}_m = 1/\sqrt{2}$, $\check{\omega}_m = 1/4$, respectively (here the check notation denotes the values obtained from the rescaled model). We see that as long as $h_1(x,t) = O(1)$ (i.e., as long as linear theory is applicable), the evolution for different choices of H_0 differs only by spatial and temporal scales. Recall that the initial conditions (4.24), (4.25), and (4.26) were chosen to scale with λ_m and H_0, so the corresponding initial conditions in the rescaled

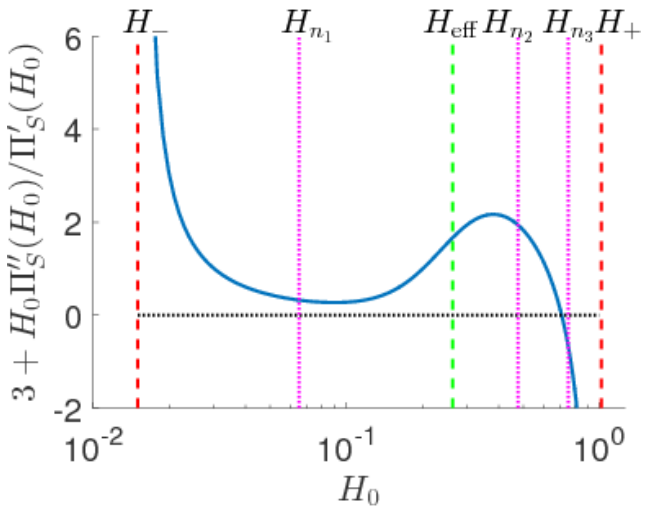

Figure 4.13 The inner square bracketed term in (4.29).

variables are identical. The governing equation for $h_2(x,t)$ is

$$h_{2,\tau}+h_{2,\zeta\zeta\zeta\zeta}+h_{2,\zeta\zeta} = -\left[h_1\frac{Q'(H_0)}{Q(H_0)}\left(h_{1,\zeta\zeta\zeta}+\left[1+\frac{Q(H_0)\Pi_{\rm eff}''(H_0)}{Q'(H_0)\Pi_{\rm eff}'(H_0)}\right]h_{1,\zeta}\right)\right]_\zeta , \quad (4.29)$$

for general $Q(h)$, and for $Q(h) = h^n$,

$$h_{2,\tau} + h_{2,\zeta\zeta\zeta\zeta} + h_{2,\zeta\zeta} = -\left[\frac{h_1}{H_0}\left(nh_{1,\zeta\zeta\zeta}+\left[n+\frac{H_0\Pi_{\rm eff}''(H_0)}{\Pi_{\rm eff}'(H_0)}\right]h_{1,\zeta}\right)\right]_\zeta . \quad (4.30)$$

For any unstable film thickness H_0, the second order equations only differ by the forcing term on the right hand side, which is independent of the inverse Capillary number, $\mathcal{C}$, suggesting that the effective disjoining pressure determines the transition between different dewetting morphologies. Figure 4.13 plots the term enclosed by inner square brackets in (4.30) for $n = 3$ and other parameters as given in § 4.1.3. Note that this term is an increasing function of H_0 in most of the R II regime (between H_{n_1} and H_{n_2}), in contrast to its behavior elsewhere. While we do not yet have a clear explanation of how this observation is related to the film breakup properties seen in the R II regime, we expect that it may be useful in future analysis of different stability regimes.

Marginal Stability Criterion: Outline Marginal stability criterion (MSC) theory analyses front propagation into an unstable state using Fourier transforms and asymptotic theory. The analysis in some cases allows one to rationalize the manner in which an unstable front (resulting from the presence of a localized perturbation) propagates into an unstable flat film. In particular, the outcome of this approach is the front speed, which can then be correlated with the time of breakup at which consecutive drops form, and their distance. To begin, we give a brief overview of MSC theory and its main results in the present context; the reader is referred to the comprehensive review by van Saarloos [72] for further details. Then in the following section we discuss the correlation of MSC predictions with our computational results.

We assume that the solution of the rescaled leading order governing equation (4.28) has a spatial Fourier series representation, i.e.

$$h_1(\zeta,\tau) = \int_{-\infty}^{\infty} \breve{h}_1(\breve{q},\tau) e^{\breve{q}\zeta i}\, d\breve{q}\ . \tag{4.31}$$

Furthermore, with the ansatz

$$\breve{h}_1(\breve{q},\tau) = \tilde{h}_1(\breve{q}) e^{-\breve{\omega}(\breve{q})\tau i}\ , \tag{4.32}$$

substituting (4.31) into (4.28) yields

$$\int_{-\infty}^{\infty} \left[-i\breve{\omega}(\breve{q}) + \breve{q}^4 - \breve{q}^2\right] \tilde{h}_1(\breve{q}) e^{\breve{q}\zeta i - \breve{\omega}(\breve{q})\tau i}\, d\breve{q} = 0\ , \tag{4.33}$$

where $\tilde{h}_1(\breve{q})$ is the Fourier transform of the initial condition (assumed analytic). Satisfying (4.28) for arbitrary $\tilde{h}_1(\breve{q})$ gives the dispersion relation,

$$\breve{\omega}(\breve{q}) = -i(\breve{q}^4 - \breve{q}^2)\ . \tag{4.34}$$

In the reference frame traveling with velocity $\breve{V} = \left(\sqrt{\mathcal{C}}/Q(H_0)\left[\Pi_{\text{eff}}{}'(H_0)\right]^{\frac{3}{2}}\right) V$, the solution can be expressed as

$$h_1(s,\tau) = \int_{-\infty}^{\infty} \tilde{h}_1(\breve{q}) e^{i\breve{q}s} e^{-i[\breve{\omega}(\breve{q}) - \breve{V}\breve{q}]\tau}\, d\breve{q}\ , \tag{4.35}$$

where $s = \zeta - \check{V}\tau$. If the above integral converges, $h_1(s,\tau)$ satisfies the rescaled governing equation (4.28), and $\check{V}$ is defined as the "linear spreading speed" [72].

Following Saarloos [72], we now consider the limit $\tau \to \infty$ and use a saddle-point approximation (steepest descent method) to approximate the integral in (4.35). The saddle-point $\check{q}^*$ satisfies

$$\check{V} = \left.\frac{d\check{\omega}(\check{q})}{d\check{q}}\right|_{\check{q}^*} . \tag{4.36}$$

To eliminate exponent terms of the integrand in (4.35) that lead to decay or growth in τ, we set

$$\check{V} = \frac{\check{\omega}_i(\check{q})}{\check{q}_i} , \tag{4.37}$$

where $\check{V} \in \mathbb{R}$ (by definition), the i subscript denotes the imaginary part of variables, and an r subscript will be used to denote the real part. Recall $\check{\omega}(\check{q})$ is a polynomial in $\check{q}$ and thus differentiable, so that (4.36) may be expressed as

$$\check{V} = \mathrm{Re}\left[\left.\frac{d\check{\omega}}{d\check{q}}\right|_{\check{q}^*}\right] = \left.\frac{1}{2}\left[\frac{\partial\check{\omega}_r}{\partial\check{q}_r} + \frac{\partial\check{\omega}_i}{\partial\check{q}_i}\right]\right|_{\check{q}^*} , \tag{4.38}$$

and

$$\mathrm{Im}\left[\left.\frac{d\check{\omega}}{d\check{q}}\right|_{\check{q}^*}\right] = \left.\frac{1}{2}\left[\frac{\partial\check{\omega}_i}{\partial\check{q}_r} - \frac{\partial\check{\omega}_r}{\partial\check{q}_i}\right]\right|_{\check{q}^*} = 0 . \tag{4.39}$$

Furthermore, by definition, $\check{\omega}_r$ and $\check{\omega}_i$ satisfy the Cauchy-Riemann equations, simplifying (4.38) and (4.39) to

$$\check{V}(\check{q}^*) = \left.\frac{\partial\check{\omega}_r}{\partial\check{q}_r}\right|_{\check{q}^*} , \quad \text{and} \quad \mathrm{Im}\left[\left.\frac{d\check{\omega}}{d\check{q}}\right|_{\check{q}^*}\right] = \left.\frac{\partial\check{\omega}_i}{\partial\check{q}_r}\right|_{\check{q}^*} = 0 , \tag{4.40}$$

respectively. Satisfying the second condition in (4.40) gives an expression for $\check{q}_r$ as a function of $\check{q}_i$ and taking the derivative of (4.37) with respect to $\check{q}_i$ yields

$$\frac{d\check{V}}{d\check{q}_i} = \frac{1}{\check{q}_i}\left[\frac{\partial\check{\omega}_r}{\partial\check{q}_r}\frac{d\check{q}_i}{d\check{q}_r}\frac{\partial\check{\omega}_r}{\partial\check{q}_i} - \frac{\check{\omega}_i(\check{q})}{\check{q}_i}\right] . \tag{4.41}$$

Evaluating the above equation at the saddle point, and substituting (4.37) and (4.40), we find

$$\left.\frac{d\check{V}}{d\check{q}_i}\right|_{\check{q}^*} = 0 \,, \tag{4.42}$$

and thus $\check{q}_i^*$ is a critical point of $\check{V}$. We note that this critical point is a minimum of $\check{V}$; however this information is not required to determine $\check{V}$ itself [72]. Equations (4.36), (4.40), and (4.42) provide the necessary conditions to determine $\check{q}_r^*$, $\check{q}_i^*$, and $\check{V}$. Therefore, with the rescaled dispersion relationship defined by (4.34),

$$\check{q}^* = \sqrt{\frac{3+\sqrt{7}}{4}} + \sqrt{\frac{1}{6}\left[\sqrt{7}-1\right]}i \approx 0.791 + 0.262i \,, \tag{4.43}$$

and

$$\check{V} = \frac{1}{9}\sqrt{1+\sqrt{7}}\left(5+\sqrt{7}\right) \approx 1.622 \quad \Rightarrow \quad V \approx 1.622\frac{Q(H_0)\left[\Pi_{\text{eff}}{}'(H_0)\right]^{\frac{3}{2}}}{\sqrt{\mathcal{C}}} \,, \tag{4.44}$$

where the second equation in (4.44) is given in the unscaled variables. We note in passing that MSC also provides the condition for when a front propagating to the right will spread with the linear spreading speed asymptotically. If the initial condition decays faster than $e^{-\check{q}^*\zeta}$ as $\zeta \to \infty$, then the instability will spread with velocity V given by (4.44), and the solution is referred to as a pulled front. For an initial condition that does not decay fast enough, the instability will propagate into the unstable state with a speed greater than V. The solution is then referred to as a pushed front and deriving an expression for the speed at which it spreads is nontrivial. For the present problem, the initial condition (4.26) is a Gaussian perturbation, thus decays sufficiently fast and a pulled front is expected.

Regarding the time scale for successive drop formation, we note that if a localised perturbation leads to a coherent pattern behind the front, it is periodic in time, i.e., $H(s) = H(\zeta - \check{V}\tau) = H(\zeta + \check{\lambda} - \check{V}\tau) = H(\zeta - \check{V}(\tau + \check{t}_{\text{MSC}}))$, where $\check{t}_{\text{MSC}}$ is the time between successive drops detaching from behind the front at distances $\check{\lambda}$ apart.

Satisfying $H(\zeta + \check{\lambda} - \check{V}\tau) = H(\zeta - \check{V}(\tau + \check{t}_{\mathrm{MSC}}))$ yields

$$\check{t}_{\mathrm{MSC}} = \frac{\check{\lambda}}{\check{V}} = \frac{2\pi}{\check{q}\check{V}} \approx 5.478 \ , \quad \text{or} \quad t_{\mathrm{MSC}} = 5.478 \frac{\mathcal{C}}{Q(H_0)\left[\Pi_{\mathrm{eff}}{}'(H_0)\right]^2} \ , \tag{4.45}$$

where, for future reference, $\check{q} = \check{q}_m$ was used in the first expression to obtain the second one. In the next section we proceed with correlating the presented MSC results with the computational ones.

The speed of the propagating front, (4.44), may alternatively be obtained by using pinch point analysis, with a key difference of how the complex integral path is chosen in the Fourier representation (4.35) (see the papers by Huerre *et al.* [73, 74] for further details on pinch point analysis). Our results in the previous chapters for flow of a thin film down an inclined plane relied on the results of such analysis to derive the velocity of wave packet boundaries (V in the MSC analysis). In that work, analytical and numerical simulations confirmed the existence of three stability regimes behind the front traveling down the inclined plane: stable, convectively unstable, and absolutely unstable. These same instabilities were discussed by Saarloos [72] within a different physical context. The two unstable regimes were further subdivided into two cases: coherent pattern formation (periodic array of drops) and incoherent pattern formation; however, a general analytical theory for predicting these cases is not yet available. We will discuss our computational results within this context briefly in the next section.

Having explicit results for the time scales on which localized and random perturbations lead to dewetting and drop formation, given by t_{MSC} and ω_m^{-1}, respectively, allows one to discuss which instability is relevant and actually destabilizes a film. Considering the ratio of these time scales, however, shows it to be independent of the film thickness. This finding at first sight appears at odds with the commonly accepted paradigm that for thin films spinodal instability is relevant, while for thick ones nucleation is dominant [53]. One explanation is that the nucleation instability

may be operational for thin films as well (assuming that nucleating centers are available), but this is not obvious due to the same wavelengths resulting from both localized and global perturbations (for example, in the R III regime, compare Figures 4.10a and 4.12a). However, more careful discussion of this important issue requires simulations in 3D, and we therefore defer to the next chapter.

Marginal Stability Criterion: Correlation with computational results We now return to simulations of our model, and consider them in light of the MSC predictions. Using the analytical result (4.44) for the linear spreading speed, V, of the propagating perturbation, simulation results may be plotted in the reference frame moving with this speed. Furthermore, to emphasize the difference between the dewetting dynamics for different regimes, the traveling wave variable, $s = x - Vt$, is scaled by λ_m.

Figure 4.14 shows typical results in R II and R III regimes (the results in R I are similar to those in R III). First, we see that the instabilities caused by the localized perturbation are essentially bounded by $s = 0$, demonstrating that MSC correctly predicts the speed with which instabilities propagate into the unstable flat region. Furthermore, since the front speed is given by MSC, we are in the pulled front case as expected. Second, the differences between the dewetting dynamics in the various regimes are easily observed, and we discuss these differences next. Movies (*Movie 1 - 4* in the online supplementary material of the published paper [26] or arXiv [1]) are also available to better illustrate the instability evolution.

In the R III regime, see Figure 4.14b and *Movie 1*, in the reference frame traveling with MSC speed V, the solution is a leftward-propagating traveling wave, with a stationary envelope (in the traveling reference frame). Furthermore, as the traveling

[1] https://arxiv.org/abs/1704.03919, accessed April 25, 2018

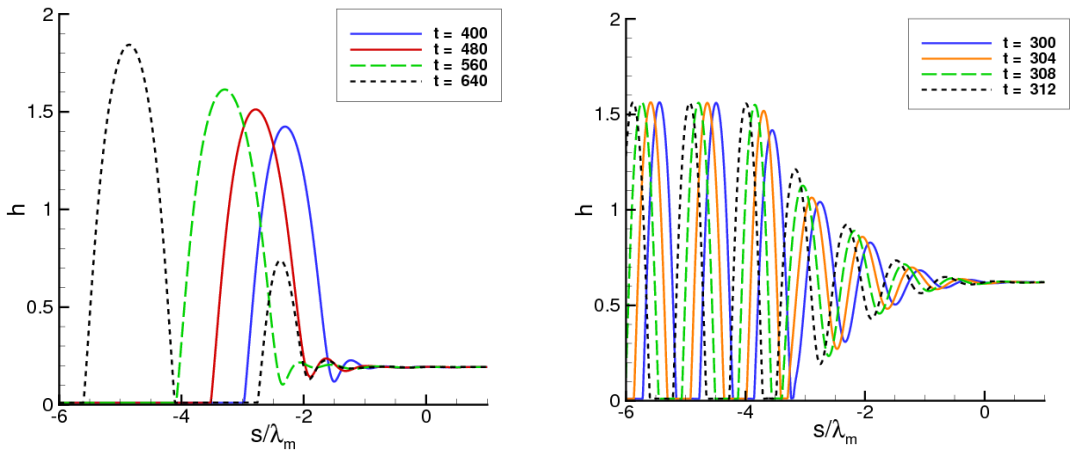

(a) (b)

Figure 4.14 Typical evolution of the film thickness in the reference frame traveling with the linear spreading speed V in (a) R II regime and (b) R III regime. Note that the x-axis has been scaled by λ_m to highlight departure from the LSA predictions in R II regime.

wave propagates to the left, its amplitude (close to the front) grows monotonically and dewets the film periodically with wavelength λ_m, therefore leading to coherent pattern formation.

In the R II regime, however, the instability evolution is more complicated. Here, the amplitude of the waves connecting the capillary ridge to the flat film (see e.g. $s/\lambda_m \in [-2, 1]$ in Figure 4.14a) does not grow monotonically as it travels to the left, but oscillates until some critical amplitude is reached. In this regime (and similarly in R IV, not discussed for brevity), both coherent and incoherent pattern formation is possible; see *Movies 2 -4* for examples that illustrate either coherent pattern formation (*Movie 2*); a bimodal pattern where drops of two different sizes are produced (*Movie 3*); or a disordered state, where the evolution resembles the R III regime sporadically interrupted by a different type of dynamics (*Movie 4*). Clearly, more work is needed to understand the details of pattern formation in R II (and R IV) regimes; we leave this for the future and for now focus on the main features of the results, without delving further into various modes of breakup in the R II regime.

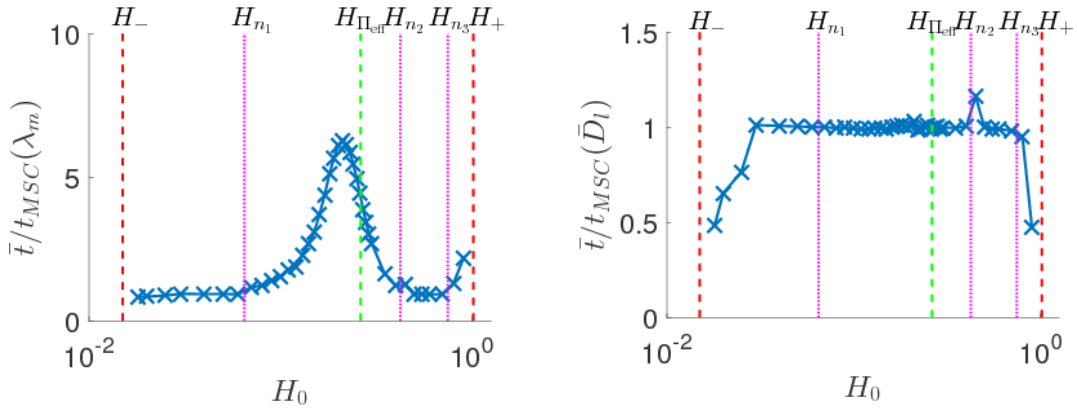

(a) (b)

Figure 4.15 The mean time between drop formation extracted from simulations, normalized by (4.45) with (a) $\lambda = \lambda_m$ and (b) $\lambda = \bar{D}_l$, i.e. the mean distance between drop centers obtained in simulations.

To compare the film breakup times predicted by MSC (4.45) to the results of simulations, we extract the mean time between formation of successive drops. The results are plotted in Figure 4.15 as a function of the initial film thickness, H_0, normalized by (4.45) with (a) $\lambda = \lambda_m$ and (b) $\lambda = \bar{D}_l$ (the mean distance between drop centers extracted from simulations). Similarly to the results given in Figure 4.12a, Figure 4.15a shows that with $\lambda = \lambda_m$ the MSC prediction (4.45) gives good agreement with the numerics in regions R I and R III; however, there is no agreement in R II and R IV. Substituting instead the mean distance between drop centers $\lambda = \bar{D}_l$ into (4.45), Figure 4.15b demonstrates that MSC gives the correct result for all film thicknesses not near the threshold values between instability and stability (dashed red lines). This result suggests that the MSC approach provides the correct result for breakup times once the instability wavelength is selected; however MSC does not provide information about this selected wavelength in the R II regime.

We note that, while a nonlinear variant of MSC has been developed, it applies only to pushed fronts [72] that are not relevant here. An alternative theory mentioned (but not thoroughly analyzed) by Saarloos [72] is the Eckhaus or Benjamin-Feir resonance, based upon interaction between unstable waves. In the next chapter, we

analyze whether such interaction could be responsible for the observed instability in R II and R IV regimes.

To summarize: for linearly unstable films subjected to a localized perturbation, we have extracted the mean spacing between drop centers and the mean formation times of successive drops, as a function of the initial film thickness, H_0. It has been shown that there exists a region, R II in Figures 4.12a and 4.15a, such that the results in the nonlinear evolution regime differ significantly from the predictions of LSA. Our understanding is that the effects leading to the existence of regimes R II and R IV are fully nonlinear.

4.3.2 Linearly Stable Regime

We now switch focus to locally perturbed films with initial film thicknesses in the linearly stable regime, in particular for $H_0 > H_+$. First, we investigate the behavior of linearly stable films exposed to a finite amplitude disturbance (metastability). Then, once dewetting is induced, we investigate the speed at which a localized perturbation propagates into the stable film region.

Metastability: Analytical findings We first adapt the results of Thiele *et al.* [54], and Diez and Kondic [55], and derive the metastable regime. Note that this regime is referred to as the heterogeneous nucleation regime by Seemann *et al.* [53]; however, in contrast to the results to be presented here, Seemann *et al.* [53] provide no upper bound to this regime.

A linearly stable film is metastable if there exists a thinner, linearly stable, film with lower energy, hence, given a perturbation of sufficient size, the perturbation can push the thicker film into the energetically preferable thinner film state (dewetting). To derive an expression for the energy per unit length of a film, we analyze steady state solutions to the governing equation (4.10) that connect two flat films of different thicknesses.

To begin, we set $h_t(x,t) = 0$ in (4.10), integrate with respect to x, and divide by $Q(h) = h^3$ to yield

$$\mathcal{C}h_{xxx} + \Pi_{\text{eff}}'(h)h_x = d_0 \ , \tag{4.46}$$

where d_0 is the constant of integration. Note that the metastability analysis from this point on is independent of the form of the mobility function $Q(h)$. Similarly to Sharma and Verma [46], we use the far-field conditions

$$h(x \to -\infty, t) = H_{\min} \ , \quad h(x \to \infty, t) = H_{\max} \ , \quad H_{\min} < H_{\max} \ , \tag{4.47}$$

and

$$h_x(x,t) = h_{xx}(x,t) = h_{xxx}(x,t) = 0 \ , \quad x \to \pm\infty \ , \tag{4.48}$$

where $H_{\min}$ and $H_{\max}$ are constants to be determined. Applying boundary conditions (4.48) to (4.46), we find $d_0 = 0$. Equation (4.46) is then integrated again in x to obtain

$$\mathcal{C}h_{xx} + \Pi_{\text{eff}}(h) = \Pi_0 \ , \tag{4.49}$$

where Π_0 is the constant of integration. To satisfy (4.47) and (4.48), we require $\Pi_{\text{eff}}(h)$ to have the same value, Π_0, for at least two different film thicknesses; i.e. ignoring the transition region between the flat films of thickness $H_{\min}$ and $H_{\max}$, the effective disjoining pressure is constant across the film. We may then parameterize steady state solutions, satisfying boundary conditions (4.47) and (4.48), by Π_0.

Recalling Figure 4.6, there are, at most, three different film thicknesses with the same disjoining pressure, hence there are at most three roots to $\Pi_{\text{eff}}(h) = \Pi_0$, which we denote as H_{m_1}, H_{m_2}, and H_{m_3}, where $H_{m_1} < H_{m_2} < H_{m_3}$. Furthermore, we define four regimes: M_I (no roots of $\Pi_{\text{eff}}(h) = \Pi_0$), M_II (two roots), M_III (three roots), and M_IV (one root), see Figure 4.16. Note that H_{m_1} and H_{m_3} correspond to the left and right solid blue curves, respectively in Figure 4.16 (thus represent linearly stable

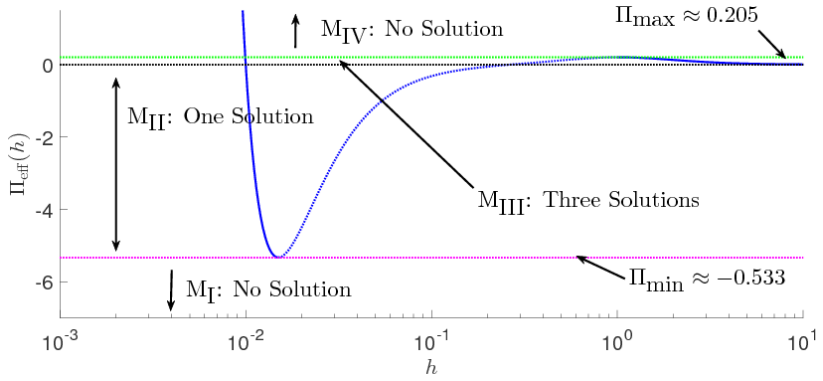

Figure 4.16 The solution space of (4.49) subject to conditions (4.47) and (4.48). Solid blue curves denote linearly stable films, and the dotted blue curve denotes linearly unstable ones.

solutions), and H_{m_2} is denoted by the central dotted blue curve (a linearly unstable solution).

A solution to the steady-state boundary value problem specified by (4.47)–(4.49) requires at least two unique roots; therefore there are no possible solutions in $\mathrm{M_I}$ or $\mathrm{M_{IV}}$, and solutions only exist for $\Pi_0 \in (\Pi_{\min}, \Pi_{\max})$, where $\Pi_{\min}$ and $\Pi_{\max}$ are the local minimum and local maximum of $\Pi_{\text{eff}}(h)$ respectively, the values of which are given in Figure 4.16 (for the chosen parameter values). In $\mathrm{M_{II}}$, there are two roots of (4.47)–(4.49), thus one solution joining these states, with $H_{\min} = H_{m_1}$ and $H_{\max} = H_{m_2}$ i.e. the solution in $\mathrm{M_{II}}$ connects a thin linearly stable film to a thicker unstable one.

In $\mathrm{M_{III}}$, there are three roots; thus we can choose two different $H_{\min}$ and $H_{\max}$, see Figure 4.17. Since H_{m_2} is a linearly unstable thickness, the corresponding steady state solutions are also unstable. Ignoring the unstable solution branch, we see that there is a one parameter family of stable steady solutions in $\mathrm{M_{III}}$; thus we set

$$\Pi_0 \in (0, \Pi_{\max}) \,, \quad H_{\min} = H_{m_1} \,, \quad \text{and} \quad H_{\max} = H_{m_3} \,. \tag{4.50}$$

Integrating (4.49) with respect to h yields

$$\frac{\mathcal{C}}{2} (h_x)^2 + e(h) = e_0 \,, \quad e(h) = r(h) + \Pi_0 h \,, \tag{4.51}$$

where $e(h)$ is the energy per unit length of the film due to the effective disjoining pressure. Here, the constant of integration e_0 may be interpreted as the total energy due to surface tension and effective disjoining pressure, and

$$r(h) = -\int^h \Pi_{\text{eff}}(s)\, ds = \frac{\mathcal{K}b^2}{2h}\left[\frac{b}{h} - 2\right] - \mathcal{N}\left[\frac{m^2(h)}{2h} - \int^h \frac{m(s)m'(s)}{s}\, ds\right] . \quad (4.52)$$

Recalling the free energy functional (4.12), we note that $F(h) = -[\mathcal{C}(1+(h_x)^2/2] - r(h)$. Setting $e_0 = e(H_{m_1})$ we plot $e(h) - e_0$ in Figure 4.17 for various Π_0, and observe that only for $\Pi_0 > 0$ are there two local minima for $e(h) - e(H_{m_1})$, see Figure 4.17b. In addition, we note that the film thicknesses at the local minima (H_{m_1} and H_{m_3}) correspond to linearly stable films, and the film thickness at the local maximum (H_{m_2}) corresponds to a linearly unstable film.

Following Thiele *et al.* [54], we seek a value of Π_0 such that the two local minima of (4.52) have the same energy. Specifically, we seek a value of Π_0 that satisfies

$$\frac{\partial e\,(H_{\min})}{\partial h} = \frac{\partial e\,(H_{\max})}{\partial h} = 0 , \quad (4.53)$$

and

$$e\,(H_{\min}) = e\,(H_{\max}) . \quad (4.54)$$

Note that

$$\frac{\partial e}{\partial h} = 0 \;\Leftrightarrow\; \Pi_{\text{eff}}(h) = \Pi_0 , \quad (4.55)$$

therefore by inspection, (4.53) and (4.54) are equivalent to satisfying the far-field conditions, (4.47) and (4.48), in (4.49) and (4.51), respectively.

We now apply these results to the specific problem in question. For the parameters chosen in § 4.1.3, $\Pi_0 = \Pi_0^* \approx 0.07273$ satisfies (4.53) and (4.54), and

$$H^*_{\min} = H^*_{m_1} \approx 0.99799\times10^{-2} , \quad H^*_{m_2} \approx 0.39024 , \quad H^*_{\max} = H^*_{m_3} \approx 3.05160 , \quad (4.56)$$

where '*' superscripts denote the values obtained by using Π_0^* in Equation (4.49). The metastability regime is thus given by

$$H_0 \in (H_{m_1}^*, H_-) \cup (H_+, H_{m_3}^*) \, . \tag{4.57}$$

The region $(H_{m_1}^*, H_-)$ corresponds to a narrow range of film thicknesses close to the equilibrium thickness, which we do not consider further. Films thicker than $H_{m_3}^*$ are absolutely stable, thus no perturbations may induce dewetting. The identified metastable region $(H_+, H_{m_3}^*)$ is considered by numerical simulations in the next section.

Before closing we note the following: (1) In Seemann *et al.* [53], the metastable regime (heterogeneous nucleation in that work) is defined as $H_0 > H_+$. Extending our presented metastability analysis to the disjoining pressure models of Seemann *et al.* [53], we find that for all positive disjoining pressures values (Π_0 in (4.51)), condition (4.54) is never satisfied; specifically, we find that for all $\Pi_0 > 0$, $e\left(H_{\min}\right) < e\left(H_{\max}\right)$, hence there is no upper bound for the metastable regime, consistent with the findings of Seemann *et al.* [53]. Therefore, the existence of absolutely stable films is one of the distinguishing features of the effective disjoining pressure considered here. (2) Satisfying (4.53) implies that $H_{\min}$ and $H_{\max}$ are critical points of $e(h)$; however, to satisfy condition (4.53) with $H_{\min} \neq H_{\max}$, there must exist at least three distinct critical points, i.e., at least three different thicknesses must be characterized by the same disjoining pressure. In our model, this corresponds to positive disjoining pressure. This finding is in agreement with other works [3, 53, 75], where it is stated that a disjoining pressure of the form shown in Figure 4.1b will lead to metastability, a coexistence of films of different thicknesses. (3) In the work of Sharma and Verma [46], the solution derived in this section is referred to as a pancake solution. We will refer to this solution as a front solution since (4.47) and (4.48) are analogous to the far-field conditions used for a traveling front solution in the previous chapters. Note that the

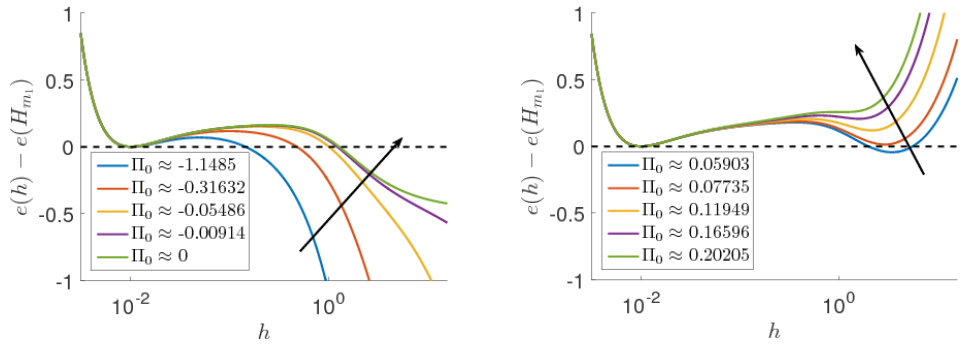

(a) $\Pi_0 < 0$ (b) $\Pi_0 > 0$

Figure 4.17 $e(h) - (H_{m_1})$ where $e(h)$ is defined in (4.51) for an initial film profile with (a) negative effective disjoining pressure, $\Pi_0 < 0$; and (b) positive effective disjoining pressure, $\Pi_0 > 0$. Arrows denote the direction of increasing Π_0.

same nomenclature is used by Thiele *et al.* [54]; the derivation of the front solution in that work is slightly different to that presented here, however, the two methods yield the same result.

Metastability: Numerical Simulations In this section, we investigate numerically the evolution of localized perturbations in the metastable regime, $H_0 \in (H_+, H^*_{m_3}) \approx (1.015, 3.0516)$. The initial condition is specified by (4.26), which is parameterized by the initial film height, H_0. To explore the influence of the perturbation properties, we vary W and d, respectively the width and depth of the perturbation. In particular, we discuss the quantity $d_{\min}(H_0; W)$, the minimum perturbation amplitude required to induce dewetting. Since we are only interested if breakup occurs for a particular set of d and W, it is not necessary to dynamically expand the right boundary in the x domain; therefore, to reduce simulation time, we fix $x \in [0, 200]$.

Figure 4.18 plots $d_{\min}(H_0; W)$ as a function of H_0 for various values of W. In the region above $d_{\min}(H_0; W)$ (solid curves) and below the dotted black line ($d = 1$), the initial condition given by (4.26) induces dewetting. We see that for all values of W considered, $d_{\min}(H_0; W) \to 0$ as $H_0 \to H_+$; i.e. as the film

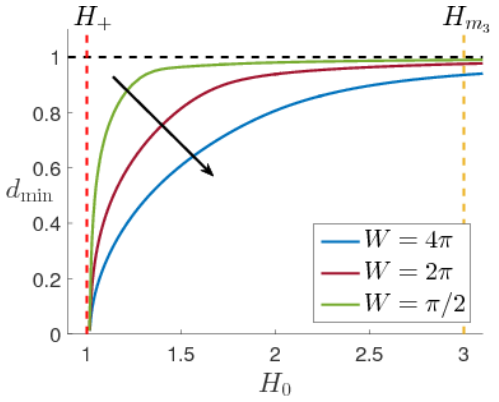

Figure 4.18 $d_{\min}(H_0; W)$ as a function of H_0 for various values of W. Black arrow denotes direction of increasing W.

thickness approaches the threshold H_+ between linear stability and instability, an infinitesimally small perturbation ($d \ll 1$) will induce dewetting, as expected. More importantly, Figure 4.18 demonstrates that as $H_0 \to H_{m_3}$, $d_{\min}(H_0; W) \to 1$; i.e. as the film thickness H_0 approaches the threshold H_{m_3} between metastability and absolute stability, the initial condition (4.26) has to essentially rupture the film ($d \approx 1$) for dewetting to be observed. This demonstrates that the analysis in § 4.3.2 provides a correct upper bound for the metastable regime. Note that $d_{\min}(H_{m_3}; W)$ is a monotonically decreasing function of the perturbation width W. This is expected, since the transition region between a film of thickness H_0 and the minimum of the initial condition (4.26) increases as W increases, thus the transition region (which was assumed to be small and ignored in § 4.3.2) is no longer negligible.

We note that the presented results suggest that our model may transition between the regimes called thermal and heterogenous nucleation, see [53]. As $H_0 \to H_+$ more and more holes are expected as the solution evolves, which may be a result of relatively small perturbations requiring more time to be experimentally measurable compared to the larger perturbations. In contrast, for H_0 significantly larger than H_+, only perturbations above the threshold value $d_{\min}$ will form holes, effectively enforcing an upper bound on the time window within which hole nucleation is observed.

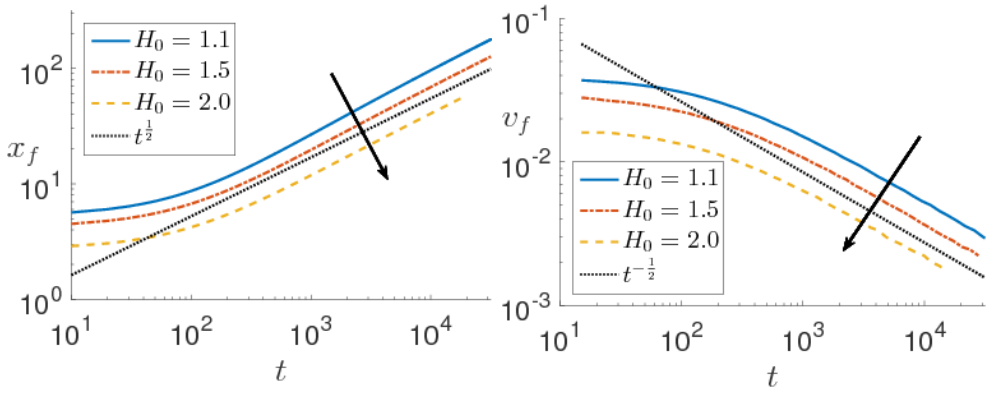

(a) (b)

Figure 4.19 (a) Front position and (b) front speed as a function of time extracted for various initial film thicknesses, H_0, within the metastable regime. Black arrows denote direction of increasing H_0.

Therefore, as $H_0 \to H_+$ from above, $d_{\min} \to 0$ and the time window ($\propto d_{\min}^{-1}$) in which holes form transitions from a sharp window, to a infinitely long time window, within which more and more holes can form.

We now briefly describe the film evolution once dewetting is induced. Similarly to our simulations in § 4.3.1, the right boundary in the x domain is dynamically expanded; we set the initial domain to $[0, 10]$. Simulations show that when dewetting occurs, a retracting front forms, and propagates without additional dewetting events into the flat film region. Similarly to Münch [76], we extract from our simulation results the front position, $x_f(t)$, and its speed, $v_f(t)$. Figure 4.19a shows that at long times, $x_f(t) \propto t^{1/2}$. Not surprisingly, this power law is different from the $t^{2/3}$, power law found by Münch [76] for a thin film model in the slip dominated regime. Figure 4.19b shows that at long times, $v_f(t) \propto t^{-1/2}$, whereas in the linearly unstable regime, simulations and analysis show that propagation speed is a constant, see § 4.3.1.

4.4 Conclusions

While the chapter has been motivated by NLC films, we have presented results that are relevant to a much wider class of problems involving thin films on substrates, such that the fluid-solid interaction involves a relatively complex form of effective disjoining pressure (sketched in Figure 4.20). Such a form has been derived in this chapter as an effective disjoining pressure that includes an elastic contribution for NLC films; however similar functional forms have been extensively considered in the literature focusing on polymer films on Si/SiO_2 substrates [4] and the references therein.

In the NLC context, novel elements include dynamic relaxation of the free surface polar anchoring, θ_F, as a function of film thickness $h(x,t)$. In addition, we have highlighted differences and similarities between the presented model, and others discussed in the literature [1, 30, 31, 47]. Furthermore, our model exhibits a range of film thickness such that a film is linearly unstable, which is analogous to the so-called "forbidden range" discussed in the literature [30].

More generally, an extensive statistical analysis of our computational results, combined with novel analytical results based on the Marginal Stability Criterion, has allowed us to identify a variety of instability mechanisms. In addition to the linearly unstable regime, where infinitesimally small perturbations induce dewetting, there are regimes that require perturbations of sufficient magnitude to induce dewetting (metastability), and regimes that are stable with respect to perturbations of any size (absolute stability). We have also identified the regimes that are linearly unstable, but susceptible to nucleation dominated dynamics. While we do not consider thermal effects, we find that for some film thicknesses (close to the stability boundaries) our results are similar to other results attributed to a thermal nucleation mechanism, suggesting that consideration of thermal effects may not in fact be needed to explain the dynamics. Also, we have formulated analytical procedures for identifying most of

the stability regimes found computationally. In particular, the application of marginal stability analysis has allowed us to reach new insight.

Figure 4.20 summarizes the various stability regimes uncovered, and correlates them with the form of effective disjoining pressure. The following regions are identified:

(**i**) Linearly unstable regime, $H_0 \in (H_-, H_+) \approx (1.5b, \beta)$, where b is the equilibrium thickness and β is the film thickness at which elastic force are relevant (see § 4.1.3 and § 4.1.4).

(**ii**) Linearly stable regime, $H_0 \notin (H_-, H_+)$.

(**iii**) Linearly unstable regime with negative disjoining pressure, $H_0 \in (H_-, H_{\Pi_{\text{eff}}})$, where $H_{\Pi_{\text{eff}}}$ is the thickness marking the sign change of Π_{eff} ($\Pi_{\text{eff}}(H_{\Pi_{\text{eff}}}) = 0$). If randomly perturbed, the film will dewet and form primary drops only (see § 4.2).

(**iv**) Linearly unstable regime with positive disjoining pressure, $H_0 \in (H_{\Pi_{\text{eff}}}, H_+)$. If randomly perturbed, the film will dewet and form primary and secondary drops.

(**v**) Absolutely stable regime, $H_0 < H^*_{m_1}$ or $H_0 > H^*_{m_3}$. The film is stable with respect to any perturbation (see § 4.3.2).

(**vi**) Metastable regime, $H_0 \in (H^*_{m_1}, H_-) \cup (H_+, H^*_{m_3})$. A linearly stable film is unstable with respect to finite size perturbations.

(**vii**) Spinodal regime, $H_0 \in (H_-, H_{n_1}) \cup (H_{n_2}, H_{n_3}) \subset (H_-,\ H_+)$. A linearly unstable film perturbed by either localized or random perturbations will result in the mean distance between drop centers, $\bar{D}_l$, as predicted by LSA, i.e. $\bar{D}_l \approx \lambda_m$ (see § 4.3.1).

(**viii**) Nucleation regime within linearly unstable regime, $H_0 \in (H_{n_1}, H_{n_2}) \cup (H_{n_3}, H_+) \subset (H_-,\ H_+)$. A linearly unstable film perturbed by a localized perturbation

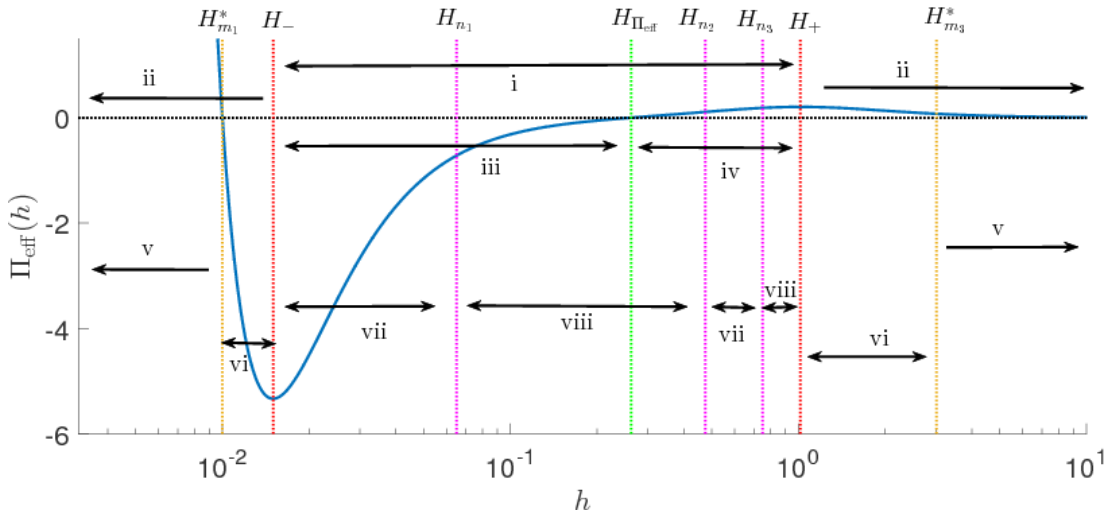

Figure 4.20 Summary of the various stability regimes discussed in this chapter in relation to the effective disjoining pressure. The dashed lines denote analytically derived values and dotted lines denote values extracted from numerical simulations. See the text for explanation of numbered regions.

will lead to $\bar{D} \not\approx \lambda_m$, and for a randomly perturbed film the variance in the distribution of inter-drop distances is significantly larger than for the spinodal regime, although we still find that $\bar{D} \approx \lambda_m$.

The regime often called 'heterogenous nucleation' includes the regimes (vi) and (viii); the 'spinodal' regime is defined under (vii).

There are several potential directions for future work. Statistical analysis has shown interesting connections between the observed phenomena and properties of the effective disjoining pressure; however, no clear physical mechanism has been identified analytically. Further investigation of the presented results is therefore required. Also, generalizing our results to three dimensional flows is another area of interest, and is the subject of the next chapter.

CHAPTER 5

GPU ADI METHOD FOR GENERAL THIN FILM EQUATIONS

In this chapter, we present a fast numerical method for the 2+1 dimensional generalized thin film equation using a Graphics Processing Unit (GPU) and the Compute Unified Device Architecture (CUDA) Application Programming Interface (API). Specifically, we implement the trapezoidal type Alternating Direction Implicit (ADI) scheme on a single GPU. With this implementation, large domain simulations can be carried out more than an order of magnitude faster than a similarly coded serial Central Processing Unit (CPU) method.

The method is applied to thin films evolving on a substrate, with particular focus on nematic thin films, although a very similar formulation applies also to polymer films spreading on silicon/silicon oxide substrates. What distinguishes different films, substrates and film thickness regimes, at least for slow flows where inertial effects are not significant, is essentially the form of (effective) disjoining pressure that, in addition to liquid/solid interaction, may include the effects of anchoring in the context of liquid crystals, interactions of electric or magnetic type in the context of ferrofluids [52], or composite substrates in the case of polymer films [4]. The influence of the functional form of such effective disjoining pressure on film stability was discussed in two spatial dimensions (2D) in Chapter 4. In that chapter, we presented numerical evidence for the formation of secondary (satellite) drops for positive values of the effective disjoining pressures, as well as discussed various regimes of instability development within linearly unstable as well as metastable regimes. In this chapter we focus on extending these results to 3D films.

The rest of this chapter is organized as follows. Section 5.1 provides the basic mathematical formulation of the problems that will be considered. The numerical methods are discussed in § 5.2, and the performance of the presented method in

§ 5.3. The aspects related to implementation on a GPU are relegated to Appendix A. An application specific to nematic liquid crystal (NLC) films is given in § 5.4, and comparison to experimental results for both NLC and polymer films in § 5.5. Conclusions are given in § 5.6.

5.1 Governing Equation

We consider the equations describing nonlinear diffusion of the following general form

$$u_t + \nabla \cdot \left[f_0(u) \nabla \nabla^2 u + f_1(u) \nabla u \right] = 0 \,, \tag{5.1}$$

where $u(x, y, t)$ is the evolving quantity of interest; $f_0(u)$ and $f_1(u)$ are some smooth nonlinear functions of u. The square bracketed term may be interpreted as the flux that governs the diffusion process. Governing equations of the form stated in (5.1) appear in a variety of models for thin fluid films, and also apply to other diffusive type physical processes such as those relevant to colloid-polymer suspensions [77].

5.1.1 Description of Model Problems

Equations of the form (5.1) commonly appear in the context of thin fluid films. In this context, the variable u describes the film thickness, h. For future reference, we specify here the governing equation for thin films in dimensional form (dimensional variables are hatted)

$$\mu \hat{h}_t + \hat{\nabla} \cdot \left[\hat{f}_0(\hat{h}) \hat{\nabla} \hat{\nabla}^2 h + \hat{f}_1(\hat{h}) \hat{\nabla} \hat{h} \right] = 0 \,, \tag{5.2}$$

where $\hat{h}(\hat{x}, \hat{y}, \hat{t})$ is film thickness and μ is the viscosity. To nondimensonalize (5.2), four scaling factors are defined: H, a representative film thickness scale, L, the lengthscale of variations in the plane of the film, $(\hat{x}, \hat{y})$; $\delta = H/L \ll 1$, the small aspect ratio; and T, the timescale of fluid flow. Scaling $(\hat{x}, \hat{y})$, $\hat{t}$ and $\hat{h}$ in the obvious way, (5.2)

becomes

$$h_t + \nabla \cdot \left[f_0(h) \nabla \nabla^2 u + f_1(h) \nabla h \right] = 0, \text{ where } f_0 = \frac{TF_0}{\mu L^4} \tilde{f}_0(h) \text{ and } f_1 = \frac{TF_1}{\mu L^2} \tilde{f}_1(h), \tag{5.3}$$

where F_0 and F_1 are some positive dimensional prefactors associated with $\hat{f}_0$ and $\hat{f}_1$, respectively, such that $\tilde{f}_0$ and $\tilde{f}_1$ are nondimensional and functions of the nondimensional variable h, for example, $\hat{f}_0(\hat{h}) = F_0 \tilde{f}_0(h)$. The prefactors of $\tilde{f}_0$ and $\tilde{f}_1$ in (5.3) are nondimensional; therefore, for simplicity, we absorb these prefactors into the definitions of the relevant functions.

5.1.2 Linear Stability Analysis (LSA)

We now present a brief overview of linear stability analysis (LSA) of a flat film of thickness H_0 in 2D (two dimensions), which will be used to validate our numerical code. To derive the dispersion relation, the solution is assumed to be of the form $h(x,t) = H_0(1 + \epsilon e^{iqx + i\omega t})$, where $\epsilon \ll 1$. Substituting this form of the solution into (5.1) yields

$$\omega = i \left[f_1(H_0) q^2 - f_2(H_0) \right] q^2 \, . \tag{5.4}$$

A film of thickness H_0 is linearly unstable if $f_2(H_0) > 0$, and in the unstable flat film thickness regime, the critical wavenumber (below which films are unstable), the most unstable mode, and the maximum growth rate are given by

$$q_c = \sqrt{\frac{f_2(H_0)}{f_1(H_0)}} \, , \quad q_m = \sqrt{\frac{f_2(H_0)}{2 f_1(H_0)}} \quad \text{and} \quad \omega_m = \frac{[f_1(H_0)]^2}{4 f_1(H_0)} \, , \tag{5.5}$$

respectively.

5.1.3 Thin Film Models

We consider in this chapter three different models i.e. different sets of $f_0(h)$ and $f_1(h)$ in (5.3). The first model considered is a test case of a simple linear partial differential

equation, i.e,

$$f_0(h) = c_0 \quad \text{and} \quad f_1(h) = c_1 \ , \tag{5.6}$$

where the sign of f_1 is chosen so that a flat film is linearly unstable. For the remaining two models, we assume f_0 and f_1 are of the form

$$f_0(h) = \mathcal{C}h^3 \quad \text{and} \quad f_1(h) = \frac{h^3\Pi'(h)}{\mathcal{C}} \ , \tag{5.7}$$

where $\mathcal{C}$ is the inverse Capillary number (ratio of surface tension forces to viscous force) and $\Pi(h)$ is the disjoining pressure, typically describing the strength of fluid/solid interaction. In our second model, the disjoining pressure will be actually specified as an 'effective' disjoining pressure derived in the context of nematic films [12, 26]. Therefore, for the second model, $\Pi(h) = \Pi_{\rm NLC}(h)$, with

$$\Pi_{\rm NLC}(h) = \mathcal{K}\left[\left(\frac{b}{h}\right)^3 - \left(\frac{b}{h}\right)^2\right] + \frac{\mathcal{N}}{2}\left[\frac{m(h)}{h}\right]^2 \ , \tag{5.8}$$

where

$$m(h) = g(h)\frac{h^2}{h^2+\beta^2} \ ; \quad g(h) = \frac{1}{2}\left[1 + \tanh\left(\frac{h-2b}{w}\right)\right] \ ; \tag{5.9}$$

the scales are taken as

$$H = 100 \text{ nm} \ , \quad L = 10 \ \mu\text{m} \ , \quad T = 1 \text{ s} \ ; \tag{5.10}$$

and the nondimensional parameters are

$$\mathcal{C} = 0.0857 \ , \quad \mathcal{K} = 36.0 \ , \quad \mathcal{N} = 1.67 \ , \quad \beta = 1 \ , \quad w = 0.05 \ , \quad b = 0.01 \ . \tag{5.11}$$

For brevity, we leave the discussion of the details of this model to § 5.4, where we focus on extending previous results from 2D to 3D films. However, for now, we note that the term in the disjoining pressure defined in (5.8) with a prefactor $\mathcal{K}$ is the power-law form of disjoining pressure consisting of Born repulsion and the van der

Waals force. The power-law form of the disjoining pressure is commonly used in the literature; see e.g., the review by Craster and Matar (2009) [59] for detailed discussion. The term with a prefactor $\mathcal{N}$ is due to the elastic response of NLC, further discussed in § 5.4.

The third model describes polymeric films [4], where $\Pi(h) = \Pi_{\mathrm{POL}}(h)$, with

$$\Pi_{\mathrm{POL}}(h) = -\frac{\partial \psi_{\mathrm{POL}}}{\partial h} , \quad \text{where} \quad \psi_{\mathrm{POL}}(h) = \frac{C}{h^8} - \frac{A_{\mathrm{SiOx}}}{12\pi h^2} + \frac{A_{\mathrm{SiOx}} - A_{\mathrm{Si}}}{12\pi (h+d)^2} \tag{5.12}$$

and the coefficients are given by

$$\mathcal{C} = 0.00581 , \quad C = 1.181 , \quad A_{\mathrm{SiOx}} = 41.25 , \quad A_{\mathrm{Si}} = -243.75 , \quad d = 191 , \tag{5.13}$$

with the scalings

$$H = 1 \text{ nm} , \quad L = 100 \text{ nm} , \quad T = 60 \text{ s} , \tag{5.14}$$

(here the physical parameters are taken from Seemann *et al.* [53]). The first term in (5.12) is due to steric effects (non-bonding intermolecular interactions), and the last two terms are van der Waals forces in a thin film of a polymer deposited on a silicon substrate (Si), coated in a silicon oxide (SiOx) layer of thickness d. Note that the notation for chemicals follows Seemann *et al.* [53].

5.2 Numerical Method

The numerical approach that we employ is based on the Alternate Direction Implicit method, discussed in the context of thin film flows by Witelski and Bowen (2003) [44] and implemented in recent works, such as [11, 12]. In the present chapter we provide a review of the method, both for completeness, and for the purpose of discussing particular issues involving implementation in a GPU computing environment. More precisely, in § 5.2.1 we discuss a finite volume scheme in terms of fluxes, temporal

discretization is described in § 5.2.2, discretization of fluxes in § 5.2.3, and boundary conditions are discussed in § 5.2.4.

5.2.1 Conservation Law

In terms of a conservation law, the governing equation may be expressed as

$$u_t + \nabla \cdot \mathbf{F}(u) = 0 \ , \quad \text{where} \quad \mathbf{F}(u) = f_0(u)\nabla\nabla^2 u + f_1(u)\nabla u \tag{5.15}$$

is the flux vector, with two components, i.e., $\mathbf{F}(u) = \{F_x(u), F_y(u)\}$. To simplify the results, we generalize the flux to linear combinations of terms of the form

$$\mathbf{F}(u) = f(u)\mathbf{L}[u] \tag{5.16}$$

where $f(u)$ is some smooth function of u and $\mathbf{L}$ is some linear differential operator with two components, i.e., $\mathbf{L}[u] = \{L_x[u], L_y[u]\}$. The results to be shown can be easily extended to the flux in our original governing equation (5.15).

Following the finite volume method, the governing equation for $\bar{u}$, the average value of u on some sub-domain Ω, is given by

$$\bar{u}_t = -\frac{1}{A} \oint_{\partial\Omega} \mathbf{F}(u) \cdot \mathbf{n} \, ds \ , \tag{5.17}$$

where A is the area of the sub-domain Ω, $\partial\Omega$ denotes its boundary, and $\mathbf{n}$ is the outward-pointing normal. To subdivide the entire domain, the solution is discretized on an equipartitioned grid; specifically, the grid points in the x and y directions are defined as

$$\begin{aligned} x_i &= X_0 + i\Delta s \quad 0 \le i \le I \quad \text{and} \\ y_j &= Y_0 + j\Delta s \quad 0 \le j \le J \ , \end{aligned} \tag{5.18}$$

where Δs is the grid spacing; $I+1$ and $J+1$ are the numbers of points in x and y domains, respectively; and X_0 and Y_0 are the initial points in x and y, respectively.

Furthermore, the cell average points are given by

$$\bar{u}_{(i,j)} = \frac{1}{A} \oint_{\Omega_{(i,j)}} u(x,y)\, dA, \text{ where } \Omega_{(i,j)} = [x_i, x_{i+1}] \times [y_j, y_{j+1}] \text{ and } A_{(i,j)} = \Delta s^2, \tag{5.19}$$

for $0 \leq i < I$ and $0 \leq j < J$; and their respective governing equations are

$$\begin{aligned} \bar{u}_{t,(i,j)} = -\frac{1}{\Delta s^2} \Bigg[& \int_{x_i}^{x_{i+1}} F_{y,(,j)}\, dx + \int_{y_{j+1}}^{y_j} F_{x,(i+1,)}\, dy \\ & - \int_{x_{j+1}}^{x_j} F_{y,(,j+1)}\, dx - \int_{y_j}^{y_{j+1}} F_{x,(i,)}\, dy \Bigg] , \end{aligned} \tag{5.20}$$

where

$$F_{x,(i,j)} = F_x(u(x_i, y_j)) , \quad F_{x,(,j)} = F_x(u(x, y_j)) , \quad F_{x,(i,)} = F_x(u(x_i, y)) , \tag{5.21}$$

and similar notation is used for F_y and $\bar{u}_t$. To solve (5.20), two second-order accurate approximations are implemented: 1) the integrals on the right-hand side of (5.20) are evaluated using the midpoint rule, e.g.,

$$\int_{x_i}^{x_{i+1}} F_{y,(,j)}\, dx = \Delta s \left[F_{y,(i+\frac{1}{2},j)} + O(\Delta s^2) \right] , \tag{5.22}$$

where

$$\begin{aligned} x_{i+\frac{1}{2}} &= X_0 + \left(\frac{1}{2} + i \right) \Delta s \quad 0 \leq i < I , \quad \text{and} \\ y_{j+\frac{1}{2}} &= Y_0 + \left(\frac{1}{2} + j \right) \Delta s \quad 0 \leq j < J , \end{aligned} \tag{5.23}$$

are the center points of the grid; and 2) the cell averaged value are approximated by the cell-centered value, i.e.,

$$\bar{u}_{(i,j)} = u_{(i+\frac{1}{2},j+\frac{1}{2})} + O(\Delta s^2) = u(x_{i+\frac{1}{2}}, y_{j+\frac{1}{2}}) + O(\Delta s^2) . \tag{5.24}$$

Substituting (5.22) and (5.24) into (5.20) yields

$$u_{t,(i+\frac{1}{2},j+\frac{1}{2})} = -\frac{1}{\Delta s} \left[F_{x,(i+1,j+\frac{1}{2})} - F_{x,(i,j+\frac{1}{2})} + F_{y,(i+\frac{1}{2},j+1)} - F_{y,(i+\frac{1}{2},j)} \right] + O(\Delta s^2) . \tag{5.25}$$

5.2.2 Temporal Discretization

Let us write (5.25) in the following general form

$$\mathbf{u}_t = -\mathbf{D}\mathbf{u} \,, \tag{5.26}$$

where $\mathbf{D}$ is a nonlinear matrix differential operator, representing the fluxes on the right-hand side of (5.25); and $\mathbf{u} = \{u_p\}$ is the collection of grid point values $u_{(i,j)}$. The grid points in $\mathbf{u}$ are ordered lexicographically and may be in row-major form, $p = Ji + j$; or column-major form, $p = Ij + i$. Note that bold notation will be used to denote vectors associated with cell centered quantities on the spatial grid.

To begin, a central difference discretization in time is applied to (5.26),

$$\mathbf{u}^{n+1} - \mathbf{u}^n = -\Delta t \mathbf{D}\mathbf{u}^{n+1/2} \tag{5.27}$$

where Δt is the time step, and n superscripts denote the value at the current time. Using a trapezoidal rule to evaluate the non-linear term at the half step, $\mathbf{D}\mathbf{u}^{n+1/2} = \left[\mathbf{D}\mathbf{u}^{n+1} + \mathbf{D}\mathbf{u}^n\right]/2 + O(\Delta t^2)$, (5.27) may be expressed as

$$\left(\mathbf{I} + \frac{\Delta t}{2}\mathbf{D}\right)\mathbf{u}^{n+1} = \left(\mathbf{I} - \frac{\Delta t}{2}\mathbf{D}\right)\mathbf{u}^n \,, \tag{5.28}$$

where $\mathbf{I}$ is the identity matrix. Equation (5.28) contains a nonlinear implicit term, i.e., nonlinear dependence on the unknown $\mathbf{u}^{n+1}$; therefore the above equation is solved numerically using a Newton iterative scheme.

Newton Iterative Scheme We rewrite (5.28) as a root solving problem; specifically, we define

$$\mathbf{G}(\mathbf{u}^{n+1}) = \left[\left(\mathbf{I} + \frac{\Delta t}{2}\mathbf{D}\right)\mathbf{u}^{n+1} - \left(\mathbf{I} - \frac{\Delta t}{2}\mathbf{D}\right)\mathbf{u}^n\right] = 0 \,, \tag{5.29}$$

and find $\mathbf{u}^{n+1}$ satisfying this equation using Newton's iterative scheme. First, we compute the Jacobian of G with respect to $\mathbf{u}^{n+1}$, yielding

$$\mathbf{J_G} = \mathbf{I} + \frac{\Delta t}{2}\mathbf{J_D} \ , \tag{5.30}$$

where $\mathbf{J_D}$ is the Jacobian of $\mathbf{D}\mathbf{u}^{n+1}$. The Newton iterative scheme may be expressed as

$$\begin{aligned} \mathbf{J}_{\mathbf{G},(k)}\mathbf{w} = \left(\mathbf{I} + \frac{\Delta t}{2}\mathbf{J_D}\right)\mathbf{w} &= -\mathbf{G}(\mathbf{u}^{n+1}_{(k)}) \\ \mathbf{u}^{n+1}_{(k+1)} &= \mathbf{u}^{n+1}_{(k)} + \mathbf{w} \ , \end{aligned} \tag{5.31}$$

where $\mathbf{u}_{(k)}$ corresponds to the values at the current iterative step, $\mathbf{w}$ is an intermediate variable, and the (k) subscript in $\mathbf{J}_{\mathbf{G},(k)}$ indicates that the nonlinear $\mathbf{u}^{n+1}$ terms in $\mathbf{J}_{\mathbf{G},(k)}$ are evaluated using $\mathbf{u}^{n+1}_{(k)}$. The iterative scheme is initialized by setting $\mathbf{u}^{n+1}_{(0)} = \mathbf{u}^n$. To reduce computational complexity, we apply an Alternating Direction Implicit (ADI) type scheme, discussed next.

Alternating Direction Implicit (ADI) Method The ADI method splits the implicit differential operator (5.30) in two parts (implicit x derivatives for a fixed y and vice versa). Specifically, the right-hand side of (5.30) may be expressed as

$$\mathbf{I} + \frac{\Delta t}{2}\mathbf{J_D} = \left(\mathbf{I} + \frac{\Delta t}{2}\mathbf{J}_y\right)\left(\mathbf{I} + \frac{\Delta t}{2}\mathbf{J}_x\right) + \frac{\Delta t}{2}\mathbf{J}_{xy} - \frac{\Delta t^2}{4}\mathbf{J}_x\mathbf{J}_y \ , \tag{5.32}$$

where $\mathbf{J}_x$ and $\mathbf{J}_y$ are the pure x and y derivative terms in $\mathbf{J_D}$, respectively; and $\mathbf{J}_{xy}$ are the remaining mixed derivative terms, i.e. $\mathbf{J}_{xy} = \mathbf{J_D} - \mathbf{J}_x - \mathbf{J}_y$.

Neglecting the implicit mixed derivatives, $\mathbf{J}_{xy}$, we may substitute (5.32) into (5.31) reducing the method to first-order accuracy; however, as noted and confirmed numerically by Witelski and Bowen [44], implementing an appropriate iterative method, the ADI scheme will converge to second order accuracy in time. We will also show second order convergence for our implementation. The Newton iterative scheme

in (5.31) becomes

$$\left(\mathbf{I}+\frac{\Delta t}{2}\mathbf{J}_{y,(k)}\right)\mathbf{w} = -\left[\left(\mathbf{I}+\frac{\Delta t}{2}\mathbf{D}\right)\mathbf{u}_{(k)}^{n+1}-\left(\mathbf{I}-\frac{\Delta t}{2}\mathbf{D}\right)\mathbf{u}^{n}\right], \quad (5.33)$$

$$\left(\mathbf{I}+\frac{\Delta t}{2}\mathbf{J}_{x,(k)}\right)\mathbf{v} = \mathbf{w}, \quad (5.34)$$

$$\mathbf{u}_{(k+1)}^{n+1} = \mathbf{u}_{(k)}^{n+1}+\mathbf{v}, \quad (5.35)$$

where $\mathbf{w}$ and $\mathbf{v}$ are intermediate variables. This pseudo-Newton iterative method reduces (by an approximation) the left hand side of (5.32) from a large sparse matrix of size $IJ \times IJ$ into two block diagonal matrices (right hand side of (5.32)). In the implicit y step, using column-major ordering, we form a block diagonal matrix, $\mathbf{J}_y$, with I blocks of size $J \times J$. Each block can be inverted independently of others, thus reducing the computational complexity. Furthermore, each block is a n-diagonal matrix, where the width of the diagonal band, n, depends on the stencil used to evaluate spatial derivatives. For our implementation, $n = 5$ (penta-diagonal system). The n-diagonal matrices can be inverted with linear complexity, further reducing computational cost, e.g., using an extension of the Thomas algorithm for an n-diagonal matrix. Similarly, in the implicit x step, using row-major ordering, we form a block diagonal matrix, $\mathbf{J}_x$, with J blocks of size $I \times I$.

Adaptive Time Stepping To control the time step, we first specify the convergence conditions. Specifically, the solution at the next time step is accepted (i.e. $\mathbf{u}^{n+1} = \mathbf{u}_{(k+1)}^{n+1}$) if

$$\max_{0\le i<I, 0\le j<J}\left|\frac{v_{(i+\frac{1}{2},i+\frac{1}{2})}}{u_{(k),(i+\frac{1}{2},i+\frac{1}{2})}}\right| < \epsilon_{\text{Tol}} \quad (5.36)$$

where ϵ_{Tol} is the error tolerance. In addition, if the error tolerance is not satisfied in a specified maximum number of iterative steps, the scheme is assumed to have failed.

Note 1: Our simulations show that setting the maximum number of iterative steps, K, to 10 gives the largest effective time steps, i.e., $\Delta t/K$ is maximized.

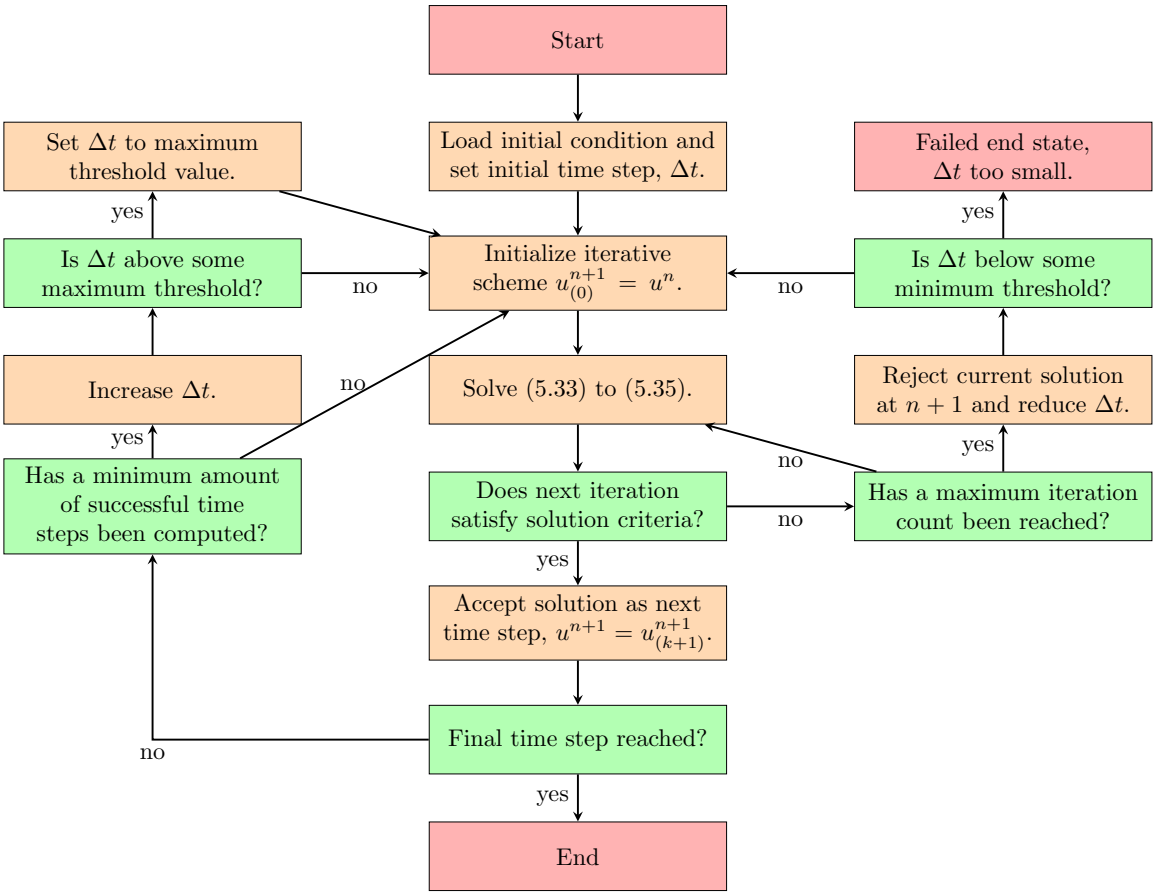

Figure 5.1 Flow chart of the adaptive time stepping with a nested pseudo-Newton iterative scheme. Note that rectangles marked in red correspond to the start of ends of the flow chart, orange designates processes, and green denotes decisions.

Note 2: Other restrictions besides the convergence of the iterative scheme may be placed on accepting the solution at the next iteration or next time step, e.g., sufficiently small truncation error, thus for generality, we will refer to the collection of such conditions as the *solution criteria*.

If the solution criteria are not met, then the time-step is reduced and the pseudo-Newton iterative scheme is performed with the new reduced time step. Furthermore, if the new reduced time step is below some minimum, the numerical scheme halts and ends in a failed state. To improve the efficiency of the numerical scheme, the time step is increased if a minimum number of successful time steps have been consecutively computed. To remove possible numerical errors, the time step is bounded from above. Figure 5.1 shows a flow chart of the adaptive time stepping procedure, coupled with the pseudo-Newton iterative method.

5.2.3 Flux Discretization

To summarize the results so far, a second-order accurate scheme has been developed in terms of a non-linear spatial differential operator $\mathbf{D}$, representing the fluxes across cell boundaries; therefore, to complete the scheme, in this section, the form of $\mathbf{D}$ is described. Recalling (5.25), we may split $\mathbf{D}$ into two parts: the fluxes across the x cell boundaries $\mathbf{D}_x$, and the fluxes across the y cell boundaries $\mathbf{D}_y$. The values of $\mathbf{D}$ are specified in terms of fluxes, i.e.,

$$\mathbf{D}_s = \frac{\mathbf{F}_{s,+} - \mathbf{F}_{s,-}}{\Delta s} \,, \tag{5.37}$$

where $\mathbf{D}_s$ is either $\mathbf{D}_x$ or $\mathbf{D}_y$, and $\mathbf{F}_{s,+}$ and $\mathbf{F}_{s,-}$ are non-linear matrix differential operators for the fluxes at the two boundaries. Similarly to § 5.2.1, the fluxes are generalized to a linear combination of functions of the form

$$\mathbf{F} = f(u)\mathbf{L} \,, \tag{5.38}$$

where $f(u)$ is a function of u, and $\mathbf{L}$ is a linear differential operator. We may express $\mathbf{D}$ as

$$\mathbf{D} = \frac{\mathbf{F}_{x,+} - \mathbf{F}_{x,-} + \mathbf{F}_{y,+} - \mathbf{F}_{y,-}}{\Delta s} \ . \tag{5.39}$$

To derive an expression for $\mathbf{J}_x$ and $\mathbf{J}_y$ in (5.33) and (5.34), we recall that mixed derivative terms have been ignored, and therefore,

$$\mathbf{J}_x = \frac{\partial}{\partial \mathbf{u}} \left[\frac{\mathbf{F}_{x,+} - \mathbf{F}_{x,-}}{\Delta s} \right] \quad \text{and} \quad \mathbf{J}_y = \frac{\partial}{\partial \mathbf{u}} \left[\frac{\mathbf{F}_{y,+} - \mathbf{F}_{y,-}}{\Delta s} \right] \ , \tag{5.40}$$

where $\partial / \partial \mathbf{u}$ denotes the Jacobian, and the non-linear matrix differential operator, $\mathbf{F}$, only contains derivatives with respect to its subscript.

To complete the derivation, expressions for $\mathbf{F}_{x,+}$, $\mathbf{F}_{x,-}$, $\mathbf{F}_{y,+}$, and $\mathbf{F}_{y,-}$ are required. For brevity, we specify these expressions by the following descriptions:

1. at the cell-centered point (i, j),
   - $\mathbf{F}_{x,+}$ is evaluated at $(x_{i+1}, y_{j+\frac{1}{2}})$,
   - $\mathbf{F}_{x,-}$ is evaluated at $(x_i, y_{j+\frac{1}{2}})$,
   - $\mathbf{F}_{y,+}$ is evaluated at $(x_{i+\frac{1}{2}}, y_{j+1})$, and
   - $\mathbf{F}_{y,-}$ is evaluated at $(x_{i+\frac{1}{2}}, y_j)$;
2. the linear matrix differential operator $\mathbf{L}$ is computed using cell-centered values;
3. $f(u)$ at a cell boundary is evaluated using interpolation, e.g.,

$$f(u_{(i+\frac{1}{2},j)}) = \frac{f(u_{(i+\frac{1}{2},j+\frac{1}{2})}) + f(u_{(i+\frac{1}{2},j-\frac{1}{2})})}{2} + O(\Delta s^2) \ ; \tag{5.41}$$

4. the total combined stencil of all terms is shown in Figure 5.2.

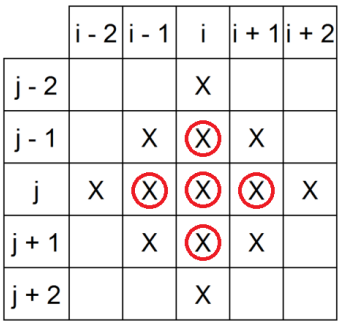

Figure 5.2 X and ◯ denote the solution cell-center values $u_{(i,j)}$ and the function cell-center values, $f_{i,j}$, respectively. These values are required to numerically evaluate the flux differences (5.37) at the cell-center (i, j).

5.2.4 Boundary Conditions

To complete the description of the numerical methods, we now discuss the boundary conditions. Typically, boundary conditions of the form

$$\begin{aligned} u_x(x_0, y) = u_{xxx}(x_0, y) = 0 \ , \qquad u_x(x_I, y) = u_{xxx}(x_I, y) = 0 \ , \\ u_y(x, y_0) = u_{yyy}(x, y_0) = 0 \ , \qquad u_y(x, y_J) = u_{yyy}(x, y_J) = 0 \ , \end{aligned} \tag{5.42}$$

are used, and may be interpreted as symmetry conditions. Furthermore, the boundary conditions correspond to zero flux at the boundary, recall (5.15).

To implement the boundary conditions, the stencil shown in Figure 5.2 includes ghost points at the boundaries. While ghost points may be used for explicit terms, $u_{(k)}^{n+1}$ and u^n, for the implicit term, $u_{(k+1)}^{n+1}$, the finite difference stencil must be modified; however, since implicit terms are derivatives of a single variable, the stencil modification is relatively simple.

Using the boundary conditions to define the ghost points, the left-hand sides of the numerical scheme (5.33) and (5.34) are computable everywhere except at the corners of the domain, e.g., at the cell-center point $i = j = 0$. There are two choices to compute the ghost points in the corner (x_i, y_j for $i, j = -2, -1$): First, the y boundary conditions are applied, computing the solution at the ghost points (x_i, y_j) for $i = 0, 1$ and $j = -2, -1$, then the x boundary conditions are applied at the new

ghost points, computing the solution at the corner ghost points. Alternatively, the order of operations may be reversed. It is relatively easy to show that both procedures lead to identical results.

5.3 Numerical Performance

We now switch focus to the numerical performance and accuracy of our implementation. The details related to implementation in the GPU computing environment are discussed in Appendix A. Here, we discuss first convergence, followed by confirmation of conservative properties, and the comparison with LSA. Then, we discuss the performance by comparing the GPU and serial CPU codes.

For the purpose of the numerical tests discussed in this section, we choose an initial condition of the form

$$u(x, y, t = 0) = H_0 \left(1 + \left[\epsilon_x \cos\left(\frac{\pi x}{\lambda}\right) + \epsilon_y \cos\left(\frac{\pi y}{\lambda}\right)\right]\right) \ , \tag{5.43}$$

where $\epsilon_x = \epsilon_y = 0.1$, $(x, y) \in [0, P\lambda] \times [0, P\lambda]$, $\lambda = 2\pi/q$, and q is the wave number. The initial film thickness, H_0, is fixed at 1 for the linear model (for simplicity), 0.5 for the NLC model, and 3.9 for the polymer model. For the last two models, the values are motivated by the experiments [2, 4].

5.3.1 Validation

To test the convergence properties, the adaptive time stepping is removed and we set the maximum number of Newton iterative steps to 5000 (allowing for a more robust selection of spatial step size). In addition, we chose $q = q_m$ and $P = 6$ in (5.43) where q_m is given by (5.5). The spatial step size, $\Delta s = P\lambda_m/I$, where $\lambda_m = 2\pi/q_m$ is the most unstable wavelength, I is the number of grid points, and simulations are carried out on a square computational domain, $I = J$; therefore, choosing I (discussed in the next sections) determines Δs. Note that the choice $P = 6$ is made so as to

maximize the range of grid sizes that fit into the GPU's memory and maintain a sufficiently large spatial step size to maximize the (common) stable time step. For the comparison with LSA, adaptive time stepping is utilized, the maximum number of Newton iterative steps is reverted back to 10, we set $P = 1$, and vary q according to the dispersion curve from LSA.

Convergence To study the convergence properties, we first define I_0, the initial spatial grid size, i.e., $I = I_0$, and Δt_0, the initial time step size. In addition, since obtaining an analytical solution for the non-linear models is not possible, we compute the error relative to the numerical solution obtained for the most refined grid.

For the purpose of checking temporal convergence, we fix $I_0 = 256$ for all simulations, and set $\Delta t_0 = 10^{-3}\omega_m^{-1}$, i.e., we scale the time step with the growth rate of the most unstable mode. The initial simulation is carried out for one time step, Δt_0, and for each subsequent simulation, the time step is halved, and the simulation is carried out to the final time, Δt_0. Figure 5.3a shows the L_2 norm of the error for all three considered problems for two implementations: i) the Newton iterative convergence error tolerance, ϵ_{Tol} in (5.36), is set close to machine precision (solid curves), $\epsilon_{\text{Tol}} = 10^{-14}$; and ii) the error tolerance is set to scale with the temporal error (dashed curves), $\epsilon_{\text{Tol}} = \max(\Delta t^2, 10^{-14})$. Note that we limit $\epsilon_{\text{Tol}} \geq 10^{-14}$ since if the relative error in the Newton iterative scheme is smaller than machine error, the iterative method will always fail. We observe that in the first case, second-order temporal accuracy is achieved (compare to the dotted black line). Note that for the linear model, the two curves lie on top of each other, as expected. Furthermore, the results show that it is sufficient to set the Newton error tolerance to be proportional to the temporal accuracy to maintain second-order accuracy, and even higher order convergence is achieved for the nonlinear models, although the error is larger.

To confirm the spatial convergence, we fix $\Delta t_0 = 10^{-8}\omega_m^{-1}$ for all simulations and set the coarsest grid size $I_0 = 36$. Recalling § 5.2.1, the numerical solution is

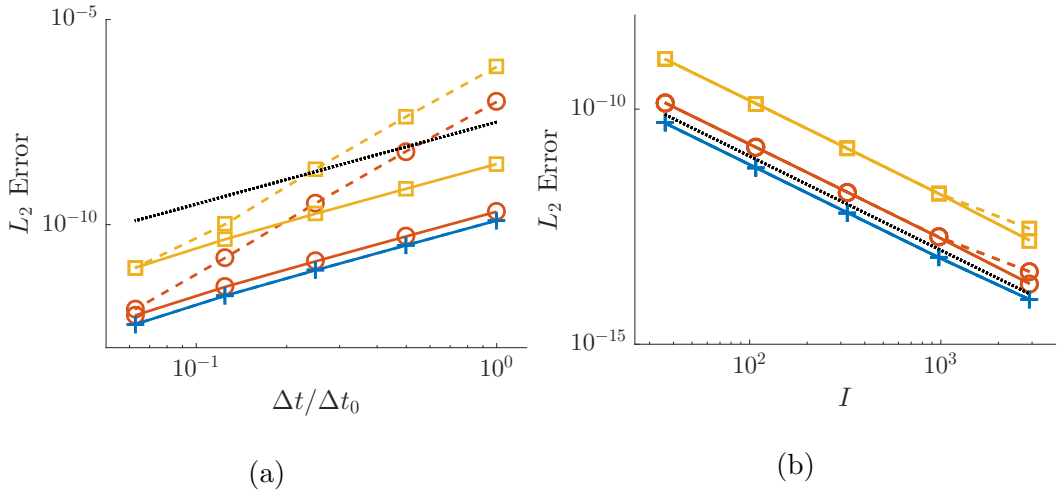

Figure 5.3 Plot of the L_2 norm of the error as a function of (a) time step size and (b) grid size for: the linear model (blue curves with '+' symbols), the NLC model (red curves with '$\circ$' symbols), and the polymer model (yellow curves with '$\square$' symbols). Solid curves denote simulations where Newton iterative convergence error tolerance is close to machine precision, $\epsilon_{\text{Tol}} = 10^{-14}$; and dashed curves denote simulations with error tolerances set to (a) $\epsilon_{\text{Tol}} = \max(\Delta s^2, 10^{-14})$ and (b) $\epsilon_{\text{Tol}} = \max(\Delta t^2, 10^{-14})$. The dotted black line denotes second order convergence. Note that in both figures for the linear model the two curves (solid and dashed) lie on top of each other, as expected.

evaluated at the cell-centers of the spatial grid; therefore, if the spatial step size is halved, the cell-centered points on the refined grid are not contained in the coarse grid. To avoid errors associated with interpolating the numerical solutions on different grid sizes to a common grid size, we instead triple the grid size (e.g., $I_k = 3^k I_0$, where k is the level of refinement) so that cell-centered points on the coarser grid are contained in the refined grid. Figure 5.3b confirms second-order spatial accuracy. Furthermore, we observe that there is little difference between setting the Newton error tolerance to $\epsilon_{\text{Tol}} = \max(\Delta s^2, 10^{-14})$ or close to machine precision, $\epsilon_{\text{Tol}} = 10^{-14}$.

To summarize, the results show that the implemented method is second-order accurate in time and space, and furthermore, that it is sufficient to set the error tolerance to scale with the order of the spatial and temporal accuracy. Such implementation significantly reduces computational time.

Conservation of Mass To verify conservation of mass, we carry out the simulations until the final time, $1000\Delta t_0$, and collect data in intervals of $100\Delta t_0$. Furthermore, motivated by the results of § 5.3.1, we fix $\epsilon_{\text{Tol}} = \max(\Delta s^2, 10^{-14})$ for spatial convergence simulations, and $\epsilon_{\text{Tol}} = \max(\Delta t^2, 10^{-14})$ for temporal convergence simulations. To compute the average mass of the solution, recall that the cell average is given by the cell-centered value (with second order accuracy), therefore, the average mass on the entire domain is given by

$$\bar{U} = \frac{1}{IJ} \sum_{i=0}^{I-1} \sum_{j=0}^{J-1} u_{(i+\frac{1}{2}, j+\frac{1}{2})} \, . \tag{5.44}$$

Figure 5.4 shows the change (relative to the initial condition) in total mass for the linear model (left column), NLC model (central column) and polymer model (right column), for fixed time step and varied spatial step (top row), and fixed spatial step and varied time step (bottom row). The results obtained when spatial step size is varied (top row) show that there is no trend in the mass error (i.e, numerical noise) with the exception of the smallest step size for the NLC model, indicated by the arrow in subpanel b; and the polymer model, subpanel c. It is interesting to note that the conservation law formulation of the governing equation in terms of fluxes, recall equation (5.25) in § 5.2.1, indicates that conservation of mass should be second order accurate in space. However, while the approximations of the fluxes are second-order accurate, cancellation of these errors across a cell boundary leads to higher order accuracy.

When time step is varied, and the spatial step fixed, the bottom row of Figure 5.4 shows that conservation of mass is at least second order accurate. For the linear model, subpanel d, the error is close to machine precision, so no trend is observed.

Comparison to LSA Here, we validate our model by showing agreement with LSA. This is done by comparing the growthrates extracted from simulations to the

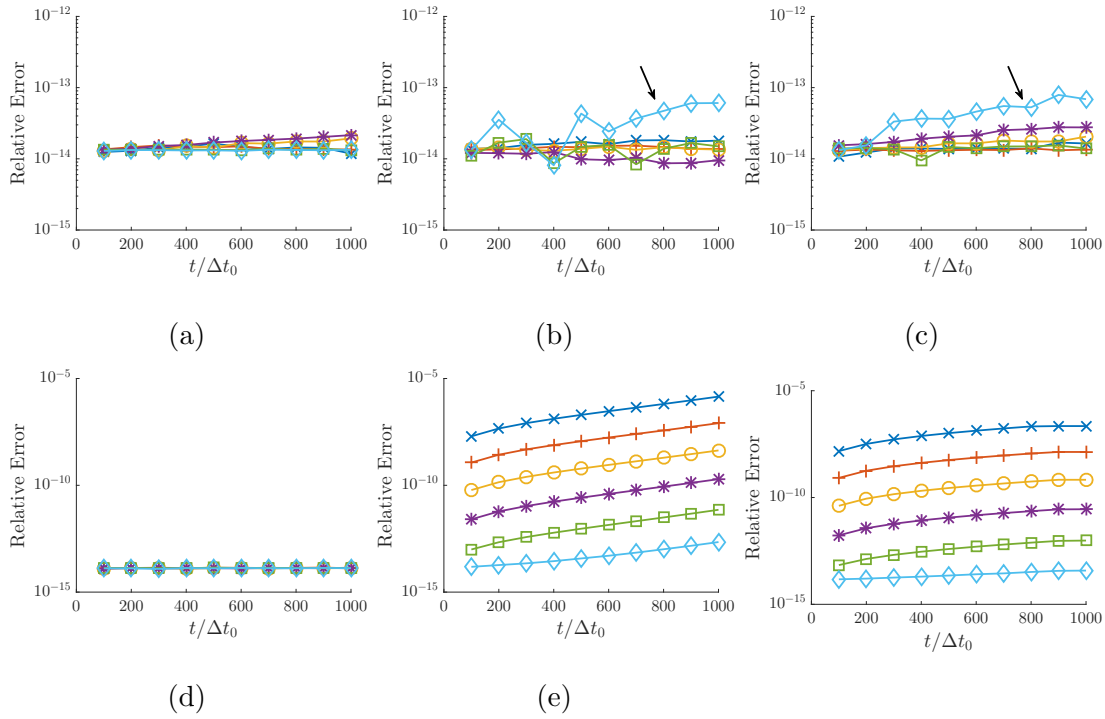

Figure 5.4 Plot of the relative mass error as a function of time for the linear model (left column), the NLC model (central column), and the polymer model (right column) for decreasing spatial step size (top row) and decreasing time step (bottom row). Spatial steps sizes and time steps sizes are the same as Figure 5.3 and '$\times$', '$+$', '$\circ$', '$*$', '$\square$', and '$\diamond$' symbols denote progressively decreasing spatial step sizes. decreasing step size, respectively. Arrows in subpanels b and e denote simulations where a trend may exist for the relative mass error. Note that for the top row of figures $\Delta t = \Delta t_0 = 10^{-8}\omega_m^{-1}$ and for the bottom row of figures $\Delta t = 2^{-i}\Delta t_0$ where $\Delta t_0 = 10^{-3}\omega_m^{-1}$ and $i = 0, 1, 2, 3, 4, 5$ is the refinement depth (decreasing step size).

dispersion relation (5.4). For each model, simulations are carried out for several q values for perturbations in either the x or y directions. In addition, the linear domain is fixed to λ_m, i.e. $P = 1$ in (5.43) with 32 points ($I = J = 32$). The final solution time is fixed at $T = \log(1.3)|\omega(q)]^{-1}|$, where $\omega(q)$ is defined in (5.4). Figure 5.5 confirms that the numerical results agree with the LSA predictions, validating the code.

5.3.2 Performance Comparison

Having validated the accuracy, convergence, and mass conservation of our numerical method, here we discuss the computational performance of our GPU implementation

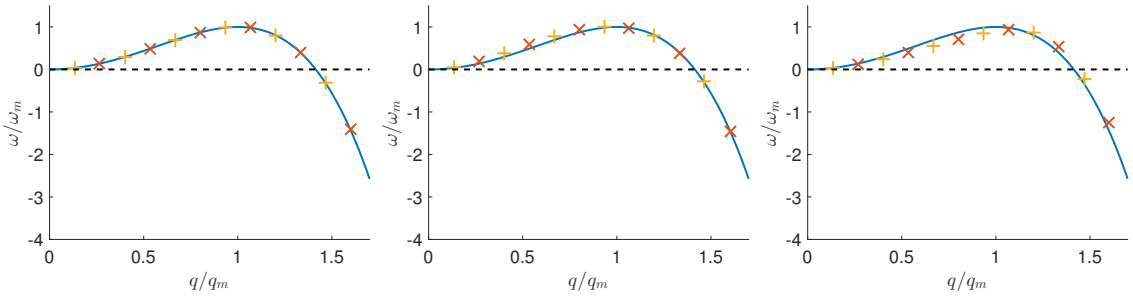

(a) $q_m = 1/\sqrt{2},\ \omega_m = 1/4$ (b) $q_m \approx 1.5,\ \omega_m \approx 0.052$ (c) $q_m \approx 1.6,\ \omega_m \approx 2.04$

Figure 5.5 Comparison between dispersion relations (blue curve) and growth rates extracted from numerical simulations (symbols) for a) the linear model, b) the NLC model, and c) the polymer model. '×' symbols (red) denote initial condition perturbed in the x direction and '+' symbols (gold) denote a perturbation in the y direction.

(details are given in Appendix A) in comparison to our serial CPU code. We note that CPU computations were performed on an Intel© Core™ i7-6700K and GPU computations were performed on a Nvidia Geforce© GTX Titan X Maxwell. For brevity, the performance results are computed only for the NLC model. For simplicity we compare two major components: inverting the penta-diagonal matrices in (5.33) and (5.34); and computing the entries of the matrices in (5.33). These particular components were chosen since they are responsible for the dominant part of the computational cost.

We begin by comparing the GPU penta-diagonal solver to the in-house serial CPU penta-diagonal solver. The serial CPU implementation is based on a method found in Numerical Recipes in FORTRAN [78]. Figure 5.6 shows that for the smallest domain size, the GPU performs about the same as the CPU code; however, for larger domains, the speedup reaches a factor of 40. The saturation of the speed up occurs when the total number of independent linear systems is greater than the total core count (3072 for the GPU used in the reported computations).

Next, we compare the second major component of the solvers, computing the entries of the matrices in (5.33) and (5.34). Since no equivalent in-house serial CPU implementation exists for computing these terms, for simplicity we only implement an

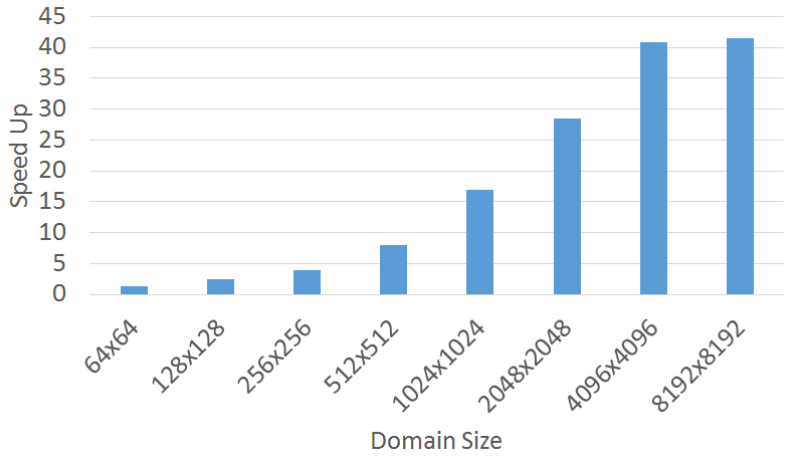

Figure 5.6 Plot of relative speedup to solve penta-diagonal system in the GPU code over the original in-house CPU code for various square domains sizes.

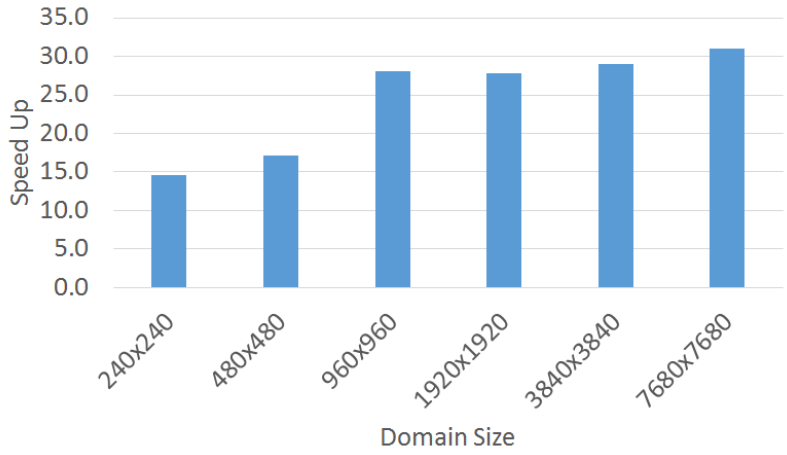

Figure 5.7 Plot of relative speedup in forming the linear system in (5.33) in the GPU code over equivalent CPU code for various square domains sizes.

equivalent version of the kernel used to compute the matrices in (5.33). We assume the time required for computing the matrix in (5.34) scales (with respect to the CPU) similarly to the computation time required to evaluate the matrices in (5.33). Figure 5.7 shows that on a large enough domain, the GPU implementation is at least 25 times faster than the serial CPU code. We note that in the GPU implementation, for the smallest two domain sizes in Figure 5.7, the domain is sufficiently large and all

cores in the GPU should be utilized, therefore, the reduced performance (compared to the 4 largest domains) may be due to bottlenecks in the memory.

We have therefore showed that on large enough domain sizes our GPU implementation can perform up to 25 times faster than the CPU code. While we have not compared the GPU implementation to an equivalent serial CPU implementation in full, we have shown significant performance increase in major components of the numerical scheme, thus it is reasonable to assume similar performance gains would be observed in a full comparison.

5.4 Nematic Liquid Crystals

In this section, we focus on the thin film model derived for nematic liquid crystals, i.e., the governing equation given by (5.1) and (5.8). The details of the model itself are discussed in detail in Chapter 4, where a weak anchoring model was presented. In Chapter 4 it was shown that the nematic contribution to the thin film model resulted in an effective disjoining pressure, given by (5.8), and plotted in Figure 5.8. Similar functional forms of the disjoining pressure, characterized by a local maximum for nonzero film thicknesses, are found in other contexts, such as polymer films [4].

We discuss some of the main features of the results from Chapter 4 in the three dimensional context. These include formation of satellite (secondary) drops, nucleation versus spinodal type instability, and metastable films. The fact that we are able to simulate accurately large domains of linear dimensions measured in tens of wavelengths of maximum growth, allows us to obtain results that are only very weakly influenced by the presence of the domain boundaries. This section is organized as follows: in § 5.4.1 we present the model in terms of the gradient dynamics formulation, § 5.4.2 gives a model outline, and the main part, § 5.4.3 presents the computational results.

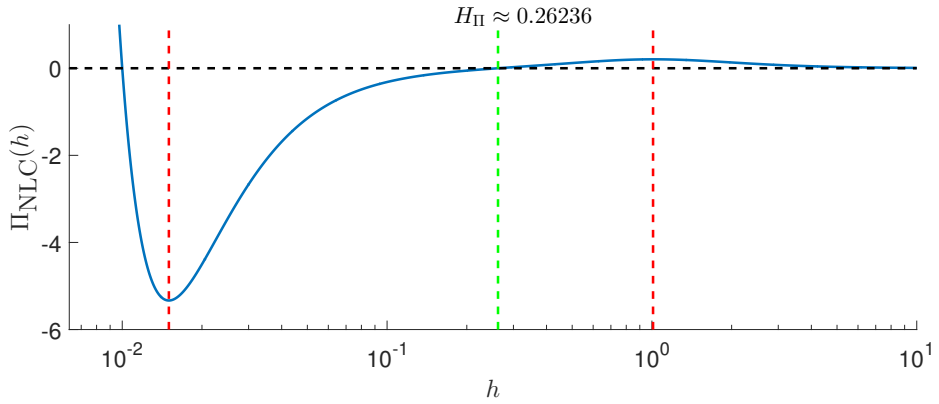

Figure 5.8 Plot of the disjoining pressure for a NLC, (5.8), as a function of the film thickness. The region between the outer dashed red vertical lines denotes linearly unstable film thicknesses, and the central dashed green line denotes the zero of the disjoining pressure, H_Π (within the linearly unstable regime).

5.4.1 Gradient Dynamics Formulation

It is convenient to express the governing equation (5.1) in terms of the gradient dynamics formulation; in particular, it is advantageous to express analytical results in terms of a disjoining pressure, $\hat{\Pi}(\hat{h})$. The benefit of this formulation is that previous analytical results for 2D films in Chapter 4 show that the form of the disjoining pressure primarily determines the transition between different stability types of a thin film as a function of its thickness.

To motivate this assertion, we perform LSA on the gradient dynamics formulation of the governing equation, which is given by

$$\mu\hat{h}_t + \hat{\nabla}\cdot\left[\hat{Q}(\hat{h})\nabla\frac{\delta\hat{F}}{\delta\hat{h}}\right] = 0, \text{ where } \hat{F}(\hat{h}) = \gamma\left[1 + \frac{\hat{\nabla}\hat{h}\cdot\hat{\nabla}\hat{h}}{2}\right] + \hat{\psi}(\hat{h}),\ \hat{\Pi}(\hat{h}) = -\frac{\partial\hat{\psi}}{\partial\hat{h}}\ , \tag{5.45}$$

$\hat{Q}(\hat{h})$ is the mobility function, $\hat{F}(\hat{h})$ is total interfacial energy (Gibbs energy), γ is the surface tension, and $\hat{\Pi}(\hat{h})$ is disjoining pressure. Relating (5.45) to the nondimensional governing equation (5.3),

$$\tilde{f}_0(h) = \tilde{Q}(h)\ , \quad \hat{F}_0 = \gamma\hat{M}\ , \quad \tilde{f}_1(h) = \tilde{Q}(h)\tilde{\Pi}'(h) \quad \text{and} \quad \hat{F}_1 = \frac{\hat{M}\hat{\Psi}}{H^2}\ , \tag{5.46}$$

where, similarly to before, $\hat{M}$ and $\hat{\Psi}$ are dimensional constant prefactors derived from expressing $\hat{Q}(\hat{h})$ and $\hat{\Psi}(\hat{h})$ as dimensionless functions of the dimensionless variable h, e.g., $\hat{Q}(\hat{h}) = \hat{M}\tilde{Q}(h)$. The nondimensional linear stability analysis results (5.5) simplify to

$$q_m = \sqrt{\frac{\Pi'(H_0)}{2\Gamma}} \quad \text{and} \quad \omega_m = \frac{Q(H_0)[\Pi'(H_0)]^2}{4\Gamma}\,, \quad \text{where} \quad \Gamma = \frac{\hat{\Psi}}{\gamma\delta^2} \tag{5.47}$$

is a dimensionless constant and may be interpreted as the ratio of disjoining pressure to surface tension forces. We note that the disjoining pressure determines the transition between linear stability ($\Pi'(H_0) < 0$) and instability ($\Pi'(H_0) > 0$). The instability wavelength is independent of the mobility function, which only affects the growth rate of instabilities.

5.4.2 Model Description

To motivate the form of the disjoining pressure shown in Figure 5.8 and defined by (5.8), here we provide a brief outline of the main features of NLC, and we refer the reader to Chapter 4 for a more detailed derivation. Typically, NLC molecules are rod-like structures with an (electrical) dipole moment, which gives rise to a state of matter intermediate between a crystal and a liquid. Specifically, similarly to a Newtonian fluid, there is no positional ordering to the NLC molecules; however, similarly to a crystal, molecules have short-range orientational order due to interactions between dipoles (elastic response). To model NLC, in addition to modeling the velocity field of molecules (as with most fluids), short-range ordering is often modeled with a director field. The director field is a unit vector, aligned with the long axis of the liquid crystal, see Figure 5.9a, and it is often convenient to consider the polar angle, θ, and azimuthal angle, ϕ, of the director field orientation as a function of Cartesian space (x, y, z).

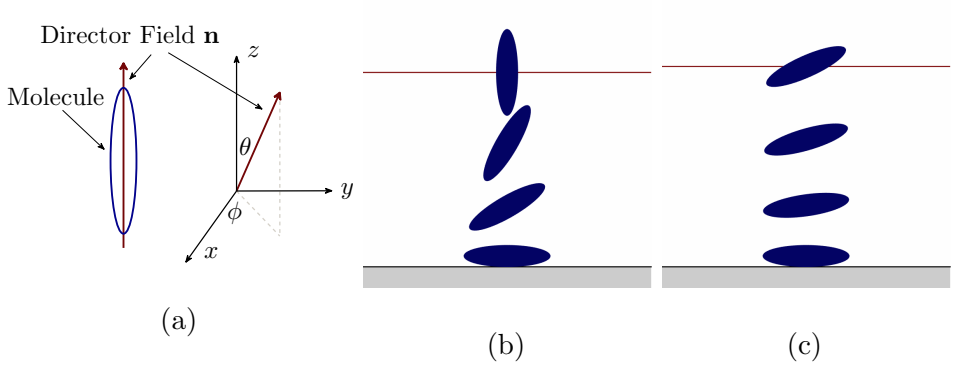

Figure 5.9 a) Schematic of director field relative to liquid crystal molecule. b) Strong free surface anchoring model example. c) Weak free surface anchoring model.

The evolution of NLC may be modeled using the Leslie-Ericksen equations, an extension of the Navier-Stokes equations, with an additional equation modeling conservation of energy. Under the long wave approximation, and assuming that the time scale of fluid flow is much faster than the time scale of the elastic reorientation, the conservation of energy equation decouples from the remaining equations and only depends on the director field. Using energy minimization, the polar and azimuthal angles of the director field are determined to be of the form

$$\theta(x, y, z) = a(x, y)z + b(x, y) \quad \text{and} \quad \phi(x, y) = c(x, y) \ , \tag{5.48}$$

where $a(x, y)$, $b(x, y)$, and $c(x, y)$ are constant with respect to z and satisfy boundary conditions, thus the director field is a function of the instantaneous fluid height.

At the interface between the NLC film and another material, liquid crystal molecules molecules satisfy certain anchoring conditions. Typically, at the free surface (air/NLC interface), molecules are normal to the free surface ($\theta(x, y, z = h) = \pi/2$), and at the NLC/substrate interface, planar anchoring is appropriate, so $\theta(x, y, z = 0) = 0$, see Figure 5.9b. However, for very thin films, or close to a contact line, this configuration induces a large energy penalty in the bulk due to rapid variations in the director field; therefore, we implement a novel weak free surface anchoring

model. In practice, the substrate anchoring is stronger than the free surface anchoring, thus we relax the free surface anchoring to that of the substrate for very thin films (weak anchoring model) to alleviate the large energy penalty in the bulk (compare Figures 5.9b and 5.9c). Specifically,

$$\theta(x, y, z) = \frac{\pi}{2}\left(1 - \frac{m(h)}{h}z\right) \tag{5.49}$$

where $m(h) \in [0, 1]$ and is defined in (5.9). The azimuthal anchoring ϕ in (5.48) is independent of z; therefore, assuming the substrate anchoring dominates, the azimuthal anchoring is determined by the substrate. The governing equation (5.1) is a simplification of the long wave approximation of the Leslie-Ericksen equations that ignores substrate anchoring. In the full (long wave) model, the mobility function may be expressed as

$$Q(h) = \left[\lambda\mathbf{I} + \nu\begin{pmatrix} \cos 2\phi & \sin 2\phi \\ \sin 2\phi & -\cos 2\phi \end{pmatrix}\right] h^3 \,, \tag{5.50}$$

where $\mathbf{I}$ is the identity matrix, and λ and ν are anisotropic viscosities. To simplify the model, we fix $\lambda = 1$ and $\nu = 0$, which removes the dependency on ϕ. Note that by definition, $\lambda > \nu$, therefore the mobility function is positive definite, thus does not change stability properties. We leave the investigation of the effects of substrate anchoring for future work.

5.4.3 Simulations

For the remainder of this section, we focus on extending the previous analysis carried out for 2D films to 3D films. This section is divided into three parts. In the first two parts, we focus on the linearly unstable regime, first investigating coarsening and satellite drop formation, and second, the nucleation dominated regime. In the third part, the metastable regime is examined. Before presenting these results, we discuss the domain size and spatial step size of simulations, and the tools used to quantify

simulation results; in particular, the Fourier transform of the film profile and the Betti numbers, a topological measure of the film profile. Note that these tools will only be applied to the results in the linearly unstable regime.

Unlike § 5.3.1, where the spatial step size was determined by I, λ_m, and P, in this section, we instead fix Δs, λ_m, and P and the grid size $I = P\lambda_m/\Delta s$. The grid sizes in this section range from 1000 to 4000 points and will be specified when discussing simulation results in this section. For all simulations, we fix the spatial step size to $\Delta s = 0.05$ except for the film thicknesses $H_0 = 0.05$, where $\Delta s = 0.01$; and $H_0 = 0.1$, where $\Delta s = 0.02$. The spatial step size was changed at these (linearly unstable) film thicknesses as to maintain a sufficient number of points per period of the most unstable wavelength λ_m. Note that for thicker films, while a larger Δs may be chosen while maintaining a sufficient number of points per period (say 50), to adequately resolve the contact line, Δs is chosen to be close to the precursor thickness $b = 0.01$. In addition, simulations in the linearly unstable regime (first two parts) are scaled in two ways: 1) the linear domain size is set to $P\lambda_m$ where P is an integer, i.e., domains are scaled by P periods of the most unstable wavelength from LSA; and 2) when comparing results for different film thicknesses as a function of time, it is convenient to define a new timescale, $\tau = t\omega_m$, i.e., we scale time by the most unstable growth rate obtained using LSA. We fixed $P = 40$ for all (linearly unstable) thicknesses with the exception of $H_0 = 0.8$, where $P = 10$.

We are primarily interested in extracting the length scale that dominates the instability pattern of the dewetting thin film as a function of time. Using a 2D Fourier transform, the most unstable wave numbers can be extracted; however, obtaining precise values is not straightforward. The procedure that we use is described in some detail in Appendix B; here we just provide an outline. Assuming that the instability pattern is isotropic, the magnitude of the 2D Fourier transform may be mapped to a one-dimensional (radial) function of the magnitude of the wave number $q_r = \sqrt{q_x^2 + q_y^2}$,

where q_x and q_y are the x and y components of the wave number. In addition, several smoothing techniques are required to reliably extract local maxima.

Next, we discuss the use of Betti numbers to quantify the results of the simulations. The Betti numbers, b_n, are n positive integers that characterize the connectivity of n-dimensional objects (simplicial complexes). To compute the Betti numbers, the Computational Homology Project (CHomP) software package [1] is implemented. In terms of a 2D (binary) black and white image, such as the example in Figure 5.10, the zeroth Betti number, b_0, is the number of connected white regions; and the first Betti number, b_1, is the number of black regions. Note that white regions, b_0, that connect with the boundary are not counted; however, black regions, b_1, that connect with the boundary are counted; thus simulations on large domains are essential for removing boundary effects. The first two Betti numbers for an example image are illustrated in Figure 5.10.

Figure 5.10 The Betti numbers of the above image are $b_0 = 3$ (white regions with blue outline) and $b_1 = 5$ (black regions with red outline). Note that white regions, b_0, that connect with the boundary (gray border) are not counted; however, black regions, b_1, that connect with the boundary are counted.

To compute the Betti numbers for our simulations requires mapping the numerical solution, $h(x, y, t)$, to some binary function (black and white), $\grave{h}(x, y, t; H^*)$, where H^* is a threshold thickness such that $\grave{h}(x, y, t; H^*) = 0$ if $h(x, y, t) \geq H^*$ (white)

[1] http://chomp.rutgers.edu/, accessed April 25, 2018

and $\grave{h}(x,y,t;H^*) = 1$ if $h(x,y,t) < H^*$(black). To examine the Betti numbers for various film thicknesses, we define the average Betti numbers, $\grave{b}_0$ and $\grave{b}_1$ per unit area of the most unstable wavelength, e.g., $\grave{b}_0 = b_0/P^2$ where $P\lambda_m$ is the linear domain size, see (5.51). Therefore, the average Betti numbers give a measure of the number of features (components, holes) per λ_m^2. Furthermore, the averaged Betti numbers are plotted as functions of the threshold value H^* scaled by the average film thickness H_0 (vertical axis) and the rescaled time τ (horizontal axis).

Evolution of films exposed to infinitesimal perturbations of global character Here we analyze the evolution of randomly perturbed films of thicknesses H_0 that are in the linearly unstable regime. The initial condition is set to a flat film that has been randomly perturbed, and to excite all modes in the 2D Fourier transform independently (combinations of q_x and q_y), pseudo-Perlin noise is used. Specifically, the initial condition is of the form

$$u(x,y,t=0) = H_0(1+\epsilon\,|\zeta(x,y)|)\ , \quad (x,y) \in [0, P\lambda_m] \tag{5.51}$$

where P is a positive integer, $\lambda_m = 2\pi/q_m$, q_m is given in (5.5), $\zeta(x,y)$ is the inverse Fourier transform of

$$\zeta(q_x,q_y) = \left| \left(q_x^2+q_y^2\right)^{-\alpha/2} \exp\left(2\pi \mathrm{i} a(q_x,q_y)\right) \right|\ , \tag{5.52}$$

$\epsilon = 0.01$, α is some positive constant, and $a(q_x,q_y)$ is a random variable which is uniformly distributed on $[-1,1]$ for each (q_x,q_y). In addition, $\zeta(x,y)$ is scaled so that $|\zeta(x,y)| \le 1$ and we fix $\alpha = 200/I$, where I is the number of discretization points in the x and y directions, so that the spatial scale of the noise is proportional to λ_m.

Figures 5.11 and 5.12 show the results for the thinnest film that we consider, $H_0 = 0.05$, and for times $\tau = 5$ and 20, respectively. The central parts of the figures show the free surface thickness. The corresponding radial Fourier Transform is shown

at top right. We see that the most unstable wavelength dominates the morphology of the film at $\tau = 5$. On the bottom right, the local maximum of the radial Fourier transform is plotted as a function of time, showing that for $1 < \tau < 6$, q_m dominates the wave pattern. At later times, drops form and coarsening is observed in the radial Fourier transform. Similar coarsening effects are also observed in Volume of Fluid based simulations of nanoscale metal films [79]. We find consistent results for all unstable film thicknesses considered, in the range $[0.05 : 0.8]$.

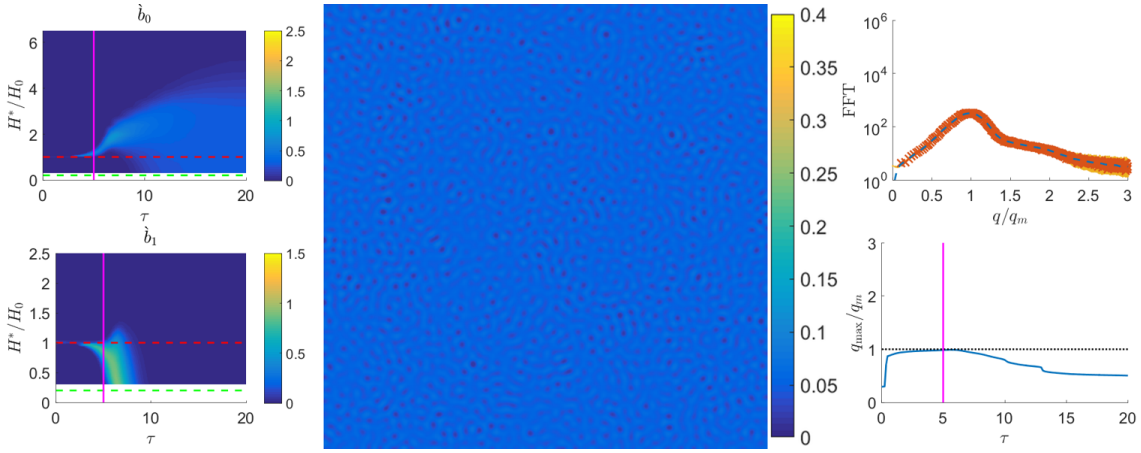

Figure 5.11 Contour plot of the free surface height (center) for $H_0 = 0.05$ at $\tau = 5$. On the right hand side, we plot the corresponding radial Fourier transform of the film height (top), and local maximum of radial Fourier transform, $q_{\max}$ (bottom) as a function of τ. On the left hand side, we show the contour plots of the average Betti numbers $\grave{b}_0$ (top) and $\grave{b}_1$ (bottom) as a function of τ and scaled threshold value H^*/H_0. The vertical magenta line corresponds to the solution time shown in the central panel. For this simulation, the grid size is 1637×1637.

The Betti numbers may be interpreted in two ways, depending on the times considered. For short time scales (before dewetting), b_0 represents the number of regions where the film height is above H^*; and b_1 is the number of regions where the height is below H^*. Assuming $H^* > b$, for longer time, $b_1 \to 1$, i.e., a fully connected precursor film forms (which is connected to the boundaries of the computational domain), and b_0 is the number of drops with a height larger than H^* that are not connected to the boundary. To further gain insight into the topological features, we

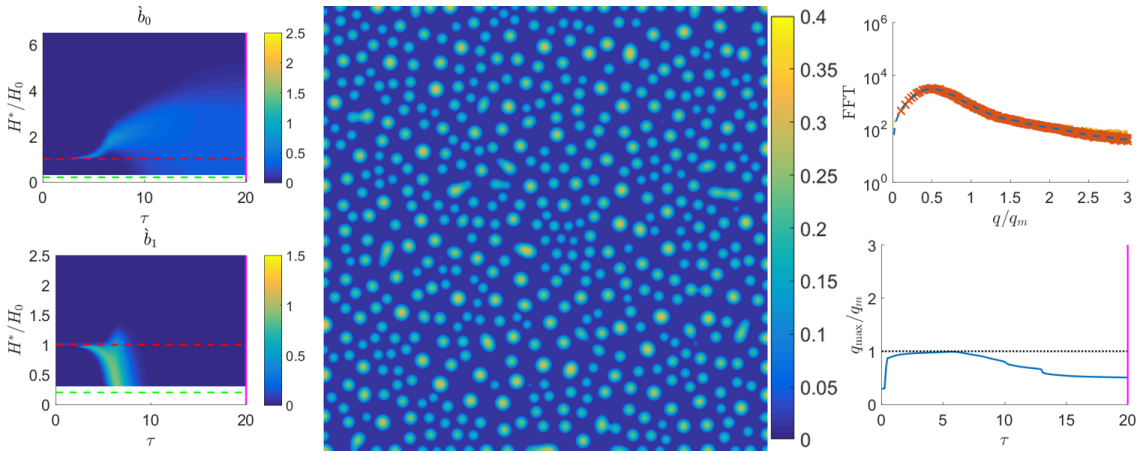

Figure 5.12 Contour plot of the free surface height (center) for $H_0 = 0.05$ at $\tau = 20$. The rest of the figure is as described in the caption of Figures 5.11. For this simulation, the grid size is 1637×1637.

compute the Betti numbers for threshold thicknesses $H^* \in [1.5b, 7H_0]$, where $b = 0.01$ is the precursor thickness.

Figures 5.11 and 5.12 also plot the average Betti numbers $\grave{b}_0$ (top left) and $\grave{b}_1$ (bottom left), as contour plots. We observe the 'peninsula' like light blue structure in $\grave{b}_0$ (top row), the tip of which starts at $\tau \approx 3$ and $H^*/H_0 \approx 1$. This corresponds to a local increase of film thickness (therefore formation of isolated hill tops). These hill tops are associated with formation of surrounding valleys, indicated by an increase of $\grave{b}_1$ around the same time. We also note that this peninsula structure forms for early times for which LSA describes the morphology of the film. At later times, when drops start to form, see Figure 5.12, the Betti number $b_1 \to 1$, corresponding to a connected precursor layer (no loops). The $\grave{b}_1$ result shows that there are no structures present for any value of the threshold, suggesting in particular that there are no structures present at small thresholds, or in other words, no satellite drops. Focusing on the results for the average Betti number $\grave{b}_0$, we observe that $\grave{b}_0$ is mostly constant for $H^*/H_0 < 3$ and begins to decay to zero above this threshold value, indicating that the majority of drop heights are approximately of the same order of magnitude.

Our previous analysis of 2D films showed the presence of satellite drops persisting on a timescale longer than dewetting ($\tau \gg 1$) for the linearly unstable film thicknesses corresponding to positive disjoining pressure. For the present choice of parameters, $\Pi(H_0) = 0$ for $H_0 = 0.2624$, see Figure 5.8. The question is whether similar behavior can be observed for the currently considered 3D films. To answer this question, we consider thicker films. Figure 5.13 shows the results for $H_0 = 0.6$. We note that the Fourier transform (and in particular, the dominant wave number) shows results similar to those for thinner films shown in Figures 5.11 and 5.12. However, there is a significant difference in $\grave{b}_0$ for threshold values below H_0; specifically we note the presence of the rectangular bright yellow region. Following the magenta line in Figure 5.13, it may be seen that $\grave{b}_0$ is large for $H^*/H_0 < 0.5$ and has a slight minimum at $H^*/H_0 \approx 1.5$ and a maximum at $H^*/H_0 \approx 2.5$. This indicates the presence of smaller secondary satellite drops (bright yellow region) and larger primary drops (constant region for $2 < H^*/H_0 < 3$). Therefore, the finding that positive values of the disjoining pressure lead to the existence of satellite drops for 2D films, is found to propagate to 3D films.

Evolution of films exposed to both localized and random perturbations

We now switch focus to linearly unstable film thicknesses that are susceptible to nucleation-type of instability. Previous results for 2D films in Chapter 4, which consider the evolution of a single localized perturbation, show that the localized perturbation would propagate into the flat regime, dewetting the film and successively forming drops. Extracting the average distance between the drop centers, four regimes were identified numerically: regions R I and R III, where the mean distance between drop centers is characterized by λ_m, the most unstable wavelength (spinodal dewetting); and regions R II and R IV, where the mean distance between drops is not characterized by λ_m (nucleation dominated regime). These stability regions as they relate to the disjoining pressure are shown in Figure 5.14. While we do not

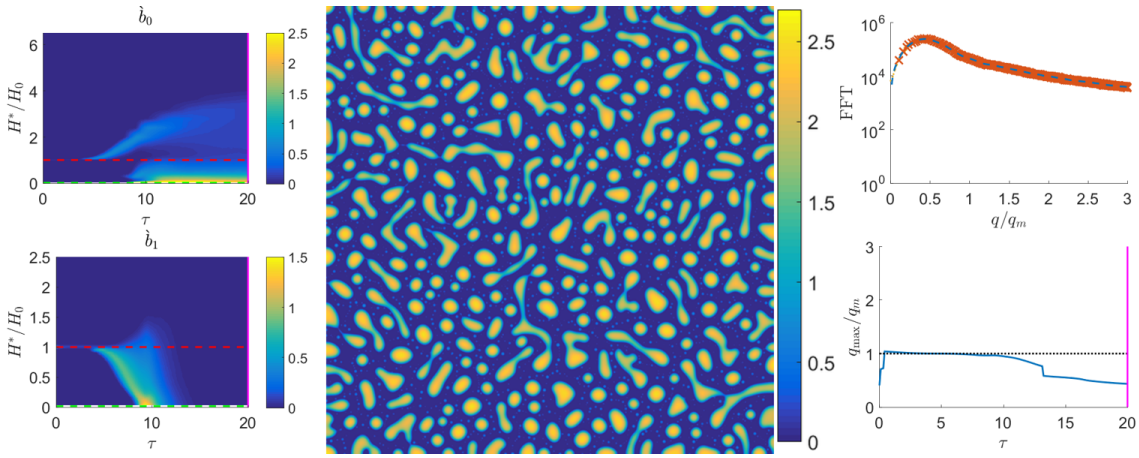

Figure 5.13 Plot of the free surface height (center) for $H_0 = 0.6$ at $\tau = 20$. Corresponding radial Fourier transform (top right) of free surface height in center, and local maximum of radial Fourier transform (bottom right) as a function of τ. Left subpanels plot the average Betti numbers $\grave{b}_0$ (top) and $\grave{b}_1$ (bottom) as a function of τ (horizontal axis) and scaled threshold valued H^*/H_0 (vertical axis). The vertical magenta line corresponds to the solution time in the respective subpanels. For this simulation, the grid size is 3882×3882.

consider directly the extension of a localized perturbation propagating in to the flat regime for long times, we note that the 2D results for the mean distance between drop centers produced by global random perturbations, while characterized by λ_m, shows an increase in the variance in the mean distance in the R II and R IV regimes. This is the feature of the results on which we focus in the current 3D simulations.

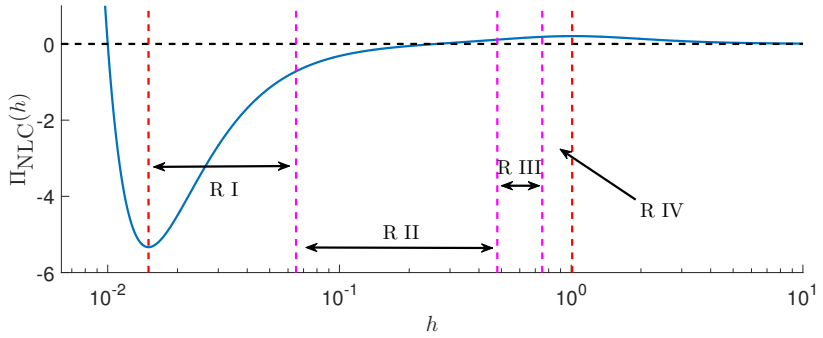

Figure 5.14 Stability regimes R I, R II, R III, and R IV as described in the text. The solid blue curve shows the disjoining pressure (5.8). The vertical dashed lines were determined numerically in Chapter 4.

To begin, we consider the evolution of a flat film of thickness H_0 perturbed by global random perturbations with superimposed larger localized perturbations with a specified average mean distance apart. Specifically, the initial condition is given by

$$u(x, y, t = 0) = H_0(1 + \epsilon|\zeta(x, y)| + 10\epsilon\eta(x, y)) \ , \tag{5.53}$$

where $\zeta(x, y)$ is the pseudo-Perlin noise (5.52), and localized perturbations are defined by

$$\eta(x, y) = \sum_{i=1}^{4}\sum_{j=1}^{4} \exp\left(-\frac{(x - \chi_i)^2 - (y - \xi_j)^2}{0.04\lambda_m^2}\right) \ , \tag{5.54}$$

where $\chi_i = (8i - 4 + 4a_i)\lambda_m$, $\xi_j = (8j - 4 + 4b_j)\lambda_m$, and a_i and b_j are random variables uniformly distributed on $[-1, 1]$ i.e. we generate a two-dimensional array of localized perturbations with mean distance $8\lambda_m$ apart.

Note that we do not consider the evolution of flat films with localized perturbations only for three reasons: 1) previous results in Chapter 4 were done in Cartesian coordinates, therefore, a radial localized perturbation is not a direct extension to the initial condition of the previous results; 2) numerical instability in the azimuthal direction dominates the radial instability which controls the distance between drops (or circular rivulets in radial coordinates); 3) in practice, global random perturbations are always present. Therefore, carrying out simulations where both local and global perturbations are present brings us closer to understanding experimental results.

Similarly to the previous section, plots similar to Figure 5.13 will be shown; however, we note that the radial Fourier transforms may have more than one local maximum; therefore, we also plot the second largest local maximum (yellow dots) of the largest local maximum (red dots), and the local maximum of the radial Fourier transform for the same film thickness with random perturbations only (dashed blue curve). Note that we ignore the second largest local maximum if it is sufficiently

small, specifically if it is less than 5% of the largest local maximum. In Figure 5.15, simulation results are plotted for $H_0 = 0.2$ (nucleation dominated regime) at $\tau = 2$. It may be seen that the localized perturbations grow into large holes and dominate the radial Fourier transform for $1 < \tau < 5$. At later times, see Figure 5.16, while drops form, the holes are still visually distinguishable (central column). Furthermore, for $\tau > 5$, there are two dominating wave numbers (top right subpanel in Figure 5.16), one of which corresponds to the coarsened value from the simulation with random perturbations only (compare to the dashed blue curve in the bottom right subpanel) and the other wave number corresponding to the average distance between localized perturbations, $q = q_m/8$. These results indicate that it is possible to identify the nucleation dominated regime; furthermore they show the importance of using large scale simulations so as to be able to extract the second, smaller, wavenumber from the radial Fourier transform.

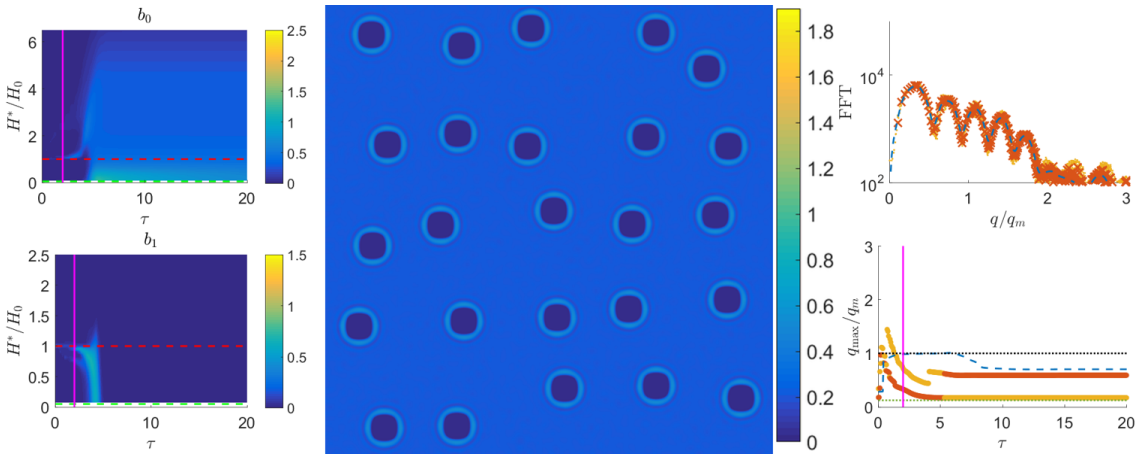

Figure 5.15 Plot of the free surface thickness (center) for $H_0 = 0.2$ at $\tau = 2$. Corresponding radial Fourier transform (top right) of free surface height in center, and the large local maximum (red dots) and second largest local maximum (yellow dots) of the radial Fourier transform (bottom right) as a function of τ. Here the dashed blue curve corresponds to the local maximum of the radial Fourier transform for a simulation carried out with the same film thickness, but with random perturbations only, and the horizontal green line is the wave number associated with the average distance between localized perturbations. Left subpanels plot the Betti numbers $\grave{b}_0$ (top) and $\grave{b}_1$ (bottom). The vertical magenta line corresponds to the solution time in the respective subpanels. For this simulation, the grid size is 1970×1970.

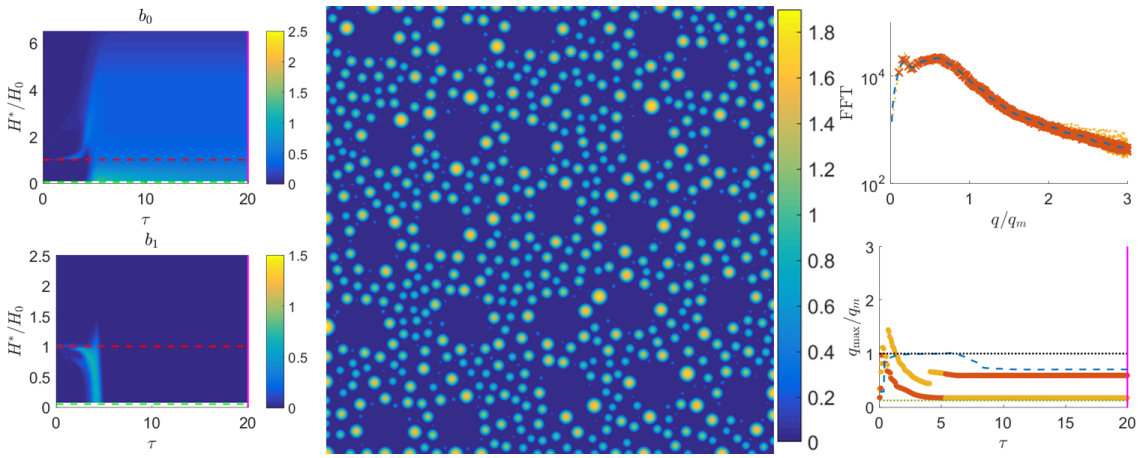

Figure 5.16 Plot of the free surface height (center) for $H_0 = 0.2$ at $\tau = 20$. The rest of the figure is as described in the caption of Figure 5.15. For this simulation, the grid size is 1970×1970.

Figure 5.17 plots, for comparison, the results for $H_0 = 0.05$ (spinodal dominated regime) at $\tau = 20$. The results show that for long times, the localized perturbations have negligible effect on the morphology, and only a single wave number (which is the same as the simulation with random perturbations only) dominates the wave pattern. Simulations were also carried out for $H_0 = 0.3$ (nucleation dominated) and $H_0 = 0.6$ (spinodal dominated), confirming the results.

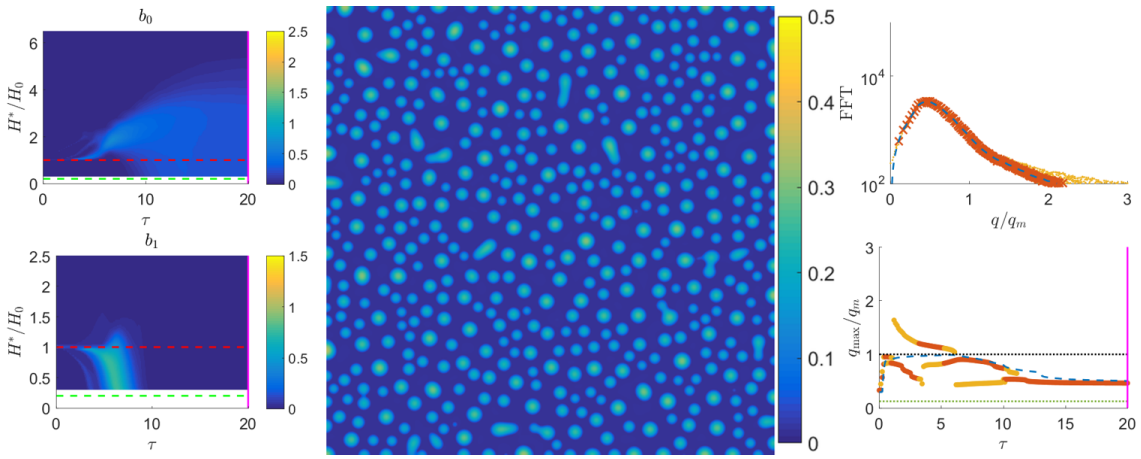

Figure 5.17 Plot of the free surface height (center) for $H_0 = 0.05$ at $\tau = 20$. The rest of the figure is as described in the caption of Figure 5.15. For this simulation, the grid size is 1637×1637.

In regard to Betti numbers, we note that there is negligible qualitative difference between simulation results with localized and random perturbations, and simulation results with random perturbations only, compare Figures 5.11, 5.12, and 5.13 to Figures 5.15, 5.16, and 5.17. However, we do note that there is a slight difference in $\grave{b}_1$ (bottom left subpanels). Specifically, for random perturbations only, there is one peninsula like structure, the tip of which starts at $H^*/H_0 = 1$ and connects with the vertical rectangular structure at $8 < \tau < 10$, whereas for the simulations in this section, there are two peninsula structures, the lower of which corresponds to the localized perturbations.

Metastable Regime Here we briefly investigate the metastability regime previously studied for 2D films. The metastability regime corresponds to the film thicknesses that are linearly stable; however, they are unstable with respect to perturbations of finite amplitude. Previous analytical results have shown that there exists a thickness regime, $H_0 \in (H_+, H_{m_3}) \approx (1.01, 3.04)$, that is metastable. Extensive numerical simulations have shown that for an initial condition of the form

$$h(x, y, t = 0) = H_0 \left[1 - d \exp\left(- \left[\frac{\sqrt{x^2 + y^2}}{0.2W} \right]^2 \right) \right] \quad , \quad W = 4\pi \tag{5.55}$$

with $y = 0$ for 2D films. For dewetting to occur, the magnitude of the perturbation, d, required to induce dewetting, approaches 1 as $H_0 \to H_{m_3}$, i.e. for film thickness near to or larger than H_{m_3}, the initial perturbation has to dewet the film for dewetting to occur, $d \approx 1$. In addition, for illustrative purposes, we consider an initial condition of the form

$$h(x, y, t = 0) = H_0 \left[1 - d\eta(x, y) \right] \ , \tag{5.56}$$

where the linear domain size is 100, $H_0 = 1.5$, $d = 0.85$, and $\eta(x, y)$ is given in (5.54) with $\lambda_m = 2.5$ (for convenience, we use the value from (5.54) although λ_m is not relevant for metastable films). An example of the free surface profile given by the

initial condition specified by (5.56) is shown in Figure 5.18a, with the film profile at $t = 1000$ in Figure 5.18b.

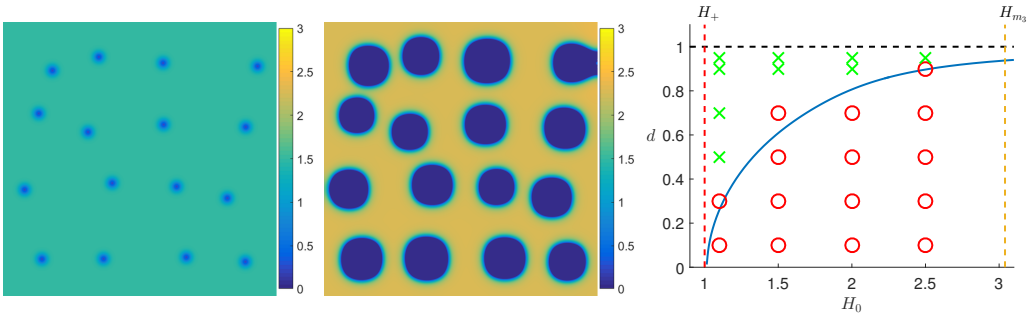

(a) (b) (c)

Figure 5.18 a) Example of the free surface profile given by the initial condition given in (5.56), and b) the resultant free surface at $t = 1000$. c) Metastability results for initial condition (5.55) as a function of the initial film thickness, H_0, and initial magnitude of the localized perturbation, d. From previous results for 2D films ($y = 0$ in (5.55)), the blue curve denotes the minimum d required to induce dewetting. For the 3D films, $\times$ denotes initial condition parameters that induced dewetting, and $\bigcirc$ denotes parameters that did not induce dewetting.

To investigate the metastable regime, simulations are carried out with the initial condition specified in (5.55) for several average film thicknesses $H_0 \in (H_+, H_{m_3})$ and several initial perturbation sizes $d \in [0, 1]$. As a function of H_0, Figure 5.18c compares the minimum d required to induce dewetting for 2D films (blue curve) to simulation results for the radial extension of the same initial condition for 3D films (5.55). Here, crosses and circles denote the parameters that do/do not induce dewetting, respectively. It may also be seen that 2D results extend to 3D; however, the minimum d required to induced breakup is slightly larger. This may be due to the difference in the geometry between the localized perturbations in 2D and 3D.

5.5 Comparison to Experimental Results

In this section, we compare simulation results for NLC and polymeric films to available experimental results. The disjoining pressures considered are given by (5.8) and (5.12),

respectively. To scale the domain and initial condition for different film thicknesses, simulations are performed on a square domain, and the linear domain size is scaled with λ_m. In addition, we fix $\Delta s = 0.05$ for both models. The initial condition is given by (5.51). For all simulations in this section, we fix $P = 40$.

The first set of experimental results considered is dewetting experiments for NLC films by Schlagowski *et al.* [1] and Vandenbrouck *et al.* [2]. In the experiments by Vandenbrouck *et al.* [2], a flat film is formed by increasing the temperature of the NLC such that a flat film is stable at the considered film thickness of interest (isotropic phase). The flat film is formed by using a spin coating method, and then cooled to a temperature so that it becomes unstable (nematic phase). Schlagowski *et al.* [1] varied the temperature of the NLC sample, alternating between the isotropic and nematic phases, observing the morphology of the film as the temperature crosses the threshold between the isotropic phase and nematic phase. Figure 5.19 compares a 3D rendering of our numerical results to experimental results of two different types of NLC. In both experiments, the characteristic wavelength of undulations is appropriately 30 μm, which is similar to $\hat{\lambda}_m = 42$ μm for the parameters stated in (5.10) and (5.11).

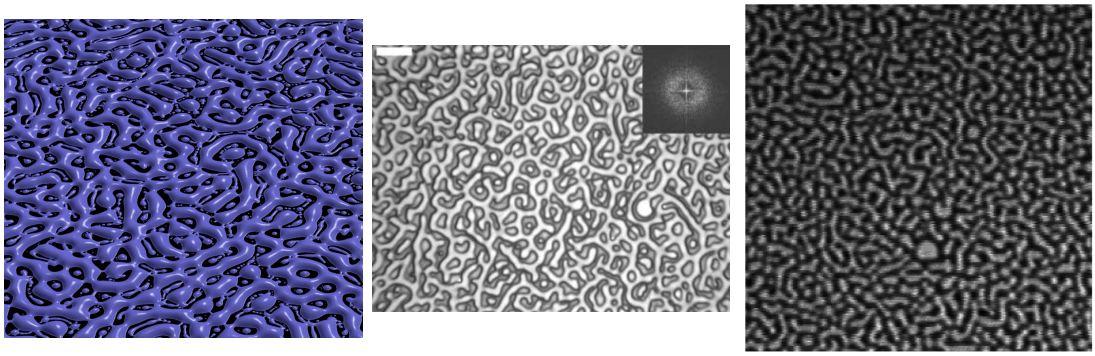

(a) (b) (c)

Figure 5.19 a) Simulation result for a 50 nm ($H_0 = 0.5$) thick film of 4-Cyano-4'-pentylbiphenyl (5CB) nematic liquid crystal vs b) experimental results from b) Schlagowski *et al.* (2002) [1] for a 85 nm thick 4-Octyl-4-Cyanobiphenyl (8CB) film and c) Vandenbrouck *et al.* (1999) [2] for a 43 nm thick 5CB film.

The next experiment we consider is that by Herminghaus *et al.* [3], who prepared flat films of NLC in a Langmuir trough. Unlike the spin coating method, transferring the flat film from the Langmuir trough to the solid substrate may induce defects in the film (localized perturbations). To simulate this initial state, large localized perturbations at random locations are added to the initial condition (5.51). Figure 5.20 demonstrates that the localized perturbations can induce the formation of large holes, leading to patterns that are visually similar to the experimental images.

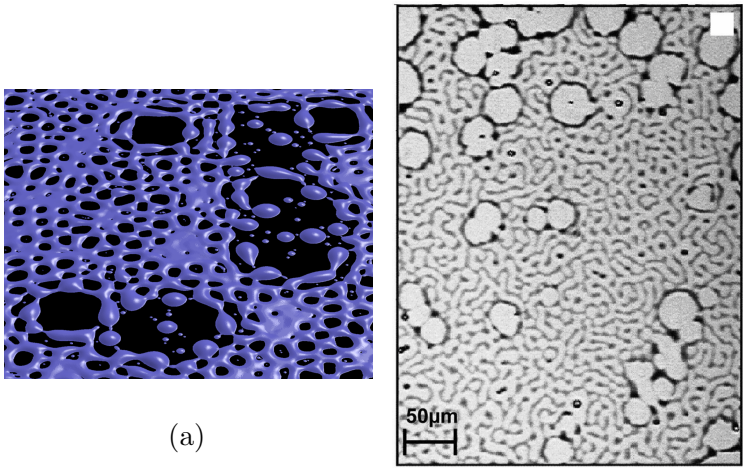

(a) (b)

Figure 5.20 a) Simulation result for a 20 nm ($H_0 = 0.2$) thick film of 4-Cyano-4'-pentylbiphenyl (5CB) nematic liquid crystal film vs b) an experimental result from Herminghaus *et al.* [3] for a 40 nm thick tris(trimethylsiloxy) silane-ethoxycyanobiphenyl ($5AB_4$) film.

The last experiment we consider is a dewetting experiment with polymeric films by Jacobs *et al.* (2008) [4]. Figure 5.21 compares simulation results with experimental results for a 3.9 nm thick polymeric film on a silicon substrate coated with a 191 nm layer of silicon oxide. It may be seen that the dominant wavelength in our simulations matches the experimental results; however, the timescales of dewetting differ. This may be due either to the choice of the initial perturbation size, or possibly to the choice of the viscosity, recall (5.47), which, in the framework of LSA, only affects the timescale of instability.

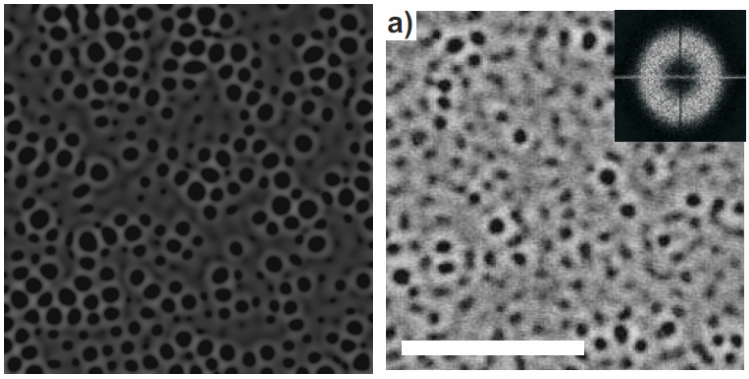

(a) (b)

Figure 5.21 Comparison between a) our numerical simulations at $t = 60s$ and b) the experiment by Jacobs *et al.* (2008) [4] for a 4.9 nm film on a silicon substrate coated with a 191 nm layer of silicon oxide. Note color scales on both subpanels are the same; specifically, black corresponds to 0 nm and white corresponds to 20 nm. The linear domain size in both subpanels is 8 μm and the scale bar for (b) corresponds to 5μm.

5.6 Conclusions

In this chapter, we describe a GPU implementation of an ADI numerical scheme applied to evolution of thin films in a three dimensional setting. The scheme has been generalized to conservation equations with nonlinear fluxes, and validated by extensive testing of its convergence and conservative properties, as well as by comparison with linear stability analysis. The computational gains obtained by carrying out simulation on a GPU are substantial, and allow for carrying out simulations in large domains with rather basic computational resources.

The main set of results presented in this chapter focuses on three dimensional (3D) simulations of unstable films. We find that the main features of the results previously presented in 2D persist in 3D. In particular, satellite (secondary) drops are still observed for positive values of the disjoining pressure, and also we find distinctive features of instability development as film thickness is varied within the linearly unstable regime. While these results are consistent with the 2D ones, they also provide much more detailed information about instability development, due to

the presence of an additional physical dimension. The large scale simulations that we present in this chapter allow also for a direct comparison with experimental results carried out with nematic liquid crystal, as well as polymer, films.

There are several possible avenues for extending the work presented in this chapter. Regarding satellite drops, the nucleation dominated regime, and the metastable regime, investigation of other thin film models (with similar disjoining pressure) would verify the generalization of our results in terms of a disjoining pressure. There are also several possible improvements that may be made to our GPU code, for example, a multi-GPU implementation, implementing adaptive mesh refinement, or improving numerical accuracy. Another important improvement would be to improve the parallelization of the linear solver using techniques such as the SPIKE method [80] or cyclical reduction [81, 82].

CHAPTER 6

CONCLUSIONS AND FUTURE WORK

To summarize this thesis, we find that using a combination of analytical and computational techniques allows us to reach novel understanding of relevant instability mechanisms, and of their influence on transient and fully developed fluid film morphologies. While numerical simulations were performed in the context of nematic liquid crystals, the analytical techniques presented may be applied to a variety of thin film models. Therefore, it is of great interest to extend these results to other thin film models.

For flow down an inclined substrate, we have explored a variety of instability types (stable, convectively unstable and absolutely unstable) that occur behind a fluid front flowing down an incline (traveling wave). The complex interactions between these instabilities and the instability transverse to the flow have also been explored using numerical simulations and analytical techniques.

On a horizontal substrate, several stability regimes have been identified for a flat film: linear instability, metastability, absolute instability, nucleation dominated, and spinodal dominated. Secondary satellite drops that exist on time scales much longer than dewetting were thoroughly investigated using extensive numerical simulations. These results were framed in terms of an effective disjoining pressure as a function of the initial film thickness, the qualitative functional form of which appears in several other thin film models.

We have also presented a GPU code developed by the author and have demonstrated the significant performance gains possible through GPU computing and, in general, parallel computing. Without such gains the simulations of Chapter 5 would not have been feasible. Several possible improvements to the GPU code have also been discussed, which would be of benefit to explore in the future.

APPENDIX A

GPU IMPLEMENTATION

In this appendix, the specifics of the GPU implementation are discussed. To begin, we give an overview on key concepts of GPU computing utilized in our implementation. The GPU is a vector type processor which processes data in the Single Instruction, Multiple Data (SIMD) framework of parallel computing [83], i.e., the same finite difference scheme (single instruction) is applied at each grid point (multiple data). A GPU consists of several multi-core processors (MPs) which share a *global* memory bank (analogous to the CPU memory). Analogous to the levels of cache memory on CPUs [1], each MP has a fast (compared to global memory) *shared* (between cores of a MP) memory bank, and an even faster *register* memory (of the individual cores); however, unlike CPU cache memory, the shared memory bank has to be explicitly handled in a code in order to reduce redundant access to the (slow) global memory. Use of register memory is automatic when defining variables within the scope of the kernel (similar to the automatic use of cache memory on a CPU). Typically, the shared memory bank is used to store data that will be reused by other threads within a thread block, whereas register memory is used to store values that will only be used by an individual thread.

In CUDA, instructions on the GPU (*device*) are executed from the CPU (*host*) in terms of *kernel* calls. There are two input parameters unique to a kernel call, each composed of 3 numbers, specifying the size of a vector, matrix, or tensor. The purpose of these parameters is to divide a domain into sub-lengths, sub-squares or sub-cubes; and assign each *sub-domain* a vector, matrix, or tensor of threads, which we will refer

[1] Technically, the shared memory bank is not a level of cache memory, and MPs already have a L1 and a L2 cache (register memory).

to as a *thread block*. The input parameters provide an intuitive way of sub-dividing a multi-dimensional domain for parallelization (sub-domains), and a natural (geometric) way of mapping threads to points on the sub-domain. On the hardware level, threads within a thread block are further sub-divided into groups called warps (32 threads to each warp for the GPU used in this paper). Instructions to the MPs are batched in terms of warp (vectors) and are executed in the SIMD architecture framework.

The last important concept for GPU computing (for our implementation) is *coalesced* data access to the global memory, i.e., adjacent data values that are adjacent in memory may be accessed in a single SIMD transaction (as opposed to multiple transactions), improving efficiency. This is an important issue for the ADI method, in particular, solving the system of penta-diagonal matrices in each direction, the details of which will be discussed in A.2.1.

Note 1: It is important to note that to fully utilize all threads on a MP, the size of the thread block is typically an integer multiple of the warp size.

Note 2: Since warps are executed in the SIMD framework, warps with threads with different instructions (*warp divergence*) are not computed in parallel, but each different instruction is executed in series, e.g., for n different sets of instructions, the warp is computed in n serial steps (each sub-group of threads, within the warp, with the same instructions, are computed in parallel). Ghost points remove warp divergence at the boundaries; however, this is only an order $I + J$ improvement (the complexity of the complete scheme is IJ).

A.1 GPU and CPU Interactions

In addition to the three levels of GPU memory, the GPU may also access the CPU memory; however, the access time for this level of memory (with respect to the GPU memory) is prohibitively slow and may drastically affect the performance of a GPU code, e.g., for simple computations, the time required for transferring the data between

the GPU and CPU can be comparable to (or even greater than) the time required to perform the computation on the GPU. Furthermore, data have to be explicitly (in code) transferred between the GPU and CPU, and memory must be allocated on both the CPU and GPU [2, 3]. To remove this bottleneck, unless necessary, all computations are performed on the GPU. Recalling the outline of the numerical scheme, controlling the adaptive time stepping is independent of grid size, therefore performed on the CPU. Computationally expensive steps (center column of steps in Figure 5.1) may be (naively) parallelized on the GPU, with the exception of evaluating the convergence criteria (restrictions on accepting the solution at the new time).

To compute the convergence criteria, we first note that for serial computations, it is simple to determine if the convergence criteria are violated at any of the grid points, i.e., the serial code may iterate through the grid points until the convergence criteria is not satisfied; once determined, the appropriate changes may be made to the time step. However, this procedure is slightly non-trivial on a GPU; specifically, a thread can not terminate the execution of warps in the queue (remaining grid points at which the convergence criteria are to be computed). Therefore, once one of the convergence criteria is determined not to be satisfied at a grid point, this information (state) cannot be returned to the CPU, nor can control be returned to the CPU in this manner; thus, the appropriate changes to the time step cannot be determined. The naive approach is to transfer the data from the GPU's memory to the CPU's

[2] Newer GPU models that support NVDIA's *Unified Memory* model, where explicit transferring of data and allocation of memory on both the CPU and GPU is no longer necessary. Our implementation was originally developed on an older GPU that did support the Unified Memory model.

[3] Data in memory are typically organized in blocks of fixed length, often called 'pages'. For higher data bandwidth between CPU and GPU, the CPU memory is page-locked to GPU memory (called 'pinned' memory in CUDA), i.e., Similar to coalesced data access, page locking provides a direct mapping between pages in the GPU's memory and the pages in CPU's memory, removing offsets between pages, allowing CUDA to improve the data bandwidth by transferring the page in a single instruction (as opposed to multiple instructions).

memory. However, as mentioned before this transfer is slow; therefore, a reduction method is used to reduce the amount of data to transfer. In more exact terms, each thread evaluates the convergence criteria at a grid point. The data are reduced on each thread block (sub-domain) by determining if any of the convergence criteria are not met within the thread block, and the reduced data (information for each thread block) are transferred to the CPU.

In our implementation, the size of the thread block is 16×16, thus reducing the total amount of data to be transferred by a factor of 256. To further reduce the data volume to be transferred, we do not store the 8 byte double precision value for the point that violates the convergence criteria, but instead store an integer value (an ID representing the convergence criterion that was not satisfied) in a 1 byte char (flag variables). In total, this method reduces total volume of data to be transferred by a factor of 2048, and the cost of transfer is therefore negligible compared to the GPU computations. The relevant information regarding convergence criteria may then be compressed (reduction) by the GPU, transferred quickly to the CPU, and using a simple loop, the CPU checks the flag on each thread block and adjusts the time-step accordingly.

Note 1: To the authors' knowledge, on a GPU, each entry in a boolean array is stored as a byte (8 bits), thus is not a true bit array (1 bit per entry); thus there is no reduction in memory usage when using a boolean array instead of a char array. While a bit array could have been implemented, this was not done as: a) memory has to be carefully accessed by threads so as to not incur inefficiencies; b) the use of char values allows information about the failure state on a sub-domain to be passed back to the host CPU (thus logged); and c) the total data size has been sufficiently reduced.

Note 2: The reduction on the GPU may be done recursively, i.e. one could further divide the flags into sub-domains, and check whether each flag on the sub-

domains (of flags) is equal to one of the convergence conditions IDs. However with each recursive step, there are diminishing returns in efficiency (less parallelization due to recursively smaller domain sizes), and furthermore, a sufficient reduction in the size of the data has already been achieved.

Having developed a hybrid method (CPU and GPU) to evaluate the convergence criteria, all computationally expensive operations (center column of steps in Figure 5.1) can be parallelized on the GPU, and only a small volume of data (relative to size of the solution) has to be transferred between the CPU and the GPU at every time step and iteration step. While the remaining computationally expensive operations (center column of steps in Figure 5.1) may have a naive parallelization, for fast computation, effective uses of the various GPU memory types is required. This applies in particular to solving (5.33) to (5.35), which we focus on in the next section.

A.2 GPU Kernels

Analogous to loop fusion (removal of loop overheads by combining similar loops), reducing the number of kernel calls (kernel fusion) can improve efficiency, in particular, by reducing repeated requests to the same data in global memory, and reducing the use of global memory to store intermediary data. Before discussing the details of the kernels solving (5.33) and (5.34), we first present the remaining GPU computations, which are computed with two kernels: the *preprocessing* kernel, which computes the solution at the ghost points and the nonlinear functions and their derivatives at the cell-center points $(x_{i+\frac{1}{2}}, y_{j+\frac{1}{2}})$ (see § 5.2.3 and 5.2.4); and the *reduction and update* kernel, which computes the solution criteria and reduces the dataset, and updates the iteration step (5.35) [4]. In both kernels, the domain is sub-divided into squares (16×16

[4] At this point it is unknown if the iteration step satisfies the solution criteria; therefore, this calculation is possibly redundant if the solution is rejected, however, this inefficiency is negligible in comparison to splitting the kernel.

in our implementation) and assigned a thread block of the same size, see Figure A.1a. Shared memory and register memory are naively used to remove repeated access to global memory.

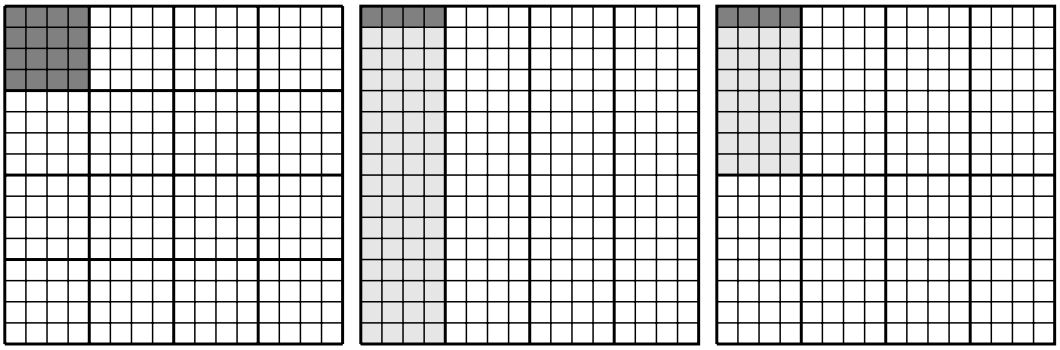

(a) Generic (b) Linear System Solver (c) Form Linear System

Figure A.1 Graph of the various sub-domain block and thread block combinations used in this GPU implementation. Thin lines denote borders between cell centers and thicker lines denotes sub-domain blocks. Light gray shaded areas mark an example subdomain, with darker gray shared areas marking thread block. Note in b) thread block and sub-domain block are the same.

To solve efficiently the penta-diagonal system defined in (5.33) and (5.34) requires care. Recall that at each time step and each iteration step, there are I penta-diagonal matrices of size $J \times J$ and J penta-diagonal matrices of size $I \times I$ to invert, (5.33) and (5.34), respectively. To show this, we arrange solution values $u_{(i,j)}$ in terms of a matrix, $\mathbf{u}$; and use the subscripts $(,j)$ and $(i,)$ to refer to the jth column of $\mathbf{u}$ (fixed y) and the ith row of $\mathbf{u}$ (fixed x). Similar notation will be used for $\mathbf{v}$ and $\mathbf{w}$. Using this notation, we may express (5.33) to (5.35) as

$$\mathbf{A}_j \left[\mathbf{w}_{(,j)}\right]^T = \left[\mathbf{a}^{n+1}_{(k),(,j)} + \mathbf{b}^n_{(,j)}\right]^T \quad 0 \le j < J \,, \tag{A.1}$$

$$\mathbf{B}_i \mathbf{v}_{(i,)} = \mathbf{w}_{(i,)} \qquad 0 \le i < I \,, \tag{A.2}$$

$$\mathbf{u}^{n+1}_{(k+1)} = \mathbf{u}^{n+1}_{(k)} + \mathbf{v} \,, \tag{A.3}$$

where

$$\begin{gathered}\mathbf{A}_j = \mathbf{I} + \frac{\Delta t}{2}\mathbf{J}_{y_j} \ , \quad \mathbf{B}_i = \mathbf{I} + \frac{\Delta t}{2}\mathbf{J}_{x_i} \ , \\ \mathbf{a}^{n+1}_{(k),(,j)} = -\left(\mathbf{I} - \frac{\Delta t}{2}\mathbf{D}_{(,j)}\right)\mathbf{u}^{n+1}_{(k),(,j)} \ , \quad \mathbf{b}^{n}_{(,j)} = \left(\mathbf{I} - \frac{\Delta t}{2}\mathbf{D}_{(,j)}\right)\mathbf{u}^{n}_{(,j)} \ .\end{gathered} \tag{A.4}$$

Note that $\mathbf{A}_j$ and $\mathbf{B}_i$ are penta-diagonal matrices representing the implicit y derivatives for a fixed x_i, and the implicit x derivatives for a fixed y_j, respectively.

We therefore solve (A.1) and (A.2) in four kernels: 1) Compute $\mathbf{A}_i$ for each i, $\mathbf{a}^{n+1}_{(k)}$ and $\mathbf{b}^n$; 2) Invert the penta-diagonal system in (A.1) and compute the transpose (coalesce data access); 3) Compute $\mathbf{B}_j$ for each j; and 4) Invert penta-diagonal systems in (A.2) and compute the transpose.

Note 1: $\mathbf{b}^n$ is independent of the iteration step, k, and is therefore only computed at the initial iteration step (for each time step), and stored in memory for use in future iterations. Furthermore, when initializing the iterative method, $\mathbf{u}^{n+1}_{(0)} = \mathbf{u}^n$, we do not explicitly copy $\mathbf{u}^n$ into $\mathbf{u}^{n+1}_{(0)}$, but instead manipulate array pointers to access the correct terms.

Note 2: While there exist pre-existing subroutine libraries to perform a matrix transpose, to remove redundant global memory access, the inverse solver is fused with an efficient transpose method.

Note 3: Kernel fusion may be used to combine steps 1) and 3); however, the time saving is negligible compared to the prohibitive total global memory cost, e.g., if M bytes are needed to store the solution, $6M$ bytes are required to store one set of penta-diagonal linear systems, plus an additional M bytes for the fixed implicit term in (A.4), $\mathbf{b}^n$. Our current implementation restricts the total domain size to be able to fit into global memory; therefore, not fusing the kernels allows almost 25% more

memory to be utilized (an additional $4M$ bytes are needed for storing the nonlinear functions and their derivatives) [5].

A.2.1 Linear System Solver

We begin with the most difficult computation to parallelize, inverting the penta-diagonal linear systems, (A.1) and (A.2). At best, a single penta-diagonal linear system may be solved with linear complexity; however, the scheme is highly non-parallelizable. To parallelize a single penta-diagonal system would require a reduction type method; however, such a method would increase the total number of calculations. To avoid this issue, we instead assign to each thread on a GPU a linear system to solve.

To invert an individual penta-system, a LU factorization [6] is implemented e.g., $\mathbf{A}_i = \mathbf{L}_i\mathbf{U}_i$. In general, solving the linear system $\mathbf{L}_i\mathbf{U}_i\mathbf{a}_i = \mathbf{c}_i$ may be separated into two operations,

$$\mathbf{U}_i\mathbf{a}_i = \mathbf{b}_i \ , \text{ and } \mathbf{L}_i\mathbf{b}_i = \mathbf{c}_i \ , \tag{A.5}$$

which may be inverted with linear complexity. To sub-divide the (x, y) domain for parallelization, the domain is divided according to the spatial direction, i.e., the domain is divided into strips. The direction that is sub-divided depends on the current direction of the ADI method being computed e.g., solving the implicit y derivatives for fixed x, the domain is divided in the x direction. The width of the strips (16 in our implementation) is the number of penta-diagonal systems in each sub-domain (strip)

[5] Our implementation uses synchronous kernel calls i.e. kernels are executed in serial by the CPU. By sub-dividing the domain into partitions (which would be further sub-divided by the kernels), clever use of asynchronous kernel calls may be used to reduce the total memory requirement, e.g., if each partition contains $M_1 \ll M$ bytes of the solution, then $5M$ plus some small multiple of $10M_1$ bytes would be required, i.e., the total memory usage may be halved (approximately).

[6] While Gaussian elimination may be used, it requires more divisions to be computed, which, on a GPU, is more expensive to evaluate when compared to a multiplication. On a CPU, typically, there is no significant difference.

e.g., different i in (A.5). Each sub-domain is assigned a vector of threads (equal to the width of the strips) which invert the subset of penta-diagonal systems by LU factorization. Figure A.1b gives an example of a 16×16 domain with strips of length 4. Since each penta-diagonal system is independent (for a given ADI direction), each step of the LU factorization is essentially a three point iterative method, therefore, register memory is used to store the previous two iterative points.

As mentioned previously, to utilize memory coalescence (threads access data points that are adjacent to each other in global memory), data must be transposed in memory. To fuse the transpose with LU factorization, the transpose is computed while inverting the second step of the LU factorization, e.g., inverting $\mathbf{U}_i a_i = b_i$ in (A.5). Since coalesced memory access is not relevant for shared memory access, it may be used to temporarily store data. For example, in the y implicit direction of the ADI method, 16 threads (each x value) compute an iteration step (fixed y value) of the U factorization, and then store the data row-wise (fixed y) in a square block of shared memory, the size of which depends on the strip width (16×16 in our implementation). Repeating the U factorization for the next 15 iteration steps, the solution is computed on a 16×16 sub-block. The transpose may be performed in a block-wise fashion by accessing the shared memory column-wise (fixed x) without any significant inefficiency, and then stored in global memory with coalesced access.

A.2.2 Computing the Linear System

We now switch focus to the remaining two kernels not yet defined, computing $\mathbf{A}_j$, $\mathbf{a}^{n+1}_{(k,(,j))}$, $\mathbf{b}^n_{(,j)}$, and $\mathbf{B}_i$ in (A.4). It is mostly trivial to parallelize the computation of $\mathbf{A}_j$, $\mathbf{B}_i$, $\mathbf{a}^{n+1}_{(k),(,j)}$ and $\mathbf{b}^n_{(,j)}$, as at a given time step, threads do not depend on the data computed by other threads; however, to compute numerical derivatives, adjacent points are required, therefore it is prudent to use shared memory to reduce redundant global memory access.

To compute $\mathbf{B}_i$ in (A.4), the domain is divided into squares and assigned a thread block of equal size (16×16 in our implementation). While we may define a shared memory block of equal size to the sub-domain, threads near the x boundaries of the sub-domain depend on data in the adjacent sub-domain; therefore analogous to the idea of ghost points, we padded that shared memory block with ghost points (corresponding to solution values in adjacent sub-domains). In our implementation, adding ghost points (2 points at each boundary) results in a 20×16 block of shared memory. Note that data must be in the transpose form; however, since shared memory is already being used and a square thread block is operating on the sub-domain, the transpose is performed block-wise when transferring the data to global memory.

While we may apply the same procedure for computing $\mathbf{A}_j$, $\mathbf{a}^{n+1}_{(k),(,j)}$, and $\mathbf{b}^n_{(,j)}$ in (A.4), unlike computing $\mathbf{B}_i$, threads near either the x or y boundaries of the sub-domain depend on data in the adjacent sub-domain; therefore, the shared memory bank is padded with ghost points in both directions (20×20 in our implementation). For the $\mathbf{B}_j$ shared memory block, ghost points could be transferred from global memory to shared memory with little inefficiency; however, for the $\mathbf{A}_i$, $\mathbf{a}^{n+1}_{(k),(,j)}$, and $\mathbf{b}^n_{(,j)}$ shared memory blocks, memory transfer is inefficient with the additional ghost points. A faster approach is to subdivide the domain into sub-rectangles and assign each sub-domain a vector of threads e.g., in our implementation the sub-domain size is 32×15, where the 32 threads are mapped to 32 x values, and each thread loops through 15 y values, see Figure 5.2. Furthermore, we note that the y derivatives, at most, depend on five points ($j-2,\ j-1,\ j,\ j+1$ and $j+2$); therefore, instead of a (32+4)×(15+4) (sub-domain plus ghost points) shared memory block, we implement five 36×1 shared memory blocks. Similarly, function values and their derivatives require three points, therefore six (three each) 36×1 [7] shared memory blocks are used

[7] While only a 34×1 shared memory block is required to store function values plus ghost points, a 36×1 domain is chosen to align shared memory indices to those of the shared memory used to store the solution, simplifying coding.

for each nonlinear function (there are two in our model). While the initial iteration (first y value on sub-domain) requires transferring seventeen 36×1 blocks of data from global memory to shared memory, in subsequent iterations, only five 36×1 blocks of data are transferred from the global memory to shared memory: the solution, the two non-linear functions and their derivatives.

Note: It is interesting to note that numerical tests show that the choice of 15 in the sub-block size for $\mathbf{A}_i$, $\mathbf{a}^{n+1}_{(k),(,j)}$, and $\mathbf{b}^{n}_{(,j)}$ leads to the fastest computation time (seemingly independent of the thread block size), which is related to our implementation. To remove explicitly copying data between shared memory location, computations for each looped y value are grouped into a subroutine, and at each loop step, the input parameters are alternated by pointer manipulation. For example, for a generic three point method, first define $v_{-1} = u_{j-1}$, $v_0 = u_j$, and $v_1 = u_{j+1}$, where u is the global memory variable and v is the shared memory variable. Performing the following operations at the next three iteration steps (three cycle):

1. Compute $f(v_{-1}, v_0, v_1)$, and then set $v_{-1} = u_{j+2}$.

2. Compute $f(v_0, v_1, v_{-1})$, and then set $v_0 = u_{j+3}$.

3. Compute $f(v_1, v_{-1}, v_0)$, and then set $v_1 = u_{j+4}$.

It may be seen that by the third step, $v_{-1} = u_{j-1+3}$, $v_0 = u_{j+3}$, and $v_1 = u_{j+1+3}$, i.e., the definitions of the shared memory variables are realigned but offset by 3. Similarly, a five point method results in a five cycle. Recalling the combined stencil in Figure 5.2, the method is a three point method with respect to function values, and a five point method with respect to solution values; therefore, combining the 3 cycle and 5 cycle, results in a 15 cycle, the most efficient choice for the y domain size according to numerical tests.

APPENDIX B

RADIAL FOURIER TRANSFORM

In this section we give an overview of the procedure for computing the radial Fourier Transform used to analyze simulations in § 5.4.3. To map the magnitude of the 2D Fourier transform to the radial Fourier Transform, a one dimensional (1D) function of the magnitude of the wave number $q_r = \sqrt{q_x^2 + q_y^2}$, six processing steps are performed. The first four steps smooth the magnitude of the Fourier transform and map the smoothed data from a 2D Cartesian definition of the wavenumber to a 1D function of the magnitude of the wave number. The remaining two steps further smooth the data so as to reliably extract the local maxima.

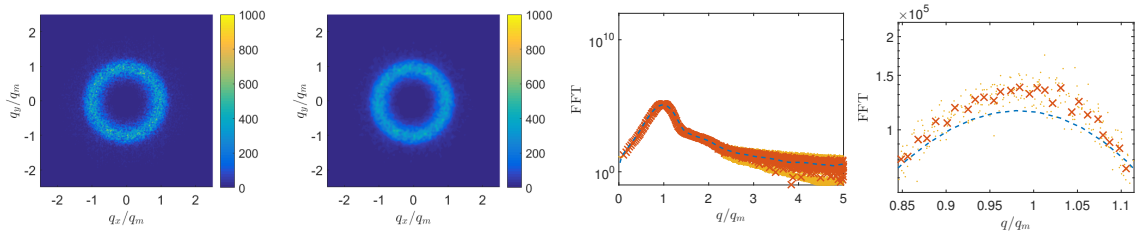

Figure B.1 a) An example the log of the magnitude of the two-dimensional Fourier transform. b) An example of smoothing the data in (a) using a convolution with a Gaussian filter. c) A plot of: i) the data in (b) mapped to a radial one-dimension function (yellow scatter plot) using equation (B.1); ii) a linear least squares fit of the scatter plot data to the piece-wise linear function (red '×' symbols); and iii) the piece-wise linear function smoothed with a moving average filter (dashed blue curve). d) Is a zoomed in version of subpanel (c) demonstrating the improved smoothness using the moving average filter.

First, the peak at the zero wave number is removed by subtracting the initial film thickness H_0, i.e., the magnitude of the Fourier transform of $\zeta(x, y) = h(x, y) - H_0$ is computed, an example of which is shown in Figure B.1a. Second, to reduce noise and smooth out the data, the magnitude of the Fourier transform data is convoluted with a

Gaussian function/filter. Third, the smoothed data, $\bar{\zeta}$ are mapped from the Cartesian coordinates (q_{x_i}, q_{y_j}) to polar coordinates (q_{r_i}, q_{θ_j}). Fourth, the polar coordinate data are mapped to a (radial) function $\bar{\bar{\zeta}}(q_{r_i})$, by averaging over the θ direction for a fixed q_{r_i}, i.e., we compute

$$\bar{\bar{\zeta}}(q_{r_k}) = \frac{1}{N_k} \sum_{(i,j)\in P_k} \bar{\zeta}(q_{r_i}, q_{\theta_i}) \ , \quad P_k = \{q_{r_i}, q_{\theta_i} \in \mathbb{R} | q_{r_i} = q_{r_k}\} \tag{B.1}$$

where N_k is the number of points in the set P_k. An example of (B.1) is given by the yellow scatter plot in Figure B.1c with Fourier transform data in Figure B.1a. To extract a local maximum (dominant wavenumber) numerically, sufficiently smooth data are required. To smooth the scattered data two final processing steps are performed: first, using a linear-least squares method, the scattered data are fitted to a piece-wise continuous function of the form

$$\bar{\bar{\bar{\zeta}}}(q) = a_k + b_k \frac{s - q_k}{q_{k+1} - q_k} \ , \quad \text{where} \quad s \in [0,1] \ , \quad q = q_k + s(q_{k+1} - q_k) \ , \tag{B.2}$$

and the domain is restricted to $q \in [0, 5q_m]$ (reducing computational cost). Note that we choose q_k's such that each interval contains 10 points. Denoting the number of intervals as K, continuity implies $b_k = a_{k+1} - a_k$ for $0 \leq k < K-1$ and choosing $a_0 = 0$ (i.e. $\zeta(q=0) = 0$) leaves K free parameters: b_{K-1} and a_k for $1 \leq k \leq K-1$, therefore the fitting procedure is fully determined.

An example of this fitting procedure is given by the red '$\times$' scatter plot in Figure B.1c. This step accurately captures the trend of the scattered data; however, we could not produce a sufficiently smooth function, see Figure B.1d for a comparison between the piece-wise continuous function (red '$\times$' symbols), and the additional smoothing step (dashed blue curve) discussed next. To smooth the piece-wise continuous function, the next step evaluates (B.3) on an equipartitioned grid of 400

points and smooths the data using a moving average filter. Specifically, we compute

$$\overset{\equiv}{\zeta}(q_k) = \frac{1}{2P+1} \sum_{p=-P}^{P} \overset{\equiv}{\zeta}(q_{k+p}) \tag{B.3}$$

where P is half the filter width, and the filter is applied three times with $P = 3, 2,$ and then 1.

To numerically extract the local maxima, a second order method is used to compute the derivative of the radial Fourier transform, and a combination of a bisection method and interpolation is used to find the roots of the derivative (critical points). To extract the local maxima, the first derivative test is used where the second derivative is computed numerically at the roots.

REFERENCES

[1] S. Schlagowski, K. Jacobs, and S. Herminghaus. Nucleation-induced undulative instability in thin films of nCB liquid crystals. *Europhys. Lett.*, 57:519, 2002.

[2] F. Vandenbrouck, M. P. Valignat, and A. M. Cazabat. Thin nematic films: Metastability and spinodal dewetting. *Phys. Rev. Lett.*, 82:2693, 1999.

[3] S. Herminghaus, K. Jacobs, K. Mecke, J. Bischof, A. Fery, M. Ibn-Elhaj, and S. Schlagowski. Spinodal dewetting in liquid crystal and liquid metal films. *Science*, 282:916, 1998.

[4] K. Jacobs, R. Seemann, and S. Herminghaus. *Stability and dewetting of thin liquid films*, pages 243–265. New Jersey, NJ: World Scientific, 2008.

[5] L. J. Cummings, T.-S. Lin, and L. Kondic. Modeling and simulations of the spreading and destabilization of nematic droplets. *Phys. Fluids*, 23:043102, 2011.

[6] J. A. Diez, A. G. González, and L. Kondic. On the breakup of fluid rivulets. *Phys. Fluids*, 21:082105, 2009.

[7] P. Ehrhand and S. H. Davis. Non-isothermal spreading of liquid drops on horizontal plates. *J. Fluid Mech.*, 229:365, 1991.

[8] L. Kondic. Instabilities in gravity driven flow of thin fluid films. *SIAM Review*, 45:95, 2003.

[9] L. Kondic and J. Diez. On nontrivial traveling waves in thin film flows including contact lines. *Physica D*, 209:135144, 2005.

[10] T.-S. Lin and L. Kondic. Thin films flowing down inverted substrates: Two dimensional flow. *Phys. Fluids*, 22:052105, 2010.

[11] T.-S. Lin, L. Kondic, and A. Filippov. Thin films flowing down inverted substrates: Three-dimensional flow. *Phys. Fluids*, 24:022105, 2012.

[12] T.-S. Lin, L. Kondic, U. Thiele, and L. J. Cummings. Modeling spreading dynamics of liquid crystals in three spatial dimensions. *J. Fluid Mech.*, 729:214, 2013.

[13] T.-S. Lin, L. J. Cummings, A. J. Archer, L. Kondic, and U. Thiele. Note on the hydrodynamic description of thin nematic films: strong anchoring model. *Phys. Fluids*, 25:082102, 2013.

[14] O. V. Manyuhina and M. Ben Amar. Thin nematic films: anchoring effects and stripe instability revisited. *Phys. Lett. A*, 377:1003, 2013.

[15] L. C. Mayo, S. W. McCue, and T. J. Moroney. Gravity-driven fingering simulations for a thin liquid film flowing down the outside of a vertical cylinder. *Phys. Rev. E*, 87:053018, 2013.

[16] S. P. Naughton, N. K. Patel, I. Seric, L. Kondic, T.-S. Lin, and L. J. Cummings. Instability of gravity driven flow of liquid crystal films. *SIAM Undergrad. Res. Online*, 5:56, 2013.

[17] U. Thiele, A. J. Archer, and M. Plapp. Thermodynamically consistent description of the hydrodynamics of free surfaces covered by insoluble surfactants of high concentration. *Phys. Fluids*, 24:102107, 2012.

[18] S. M. Troian, E. Herbolzheimer, S. A. Safran, and J. F. Joanny. Fingering instabilities of driven spreading films. *Europhys. Lett.*, 10:25, 1989.

[19] L. Yang and G. M. Homsy. Capillary instabilities of liquid films inside a wedge. *Phys. Fluids*, 19:044101, 2007.

[20] J. A. Castellano. *Liquid gold the story of liquid crystal displays and the creation of an industry.* Hackensack, NJ: World Scientific, 2005.

[21] B. Johnstone. *Japanese entrepreneurs and the forging of the electronic age.* New York, NY: Basic Books, 1999.

[22] Z. Liu, H. Lee, Y. Xiong, C. Sun, and X. Zhang. Far-field optical hyperlens magnifying sub-diffraction-limited objects. *Science*, 315:1686, 2010.

[23] P. Palffy-Muhoray. The diverse world of liquid crystals. *Phys. Today*, 60:54, 2014.

[24] M. A. Lam, L. J. Cummings, T.-S. Lin, and L. Kondic. Modeling flow of nematic liquid crystal down an incline. *J Eng. Math.*, 94:97, 2014.

[25] M. A. Lam, L. J. Cummings, T.-S. Lin, and L. Kondic. Three-dimensional coating flow of nematic liquid crystal on an inclined substrate. *Eur. J. Appl. Maths*, 25:647, 2015.

[26] M.-A. Y.-H Lam, L. Cummings, and L. Kondic. Stability of thin fluid films characterised by a complex form of effective disjoining pressure. *J. Fluid Mech.*, 841:925–961, 2018.

[27] M. Ben Amar and L. J. Cummings. Fingering instabilities in driven thin nematic films. *Phys. Fluids*, 13:1160, 2001.

[28] L. J. Cummings. Evolution of a thin film of nematic liquid crystal with anisotropic surface energy. *Eur. J. Appl. Maths*, 15:651, 2004.

[29] S. Mechkov, A. M. Cazabat, and G. Oshanin. Post-Tanner spreading of nematic droplets. *J. Phys.: Condens. Matter*, 21:464134, 2009.

[30] A. M. Cazabat, U. Delabre, C. Richard, and Y. Yip Cheung Sang. Experimental study of hybrid nematic wetting films. *Adv. Colloid Interface Sci.*, 168:29, 2011.

[31] D. van Effenterre and M. P. Valignat. Stability of thin nematic films. *Eur. Phys. J. E*, 12:367, 2003.

[32] C. Poulard and A. M. Cazabat. Spontaneous spreading of nematic liquid crystals. *Langmuir*, 21:6270, 2005.

[33] A. D. Rey and M. M. Denn. Dynamical phenomena in liquid-crystalline materials. *Annu. Rev. Fluid Mech.*, 34:233, 2002.

[34] F. M. Leslie. Theory of flow phenomena in liquid crystals. *Adv. Liq. Cryst.*, 4:1, 1979.

[35] U. Delabre, C. Richard, and A. M. Cazabat. Thin nematic films on liquid substrates. *J. Phys. Chem. B*, 113:3647, 2009.

[36] A. D. Rey. Generalized Young-Laplace equation for nematic liquid crystal interfaces and its application to free-surface defects. *Mol. Cryst. Liq. Cryst.*, 369:63, 2008.

[37] P. Ziherl and S. Žumer. Morphology and structure of thin liquid-crystalline films at nematic-isotropic transition. *Eur. Phys. J. E*, 12:361, 2003.

[38] B. Jerome. Surface effects and anchoring in liquid crystals. *Rep. Prog. Phys.*, 54:391, 1991.

[39] L. Kondic and J. Diez. Pattern formation in the flow of thin films down an incline: Constant flux configuration. *Phys. Fluids*, 13:3168, 2001.

[40] H.-C. Chang, E. A. Demekhin, and D. I. Kopelevich. Stability of a solitary pulse against wave packet disturbances in an active medium. *Phys. Rev. Lett.*, 75:1747, 1995.

[41] J. A. Diez, L. Kondic, and A. Bertozzi. Global models for moving contact lines. *Phys. Rev. E*, 63:011208, 2000.

[42] J. Q. Carou, N. J. Mottram, S. K. Wilson, and B. R. Duffy. A mathematical model for blade coating of a nematic liquid crystal. *Liq. Cryst.*, 35:621, 2007.

[43] A. Rapini and M. Papoular. Distorsion d'une lamelle nèmatique sous champ magnètique conditions d'ancrage aux parios. *J. Phys. Colloques*, 30:C4–54, 1969.

[44] T. P. Witelski and M. Bowen. ADI schemes for higher-order nonlinear diffusion equations. *Appl. Num. Math.*, 45:331, 2003.

[45] R. Seemann, S. Herminghaus, and K. Jacobs. Dewetting patterns and molecular forces: a reconciliation. *Phys. Rev. Lett.*, 86:5534, 2001.

[46] A. Sharma and R. Verma. Pattern formation and dewetting in thin films of liquids showing complete macroscale wetting: From "pancakes" to "swiss cheese". *Langmuir*, 20:10337, 2004.

[47] P. Ziherl, R. Podgornik, and S. Žumer. Pseudo-casimir structural force drives spinodal dewetting in nematic liquid crystals. *Phys. Rev. Lett.*, 84:1228, 2000.

[48] C. Favazza, J. Trice, R. Kalyanaraman, and R. Sureshkumar. Self-organized metal nanostructures through laser-interference driven thermocapillary convection. *Appl. Phys. Lett.*, 91:043105, 2007.

[49] J. D. Fowlkes, L. Kondic, J. Diez, and P. D. Rack. Self-assembly versus directed assembly of nanoparticles via pulsed laser induced dewetting of patterned metal films. *Nano Letters*, 11:2478, 2011.

[50] V. S. Ajaev and D. A. Willis. Thermocapillary flow and rupture in films of molten metal on a substrate. *Phys. Fluids*, 15:3144, 2003.

[51] Y. Wu, J.D. Fowlkes, P. D. Rack, J.A. Diez, and L. Kondic. On the Breakup of Patterned Nanoscale Copper Rings into Droplets via Pulsed-Laser-Induced Dewetting: Competing Liquid-Phase Instability and Transport Mechanisms. *Langmuir*, 26:11972, 2010.

[52] I. Seric, S. Afkhami, and L. Kondic. Interfacial instability of thin ferrofluid films under a magnetic field. *J. Fluid Mech. Rapids*, 755:R1, 2014.

[53] R. Seemann, S. Herminghaus, and K. Jacobs. Gaining control of pattern formation of dewetting liquid films. *J. Phys.: Condens. Matter*, 13:4925, 2001.

[54] U. Thiele, M. G. Velarde, K. Neuffer, and Y. Pomeau. Film rupture in the diffuse interface model coupled to hydrodynamics. *Phys. Rev. E*, 64:031602, 2001.

[55] J. A. Diez and L. Kondic. On the breakup of fluid films of finite and infinite extent. *Phys. Fluids*, 19:072107, 2007.

[56] N. V. Churaev. Contact angles and surface forces. *Adv. Colloid Interface Sci.*, 58:87–118, 1995.

[57] V. M. Starov. Equilibrium and hysteresis contact angles. *Adv. Colloid Interface Sci.*, 39:147–173, 1992.

[58] D. van Effenterre, R. Ober, M. P. Valignat, and A. M. Cazabat. Binary separation in very thin nematic films: Thickness and phase coexistence. *Phys. Rev. Lett.*, 87:125701, 2001.

[59] R. V. Craster and O. K. Matar. Dynamics and stability of thin liquid films. *Rev. Mod. Phys.*, 81:1131, 2009.

[60] J. N. Israelachvili. *Intermolecular and surface forces*. Academic Press, New York, 1992. second edition.

[61] V. S. Mitlin. Dewetting of solid surface: analogy with spinodal decomposition. *J. Colloid Interface Sci.*, 156:491, 1993.

[62] U. Thiele, A. J. Archer, and L. M. Pismen. Gradient dynamics models for liquid films with soluble surfactant. *Phys. Rev. Fluids*, 1:083903, 2016.

[63] D. Ausserré and J.-L. Buraud. Late stage spreading of stratified liquids: Theory. *J. Chem. Phys.*, 134:114706, 2011.

[64] B. Schulz and C. Bahr. Surface structure of ultrathin smectic films on silicon substrates: Pores and islands. *Phys. Rev. E*, 83:041710, 2011.

[65] U. Delabre, C. Richard, G. Guéna, J. Meunier, and A. M. Cazabat. Nematic pancakes revisited. *Langmuir*, 24:3998, 2008.

[66] M. Inoue, K. Yoshino, H. Moritake, and K. Toda. Evaluation of nematic liquid-crystal director-orientation using shear horizontal wave propagation. *J. Appl. Phys.*, 95:2798, 2002.

[67] A. D. Rey. The Neumann and Young equations for nematic contact lines. *Liq. Cryst.*, 27:195, 2000.

[68] K. B. Glasner and T. P. Witelski. Coarsening dynamics of dewetting films. *Phys. Rev. E*, 67:016302, 2003.

[69] F. Ruffino, A. Pugliara, E. Carria, L Romano, C. Bongiorno, C. Spinella, and M. G. Grimaldi. Novel approach to the fabrication of au/silica coreshell nanostructures based on nanosecond laser irradiation of thin au films on si. *Nanotechnology*, 33:045601, 2012.

[70] S. Saritaş, E. S. Özen, and A. Aydinli. Laser induced spinodal dewetting of ag thin films for photovoltaic applications. *J. Optoelectron Adv. M.*, 15:10, 2013.

[71] U. Thiele, K. Neuffer, Y. Pomeau, and M. G. Velarde. On the importance of nucleation solutions for the rupture of thin liquid films. *Colloid Surf. A*, 206:135–155, 2002.

[72] W. van Saarloos. Front propagation into unstable states. *Phys. Reports*, 386:29, 2003.

[73] P. Huerre. In J. E. Wesfreid, H. R. Brand, P. Manneville, G. Albinet, and Boccara N., editors, *Propagation in Systems Far from Equilibrium*. Berlin, Germany: Springer-Verlag, 1988.

[74] P. Huerre and M. Rossi. Hydrodynamic instabilities in open flows. In C Godréche and P. Manneville, editors, *Hydrodynamics and Nonlinear Instabilities*. Cambridge, UK: Cambridge University Press, 1998.

[75] C. Poulard, M. Voué, J. De Coninck, and A. M. Cazabat. Spreading of nematic liquid crystals on hydrophobic substrates. *Colloids and Surfaces A: Physicochem. Eng. Aspects*, 282:240, 2006.

[76] A. Münch. Detwetting rates of thin liquid films. *J. Phys.: Condens. Matter*, 17:309, 2005.

[77] R. M. L. Evans, W. C. K. Poon, and F. Renth. Classification of ordering kinetics in three-phase systems. *Phys. Rev. E.*, 64:031403, 2001.

[78] W. H. Press, S. A. Teukolsky, W. T. Vetterling, and B. P. Flannery. *Numerical Recipes in FORTRAN (2Nd Ed.): The Art of Scientific Computing*. New York, NY: Cambridge University Press, 1992.

[79] K. Mahady, S. Afkhami, and L. Kondic. A numerical approach for the direct computation of flows including fluid-solid interaction: Modeling contact angle, film rupture, and dewetting. *Phys. Fluids*, 062002:28, 2016.

[80] E. Polizzi and A. H. Sameh. A parallel hybrid banded system solver: the spike algorithm. *Parallel Comput.*, 32:177–192, 2006.

[81] D. Heller. Some aspects of the cyclic reduction algorithm for block tridiagonal linear systems. *SIAM J. Numer. Anal.*, 13:484496, 1975.

[82] U. Meier. A parallel partition method for solving banded systems of linear equations. *Parallel Comput.*, 2:33–34, 1985.

[83] M. J. Flynn. Some computer organizations and their effectiveness. *IEEE Trans. Comput.*, C-21(9):948–960, 1972.